AFFDL - TR - 70 - 1
PART I, VOLUME 2

STUDY AND DESIGN OF AN EJECTION SYSTEM FOR VTOL AIRCRAFT

PART I, VOLUME 2

ESCAPE SYSTEM PARAMETERS ANALYSES

I. L. Clinkenbeard
E. O. Cartwright, Jr.
C. R. Eldredge

Vought Aeronautics Division
LTV Aerospace Corporation

Technical Report AFFDL - TR - 70 - 1, PART I, VOLUME 2

APRIL 1970

AIR FORCE FLIGHT DYNAMICS LABORATORY
AIR FORCE SYSTEMS COMMAND
WRIGHT PATTERSON AIR FORCE BASE, OHIO

2lew

NOTICE

When Government drawings, specifications, or other data are used for any purpose other than in connection with a definitely related Government procurement operation, the United States Government thereby incurs no responsibility nor any obligation whatsoever; and the fact that the government may have formulated, furnished, or in any way supplied the said drawings, specifications, or other data, is not to be regarded by implication or otherwise as in any manner licensing the holder or any other person or corporation, or conveying any rights or permission to manufacture, use, or sell any patented invention that may in any way be related thereto.

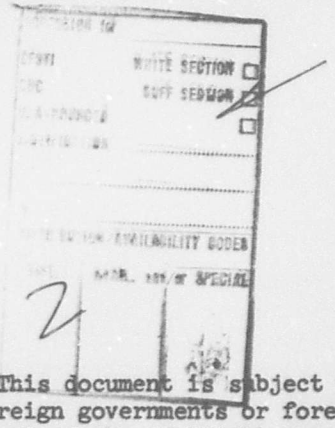

This document is subject to special export controls and each transmittal to foreign governments or foreign nationals may be made only with prior approval of the AF Flight Dynamics Laboratory (FDFR), Wright-Patterson AFB, Ohio.

The distribution of this report is limited because it describes the capabilities and limitations of crew escape concepts for aerospace vehicles in VTOL and conventional take off and landing situations.

Copies of this report should not be returned unless return is required by security considerations, contractual obligations, or notice on a specific document.

AFFDL - TR - 70 - 1

STUDY AND DESIGN OF AN EJECTION SYSTEM FOR VTOL AIRCRAFT

PART I, VOLUME 2
ESCAPE SYSTEM PARAMETERS ANALYSIS

I. L. CLINKENBEARD
E. O. CARTWRIGHT, JR.
C. R. ELDREDGE

FOREWORD

This report was prepared by the Vought Aeronautics Division of the LTV Aerospace Corporation, a subsidiary of Ling-Temco-Vought, Inc., under Air Force Contract F33615-69-C-1692. This contract was initiated under Project 1362, "Crew Escape for Flight Vehicles", Task No. 136203, "Crew Escape Techniques Research". The program was administered under the direction of Recovery and Crew Station Branch, Vehicle Equipment Division, Air Force Flight Dynamics Laboratory, Air Force Systems Command, Wright-Patterson Air Force Base, Ohio. Mr. B. J. White (FDFR) was the Air Force Project Engineer. Mr. W. K. Hawkins was the project engineer for LTV Aerospace Corporation.

This report covers work conducted during the period April 1969 to January 1970. It was submitted by the authors in January 1970.

The authors wish to express their gratitude to the following LTV Aerodynamics Engineers whose advice and assistance made an impossible task possible: Mrs. Eleanor Roch for her superb control of the computer program; Jim Lacy, for his contributions to the parachute simulation; Eddie Smart, for his description of seat tip-off and contributions to the development of the bridle equations.

The voluminous documentation of this project necessitates publication in several parts. The total documentation includes:

Part I

Volume 1 - VTOL Aircraft Equations and Failure Mode Analysis
Volume 2 - Escape System Parameters Analysis
Volume 3 - Computer Program User's Manual for VTOL Escape System Simulation

Part II

Volume 1 - Escape Seat Systems Concept Analysis
Volume 2 - Escape Seat Subsystems and Detail Drawings

This technical report has been reviewed and is approved.

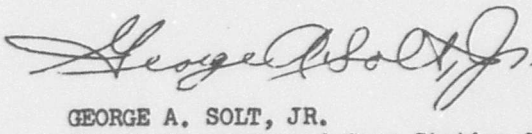

GEORGE A. SOLT, JR.
Chief, Recovery and Crew Station Branch
Vehicle Equipment Division
Air Force Flight Dynamics Laboratory

ABSTRACT

Ejection seat system differential equations are derived which describe the system trajectories from escape initiation to crew recovery. The equations are solved by digital computer through a numerical integration algorithm, and time history plots are presented for preliminary design information. Trajectory dynamics are computed for the seat as it is catapulted along a set of flexible rails constrained to translate with the aircraft. The impetus of seat-rail separation is simulated, and the airplane and seat trajectories are portrayed as the seat responds to a sequence of forces from rockets and parachutes. Acceleration loads on the man are computed throughout the time history, demonstrating the effects of parachute projection, snatch forces, and opening shocks as well as catapult and sustainer rocket forces. A comparative analysis of catapult and sustainer rocket techniques is included.

(Page iv is blank)

TABLE OF CONTENTS

TABLE OF CONTENTS (continued)

TABLE OF CONTENTS (continued)

LIST OF ILLUSTRATIONS

LIST OF TABLES

(Page xxii is blank)

BLANK PAGE

SECTION I

INTRODUCTION AND SUMMARY

The basic objective of this study is to design a complete ejection seat escape system that has the capability of providing safe crew escape from fighter/close support VTOL aircraft during emergencies in the VTOL and the low altitude, high speed flight regimes. The established ground rule is that the design must be achieved through a totally analytical effort employing a computer simulation which will account for all system interactions from aircraft failure occurrence to crew recovery.

To fulfill the ultimate design objective, a logical sequence of intermediate objectives were planned. In Part I, Volume 1, of this five volume report the first series of objectives were attained. They were:

- Select a hypothetical aircraft as a basis for escape system preliminary design.
- Establish the failure modes which influence the escape system concept.
- Provide a post-failure aircraft dynamic simulation for use in preliminary design of the escape system.

In this volume, another set of interim objectives are accomplished. They are:

- To conduct an analytical study program to arrive at approximations of the performance of drag chute stabilizers while operating behind an ejection seat in flight.
- To conduct an analysis that will constitute a detailed study of the separation dynamics of the ejection seat escape system as it travels along and separates from the guide rails.
- To evaluate ejection propulsion techniques through a comparative analysis of rocket/catapult designs, determining the consequences of the different design approaches on performance and trajectory.

The first objective of this volume, the drag parachute analysis, is discussed in Section III, where five candidate canopy types are compared and a "hemisflo" ribbon parachute is selected on the basis of its superior stabilizing and retardation characteristics throughout the crew escape envelope shown in Figure 1.

The second objective of this volume, the seat separation (tip-off) analysis, is reported in Section IV, where seat parameter variations from a nominal subject seat are analyzed and the effects shown through time history multiple plots.

The third objective of this volume, the ejection propulsion comparative analysis, is discussed in Section V, where rocket systems employing liquid, solid, and hybrid fuels are compared and a solid fuel type is selected.

The details explaining the attainment of these objectives are summarized in Section II and the system equations are given in Appendices I through IV.

The computer program mechanizing the equations in these first two volumes is documented in Part I, Volume 3 - "Computer Program User's Manual for VTOL Escape System Simulation."

In Part II, Volume 1 - "Escape Seat Systems Concept Analysis" the final escape system design is determined through computer analyses in which an optimum system configuration is derived by systematic parameter variations of the selected system components. For example, the hemisflo parachute selected as the basic drag device for the nominal seat analyzed in this volume is shown to be clearly superior to the other four candidate canopies but no concerted effort has been made to size the canopy for best performance, to select a specific bridle arrangement or to define the most desirable riser length.

The escape modes that were envisioned during the early stages of the program indicated that a variable total impulse and thrust as well as a stop-start capability might be required. Therefore, all three types of rocket motors,(liquids, hybrids, and solids) were investigated and compared with requirements. The solid rocket motor was selected for a comparative analysis of several ejection seat propulsion techniques. Because of the increased complexity and decreased reliability, the escape modes that were selected for final intensive investigation did not require the variable thrust, variable total impulse or the stop-start capability. The effects of the propulsion system configuration, thrust vector accuracy and installation requirements in the performance of the ejection seat are also discussed.

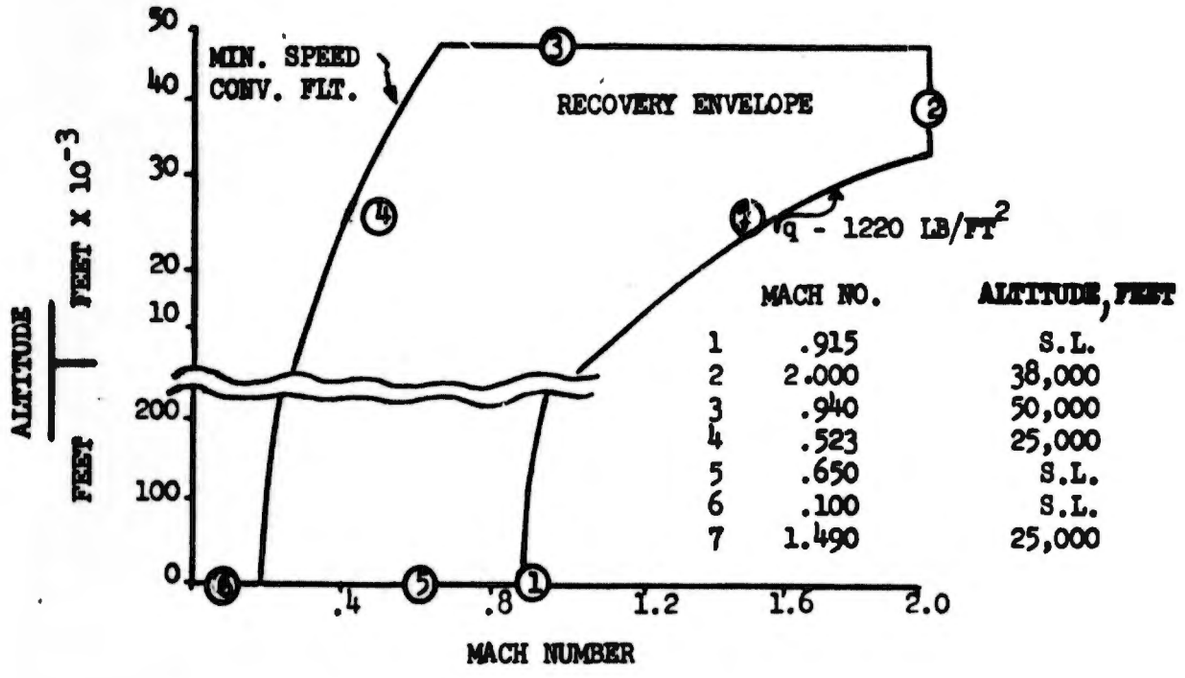

FIGURE 1 CREW RECOVERY ENVELOPE

SECTION II

BACKGROUND

Accomplishing the primary objective of designing a complete VTOL escape seat system analytically, without recourse to physical experimentation, is possible under the following conditions:

- Adequate test data already exist or are derivable through interpolation or rational extrapolation. If sufficient experimental data are obtained for each component of the system, the individual elements can be mathematically linked to form a complete system which can be made optimum through simulation experimentation in which the component characteristics are varied parametrically. For all the components analyzed in the subject escape system, voluminous data were available from the listed references, mostly from References 3, 4, and 9. These data were analyzed numerically and transformed to a format compatible with computer analysis and are included in this volume in the appendices.

- Enough computer capacity is available to contain the program and data needed to simulate a sequence of events as complex as a crew escape maneuver. For example, to investigate all conceivable emergencies occurring in the crew recovery envelope of Figure 1 an airplane simulation must be mechanized that will portray complete 6 degree-of-freedom inputs to the escape seat subsystem from hovering to supersonic flight. A full explanation is included in Part I, Volume 1. The rail system linking the airplane to the seat must be simulated in such a way that the mutual seat-rail reactions are represented with a fidelity sufficient to allow a confident appraisal of the effects of seat design changes. The rail equations are developed in Appendix III, where the dominant elements of a stiffness-rigidity matrix are used to enforce three dimensional geometric constraints on the seat-rail-airplane system as the airplane translates and rotates in inertial space while the seat moves along the rails. For crew recovery and seat-man retardation and stabilization, parachute equations must be developed in enough detail to clarify seat-man-parachute interaction effects as system parameters are changed. The equations of Appendix II are for any parachute moving in three dimensional inertial space under the influence of lift-drag forces, deployment and spreading gun forces, pilot chute forces, seat/man-to-canopy suspension line flexure and gravitational force. Rocket-catapult equations are needed that reveal realistic responses to system changes, such as seat weight or propellant charge variation. The rocket-catapult equations of Appendix IV account for thrust variations with propellant burn rate, internal pressure, piston friction, heat loss and grain geometry. These variables are, in turn, affected by external changes - such as seat weight variations which cause a change in the seat resistance to forces which then modify catapult piston rate which is then reflected in volume and pressures variations which cause a change in the burn rate, etc. Finally, six degree-of-freedom equations for the seat-man combination and man-alone are needed to assess the crew survival and injury potential when system components - such as catapult

propellant charge - are modified. Appendix I is a presentation of the seat/man equations. In mechanizing a computer program of this magnitude, an IBM S/360 requiring 260,000 bytes of core storage was employed.

- Finally, a massive amount of data is generated by the computer in analyzing a system with so many variables and these data must be presented in a form assimilable by the human brain in time to respond with design modifications. Plots, cross-plots and multiple plots are more easily interpreted than tabulated data and the computer program was linked to an automatic plotter to facilitate system design.

The computer program generated under the above mentioned philosophy has been used to analyze the responses of a typical high performance VTOL vehicle to a variety of deterministic failure modes, reported in Part I, Volume 1, of this five volume report. The critical failure modes discovered in the aircraft analysis are employed to test the feasibility of the escape system design reported in Part II, Volume 1 - Escape Seat System Concept Design. To achieve the interim objectives of the report now under discussion, (Part I, Volume 2) the critical failure modes are not necessary; therefore, the aircraft responses are merely reactions to rocket-catapult forces and rail transmitted forces and moments from the escape seat as it reacts to system inputs. For example:

- The first objective, the drag parachute study, is realizable better if a complex aircraft failure mode does not obscure the essential nature of each parachute performance while operating behind an ejection seat in flight. The intrinsic stability and deceleration traits of a particular canopy are not changed by the dynamics of the retarded body; consequently, in this volume, standard aircraft initial conditions are chosen for escape initiation and the canopy type is selected under these controlled conditions. The selection procedure is explained in Section III of this report.

- The second objective, evaluation of seat tip-off effects, is attained from a standard airplane hovering condition using a nominal escape seat configuration with systematic variation of seat geometry, catapult stroke, catapult thrust, sustainer rocket thrust and seat weight and inertia values. The basic superiority of a particular slider block-catapult stroke relationship is not changed by the onset of seat aerodynamic forces or increased airplane stability; therefore, the analysis of the tip-off effects for the complete flight envelope shown in Figure 1 is presented for the final escape seat design detailed in Part II, Volume 1, rather than in this volume. The results of the present investigation are discussed in Section IV of this report.

- The third objective, the comparative analysis of ejection propulsion techniques, is discussed in Section V of this volume.

SECTION III

PARACHUTE TYPE SELECTION

The shape of an escape seat must conform to human and airplane geometric constraints that inevitably produce an aerodynamically unstable seat for which a stabilization subsystem must be provided to prevent tumbling. The tumbling may impose destructive loads on the human occupant for high dynamic pressure escape conditions. At all conditions, when safe escape altitudes are to be achieved by sustainer rocket, stabilization must be afforded to preclude driving the seat earthward. In addition to stabilization, some method of retardation is necessary to reduce the seat or occupant speed to a safe earth impact terminal velocity.

The objective of this section is to determine the requirements for one method of stabilization and retardation -- a drag parachute. The objective is attained by computer analysis of five parachute canopy types (Figures 2 and 3) operating within the crew escape envelope shown in Figure 1. A nominal escape seat configuration (Figure 224) is used, which will suffice to demonstrate the superiority of a particular type of parachute. The final bridle arrangement, parachute size, reefing requirements, etc. are chosen through parametric studies of the complete escape system in Part II, Volume 1 - "Escape Seat Systems Concept Analysis".

1. DRAG PARACHUTE

The decision to use a parachute for escape seat retardation and stabilization was influenced by the following considerations:

- The textile parachute canopy is lighter in weight and occupies a smaller packed volume for a comparable drag area than most other deceleration and stabilization devices.

- Other mechanisms for short-term trajectory control, such as deployable fins, rockets, ballutes, gyroscopic stabilization, or seat-airplane tethering, suffer the liabilities of excessive control complexity or restricted operational envelopes when compared to the parachute.

- The history of parachute research is well documented and sufficient reliable data have been published to instill confidence in an escape seat system designed solely from an analytical approach.

Once the decision to use a drag parachute has been made, a particular type must be chosen or synthesized from the many configurations which have been built from the two textile types -- solid cloth and ribbon. From the many designs available, five basic configurations may be selected which encompass the full range of proven parachute designs used for retardation and stabilization within the complete crew recovery envelope (Figure 1). These five designs may be categorized as:

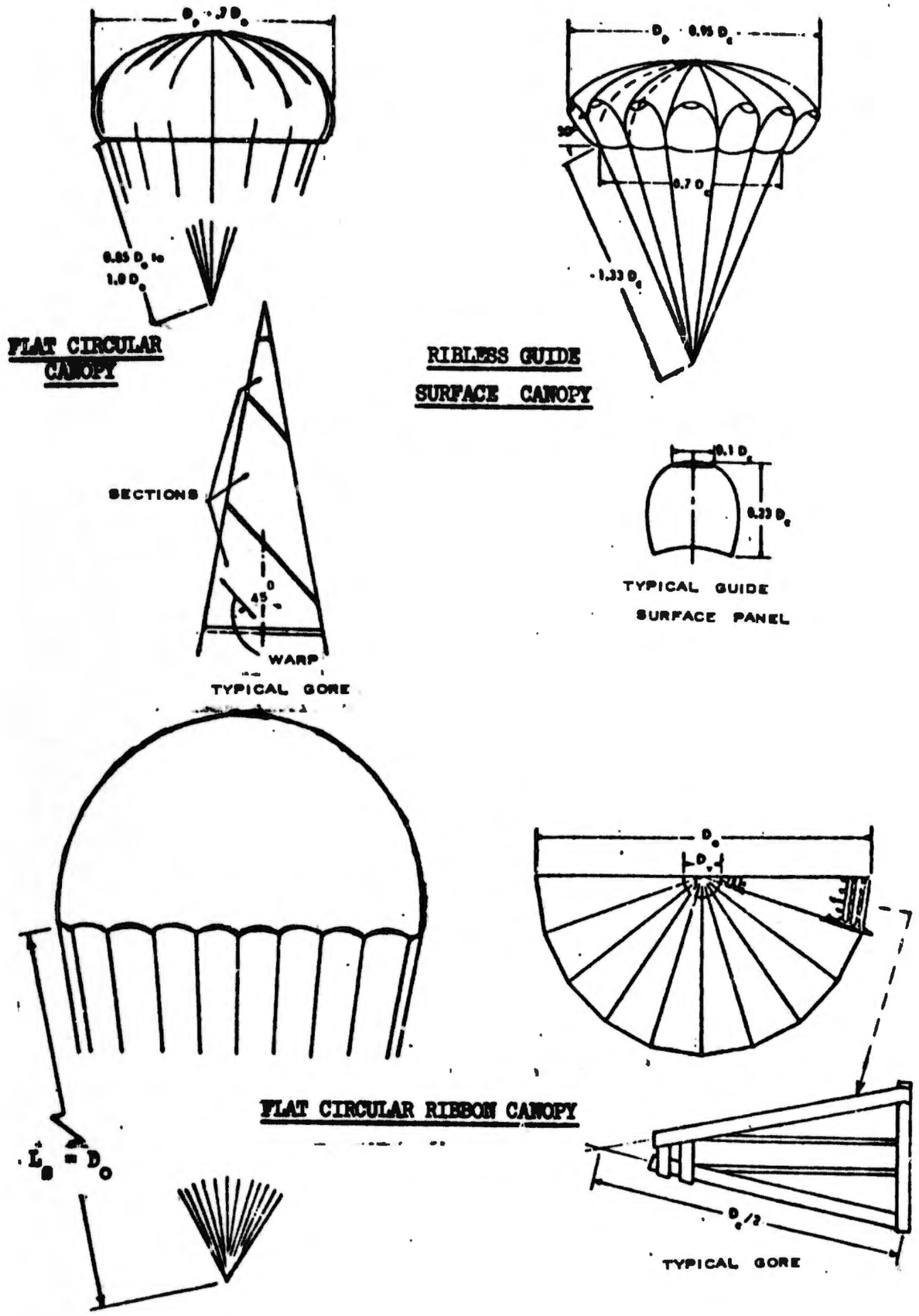

FIGURE 2 CANDIDATE DRAG PARACHUTES

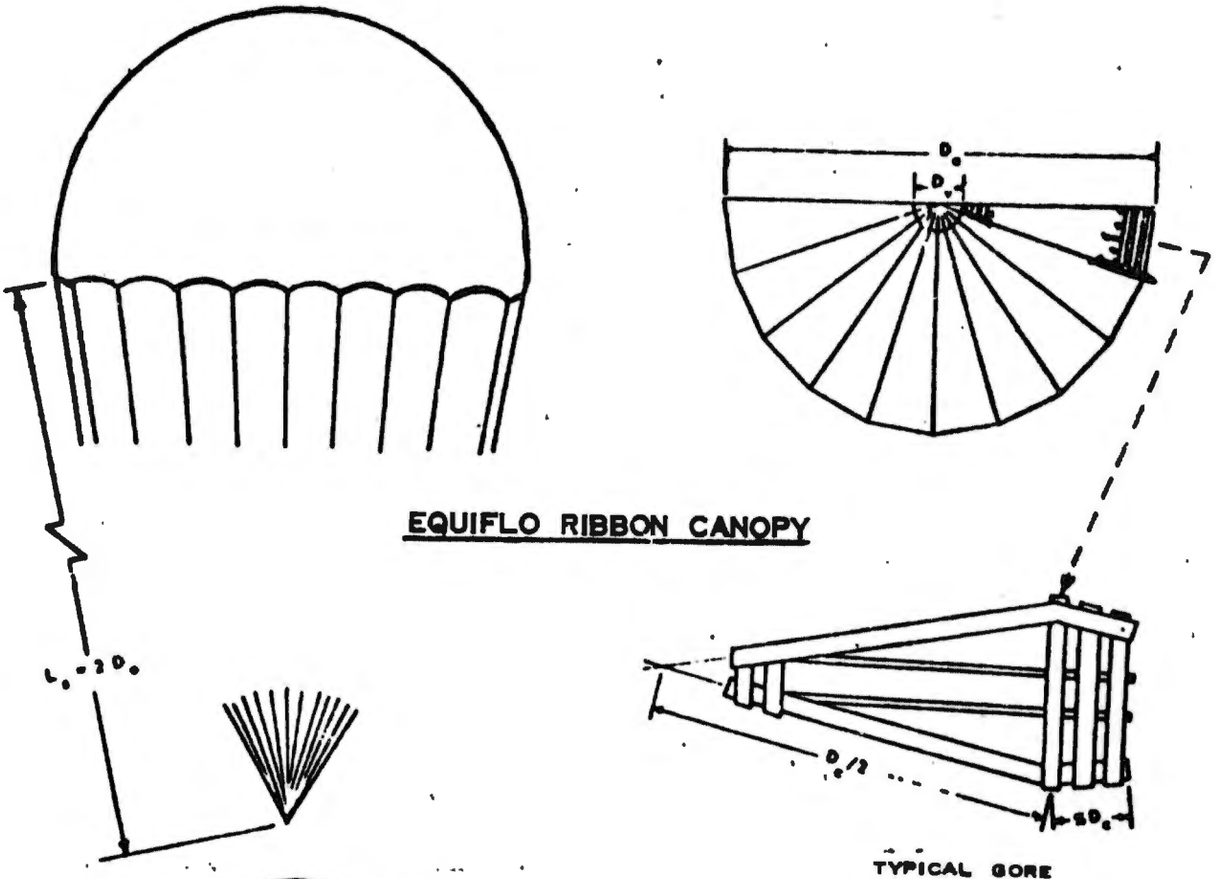

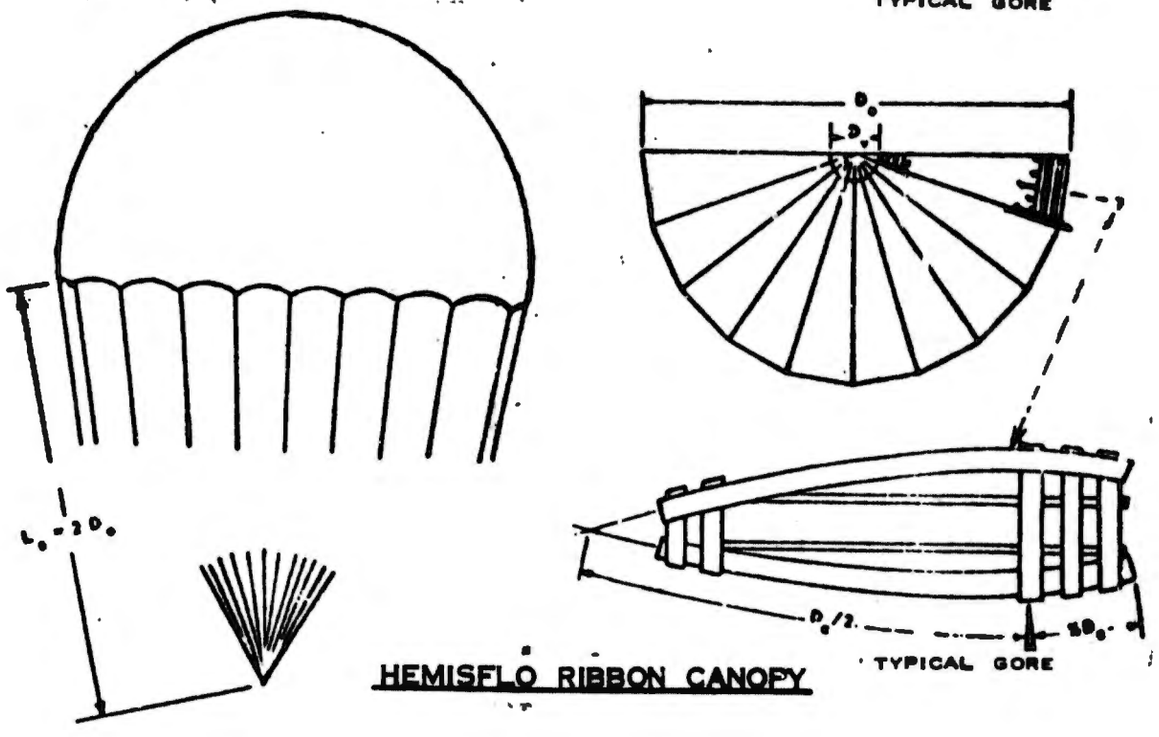

FIGURE 3 CANDIDATE DRAG PARACHUTES

- o Solid Cloth Types
  - Flat Circular Cloth
  - Guide Surface

- o Ribbon Types
  - Flat Circular Ribbon
  - Equiflo
  - Hemisflo

For all except the flat circular solid cloth parachute, the length of the shroud lines is a fixed percentage of the diameter, but the bridle geometry may be adjusted, the riser length changed, and the parachute size varied. The effects on parachute performance of varying these parameters may be determined by time history comparisons of the 12 Cases chosen for computer analysis tabulated in Table I.a. For any of the five parachute types, the parameters in Table I.a may be used to optimize the configuration throughout the crew recovery envelope by the comparisons indicated in Table I.b.

The computer analysis consists of time histories integrated from the differential equations presented in Appendices I through IV. The time histories are plotted to show the seat-man-airplane spatial orientations and positions, along with the acceleration loads inflicted on the man as the seat reacts to catapult, rockets, parachutes, and rail forces and moments.

Each time history is begun with the first movement of the seat relative to the rails, with the aircraft trimmed longitudinally for 1 g level flight and with an off-trim sideslip angle of 1° to excite all 6 seat degrees of freedom. The trimmed condition provides a standard basis for evaluating parachute performance, a basis which would be obscured if a complex aircraft failure mode were initiated. The subsequent aircraft motions are the result of catapult and seat-rail reactions only, the airplane controls remaining fixed.

The initial travel up the rails is by propellant actuated catapult. At the end of the catapult stroke, a sustainer rocket fires, except for Case 2 in which the sustainer burn is suppressed. At the first opportunity, before the seat is separated from the rails, the drag parachute is projected by a rocket attached to a deployment bag. At first line stretch, the rocket strips off the deployment bag and the parachute begins filling aerodynamically. A four-line bridle is used for all parachutes to assure axial pilot load factors during the initial stabilization phase, as required by paragraph 3.4.2.4.b, Reference 5. All time histories are terminated after one second, a time length sufficiently long to assess the parachute retardation and stabilization capability.

Each parachute type is sized to provide the same area drag coefficient in low subsonic flight at zero parachute angle of attack. This requires a larger size for the less efficient parachutes, with a resulting weight variation. Because compressibility and stability affect the drag efficiency differently for each canopy type, the basic area drag coefficient is not realized in the dynamic environment of an escape operation. The relative performance degradation from these dynamic influences is revealed by time

TABLE I.a

PARACHUTE PARAMETER SCHEDULF

Canopy Type	Case	Alt	Mach No.	Dyn. Pres.	Diam. (proj.)	Ca We
Ribless Guide Surface	1	S.L.	.915	1220	2.95	6.
	2					
	3					
	4					
	5	38000	2.0			
	6	50000	.94	150		
	7,(12)	25000	.523(1.49)	150(1220)		
	8	S.L.	.65	626		
	9		.10	15.0		
	10		.915	1220	4.32	1
	11				6.11	1
Flat Circ. Cloth	1	S.L.	.915	1220	2.22	1
	2					
	3					
	4					
	5	38000	2.00			
	6	50000	.94	150		
	7,(12)	25000	.523(1.49)	150(1220)		
	8	S.L.	.65	626		
	9		.10	15.0		
	10		.915	1220	3.15	
	11				4.45	
Flat Circ. Ribbon	1	S.L.	.915	1220	2.95	
	2					
	3					
	4					
	5	38000	2.00			
	6	50000	.94	150		
	7,(12)	25000	.523(1.49)	150(1220)		
	8	S.L.	.65	626		
	9		.10	15.0		
	10		.915	1220	4.32	
	11				6.14	
Equiflo	1	S.L.	.915	1220	3.04	
	2					
	3					
	4					
	5	38000	2.00			
	6	50000	.94	150		
	7,(12)	25000	.523(1.49)	150(1220)		
	8	S.L.	.65	626		
	9		.10	15.0		
	10		.915	1220	4.45	
	11				6.27	
Hemisflo	1	S.L.	.915	1020	3.18	
	2					
	3					
	4					
	5	38000	2.00			
	6	50000	.94	150		
	7,(12)	25000	.523(1.49)	150(1220)		
	8	S.L.	.65	626		
	9		.10	15.0		
	10		.915	1220	4.66	
	11				6.60	

(ALL SYMBOLS DEFINED IN APPENDIX II, SEC

* Distance from bridle apex to parachute c.g.

** The distance from the seat to the parachute c.g. divided by the seat height.

TABLE I.a
PARAMETER SCHEDULE

	Diam. (proj.)	Canopy Weight	R_{L_o} *	L_{c_s}/D** S	Sustainer Rocket
)	2.95 ↓ 4.32 6.11	6.00 ↓ 10.0 18.2	10' ↓ 3.33' 22' 10' ↓ 22' ↓	3 ↓ 1 6 ↓ 6 ↓	Burn Not Burn Burn ↓
)	2.22 ↓ 3.15 4.45	1.80 ↓ 3.70 7.50	10' ↓ 3.33' 22' 10' ↓ 22' ↓	3 ↓ 1 6 3 ↓ 6 ↓	Burn Not Burn Burn ↓
)	2.95 ↓ 4.32 6.14	5.22 ↓ 12.50 25.00	10' ↓ 3.33' 22' 10' ↓ 22' ↓	3 ↓ 1 6 3 ↓ 6 ↓	Burn Not Burn Burn ↓
)	3.04 ↓ 4.45 6.27	5.28 ↓ 12.68 26.95	10' ↓ 3.33' 22' 10' ↓ 22' ↓	3 ↓ 1 6 3 ↓ 6 ↓	Burn Not Burn Burn ↓
)	3.18 ↓ 4.66 6.60	5.90 ↓ 14.04 29.94	10' ↓ 3.33' 22' 10' ↓ 22' ↓	3 ↓ 1 6 3 ↓ 6 ↓	Burn Not Burn Burn ↓

NED IN APPENDIX II, SECTION II)

eight.

(Page 10 is blank)

B

TABLE I.b

PARACHUTE OPTIMIZATION

PARAMETERS	PARAMETER EFFECTS
Sustainer Rocket Burning	Compare Cases 1 and 2 from Table I.a.
Parachute Distance Aft of Seat	Compare Cases 1, 3 and 4 from Table I.a.
Mach Number	Compare Cases 1, 5 and 12 from Table I.a.
Dynamic Pressure	Compare Cases 1, 8 and 9 from Table I.a.
Altitude	Compare Cases 6, 7 and 9 from Table I.a.
Parachute Diameter	Compare Cases 4, 10 and 11 from Table I.a.

history comparison plots, enabling the selection of an optimum parachute for use within the operational flight envelope (Figure 1).

The drag parachute comparison discussion begins with paragraph 1.a(3), "Solid Cloth Performance Comparisons"; but before beginning that analysis an explanation of the choice of variables displayed in the time histories is in order. To help understand this explanation refer to time histories 8 through 31 which are representative of the computer output for each of the 12 computer cases, the plotted variables being the same for each case.

Figures 8 through 11 are plots and trajectory cross-plots of the earth axis relative position of the seat-man center of gravity (cg) and the tip of the airplane vertical tail. (Reference 5, paragraph 3.4.2.4 Propulsion subsystem. "The ejection seat system shall be provided with a rocket-catapult propulsion subsystem with sufficient impulse to assure aircraft tail clearance throughout the performance envelope....")

Figures 12, 13, and 14 are load factor components at the seat bucket. (Reference 5, paragraph 3.4.2.12 Acceleration limitations. "The acceleration limits defined herein pertain to acceleration inputs measured at or near the seat bucket . . . The limits specified . . . are not nominal limits for 'no injury' but rather are maximum limits beyond which disabling injury can be expected. ") Figure 4 is a chart for quickly determining the probable load factor acceptability. Reference 5, with acceleration criteria which are more cumbersome to apply, must be the final arbiter, however.

Figure 15 is a plot of the Dynamic Response Index (DRI) of the human vertebral column. (Reference 5, paragraph 3.4.2.12.1 Catapult acceleration. "The acceleration imposed on the seat occupant parallel to the spine (eyeballs down) by the ejection rocket catapult shall be limited in terms of Dynamic Response Index ... a. The mean acceleration-time history generated at a rocket catapult temperature of 70°F shall not produce a DRI value in excess of 18.0. The maximum allowable DRI ... shall not exceed 21.0. b. The mean acceleration-time history generated at a rocket catapult temperature of 200°F shall not produce a DRI value in excess of 22.2. The maximum allowable DRI ... at catapult temperatures of 200°F shall not exceed 25.4." Paragraph 3.4.2.12.2 Seat acceleration after separation. "The accelerations measured on the seat by the combination of rocket catapult thrust and aerodynamic forces shall not exceed the limits specified in ....") Paragraph 6.4.1 of Reference 5 defines the DRI in detail. The equations are given in Appendix I of this report.

Figure 16 is a seat airspeed time history, showing the retardation effectiveness of each parachute when operating against the acceleration capabilities of rockets and catapults.

The distance from the bridle apex to the parachute cg is given by the time history plot of Figure 17. Until the parachute hits line stretch, a point in space behind the seat is computed as the bridle apex reference point. The apex point moves as if rigidly attached to the seat until line stretch and, thereafter, translates relative to the seat-subject to geometric contraints to maintain tension in the lines of the bridle. Therefore, at

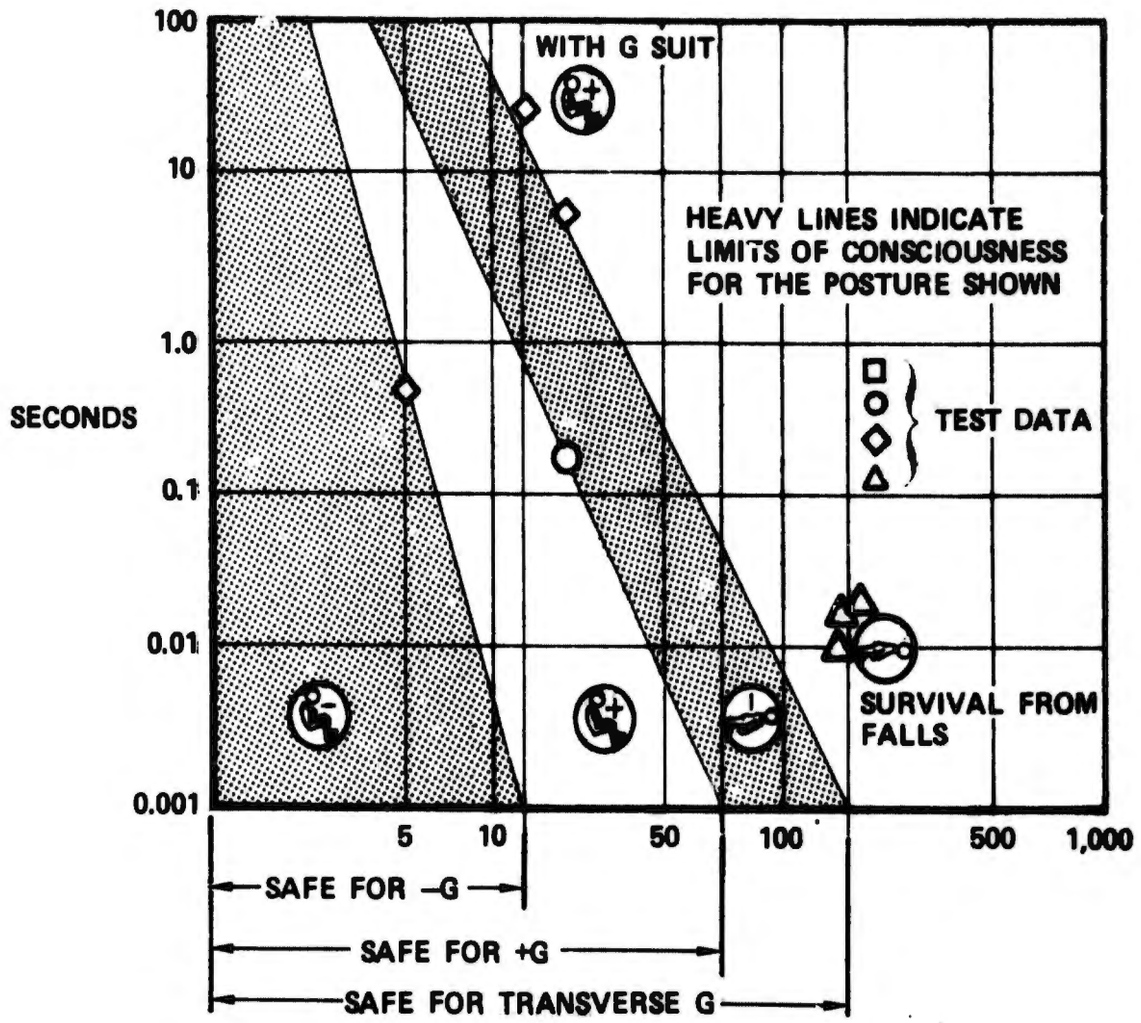

NOTE MIL-S-9479A PREFERRED

FIGURE 4 ACCELERATION LIMITS OF THE HUMAN BODY

time history initiation, the parachute packed location will be in front of the apex reference point. At parachute ejection time, the reefed parachute moves aft toward the reference apex, passes it and continues aft, still reefed, until line stretch. The overshoot at line stretch is the combined effects of line elasticity and parachute "squidding". The reaction on the seat from this overshoot is an acceleration spike called a "snatch" force (Figures 12, 13, 14). For heavy parachutes operating at low q conditions, repeated snatch forces can occur as line flexure snaps the parachute back against a light drag force to a position too close to the seat for tension to be maintained in the lines. With no line compression opposing the drag force, the parachute again moves outward to a second, third, etc., line stretch. At low q conditions, the ribbon parachutes take much longer to inflate than the flat circular cloth canopy and the resulting slow drag build up combined with the heavier weight of the ribbon type aggravates the repeated snatch force phenomenon.

Figures 18 and 19 are the line-of-sight azimuth and elevation angles from the seat to the trailing parachute. These angles are more revealing of the system dynamic stability than the parachute angle of attack because the seat-parachute relative angular motion is shown while the parachute angle of attack is with respect to the relative wind. For example, the parachute could trail perfectly into the relative wind but a bad bridle arrangement or asymmetrical rocket thrust could cause seat angular excursions with respect to the parachute. These angles can be visualized easily if one thinks of positioning himself, facing aft in the seat axis system, with his eyes at the bridle apex. The parachute is then located by traversing his line of sight laterally - in azimuth - until the parachute, the line of sight, and the seat vertical axis lie in the same plane. The line of sight is then elevated or depressed until it intersects the parachute. Right azimuth angles are positive and the elevation angle is positive looking up.

The seat-man climb rate, Figure 20, is useful information for determining the loads at earth impact and the rocket-catapult seat-rail separation effectiveness. These time histories, however, are not run to earth impact because this is not necessary for drag parachute comparisons.

Figures 21, 22, and 23 are the Euler angles referencing the seat-man angular orientation with respect to the earth through a conventional yaw-pitch-roll order of transformation. The angles are computed from integrated direction cosines, Appendix I, Equation 15. A common mistake in interpreting the Euler angles is to consider only one, such as the bank angle, in visualizing an airplane or seat orientation. A zero bank angle does not mean that the seat is in straight and level flight. One must consider all three angles at the same time point in the same yaw-pitch-roll order in which the angles were developed. Obviously, any order of transformation could have been used, with the proviso that they be interpreted in the proper order.

Figures 24, 25, 26 and 27 are plots and cross-plots of the seat-man earth axis position. For drag parachute selection purposes, these variables are not as important as the seat-airplane relative positions shown in Figures 8 through 11. For a trajectory run to terminal velocity, however, the earth axis positions assume paramount significance.

The seat-man aerodynamic angles are shown in Figures 28 and 29. One interpretation of paragraph 3.4.2.5.b, Reference 5, implies that the aerodynamic angles must be shown. (The paragraph states, in part -- "Stabilization subsystem ... Damped oscillations about the neutral direction of aerodynamic deceleration shall not exceed 20° in the pitch and yaw plane.) This paragraph could also be construed to mean the Euler angles, but repeated use of the word "aerodynamic" and exclusion of the roll angle argue against this interpretation.

The drag parachute angle of attack and area drag coefficient are portrayed in Figures 30 and 31. The angle of attack - Appendix II, Equation 24 - is the key variable through which the parachute aerodynamic stability is revealed. A lower tangential force coefficient will result in larger angles and a normal force static instability will force the parachute away from zero angle of attack. The area drag coefficient (Figure 31) computed from the normal force and tangential force coefficients from Equation 28, Appendix II, shows the parachute retardation effectiveness. The effects of angle of attack, Mach number, and seat-parachute relative position on drag effectiveness may be ascertained by comparing the drag coefficient with the appropriate variables previously discussed.

a. Solid Cloth Types

The solid cloth parachutes (Figures 2 and 3) are characterized by high opening shock loads relative to ribbon parachutes, both subsonically and supersonically, because of low effective porosity. Supersonically, the solid cloth type suffers greater drag attenuation than the ribbon parachutes. The advantages of the solid cloth parachute are emphasized at low subsonic airspeeds where the greater tensile strength of the closely woven mesh provides reduced weight relative to ribbon parachutes for comparable drag. The lighter weight results in lesser snatch forces and faster damping of parachute elastic induced oscillations, and filling times are shorter than ribbon types because of the lower effective porosity and lighter weight.

(1) Flat Circular Cloth, General

The flat circular solid cloth canopy is the most widely used general purpose parachute in the low subsonic regime, where its static instability in normal force near zero angle of attack is not critical and the dynamic pressure is low enough to preclude destructive opening shocks. At high subsonic and supersonic speeds, the normal force instability is great enough to cause this parachute to trail the seat at angles of 20-30 degrees, whipping erratically from stable trim angles at the high angles of attack through the unstable region (between about 0-20°, depending on the porosity) to other stable trim angles. Figures 5 and 6 are typical tangential force and normal force coefficient curves useful in understanding this phenomenon.

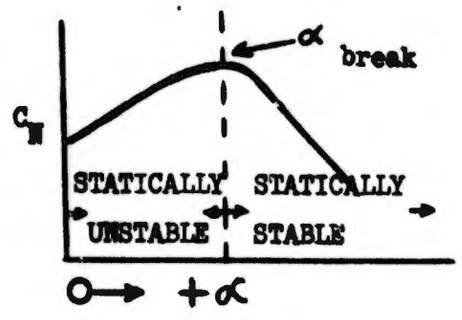

FIGURE 5
TYPICAL PARACHUTE NORMAL FORCE COEFFICIENT

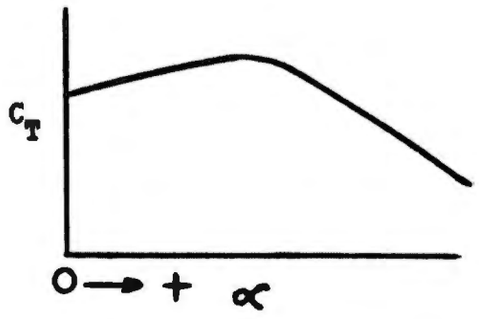

FIGURE 6
TYPICAL PARACHUTE TANGENTIAL FORCE COEFFICIENT

From Figure 7 it can be seen that the parachute-seat system will be in equilibrium when the force reaction, Fsp, from the seat exactly cancels the parachute tangential force and normal force. (For discussion purposes only, all other forces such as gravity are ignored.) However, from Figure 5 the statically unstable normal force will drive the system toward dynamic instability with any infinitesimal disturbance until the angle of attack becomes greater than α_{break} at which point the system becomes statically stable and trims at some large angle of attack until a seat-parachute relative movement reduces the angle of attack again to the unstable region. Large rolling, pitching, and yawing escape seat motions with repeated high load factor transients are the consequences of this kind of regional instability.

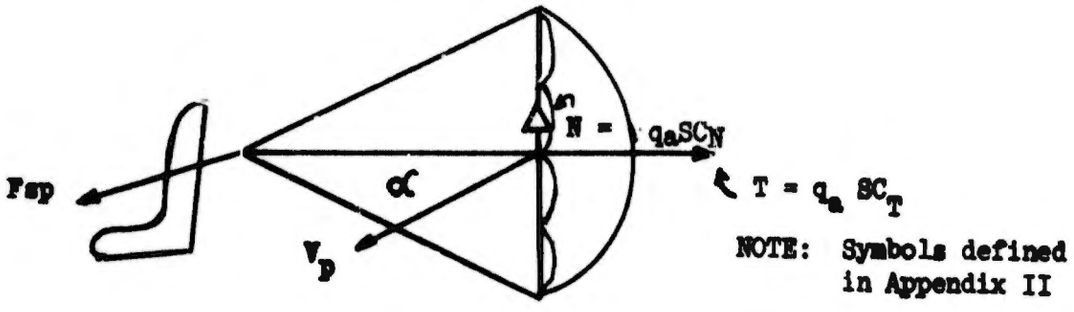

NOTE: Symbols defined in Appendix II

FIGURE 7
SEAT PARACHUTE TRANSIENT EQUILIBRIUM CONDITION

(2) Guide Surface, General

The guide surface parachute (Figures 2 and 3) is a solid cloth type which becomes statically stable in normal force at much lower angles of attack than the flat circular parachute. By increasing porosity, static stability is achieved at the expense of increased filling time. The stability is accomplished by joining guide surface panels to the roof panels, leaving a ring of vents around the outer diameter of the gores. The air flow through the vents keeps the guide surfaces inflated, increasing the static stability through the larger normal force restoring contribution. The opening shock is reduced by about 30% relative to the flat circular canopy because of the increased air flow, and opening reliability is not appreciably degraded.

The ribbed guide surface parachute is an intricate design, more difficult to manufacture than the ribless guide surface type, with enhanced stability. The increase in stability, however, is not great enough to warrant the attendant manufacturing and maintenance complications; consequently, only the ribless guide surface canopy is considered in the following analysis.

(3) Solid Cloth Performance Comparisons

For the purpose of eliminating a parachute type from further consideration, all 12 Cases from Table I need not be analyzed. For example, comparing two parachutes for Case 1 shows their relative subsonic performance at the highest dynamic pressure encountered in the crew recovery envelope (Figure 1). Comparing the same two parachutes for Case 5 will demonstrate the relative supersonic performance at the same high q (dynamic pressure). The time histories plotted in Figures 8 through 31 were run with the parameters from Case 1 to show the relative merits of the flat circular cloth and the ribless guide surface in high q subsonic flight. Figures 32 through 55 are the time histories for Case 5, the supersonic high q condition, through which the same two parachutes may be compared.

For a subsonic high dynamic pressure escape environment (Case 1) Figures 12 through 15 demonstrate graphically that the flat circular cloth parachute inflicts larger load factors on the human passenger than the ribless guide surface canopy. The spinal compression factor, Figure 15, is about twice as large, exceeding the limits of human tolerance (Reference 5) near the time point at 0.32 second. The relatively large load factors and vertebral flexure are attributable to the comparatively low dynamic stability of the escape system when employing the flat circular canopy with its regional static instability. This low stability is evidenced by the poor trailing angles plotted in Figures 18 and 19. The guide surface parachute stabilizes the seat in yaw (Figure 18) nearly perfectly and trails predictably below the seat (Figure 19) -- as it should, with the sustainer rocket increasing the seat altitude (Figure 24). Figures 28 through 31 contain additional evidence of the stabilizing and retarding superiority of the guide surface type. Figure 30 is the parachute angle of attack which demonstrates the intrinsic stability level of both parachutes, a level which will remain about the same regardless of the object being decelerated because the angle is with respect to the relative wind.

Characteristically, the flat circular parachute develops an angle of attack of about 35° (which would be a little less if the seat were not climbing), a trait which has been observed empirically for parachutes of this type with diameters less than 32 ft. (Reference 4). Although the basic drag coefficient is the same for both parachutes, the full drag performance (Figure 31) is not realized for the flat circular type because of the development of the large angle of attack. The drag coefficient (Figure 31) shows about 20% less drag capability of the flat circular, in addition to the 29% decrement suffered by both parachutes from the seat wake effect (Figure 312). The seat aerodynamic angle (Figures 28 and 29) are well within the implied requirements of paragraph 3.5.2.5.b of Reference 5 for the guide surface parachute, but both angles exceed the specified ±20° limit for the flat circular parachute; however, at this stage of the analysis, no effort has been made to adhere to all the military specifications of Reference 5. It is expected that improved performance will be obtained for either parachute by modification of the bridle-riser geometry or parachute size, and that the required changes can be determined through investigation of all 12 Cases from Table I. At this point, the only purpose is to compare two parachutes operating in similar environments with the intent of selecting the better one for further study.

For a supersonic high dynamic pressure escape environment (Case 5), Figure 55 demonstrates the drag reduction effects of compressibility (Figure 303 Appendix II) when an attempt is made to deploy solid cloth parachutes at extreme Mach numbers. The drag performance of the flat circular type is reduced by 80% to an area drag coefficient of about 1.0 near zero angle of attack. (A 29% reduction from seat wake effects combined with a 2% increase from an altitude induced porosity decrement resulted in a basic area drag coefficient of 5.07 before accounting for Mach number losses.) Under the same conditions, the guide surface drag loss is 71%. (In contrast to the porosity induced <u>increase</u> in drag coefficient for the flat circular canopy, a <u>decrease</u> of 3% is caused by the smaller porosity in the guide surface parachute.) Note the characteristic increase of drag coefficient with the reduction of airspeed, as predicted by the data presented in Figure 303 Appendix II, Section IV.

The seat angle of attack, Figure 52, is excessive for both parachutes but is much smaller for the guide surface system, the maximum value rising to approximately 1/3 of that imposed by the flat circular canopy. The seat sideslip angle (Figure 53) shows the same trend as the angle of attack. The angles resulting from deploying the guide surface are more nearly sinusoidal in nature and, if a curve drawn through the points of inflection is considered as an origin for the oscillation (in other words, ". . . The neutral direction of aerodynamic deceleration . . .") the guide surface canopy nearly satisfies the military specifications of paragraph 3.4.2.5.b of Reference 5.

The desired positive axial load factor (Figure 36) is maintained more consistently by the guide surface parachute but the lateral translation of both parachutes (note the azimuth angle, Figure 42) imparts an undesirable side load factor (Figure 37). The normal load factor (Figure 38) stresses the spine (Figure 39) much more from the flat circular parachute force, after about 0.5 sec.

At the end of one second the deceleration effectiveness is about 8% better for the guide surface canopy as demonstrated by Figure 40 with a 160 ft/sec difference in airspeed.

Both parachutes position the seat improperly at earth reference attitudes (Figures 45, 46, 47) but the guide surface performance is not as bad.

(4) Conclusions

The conclusions to be drawn from the comparisons of Case 1 are:

- o The ribless guide surface parachute type is markedly superior to the flat circular cloth canopy in stabilizing the subject seat-man combination because of its inherent static stability superiority.
- o The ribless guide surface parachute is the preferred solid cloth parachute for subsonic high dynamic pressure escape environments.

The conclusions to be drawn from the comparisons of Case 5 are:

- o The ribless guide surface canopy is better than the flat circular cloth type, both in stabilizing and decelerating the subject seat in a supersonic high q escape maneuver.
- o With the basic bridle geometry, neither parachute stabilizes the seat satisfactorily.

b. Ribbon Types

The ribbon parachutes (Figure 2 and 3), constructed of concentric and radial ribbons, are much more porous than the solid cloth parachutes and, consequently, require a longer time to fill with an attendant reduction in opening shock loads. One advantage of the ribbon design over solid cloth types is greatly increased static stability for a much larger range of airspeeds. The increased stability and superior supersonic drag performance over solid cloth parachutes are related to the decreased choking of air flow through the more porous ribbon mesh as the local flow exceeds sonic velocity.

(1) Flat Circular Ribbon, General

In contrast to the solid cloth flat circular canopy, the ribbon design is statically stable in normal force through the high subsonic and transonic airspeed ranges. At Mach numbers above the transonic, compressibility effects are reflected in a large drag coefficient attenuation -- not as large as the solid cloth type, however -- which diminishes the line tension forces maintaining seat-parachute separation. This loss of tension results in an axial pulsation causing the parachute to translate

laterally and longitudinally with respect to the seat, imparting repeated snatch forces to the seat and man. Modifications to extend the desirable drag characteristics and static stability to supersonic speeds led to the "equiflo" and "hemisflo" parachutes.

(2) Equiflo, General

The equiflo parachute is a modification of the triangular gore, flat circular ribbon type. Greater supersonic stability and less drag attenuation are accomplished by adding a conical skirt and extending the suspension lines. The conical extension area is 10% of the nominal canopy area and the suspension line length is twice the nominal diameter. The enhanced static stability is reflected in a steeper stable slope of the normal force coefficient versus parachute angle of attack. The increased static stability combined with greater tangential force, relative to the flat circular ribbon canopy, are dynamically stabilizing in a seat-parachute system because line tension is more reliably maintained and lateral parachute excursions reduced.

(3) Hemisflo, General

The triangular gore pattern of the equiflo ribbon canopy appears to be suboptimal for supersonic drag. By shaping the gores in a hemispherical design, a better supersonic configuration is obtained with improvements in drag performance. The dynamic stability of the seat-parachute combination is improved over the equiflo-seat system.

(4) Ribbon Type Performance Comparisons

The relative performance of the three ribbon canopies can be compared through the parameter variations of Cases 1 and 5, Table I. Figures 56 through 79 are time history plots portraying the subsonic dynamic stability of a seat-parachute system employing a flat circular ribbon canopy, an equiflo parachute, and a hemisflo parachute. Figures 80 through 103 provide the same information at a supersonic flight condition.

The most important parameters for determining the stability and deceleration capabilities of the three ribbon canopies at subsonic, high q escape conditions are included in Figures 56 through 79. Referring to these figures, the performance of the three ribbon canopies can be compared.

Figure 63 shows the dynamic response index or relative spinal stress experienced by the pilot through one second of an escape sequence incorporating the flat circular ribbon, equiflo, and hemisflo canopies. The differences are negligible, indicating that these three ribbon canopies have equivalent stabilizing capability in the pitch plane under these escape conditions. This capability is also realized in Figure 62, which reveals negligible differences in the normal load factor for the ribbon chutes.

Figures 66 and 67 show the angular excursions in the yaw and pitch planes of the three ribbon chutes and, therefore, their ability to track the escape seat. The flat circular ribbon parachute is slightly

superior to the equiflo or hemisflo in tracking the seat in the yaw plane and, consequently, is better at stabilizing the escape system in that plane. The escape seat Euler angles, Figures 69 through 71, show that the flat circular ribbon stabilizes the seat in yaw somewhat better than the equiflo or hemisflo; however, the flat circular ribbon chute and the hemisflo chute allow a larger excursion in bank angle at the end of one second than the equiflo. Figures 76 and 77 present the aerodynamic angles of the escape seat. The stability of the escape system and the ability of a particular chute to stabilize the escape system can best be determined from these angles. The angle of attack supports the previous conclusion that all three ribbon parachutes are equally stabilizing in the pitch plane with each chute producing approximately 7½ degrees average angle of attack through one second. The sideslip angle supports again the conclusion that the flat circular ribbon chute better stabilizes the escape seat in the yaw plane than either the hemisflo or equiflo, though by a minimal amount.

Figure 64 shows the reduction in airspeed of the escape seat and, therefore, the deceleration capability of the three ribbon chutes. It is apparent that all three chutes have equal capability in this respect since the total airspeed reduction at the end of one second was the same. It should be noted that if all three chutes had operated at zero angle of attack throughout the time history, their drag areas (SCD) would have been exactly equal since they were sized to obtain this. Although there was some small excursion in parachute angle of attack (Figure 78), from 0 to 3 degrees, the parachute drag area (Figure 79) reveals that the flat circular ribbon, the equiflo, and the hemisflo had approximately the same SCD. This would then explain the equivalent reduction in airspeed produced by the three ribbon chutes.

Referring to Figures 80 through 103, the performance of the ribbon type canopies may be compared for supersonic, high q escape initiation (Case 5).

Figure 88 shows the retardation effectiveness of the flat circular ribbon, the equiflo, and hemisflo canopies. The reduction in airspeed at the end of one second is about 40 ft/sec greater for the equiflo than for the hemisflo, and the flat circular type is also less effective than the equiflo by about 30 ft/sec. The hemisflo is the most stable of the three parachutes as shown in Figures 90 and 91 where the azimuth and elevation angles indicate that the hemisflo trails the seat with the smallest angular excursions. The result of this more favorable trailing characteristic is the reduction of lateral pilot load factors (Figure 85) to about half that of the other two parachutes. The DRI, Figure 87, is about the same for all three chutes, initially, but after 0.4 seconds, the spine is being stressed less by the hemisflo. The seat Euler angles, Figures 93 through 95, show the hemisflo stabilizing the seat in yaw, pitch, and roll much better than the other two, with the flat circular ribbon tumbling the seat through two revolutions at the end of one second. The seat-man aerodynamic angles, Figures 100 and 101, are also favorably affected by the superior hemisflo stability which is confirmed by the magnitudes of the parachute angles of attack, Figure 100. Figure 103 is a plot of the area drag force coefficient, demonstrating how the angle of attack and Mach number changes affect the three parachutes. For all

three paraclutes, a reduction of airspeed (Figure 88) with the concomitant decrease in Mach number increases the drag capability, as expected, in supersonic flight. The influence of the angle of attack is shown by relating Figures 102 and 103, with the flat circular ribbon canopy demonstrating the most prominent effect because of the larger angles.

At this stage of the comparisons, no attempt is being made to satisfy all the requirements of Reference 5; in fact, paragraph 3.4.2.5.b, for one, is being violated by the most stable parachute, the hemisflo, by failure to maintain the sideslip angle (Figure 101) below $\pm 20^{\circ}$ -- by one interpretation of the specification. The intent of this part of the analysis is to select the best parachute when all are operating in the same environment. Acceptable system stability, using the selected parachute, can be mechanized subsequently without changing the canopy configuration -- by employing a longer bridle, for example (Case 4). The 12 cases tabulated in Table I.a will be used to refine the selected configuration.

(5) Conclusions

The conclusions to be drawn from the comparisons made in Case 1 are:

- For subsonic, high q escape conditions, the flat circular ribbon, the equiflo, and the hemisflo parachutes stabilize the seat equally well in the pitch plane. The flat circular ribbon canopy is slightly superior to the equiflo or hemisflo in stabilizing the seat in the yaw plane.
- All three ribbon parachutes are equally effective in decelerating the escape seat system through the first second of the escape sequence.
- All three ribbon parachutes are equally acceptable as stabilization, deceleration devices for subsonic, high q escape conditions.

The conclusions to be drawn from the comparisons of Case 5 are:

- The hemisflo parachute is better than the equiflo or flat circular ribbon at stabilizing the seat-man combination in high q supersonic flight because of its superior static stability.
- The retardation effectiveness of the hemisflo in high q supersonic flight is less than either of the other ribbon parachutes, but not by an amount significant enough to negate its superior stability.
- The hemisflo parachute more nearly satisfies the military specifications of Reference 5 than either the equiflo or flat circular ribbon parachute for high q supersonic flight conditions, with the bridle geometry of Case 5.

The conclusions to be drawn from the comparisons of both Case 1 and Case 5 are:

- For subsonic, high q escape conditions, the three ribbon parachutes - flat circular, equiflo and hemisflo - have similar stabilization and retardation capabilities while the hemisflo parachute demonstrates a marked stabilizing superiority at supersonic, high q flight conditions with about the same deceleration characteristics as the other two canopies.

- Therefore, the hemisflo parachute is selected for further comparisons with the selected solid cloth parachute. The better of these two will then be investigated for configurational changes required to conform to all specifications of Reference 5 through use of all 12 Cases on Table I.

c. Drag Parachute Type Selection

The conclusions from the comparisons in paragraphs 1.a and 1.b were that the ribless guide surface canopy is the better of the two solid cloth candidates and the hemisflo parachute was superior to the other two ribbon types. The following examination of the same time history plots previously discussed (Figures 8 through 103) will show that the hemisflo type offers more promising performance than the guide surface canopy.

The subsonic high q comparison of the two remaining candidate parachutes is not definitive because the guide surface type and the hemisflo configuration have similar stabilization and deceleration traits. This is confirmed by comparing Figure 8 with Figure 56, Figure 9 with Figure 57, etc. In no instant does either parachute decisively out-perform the other. The conclusion is incontrovertible, however, that the hemisflo parachute performs better supersonically. For instance, the undesirable side load factors (Figures 37 and 85) imparted to the seat by the guide surface type are about twice as large as those from the hemisflo canopy. The DRI (Figures 39 and 87) shows less passenger trauma because of the smoother spinal stress. The retardation effectiveness is about the same (Figure 40 and 88) while the hemisflo parachute shows a definite superiority in stabilizing the seat - as confirmed by Figures 52, 53, 100, and 101.

Therefore, the hemisflo canopy is chosen for configurational studies through investigations employing the cases of Table I.

2. DRAG PARACHUTE SYSTEM PERFORMANCE

a. Rocket Burn Time Effects

The significant parameters needed for comparison of an escape seat-drag chute system operating with or without a sustainer rocket are presented in Figures 104 through 127 (Cases 1 and 2, Table I.a). The chute used in this comparison is the hemisflo ribbon canopy which was previously selected as the most superior chute of the five analyzed.

The basic functions of the sustainer rocket are to help the seat-pilot combination clear a disabled aircraft and gain sufficient altitude for a favorable recovery. Also, under high q conditions, the sustainer rocket helps reduce the snatch force and opening shock produced by the drag chute. Figure 108, which shows the axial load factor of the seat-man combination shows a reduction due to the sustainer of 9 g's in the opening shock loads which occur at .165 seconds. However, a more favorable normal load factor, Figure 110, is experienced throughout the time history with the sustainer not burning. This, of course, results in a more favorable DRI, Figure 111, which is a measure of the spinal stress experienced by the pilot. The influence of the sustainer on both the normal and axial load factor is produced because the sustainer thrust line is oriented 40° up from the X-body axis of the escape seat to give optimal performance.

Figure 106 is a crossplot of the altitude and downrange miss distance between the seat-man C.G. and the tip of the vertical stabilizer. With the sustainer rocket burning the escape seat system avoids the vertical tail, represented by the origin of coordinates, with several feet to spare. However, if the rocket is not burning, the escape seat collides with the vertical tail as shown by the close proximity of the seat C.G. to the tail. This problem could be improved by using a shorter riser or by delaying projection of the drag chute; however, both these ideas are undesirable because of the decrease in system stability with the shorter riser or the delay in seat stabilization with the deployment lag. It should also be pointed out that the time to reach line stretch in both cases was the same. This shows that the difference in chute velocity and thus time to line stretch is affected very little by the difference in the escape seat velocity produced by the sustainer rocket. The major factor determining the time to line stretch when no large excursions in total airspeed are experienced is the mortar or rocket impulse propelling the drag chute aft.

Referring to Figures 114 and 115, the chute elevation angle and azimuth angle from the seat, and the seat-man Euler angles, Figures 117 through 119, it is evident that there is a slight decrease in the stability of the escape seat system due to the sustainer rocket burning. The chute, however, does track the seat well in both cases.

b. Shroud Line and Bridle Length Effects

A comparison of drag chute performance as a function of distance aft of a typical ejection seat is presented in Figures 128 through 151. A $4\frac{1}{2}$ foot diameter hemisflo ribbon chute was used in the analysis. The parameter varied was the chute C.G. position aft of the seat back at full inflation. Reference to Table Ia, Cases 1, 3, and 4 will supply the values of the parameters used in this comparison. Also, the effect of the escape seat wake on the parachute drag coefficient as a function of its distance aft of the seat is presented in Figure 311, Appendix II.

Referring to Figure 132 it can be seen that the snatch load and opening shock increase with distance aft of the seat. There are two reasons for this. First, the parachute drag area (Figure 151) increases as the wake becomes less prominent. Second, the parachute velocity at line stretch from the deployment rocket, and therefore its momentum, increases as the distance is increased. The spinal stress experienced by the pilot, Figure 135, is only slightly affected by the chutes proximity to the seat.

The deceleration capability of the parachute is enhanced as its distance aft increases. This is due to the increase in its drag coefficient. However, this trend is short lived because as the chute distance aft of the seat increases and removes it from the wake effects, the time to line stretch has increased. Therefore, the amount of time the chute actually decelerates the seat is reduced. Figure 136 shows the total airspeed of the seat-man combination through one second of the time history. The escape seat total airspeed is reduced 40 ft/sec more at the end of one second with the chute located 10 feet aft of the seat than with it located 3 1/3 feet aft. But the total airspeed of the escape seat is reduced only 8 ft/sec more at the end of one second with the chute located 22 feet aft than with it located 10 feet aft. However, the optimum distance behind an escape seat for a chute with a given geometry and drag area will have to be determined from a consideration of the snatch load and opening shock produced by the chute under all flight conditions in which it is to be employed.

Figures 138 and 139, which show the chute's ability to track the seat, reveal a slight increase in the chute's stability with increasing distance aft. This increase can also be seen in the parachute angle of attack, Figure 150. The seat-man angle of attack is little affected by the chutes distance aft but the sideslip angle is reduced by an appreciable amount. (A greater increase in stability with the longer bridle would have been realized if a more unstable escape condition had been chosen as the comparison basis - such as Case 5. The high q subsonic base condition is so stable because of greater parachute static stability and drag efficiency that bridle length effects are not easily discernible. This belated discovery occurred as a result of the computer runs planned in Table I. An indication of the improved stability is noted later in the comparison discussion of Cases 4, 10 and 11.)

c. Flight Condition Effects

The performance degradation of the hemisflo canopy from compressibility induced drag reduction is delineated in Figures 152 through 175 where Cases 1, 5 and 12 from Table I are presented as multiple time history plots.

Figure 156, the seat-man axial load factor, shows an increase in the opening shock with increasing Mach number. This can be explained by the fact that an increase in velocity decreases the time for the parachute to fill. This presents the interesting fact that the mass acquisition forces operating on the filling chute are of more significance in determining the opening shock loads than the actual full inflated drag area (Figure 175) if the chute is operating at an equivalent dynamic pressure.

A marked increase in seat-man side load factor, Figure 157, is also noticed. This is due mainly to the fact that the parachutes ability to stabilize the seat decreases with increasing Mach number due to the compressibility induced drag reduction. The effects of Mach number on normal load factor and the related dynamic response index are slight.

It was pointed out previously that the parachute loses its ability to stabilize the seat with increasing Mach number (at constant dynamic pressure). This is apparent in Figure 162 which shows the parachute azimuth angle as a function of time. At Mach 2.0 the chute trails about 20 degrees to the right of the seat-man pitch plane through most of the time history and is unable to stabilize the seat at zero sideslip. This, therefore, is what produces the increased side load factor. The escape seat Euler angles, Figures 165 through 167, also reflect this general loss of stability. In fact, the seat rolls through more than one revolution in Case 5 (MN = 2.0) through one second of the time history while yawing and pitching more than 20 degrees. On the other hand, Case 1 (MN = .9) shows a very stable condition. Figure 173, the seat-man sideslip angle, shows that the escape seat is unstable in yaw through one second of the time history for the Mach 2.0 condition. It is interesting to note that the Mach number effect on the stability of the escape seat system is not linear. Case 12, which represents an intermediate Mach number of 1.5, shows only a slight degradation in stability from that of Case 1 (MN = .9).

Reference to Figure 160, the seat-man total airspeed, reveals that the deceleration capability through one second is little affected by Mach number. However, the chute chosen for this analysis was a 3.18 foot diameter hemisflo chute which primarily provides stability. Since the magnitude of the drag area provided by the chute is close to that provided by the escape seat itself it would be hard to realize the effect on total airspeed produced through one second between Cases 1, 5, and 12. A larger chute would show an improved deceleration capability as the Mach number is decreased and its drag area increased providing the dynamic pressure was equal at escape initiation.

Figures 176 through 199 are time history multiple plots of Cases 1, 8 and 9 from Table I demonstrating the loss of parachute performance with the reduction of dynamic pressure. In practice, the Case 9 escape environment does not warrant the use of a drag parachute. The initial airspeed is low enough to allow immediate deployment of the personnel recovery parachute without excessive seat occupant loads. (The authors - one a former airborne infantryman and another a pilot of a C-46 carrying airborne troops - are intimately familiar with parachute jumps using fast static line deployment at twice the dynamic pressure of Case 9.) To emphasize the effect of low dynamic pressures, however, the 15 psf was chosen.

The primary effect on chute performance due to a dynamic pressure variation is the ability of the chute to stabilize the seat. There is a sharp decrease in its ability to track the escape seat at low dynamic pressure. Figures 186 and 187 show the chute tracking the seat well in Cases 1 and 8, but very poorly in Case 9. At low dynamic pressures the drag force produced by the chute becomes less capable of stabilizing the seat when adverse seat attitudes are experienced. This is evident in

Figures 189 through 191 which show the seat Euler angles and also in Figure 196 and 197 which represent the seat-man angle of attack and side-slip angle. At higher dynamic pressures the parachute is capable of stabilizing the seat in a favorable attitude while at lower dynamic pressures this ability is lessened. Figure 198 shows also that the angle of attack of the parachute becomes very erratic at low dynamic pressures. This is due in part to the low aerodynamic damping operating on the chute. Figure 185, which represents the distance from the apex of the bridle to the chute C.G., shows that the chute oscillates with a forward and aft motion for over .3 of a second after first reaching line stretch. This oscillation induces perturbation velocities which result in erratic angles of attack.

The load factors produced by the aerodynamic decelerating forces acting on the escape seat in this comparison are a function of the square of the velocity at a constant altitude and increase with increasing dynamic pressure. This variation is easily discernable in the crossplots of axial load factor versus time (Figure 180) and normal load factor versus time (Figure 182).

d. Canopy Diameter Effects

Figures 200 through 223 are multiple plots of Cases 4, 10 and 11 (Table I) showing the performance of three hemisflo-parachutes of different diameters positioned at the same point behind the subject seat-man combination. The distance was chosen for the largest parachute with no risers. Riser lengths were added to the two smaller parachutes for proper positioning. Because the seat wake effects vary with parachute size, the drag effectiveness is attenuated more for the smaller parachutes - from 29% for the 3.18 ft. diameter canopy to only 5% for the 6.6 ft. diameter parachute. Figure 223, a plot of the three drag coefficients, shows the relative performance and the angle of attack plot, Figure 222, reveals that virtually no drag degradation occurred from parachute oscillation.

The seat aerodynamic angles, Figures 220 and 221, are all acceptably small, with the smallest parachute showing the best stabilizing trait. Because smaller parachutes are lighter in weight, they trail the seat better in both elevation angle (Figure 211) and azimuth angle (Figure 210). The smaller, lighter parachutes also lag the climbing seat more in altitude, as shown by the elevation angle, where the negative magnitudes of the three canopies are not appreciably different but the heavier parachutes overshoot more in the positive direction (looking up, facing aft). The result of this lag is to shift the normal load factor (Figure 206) and the DRI (Figure 207) toward a more negative (spinal tension) value. The DRI magnitudes for the two largest parachutes exceed the maximum allowed (21) by the specifications of Reference 5.

For all three parachutes, the seat attitude with respect to the earth is satisfactory, as shown by the Euler angles in Figures 213, 214 and 215. The distance from the seat to the parachute is over twice as great as the ten foot length of the basic configuration and the stability is remarkably improved as a consequence.

For the subject seat, in a high q subsonic escape regime the hemisflo parachute projected diameter must be less than 4.66 feet and may be greater than 3.18 feet, for a 22 foot seat-parachute distance, to stabilize the seat satisfactorily in accordance with the specifications of Reference 5.

With increasing altitude, a reduction in parachute porosity occurs resulting in large changes in aerodynamic coefficients for solid cloth parachutes but having negligibly small influence on a ribbon canopy. Note that no changes in aerodynamic coefficients for ribbon parachutes is indicated in Table II , Appendix II, as altitude varies. Consequently, the comparisons of Cases 6, 7 and 9 are ignored. (Had a solid cloth canopy been chosen from the candidate parachutes, these Cases would have been valid.)

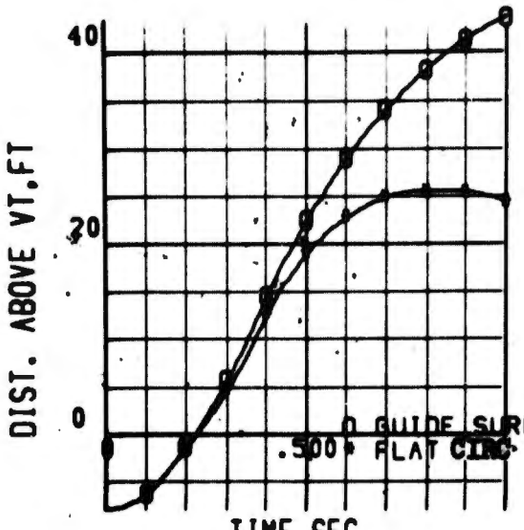

FIG 8 SOLID CLOTH PARACHUTES
VERT. TAIL VERT. CLEARANCE

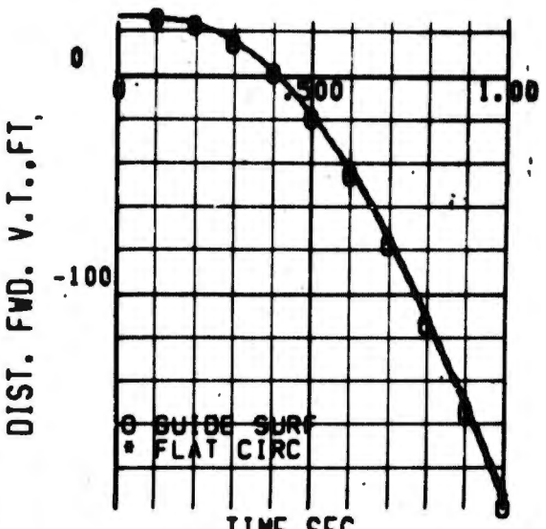

FIG 9 SOLID CLOTH PARACHUTES
VERT. TAIL LONG. CLEARANCE

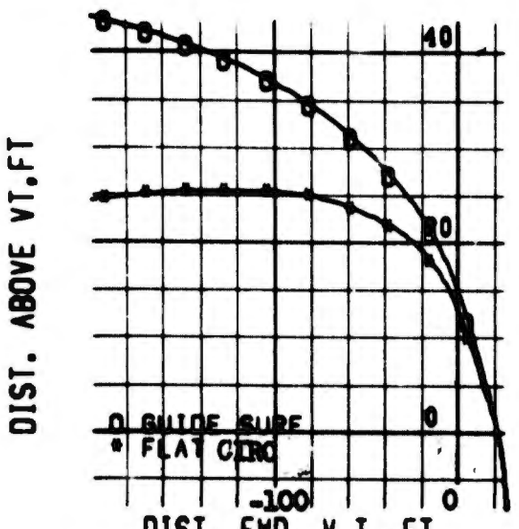

FIG 10 SOLID CLOTH PARACHUTES
VERTICAL TAIL CLEARANCE

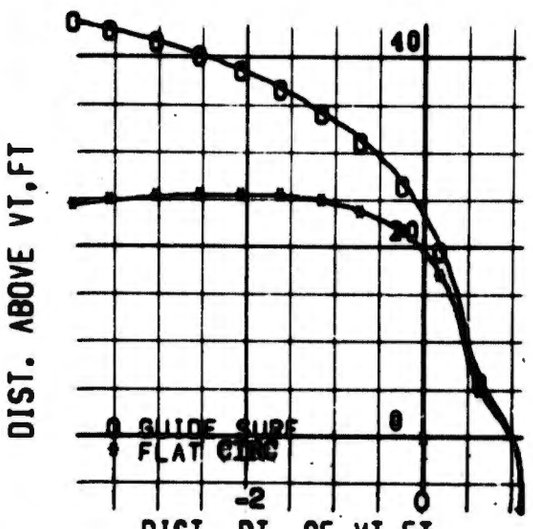

FIG 11 SOLID CLOTH PARACHUTES
VERTICAL TAIL CLEARANCE

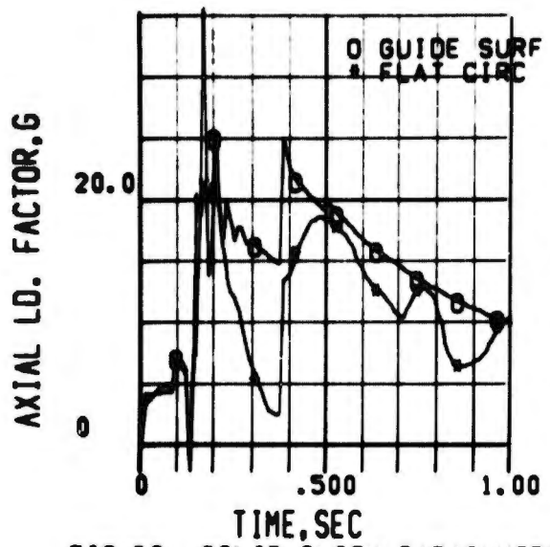

FIG 12 SOLID CLOTH PARACHUTES
SEAT AXIAL LOAD FACTOR

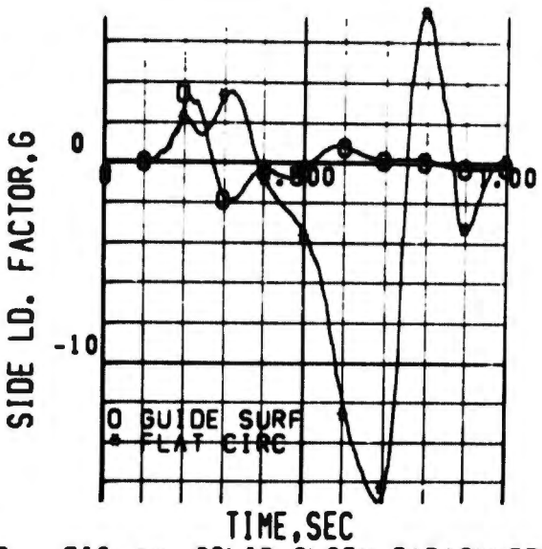

FIG 13 SOLID CLOTH PARACHUTES
SEAT SIDE LOAD FACTOR

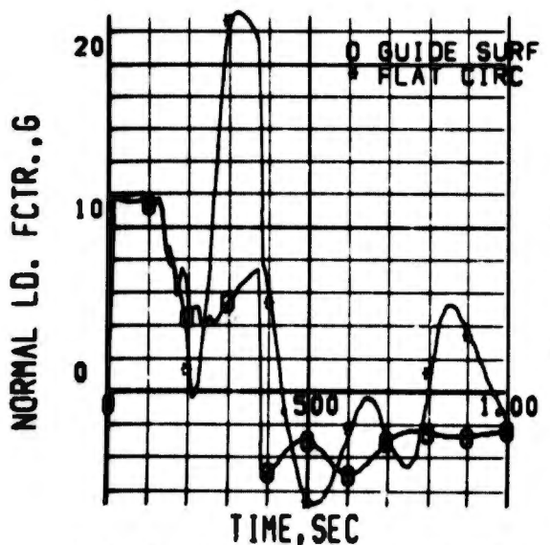

FIG 14 SOLID CLOTH PARACHUTES
SEAT NORMAL LOAD FACTOR

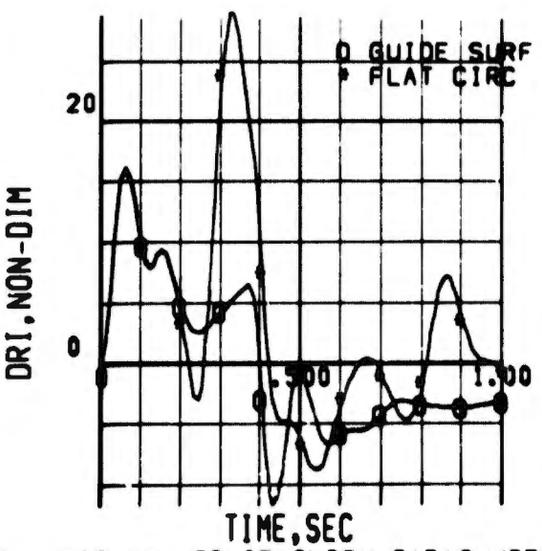

FIG 15 SOLID CLOTH PARACHUTES
MAN DYNAMIC RESPONSE INDEX

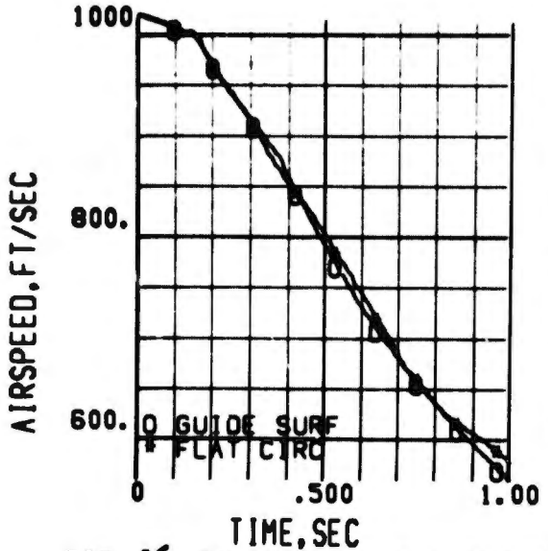

FIG 16 SOLID CLOTH PARACHUTES SEAT AIRSPEED

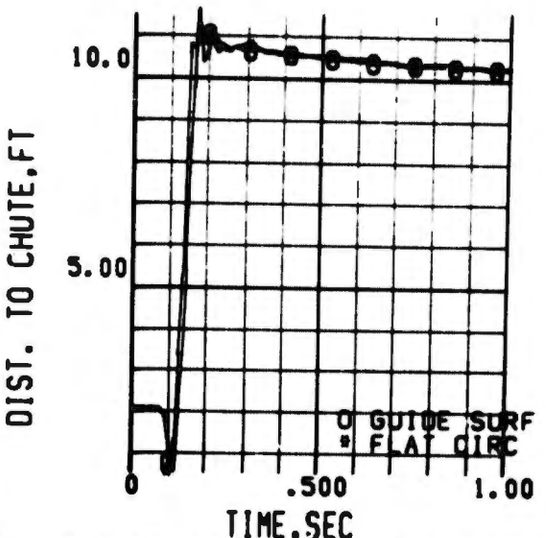

FIG 17 SOLID CLOTH PARACHUTES DIST. FROM BRIDLE TO CHUTE CG

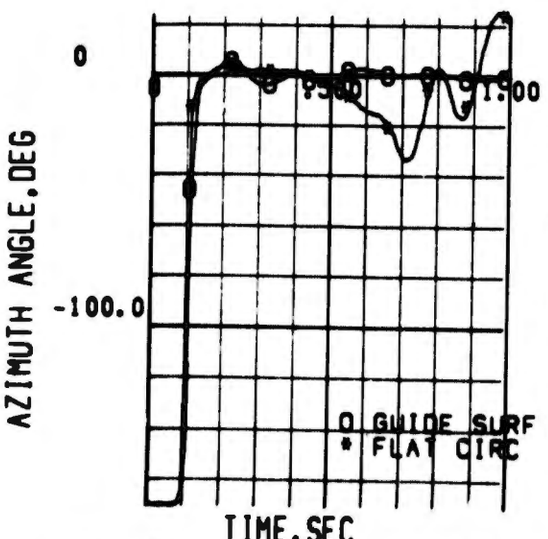

FIG 18 SOLID CLOTH PARACHUTES SEAT-PARACHUTE AZIMUTH ANGLE

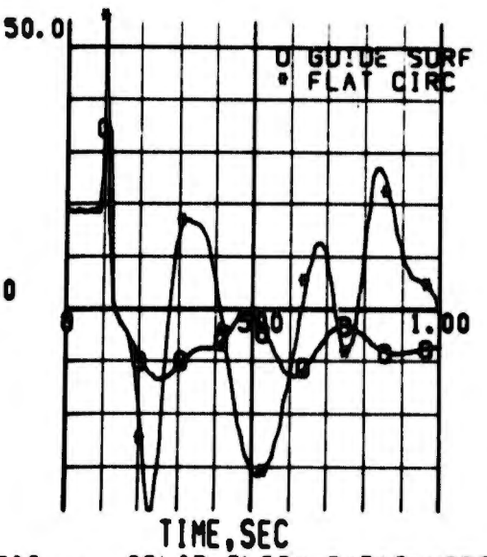

FIG 19 SOLID CLOTH PARACHUTES SEAT-PARACHUTE ELEVATION ANGLE

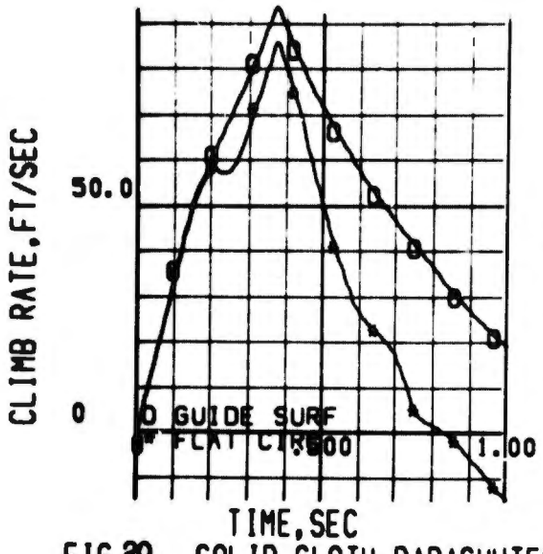

FIG 20 SOLID CLOTH PARACHUTES SEAT CLIMB RATE

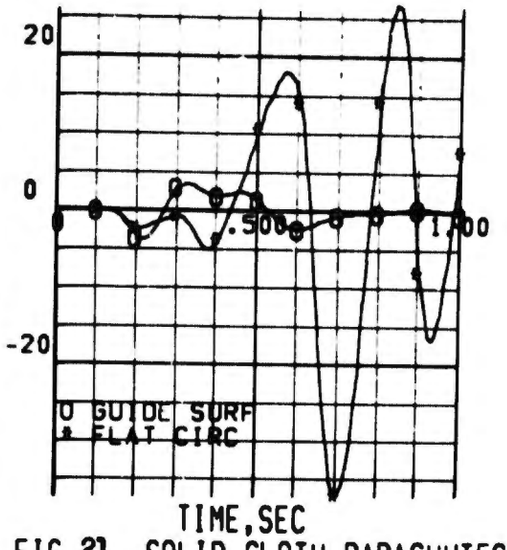

FIG 21 SOLID CLOTH PARACHUTES SEAT EARTH AXIS YAW ANGLE

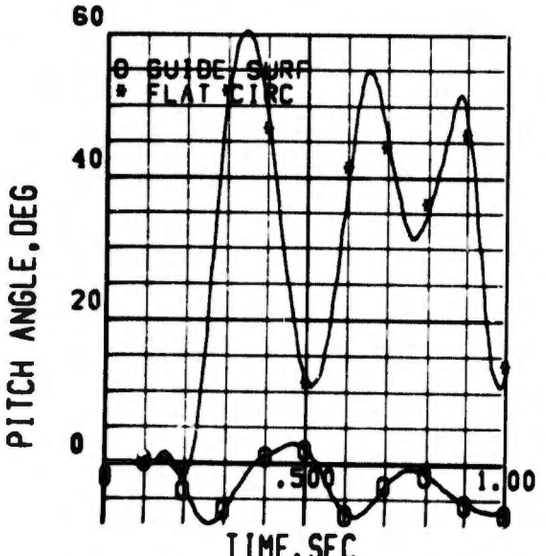

FIG 22 SOLID CLOTH PARACHUTES SEAT EARTH AXIS PITCH ANGLE

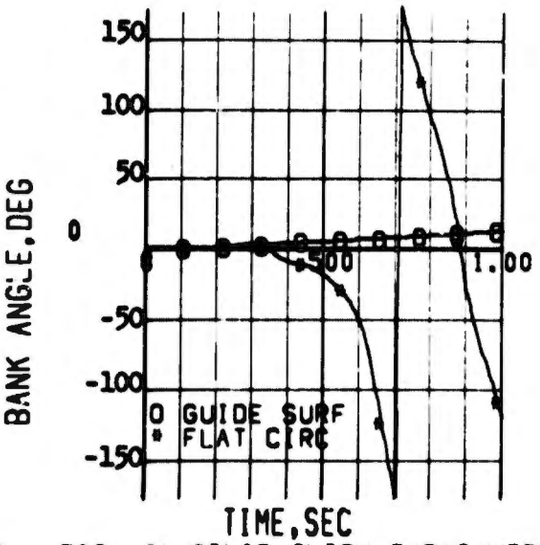

FIG 23 SOLID CLOTH PARACHUTES SEAT EARTH AXIS BANK ANGLE

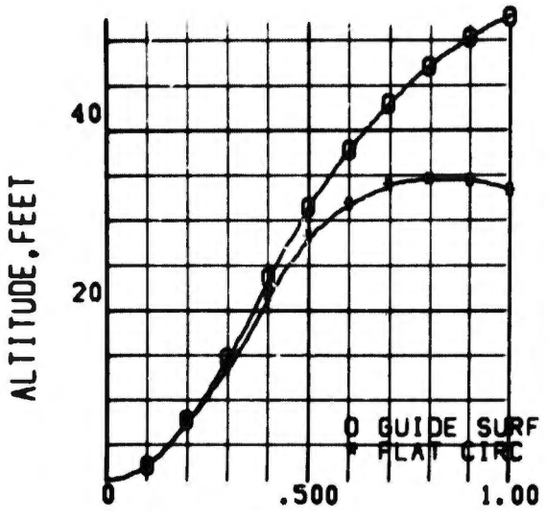

FIG 24 SOLID CLOTH PARACHUTES
SEAT ALTITUDE

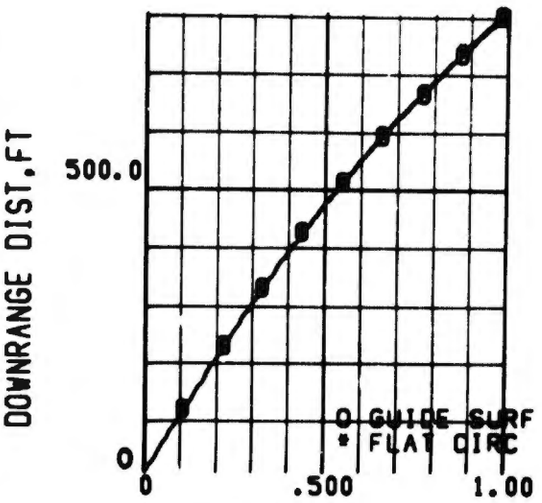

FIG 25 SOLID CLOTH PARACHUTES
SEAT DOWNRANGE DISTANCE

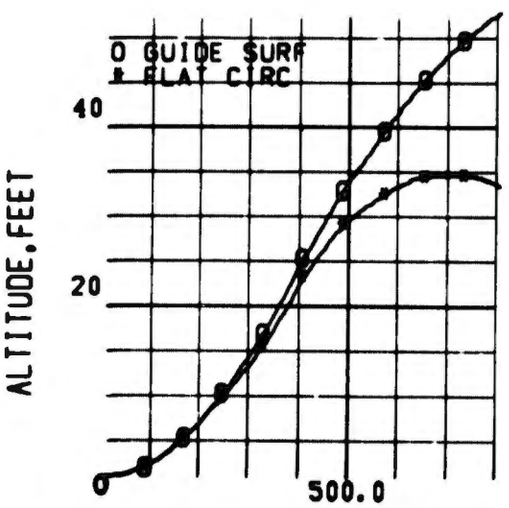

FIG 26 SOLID CLOTH PARACHUTES
SEAT TRAJECTORY

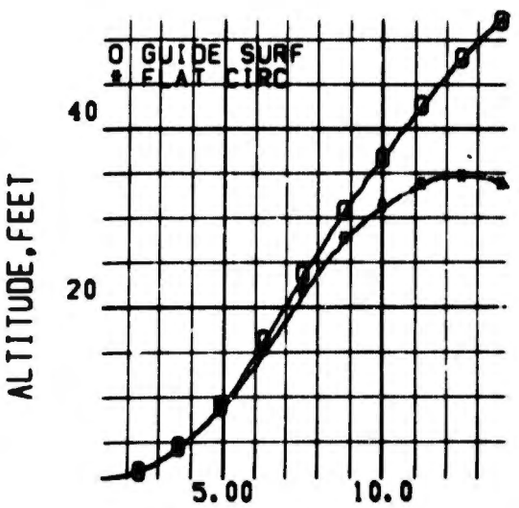

FIG 27 SOLID CLOTH PARACHUTES
SEAT TRAJECTORY

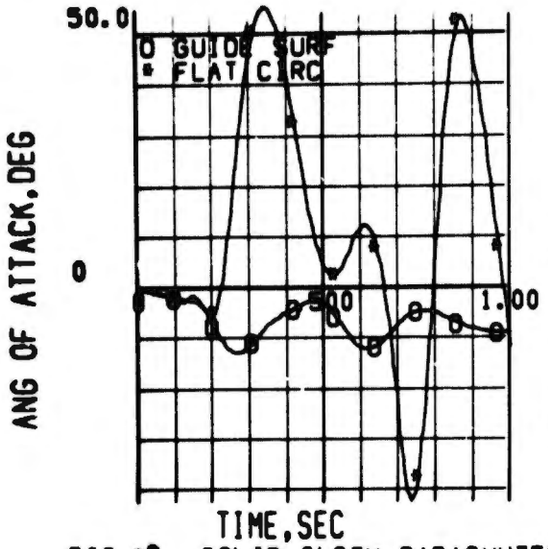

FIG 28 SOLID CLOTH PARACHUTES
SEAT ANGLE OF ATTACK

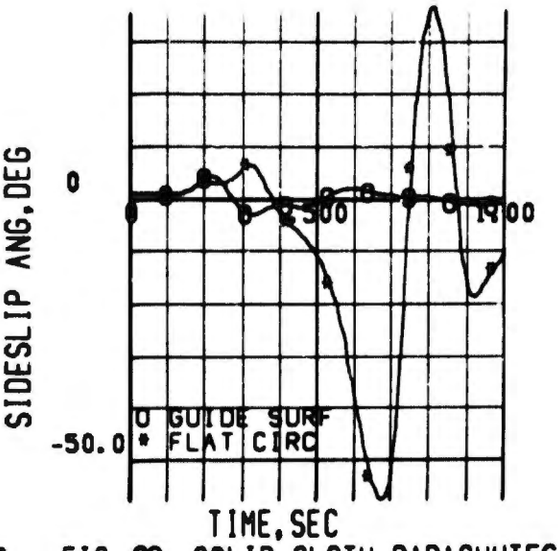

FIG 29 SOLID CLOTH PARACHUTES
SEAT SIDESLIP ANGLE

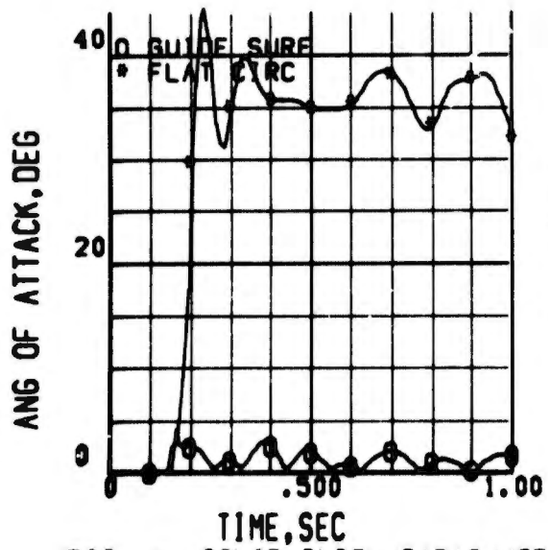

FIG 30 SOLID CLOTH PARACHUTES
PARACHUTE ANGLE OF ATTACK

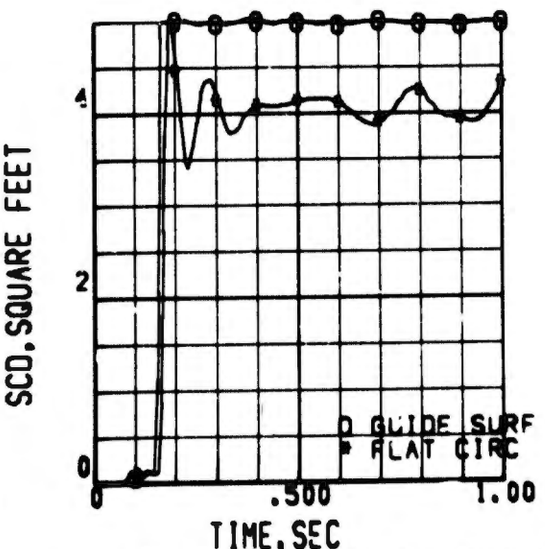

FIG 31 SOLID CLOTH PARACHUTES
PARACHUTE AREA DRAG COEFF

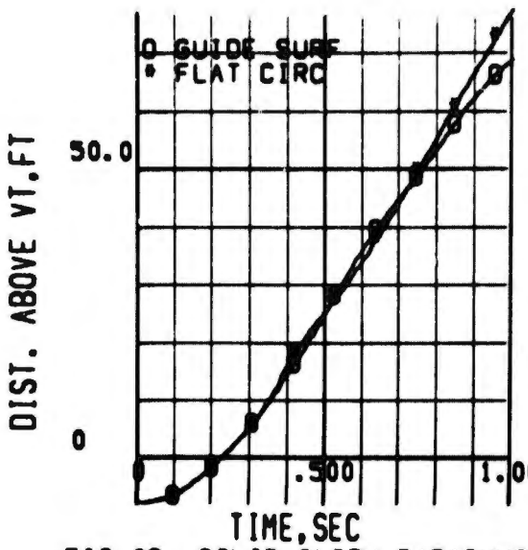

FIG 32 SOLID CLOTH PARACHUTES
VERT. TAIL VERT. CLEARANCE

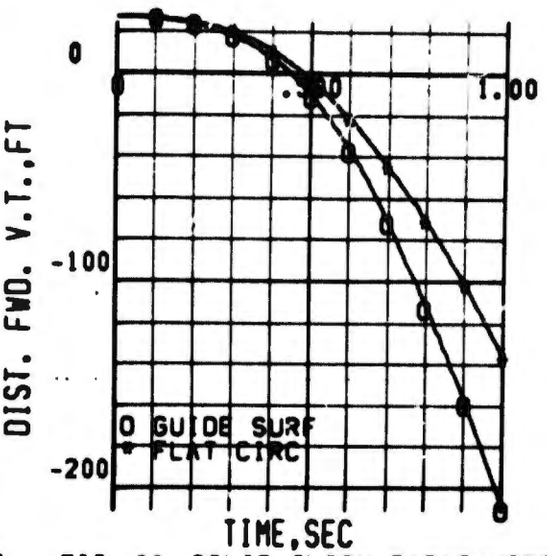

FIG 33 SOLID CLOTH PARACHUTES
VERT. TAIL LONG. CLEARANCE

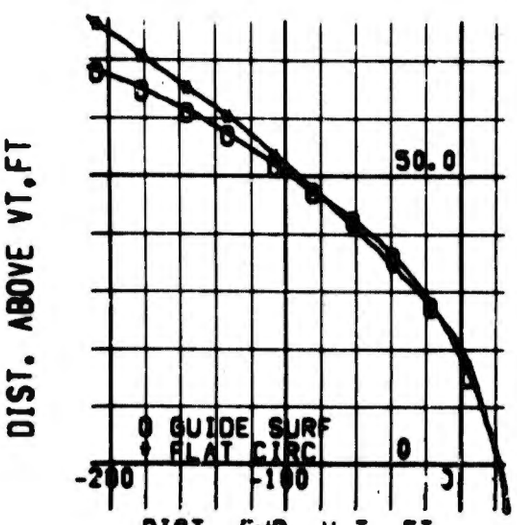

FIG 34 SOLID CLOTH PARACHUTES
VERTICAL TAIL CLEARANCE

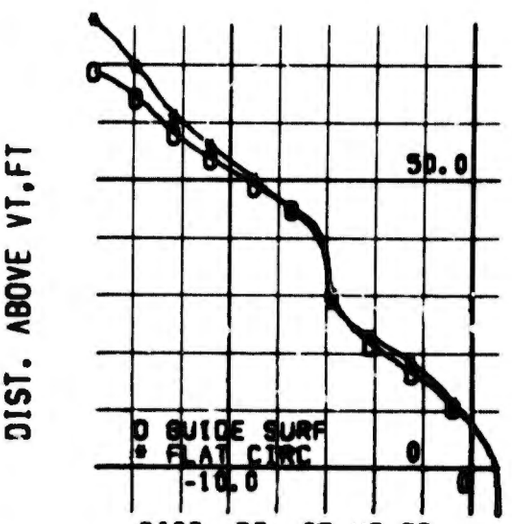

FIG 35 SOLID CLOTH PARACHUTES
VERTICAL TAIL CLEARANCE

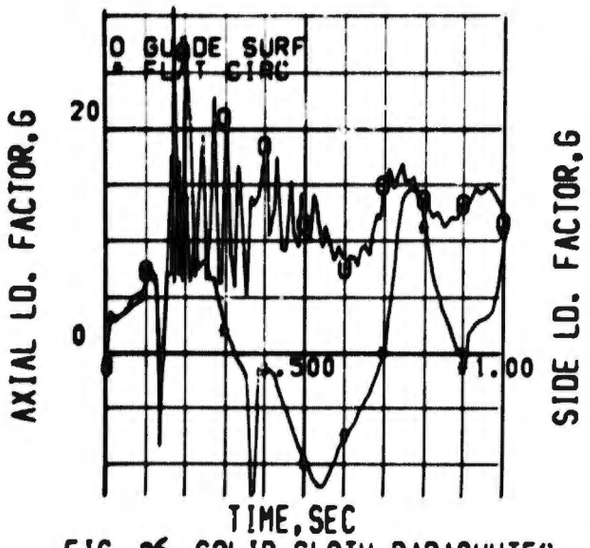

FIG 36 SOLID CLOTH PARACHUTES
SEAT AXIAL LOAD FACTOR

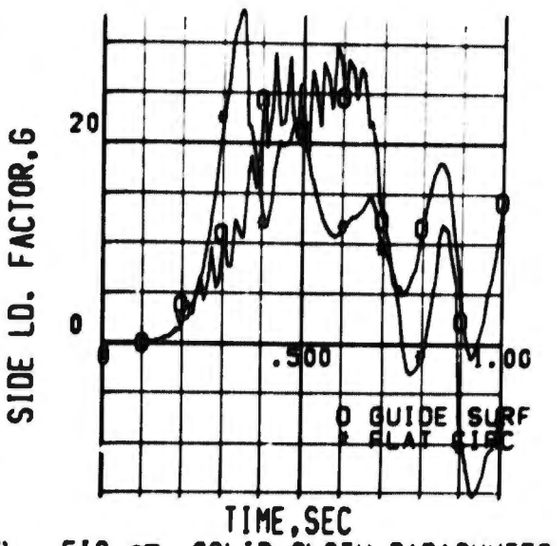

FIG 37 SOLID CLOTH PARACHUTES
SEAT SIDE LOAD FACTOR

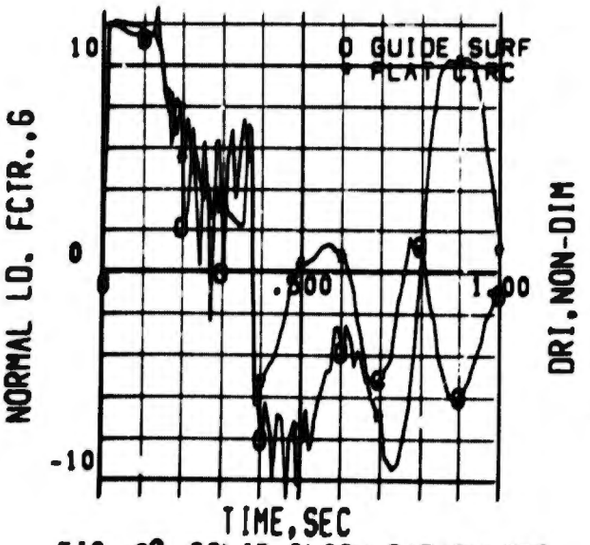

FIG 38 SOLID CLOTH PARACHUTES
SEAT NORMAL LOAD FACTOR

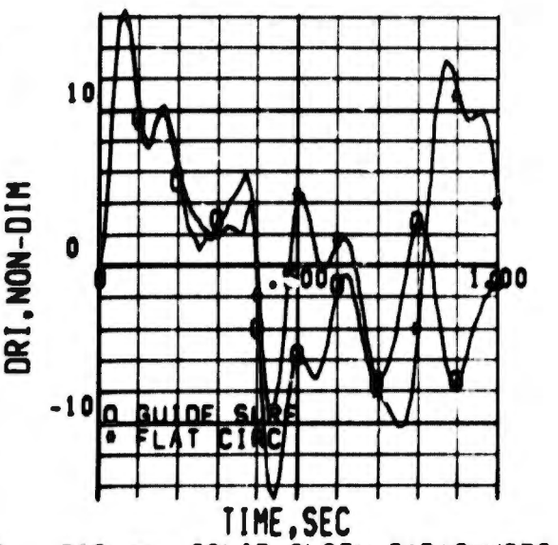

FIG 39 SOLID CLOTH PARACHUTES
MAN DYNAMIC RESPONSE INDEX

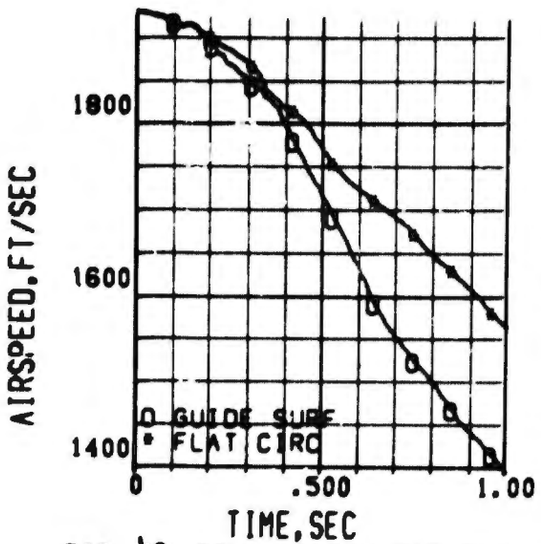

FIG 40 SOLID CLOTH PARACHUTES SEAT AIRSPEED

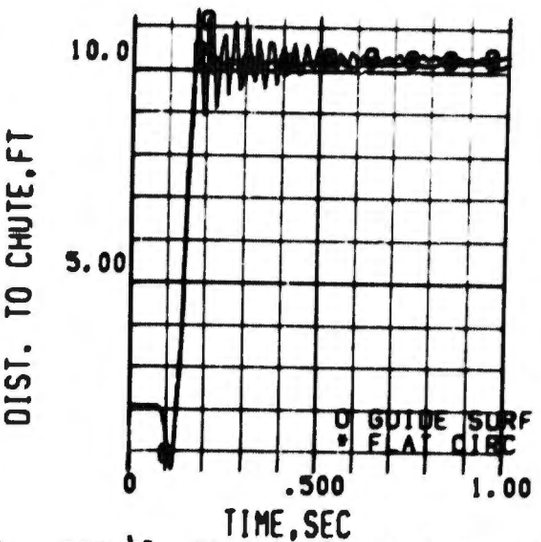

FIG 41 SOLID CLOTH PARACHUTES DIST. FROM BRIDLE TO CHUTE CG

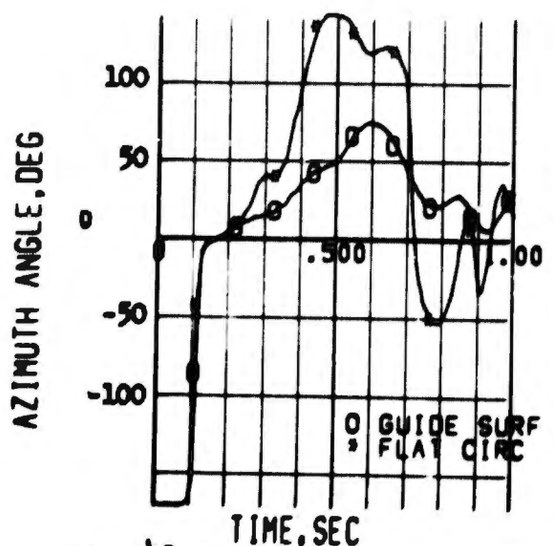

FIG 42 SOLID CLOTH PARACHUTES SEAT-PARACHUTE AZIMUTH ANGLE

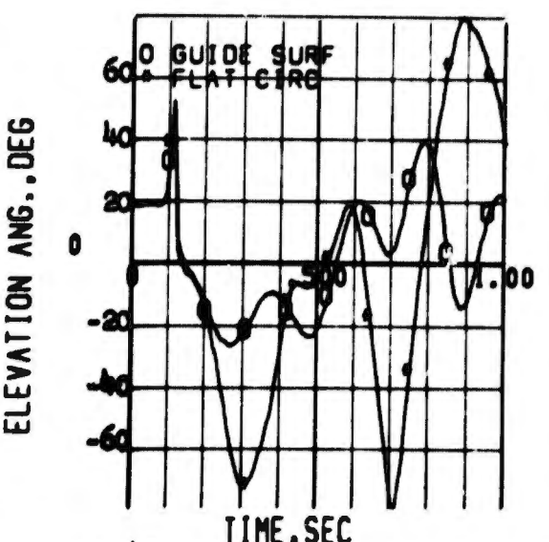

FIG 43 SOLID CLOTH PARACHUTES SEAT-PARACHUTE ELEVATION ANGLE

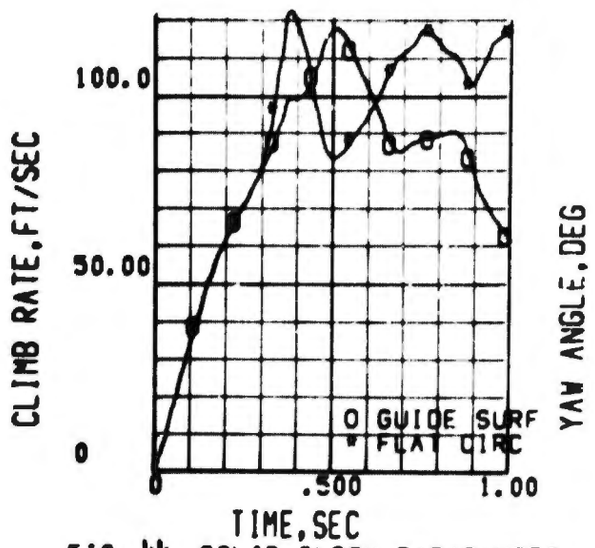

FIG 44 SOLID CLOTH PARACHUTES
SEAT CLIMB RATE

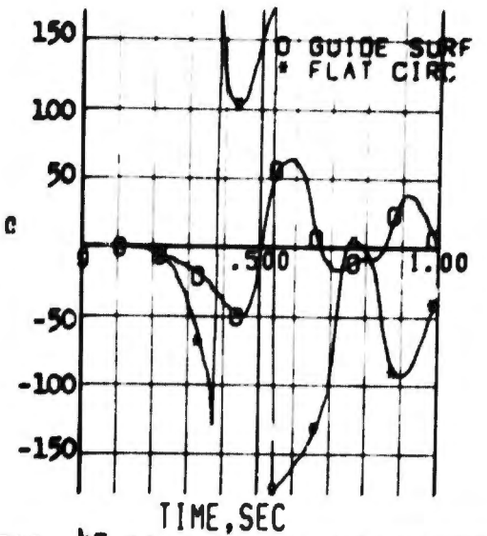

FIG 45 SOLID CLOTH PARACHUTES
SEAT EARTH AXIS YAW ANGLE

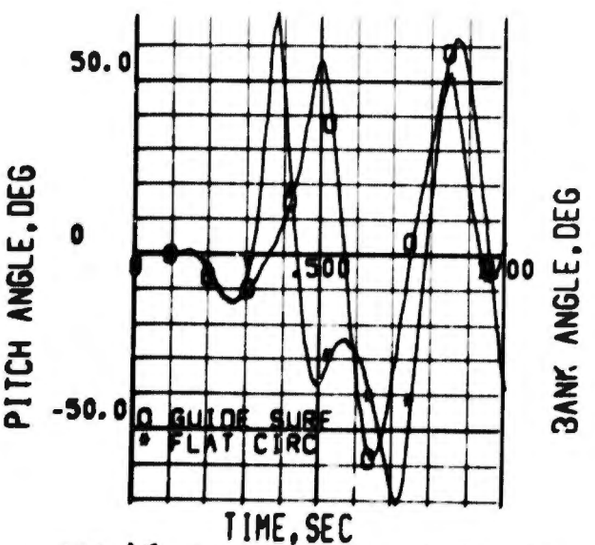

FIG 46 SOLID CLOTH PARACHUTES
SEAT EARTH AXIS PITCH ANGLE

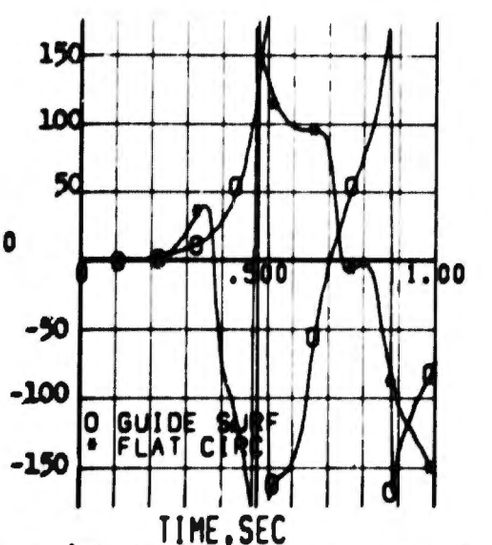

FIG 47 SOLID CLOTH PARACHUTES
SEAT EARTH AXIS BANK ANGLE

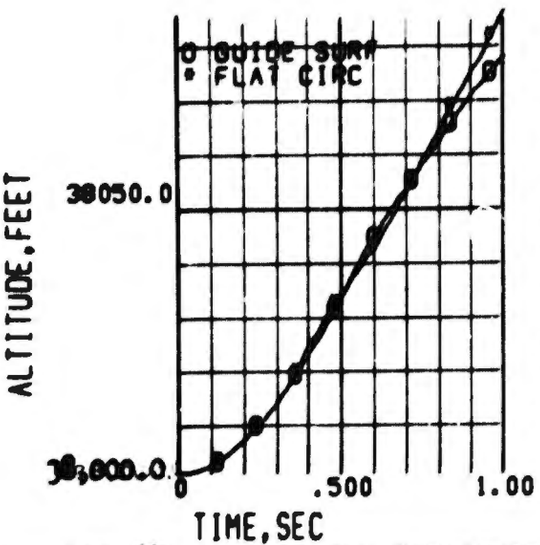

FIG 48 SOLID CLOTH PARACHUTES
SEAT ALTITUDE

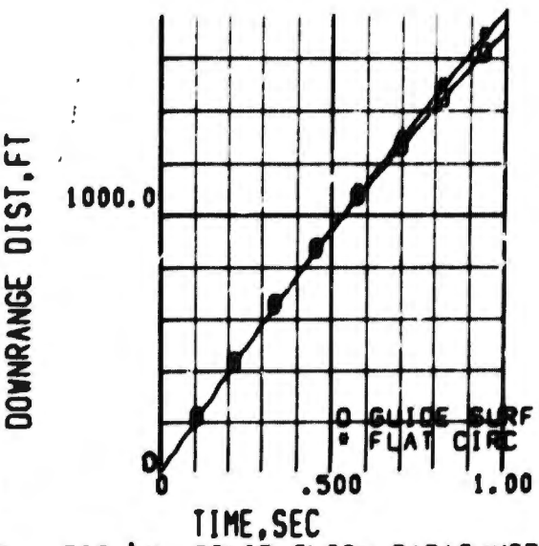

FIG 49 SOLID CLOTH PARACHUTES
SEAT DOWNRANGE DISTANCE

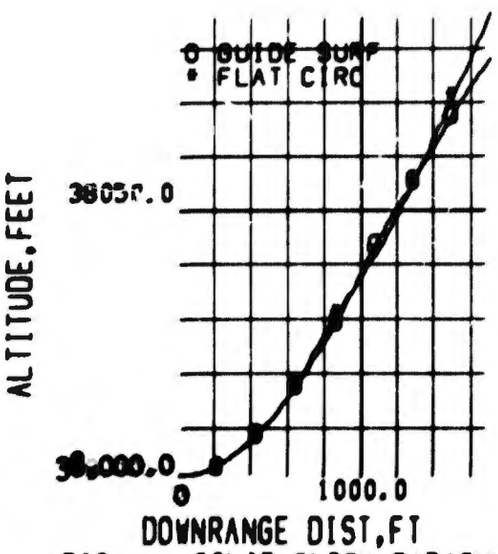

FIG 50 SOLID CLOTH PARACHUTES
SEAT TRAJECTORY

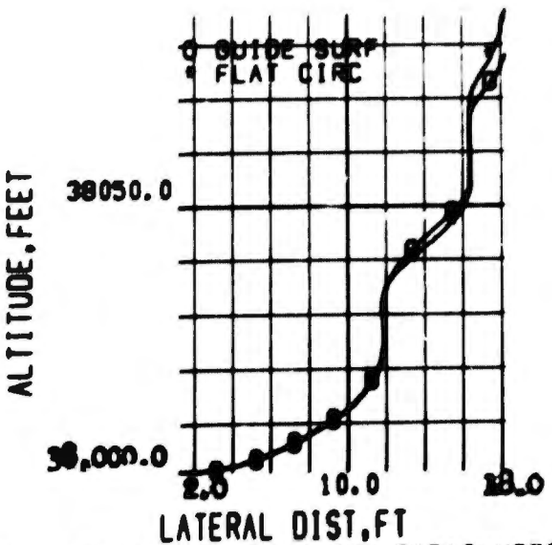

FIG 51 SOLID CLOTH PARACHUTES
SEAT TRAJECTORY

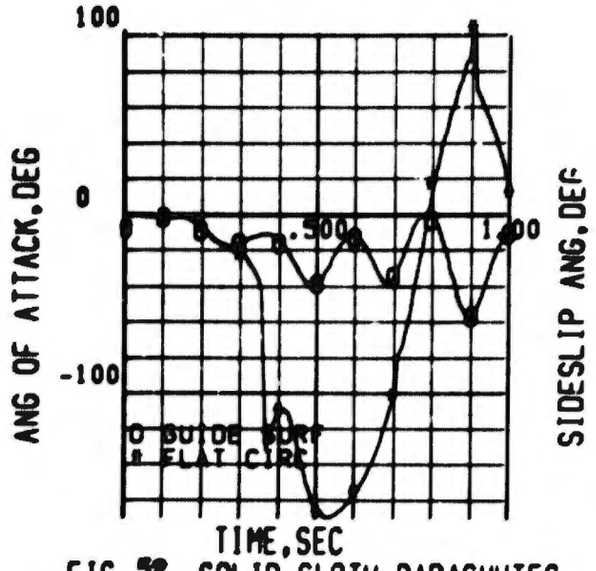

FIG 52 SOLID CLOTH PARACHUTES SEAT ANGLE OF ATTACK

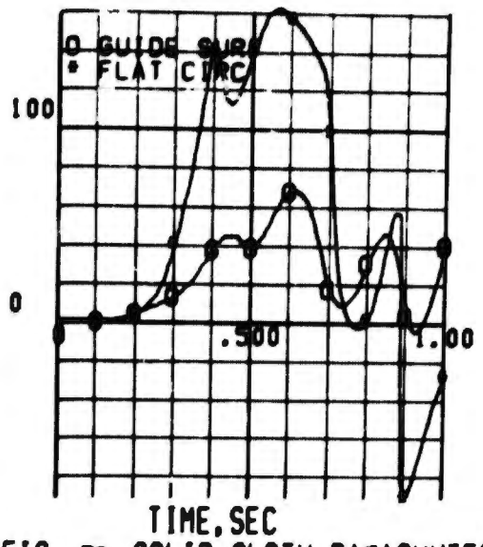

FIG 53 SOLID CLOTH PARACHUTES SEAT SIDESLIP ANGLE

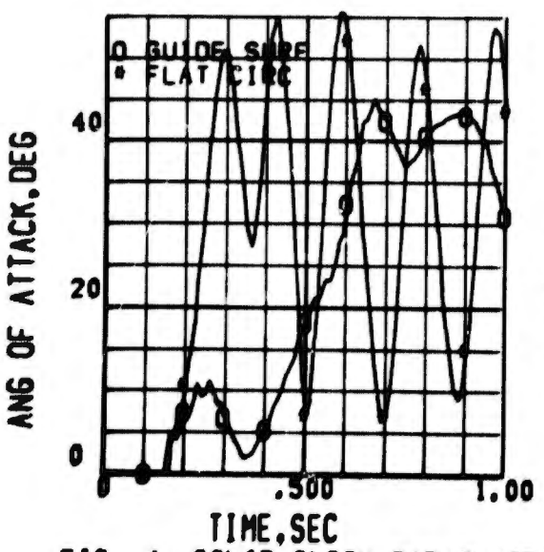

FIG 54 SOLID CLOTH PARACHUTES PARACHUTE ANGLE OF ATTACK

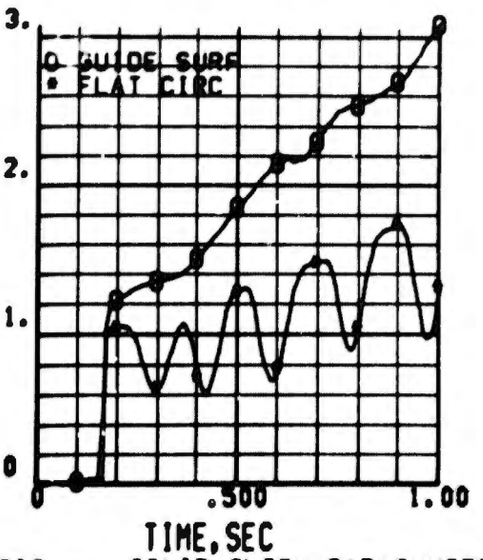

FIG 55 SOLID CLOTH PARACHUTES PARACHUTE AREA DRAG COEFF

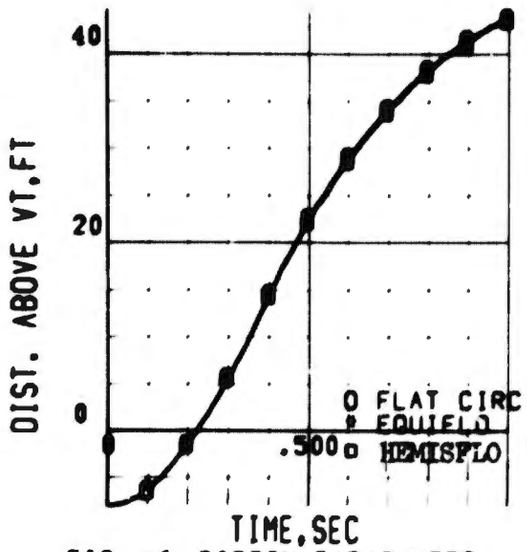

FIG 56 RIBBON PARACHUTES
VERT. TAIL VERT. CLEARANCE

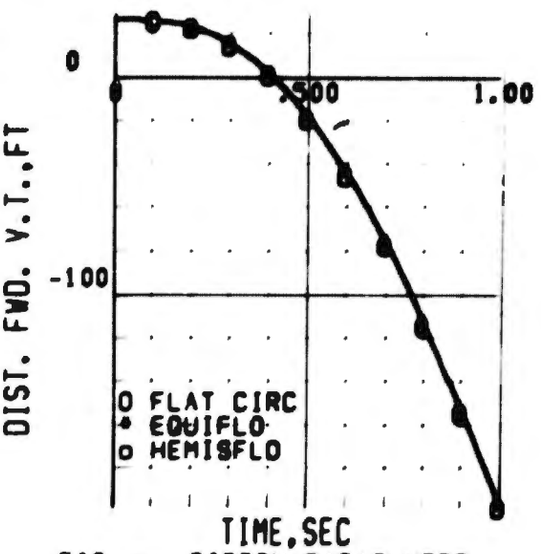

FIG 57 RIBBON PARACHUTES
VERT. TAIL LONG. CLEARANCE

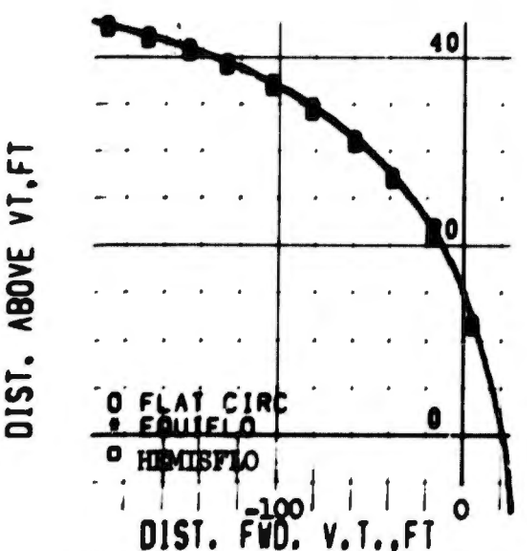

FIG 58 RIBBON PARACHUTES
VERTICAL TAIL CLEARANCE

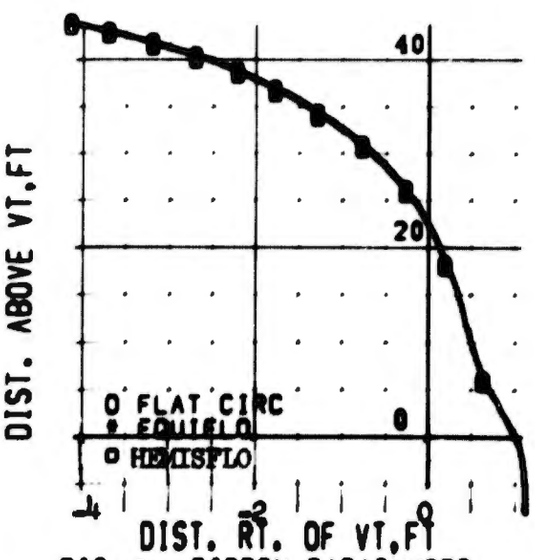

FIG 59 RIBBON PARACHUTES
VERTICAL TAIL CLEARANCE

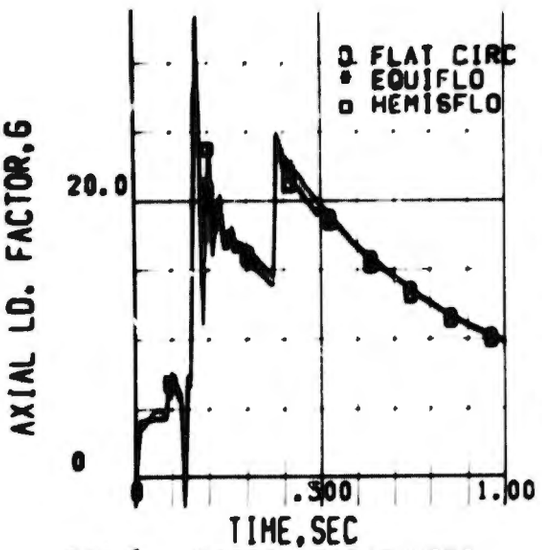

FIG 60 RIBBON PARACHUTES
SEAT AXIAL LOAD FACTOR

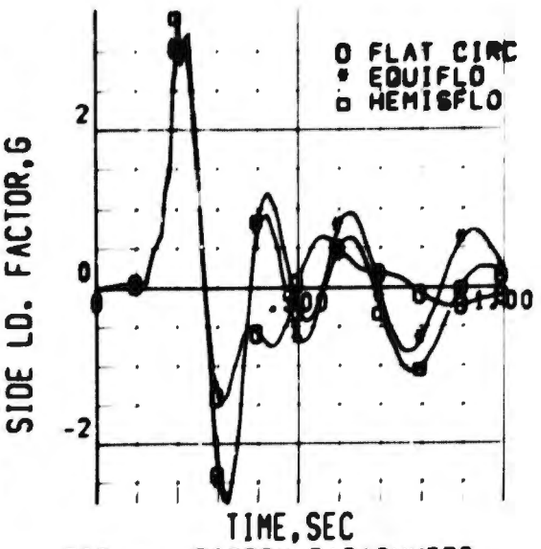

FIG 61 RIBBON PARACHUTES
SEAT SIDE LOAD FACTOR

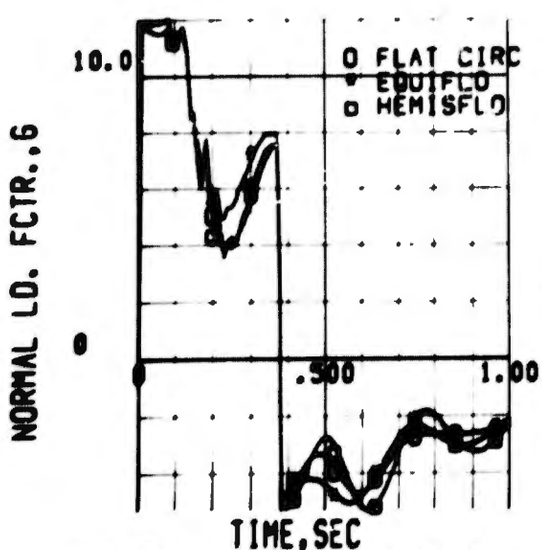

FIG 62 RIBBON PARACHUTES
SEAT NORMAL LOAD FACTOR

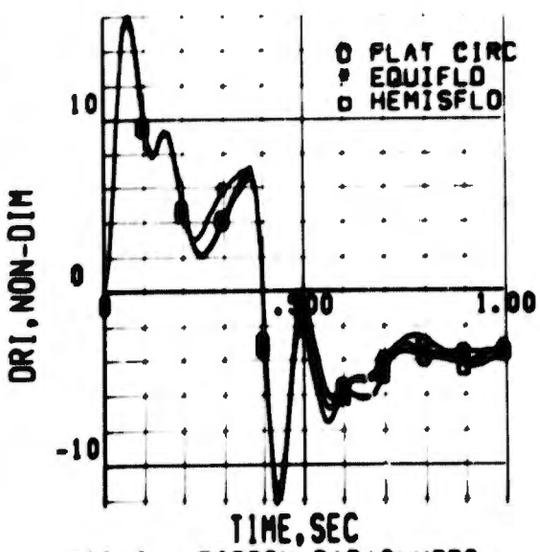

FIG 63 RIBBON PARACHUTES
MAN DYNAMIC RESPONSE INDEX

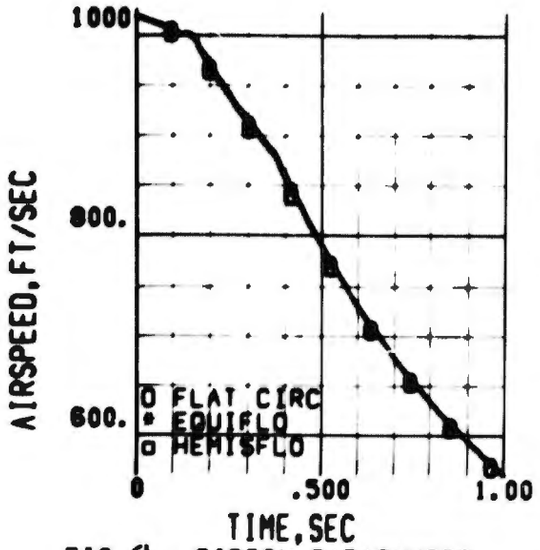

FIG 64 RIBBON PARACHUTES
SEAT AIRSPEED

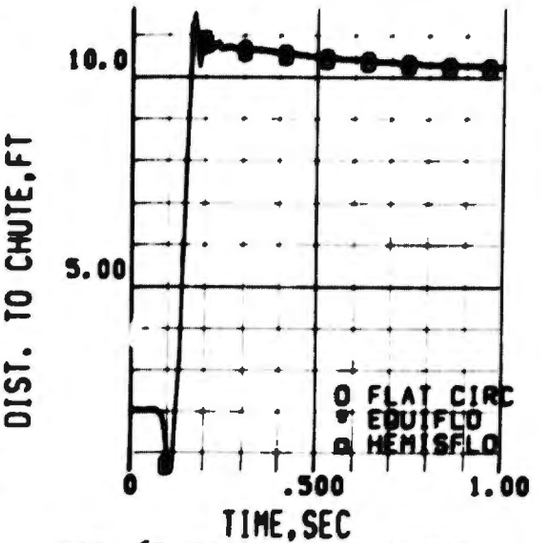

FIG 65 RIBBON PARACHUTES
DIST. FROM BRIDLE TO CHUTE CG

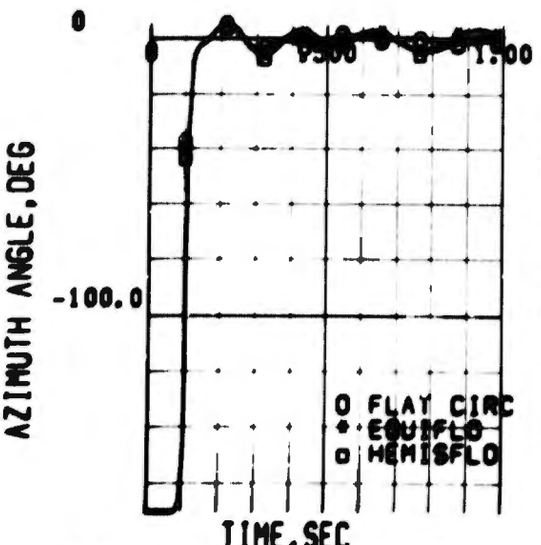

FIG 66 RIBBON PARACHUTES
SEAT-PARACHUTE AZIMUTH ANGLE

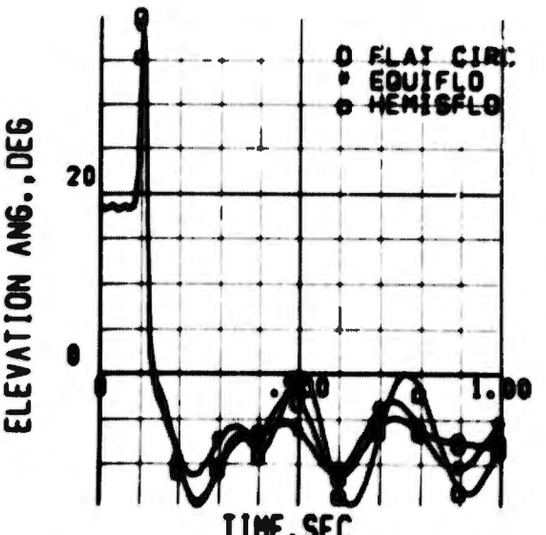

FIG 67 RIBBON PARACHUTES
SEAT-PARACHUTE ELEVATION ANGLE

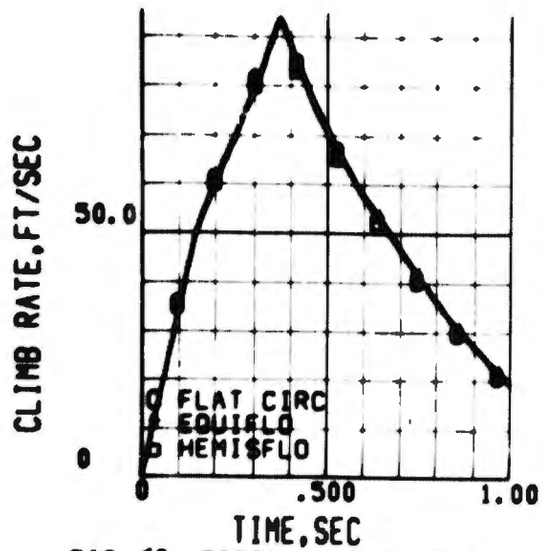

FIG 68 RIBBON PARACHUTES
SEAT CLIMB RATE

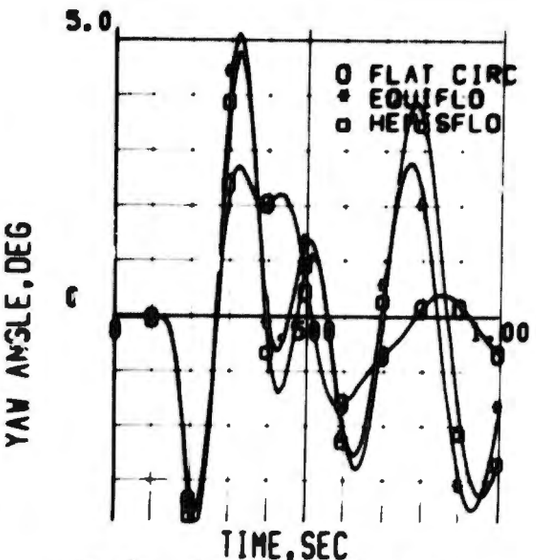

FIG 69 RIBBON PARACHUTES
SEAT EARTH AXIS YAW ANGLE

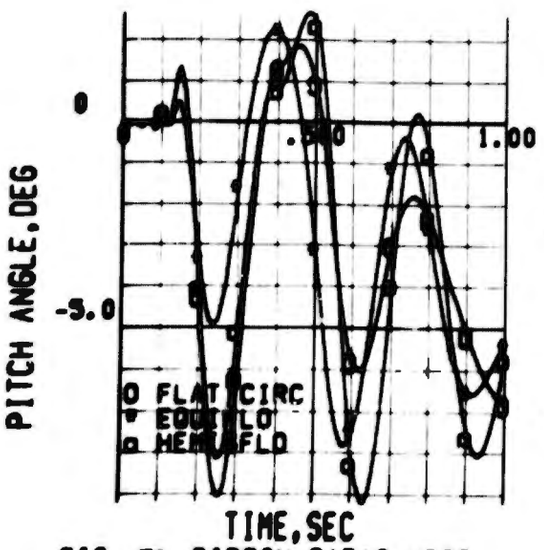

FIG 70 RIBBON PARACHUTES
SEAT EARTH AXIS PITCH ANGLE

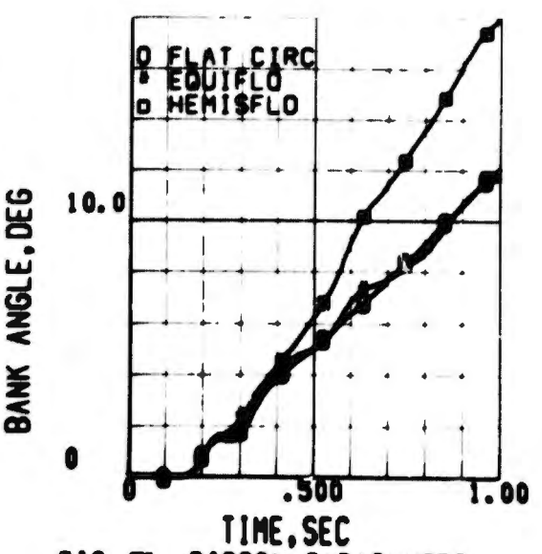

FIG 71 RIBBON PARACHUTES
SEAT EARTH AXIS BANK ANGLE

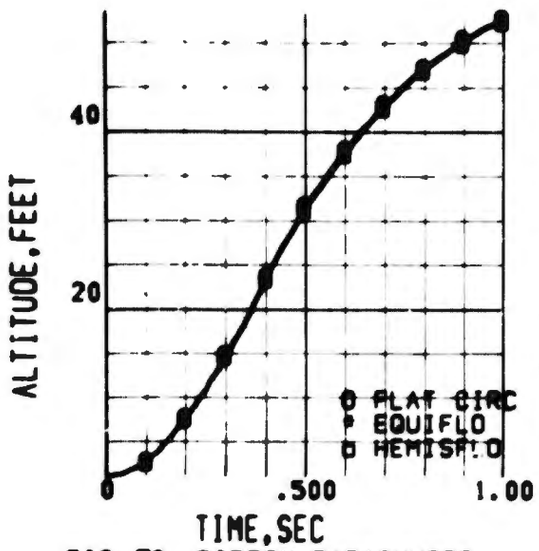

FIG 72 RIBBON PARACHUTES
SEAT ALTITUDE

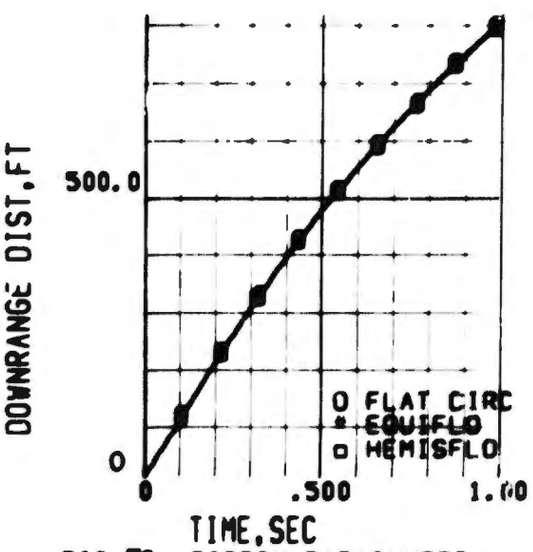

FIG 73 RIBBON PARACHUTES
SEAT DOWNRANGE DISTANCE

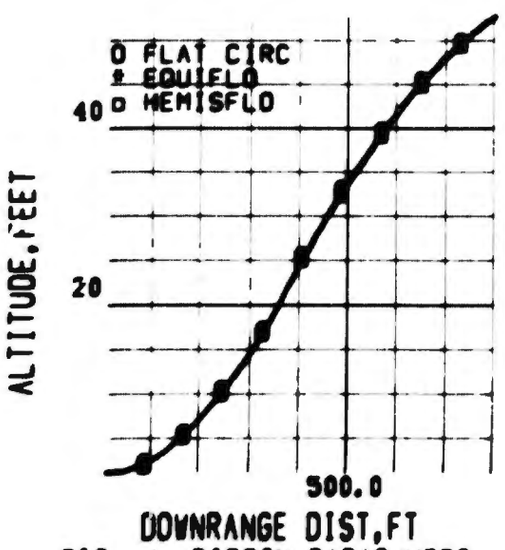

FIG 74 RIBBON PARACHUTES
SEAT TRAJECTORY

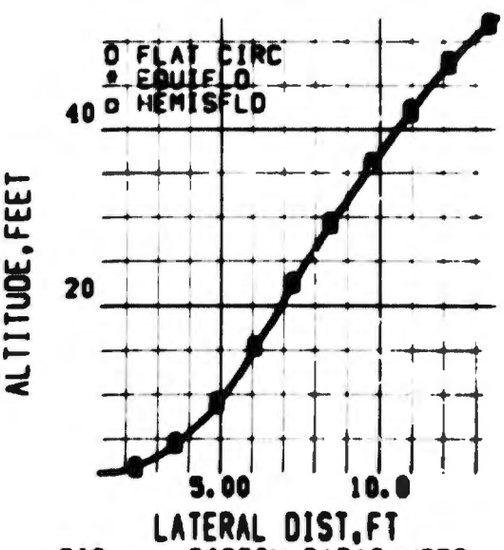

FIG 75 RIBBON PARACHUTES
SEAT TRAJECTORY

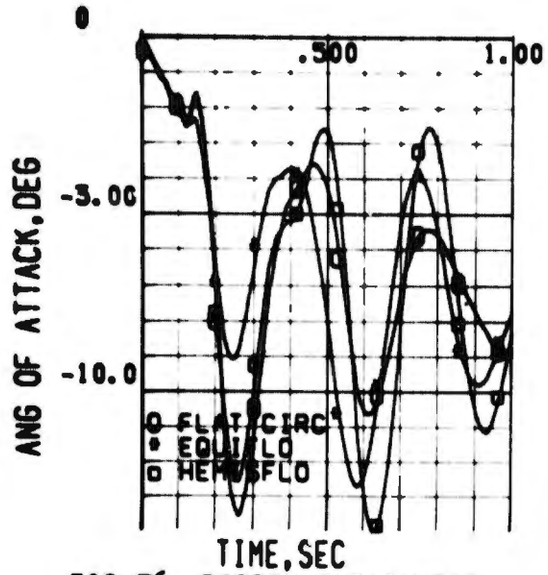

FIG 76 RIBBON PARACHUTES
SEAT ANGLE OF ATTACK

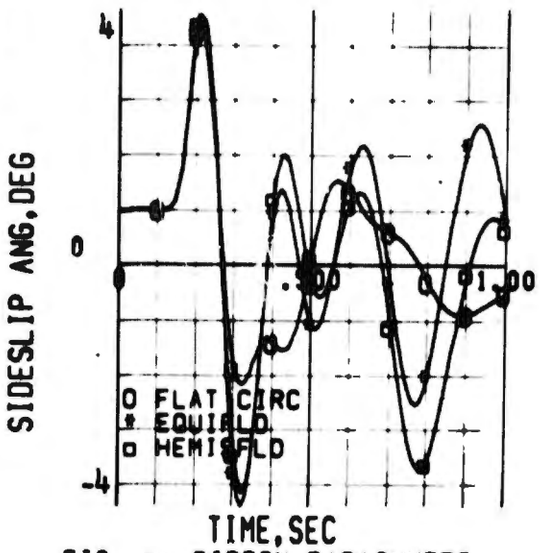

FIG 77 RIBBON PARACHUTES
SEAT SIDESLIP ANGLE

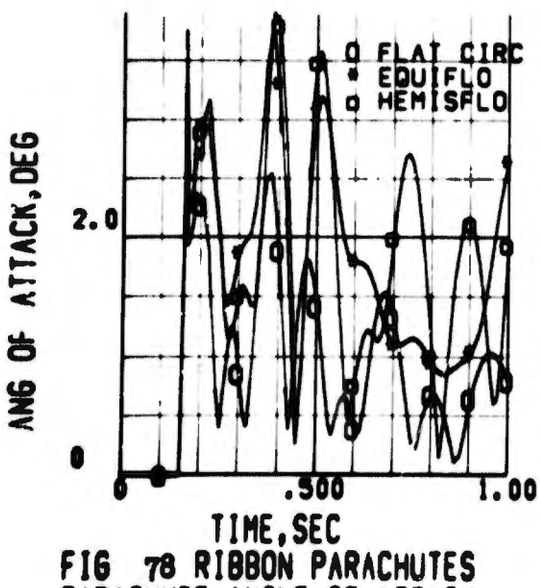

FIG 78 RIBBON PARACHUTES
PARACHUTE ANGLE OF ATTACK

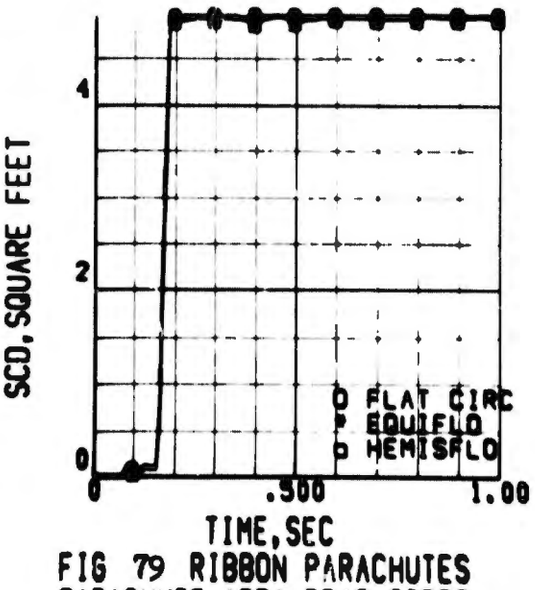

FIG 79 RIBBON PARACHUTES
PARACHUTE AREA DRAG COEFF

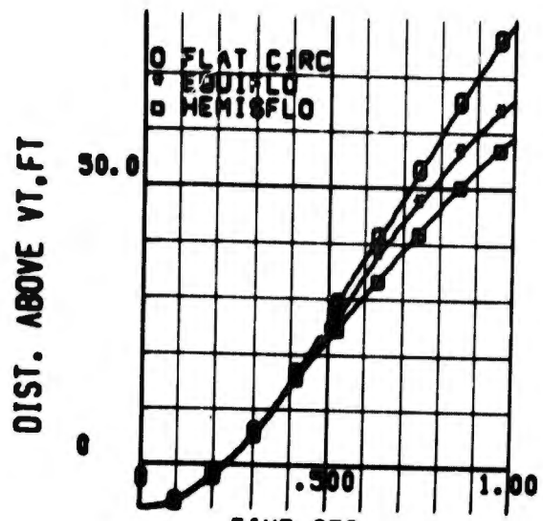

FIG 80 RIBBON PARACHUTES
VERT. TAIL VERT. CLEARANCE

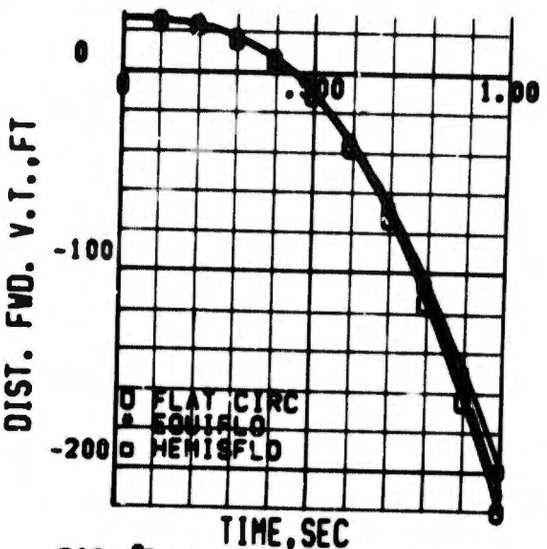

FIG 81 RIBBON PARACHUTES
VERT. TAIL LONG. CLEARANCE

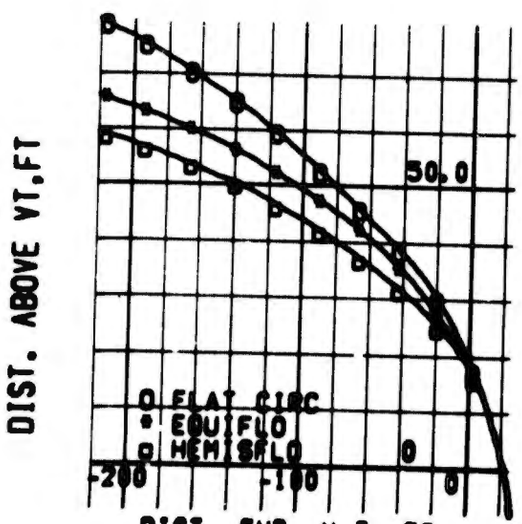

FIG 82 RIBBON PARACHUTES
VERTICAL TAIL CLEARANCE

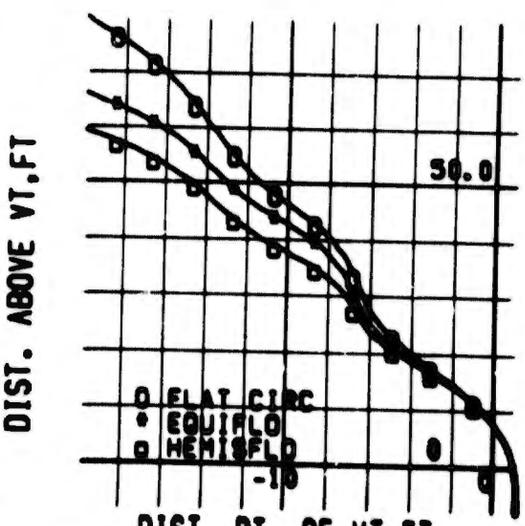

FIG 83 RIBBON PARACHUTES
VERTICAL TAIL CLEARANCE

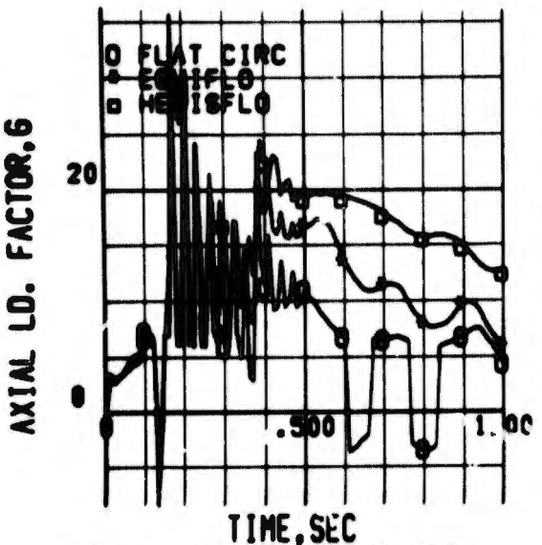

FIG 84 RIBBON PARACHUTES
SEAT AXIAL LOAD FACTOR

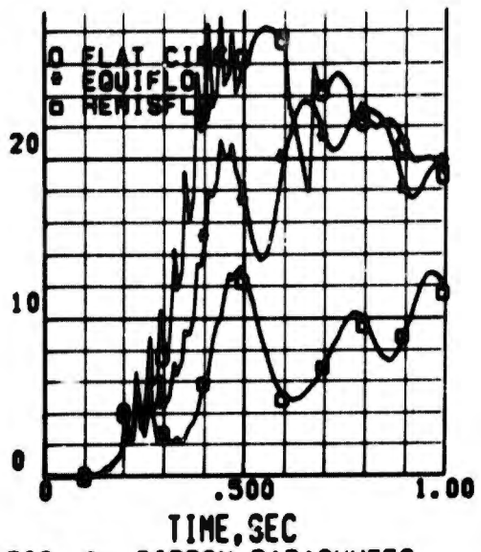

FIG 85 RIBBON PARACHUTES
SEAT SIDE LOAD FACTOR

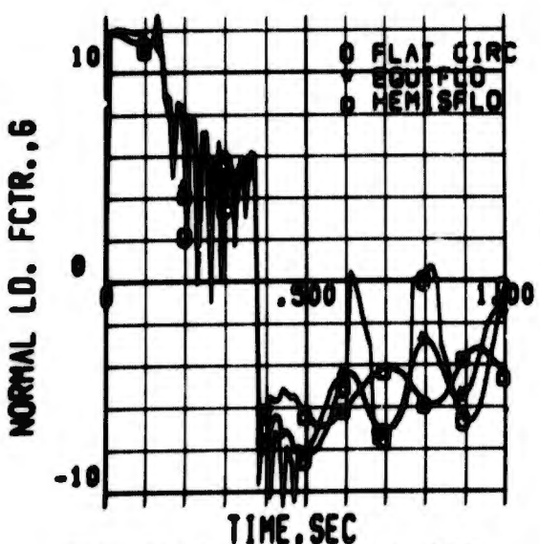

FIG 86 RIBBON PARACHUTES
SEAT NORMAL LOAD FACTOR

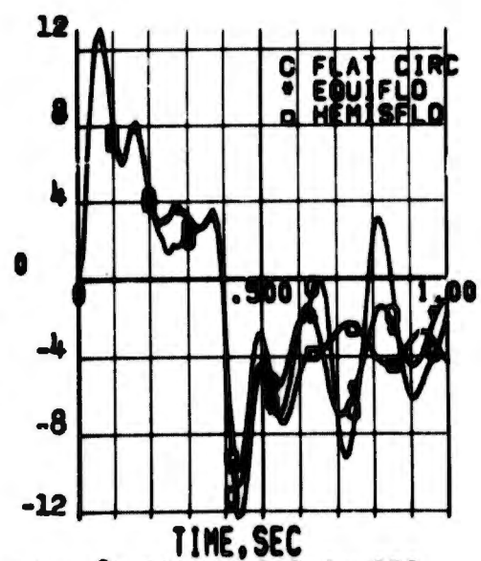

FIG 87 RIBBON PARACHUTES
MAN DYNAMIC RESPONSE INDEX

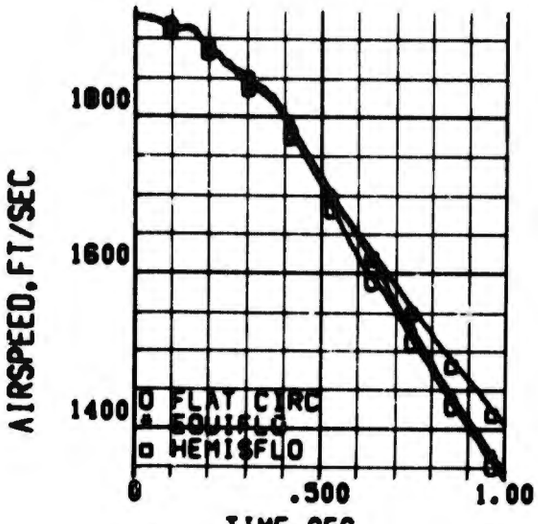

FIG 88 RIBBON PARACHUTES
SEAT AIRSPEED

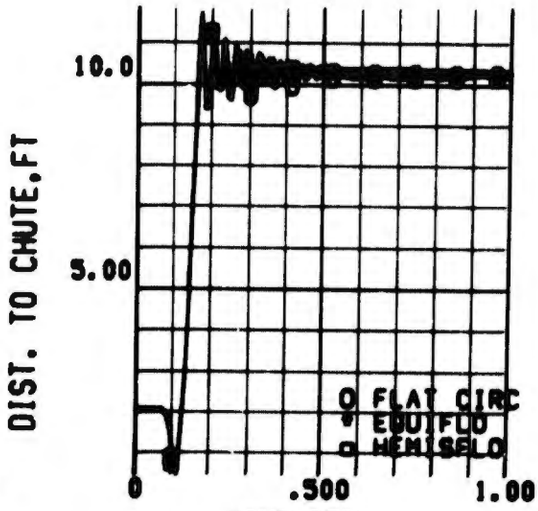

FIG 89 RIBBON PARACHUTES
DIST. FROM BRIDLE TO CHUTE CG

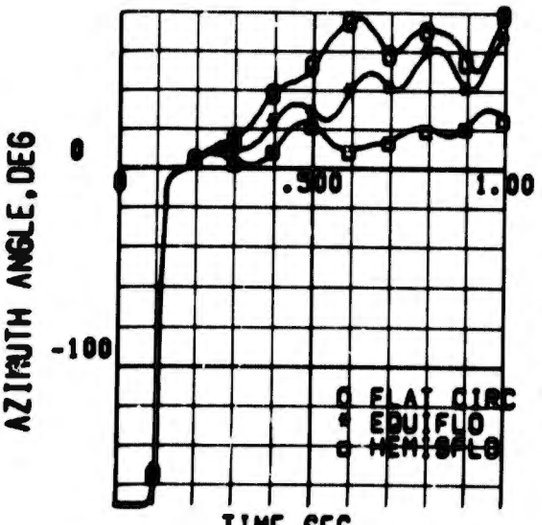

FIG 90 RIBBON PARACHUTES
SEAT-PARACHUTE AZIMUTH ANGLE

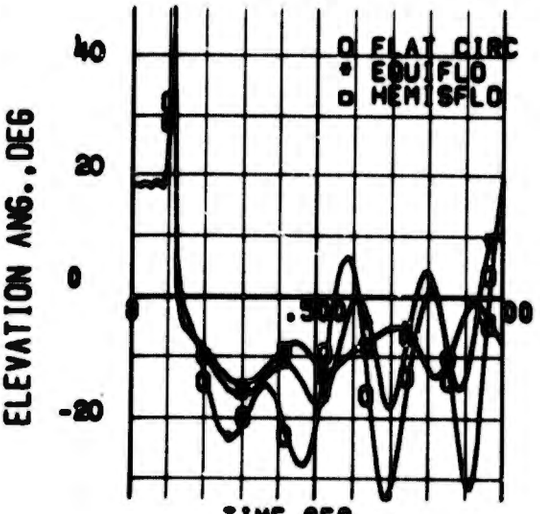

FIG 91 RIBBON PARACHUTES
SEAT-PARACHUTE ELEVATION ANGLE

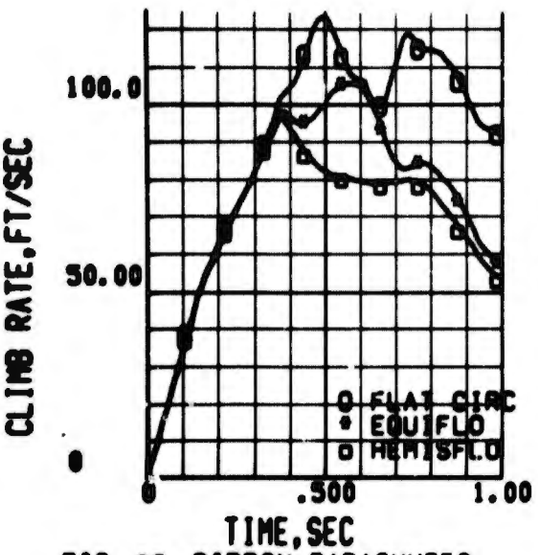

FIG 92 RIBBON PARACHUTES
SEAT CLIMB RATE

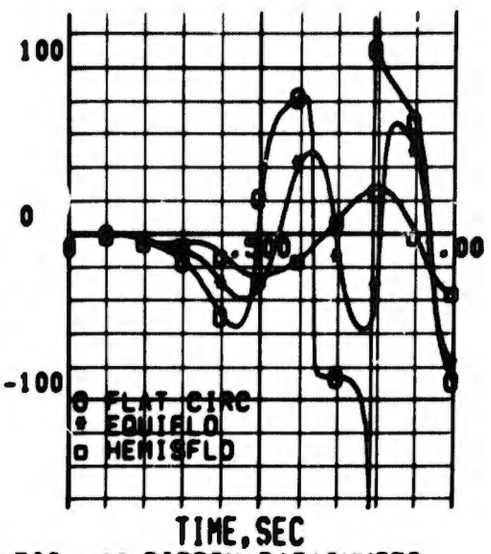

FIG 93 RIBBON PARACHUTES
SEAT EARTH AXIS YAW ANGLE

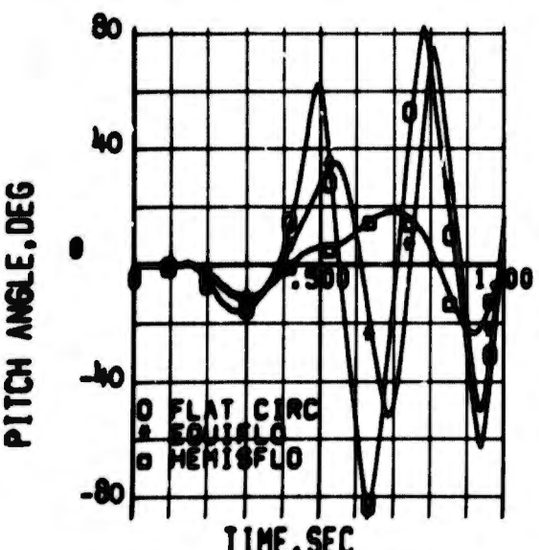

FIG 94 RIBBON PARACHUTES
SEAT EARTH AXIS PITCH ANGLE

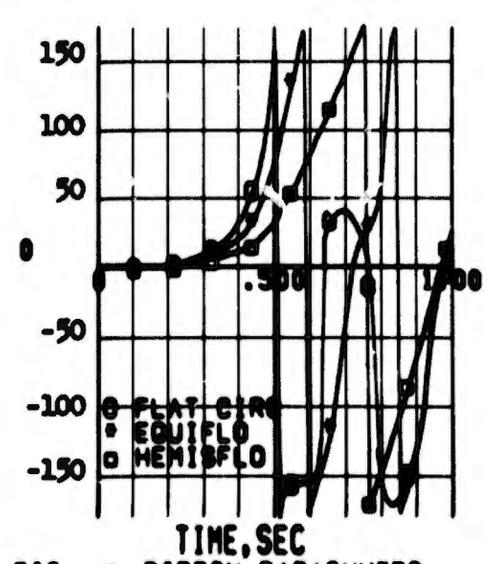

FIG 95 RIBBON PARACHUTES
SEAT EARTH AXIS BANK ANGLE

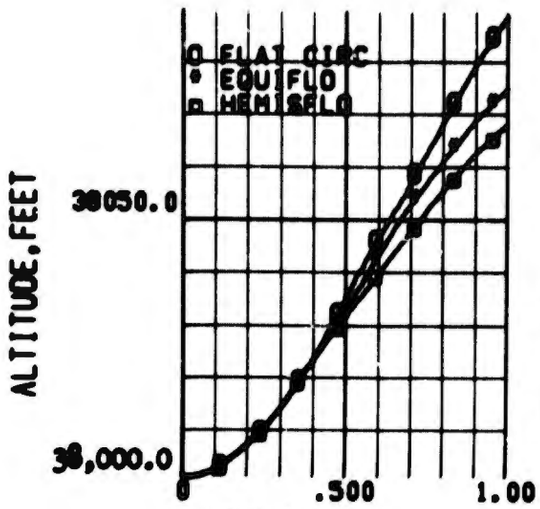

FIG 96 RIBBON PARACHUTES
SEAT ALTITUDE

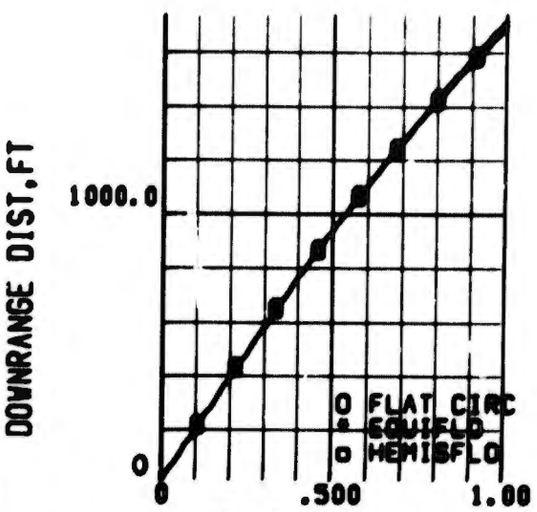

FIG 97 RIBBON PARACHUTES
SEAT DOWNRANGE DISTANCE

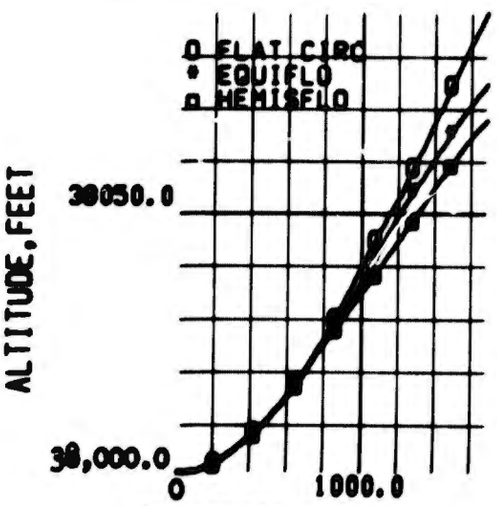

FIG 98 RIBBON PARACHUTES
SEAT TRAJECTORY

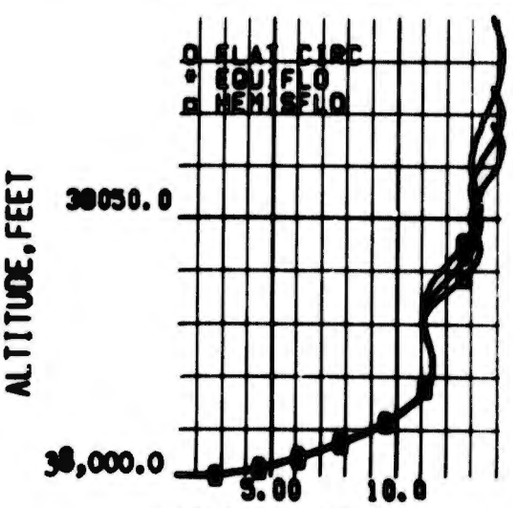

FIG 99 RIBBON PARACHUTES
SEAT TRAJECTORY

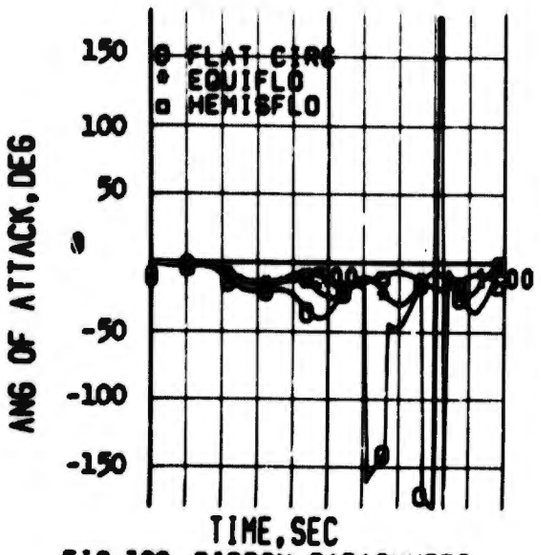

FIG 100 RIBBON PARACHUTES
SEAT ANGLE OF ATTACK

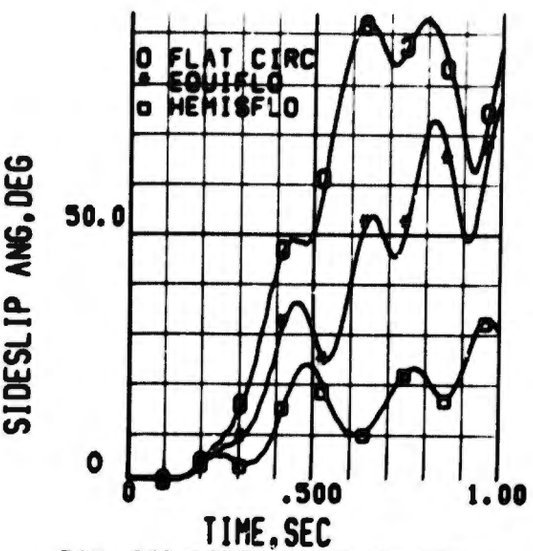

FIG 101 RIBBON PARACHUTES
SEAT SIDESLIP ANGLE

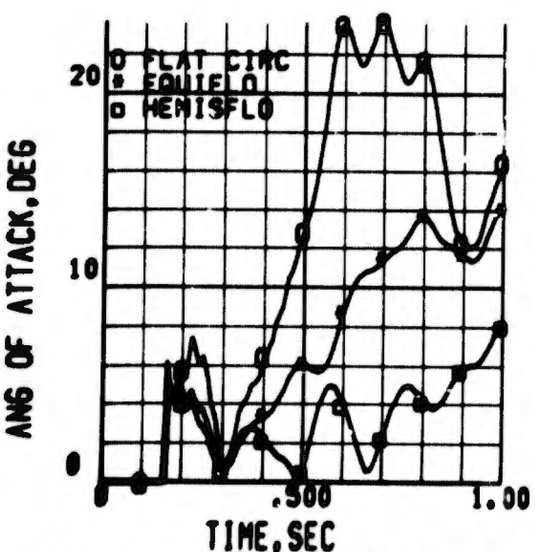

FIG 102 RIBBON PARACHUTES
PARACHUTE ANGLE OF ATTACK

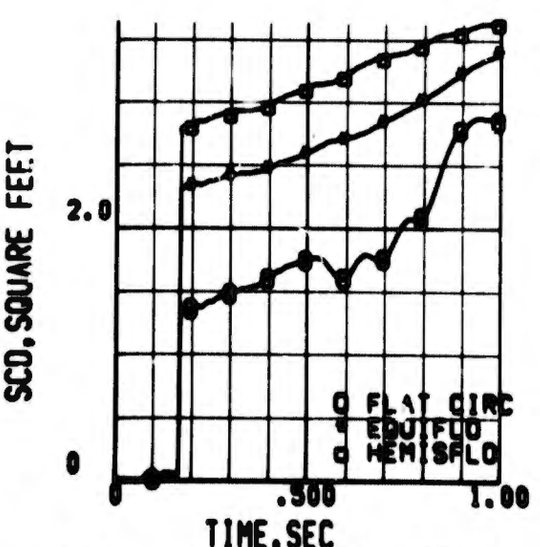

FIG 103 RIBBON PARACHUTES
PARACHUTE AREA DRAG COEFF

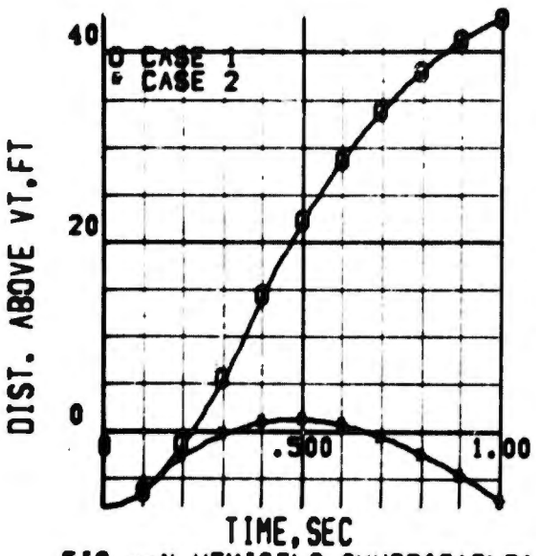

FIG 104 HEMISFLO CHUTE(TABLE1)
VERT. TAIL VERT. CLEARANCE

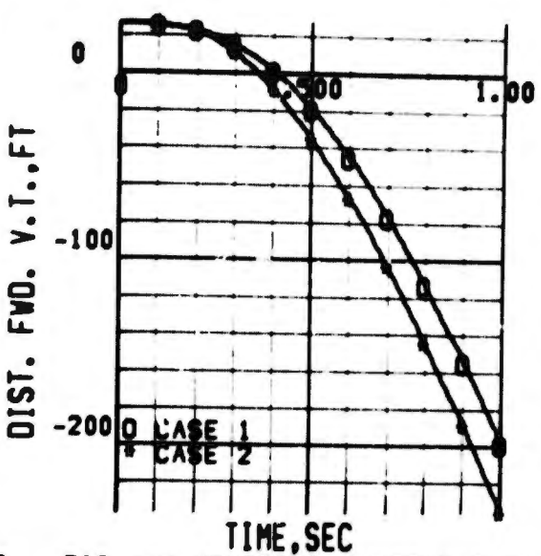

FIG 105 HEMISFLO CHUTE(TABLE1)
VERT. TAIL LONG. CLEARANCE

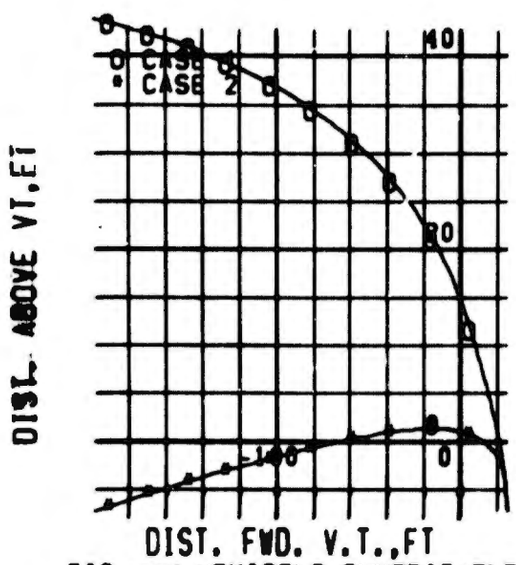

FIG 106 HEMISFLO CHUTE(TABLE1)
VERTICAL TAIL CLEARANCE

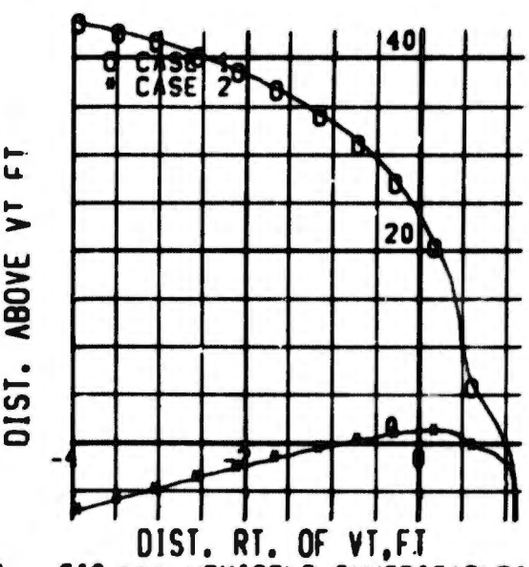

FIG 107 HEMISFLO CHUTE(TABLE1)
VERTICAL TAIL CLEARANCE

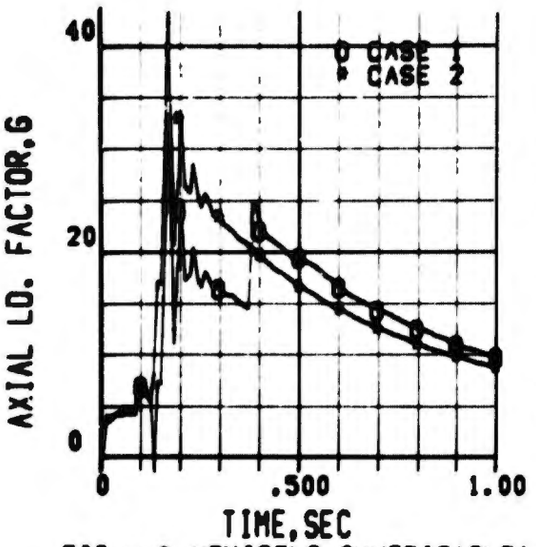

FIG 108 HEMISFLO CHUTE(TABLE1)
SEAT AXIAL LOAD FACTOR

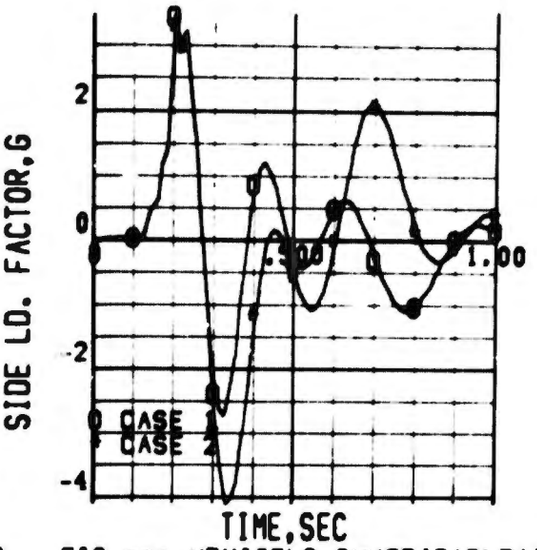

FIG 109 HEMISFLO CHUTE(TABLE1)
SEAT SIDE LOAD FACTOR

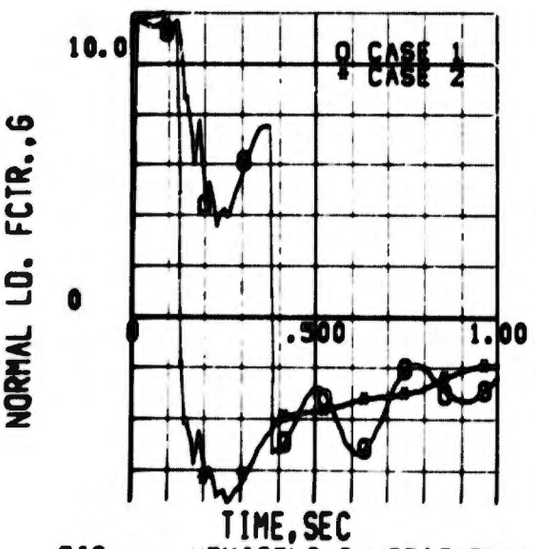

FIG 110 HEMISFLO CHUTE(TABLE1)
SEAT NORMAL LOAD FACTOR

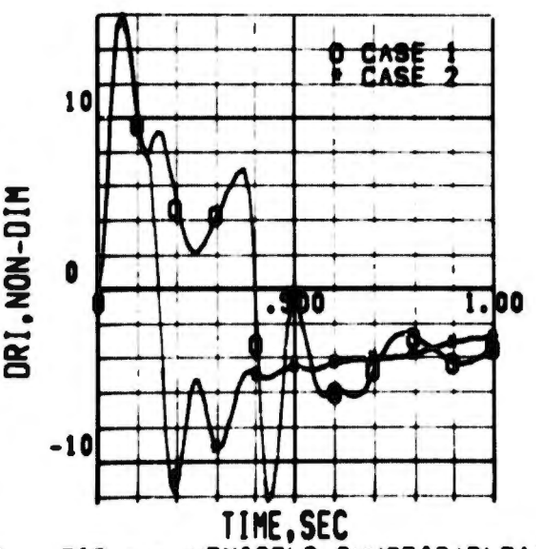

FIG 111 HEMISFLO CHUTE(TABLE1)
MAN DYNAMIC RESPONSE INDEX

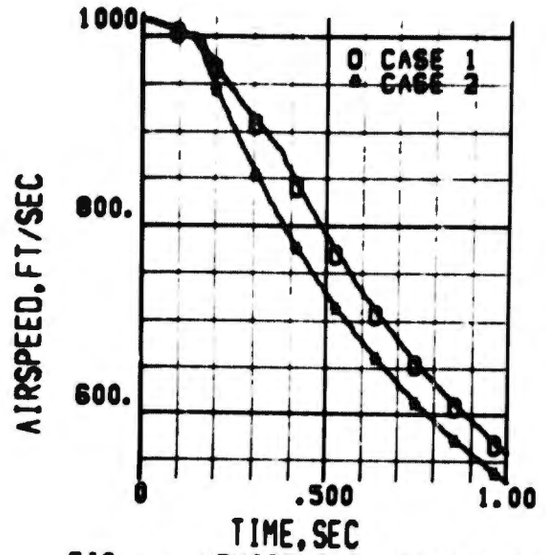

FIG 112 HEMISFLO CHUTE(TABLE1)
SEAT AIRSPEED

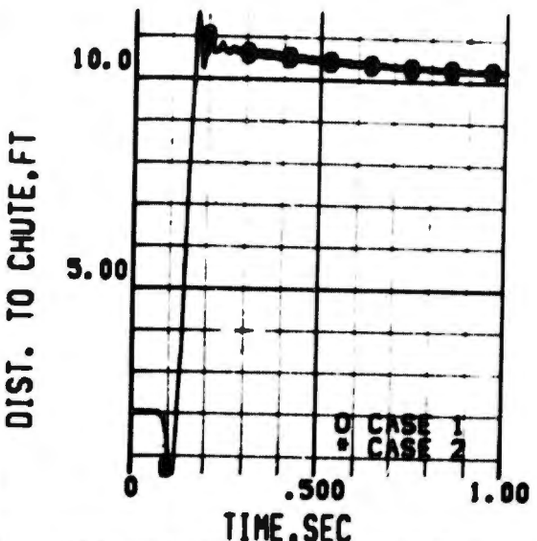

FIG 113 HEMISFLO CHUTE(TABLE1)
DIST. FROM BRIDLE TO CHUTE CG

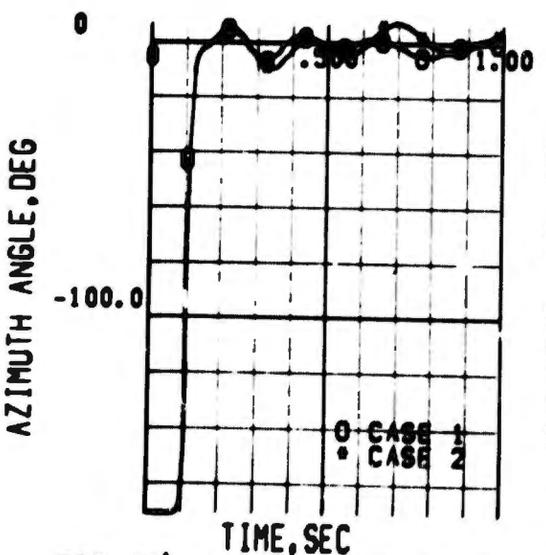

FIG 114 HEMISFLO CHUTE(TABLE1)
SEAT-PARACHUTE AZIMUTH ANGLE

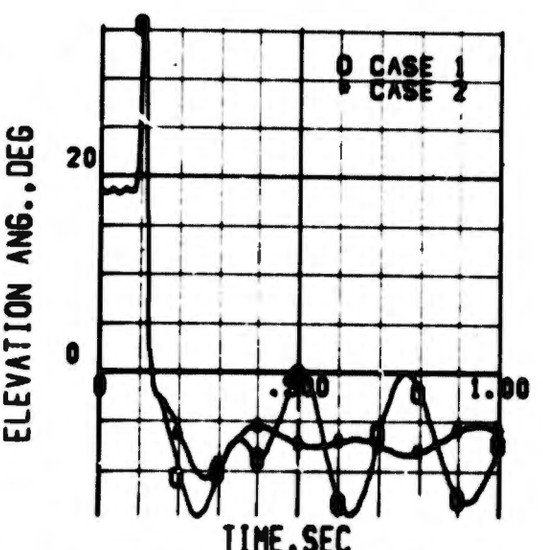

FIG 115 HEMISFLO CHUTE(TABLE1)
SEAT-PARACHUTE ELEVATION ANGLE

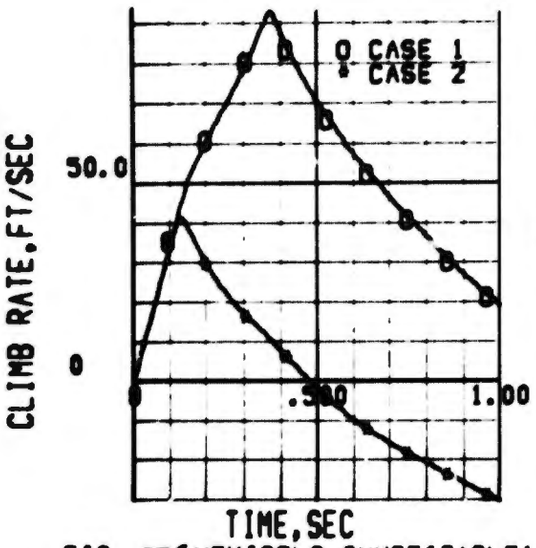

FIG 116 HEMISFLO CHUTE(TABLE1)
SEAT CLIMB RATE

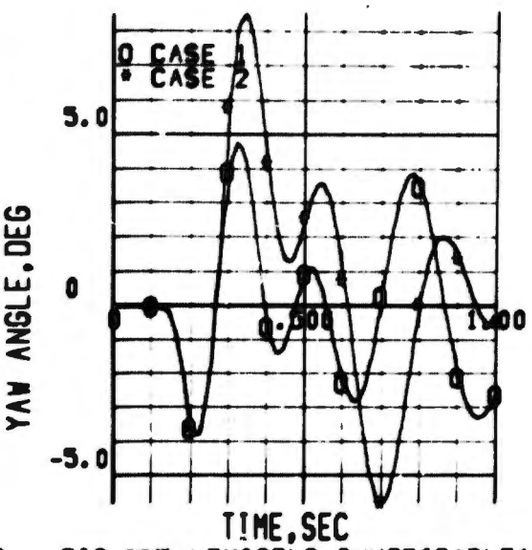

FIG 117 HEMISFLO CHUTE(TABLE1)
SEAT EARTH AXIS YAW ANGLE

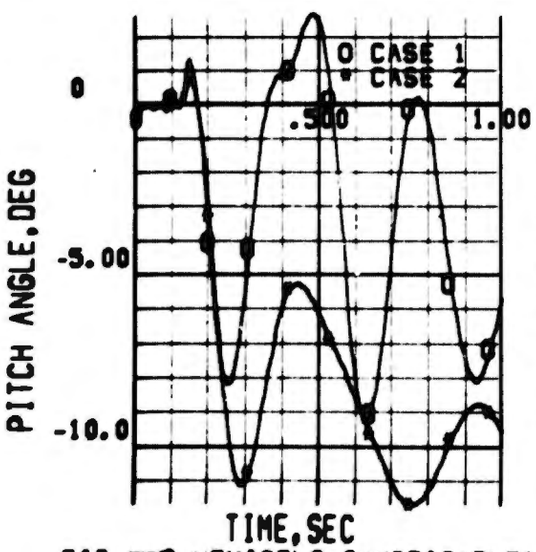

FIG 118 HEMISFLO CHUTE(TABLE1)
SEAT EARTH AXIS PITCH ANGLE

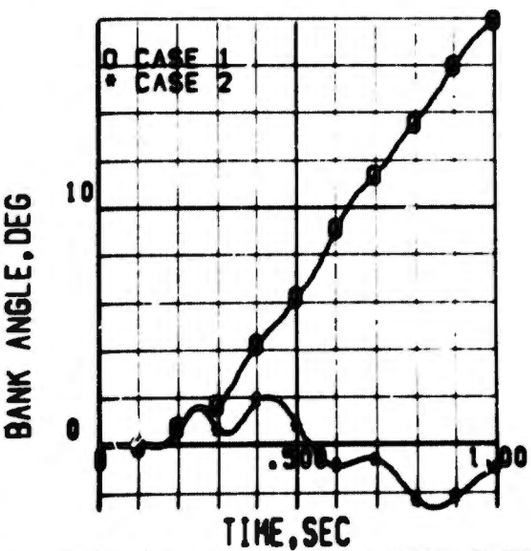

FIG 119 HEMISFLO CHUTE(TABLE1)
SEAT EARTH AXIS BANK ANGLE

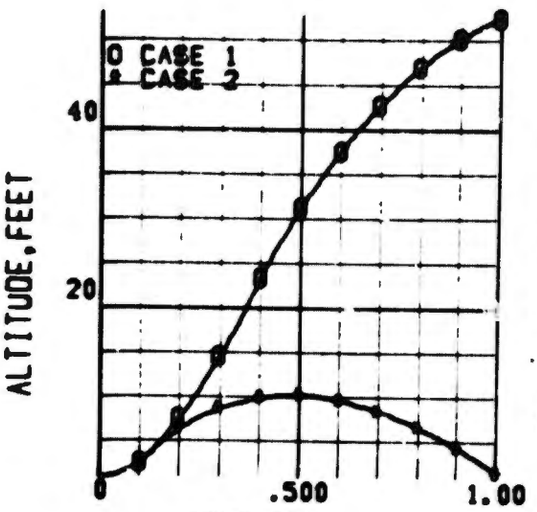

FIG 120 HEMISFLO CHUTE(TABLE1)
SEAT ALTITUDE

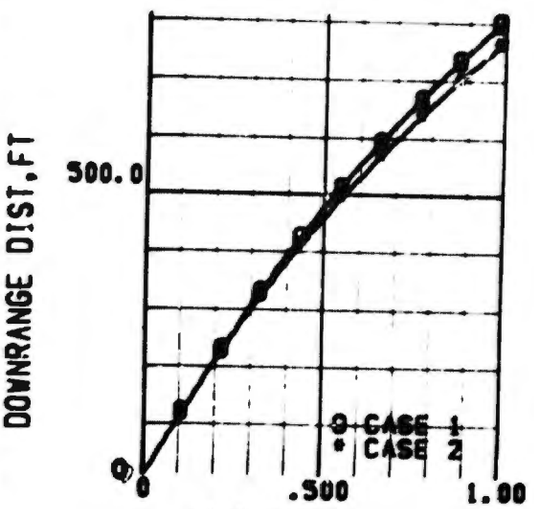

FIG 121 HEMISFLO CHUTE(TABLE1)
SEAT DOWNRANGE DISTANCE

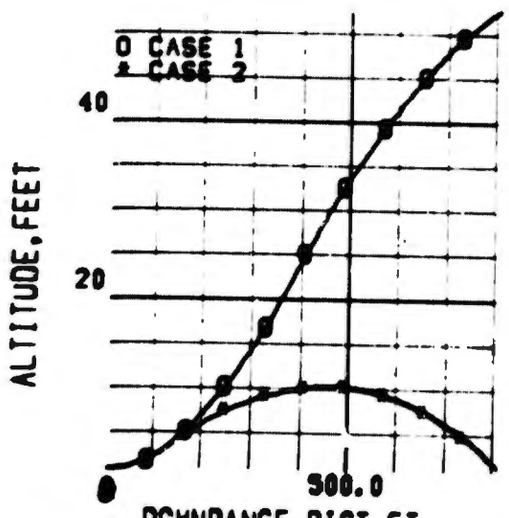

FIG 122 HEMISFLO CHUTE(TABLE1)
SEAT TRAJECTORY

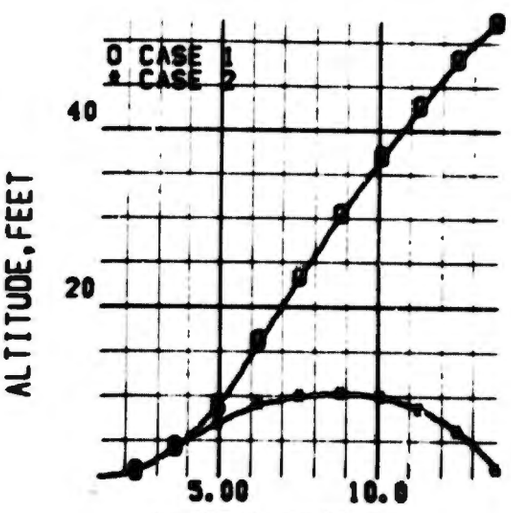

FIG 123 HEMISFLO CHUTE(TABLE1)
SEAT TRAJECTORY

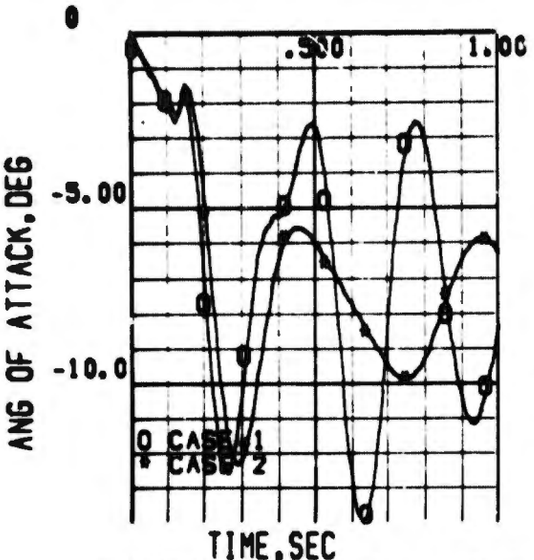

FIG 124 HEMISFLO CHUTE(TABLE1)
SEAT ANGLE OF ATTACK

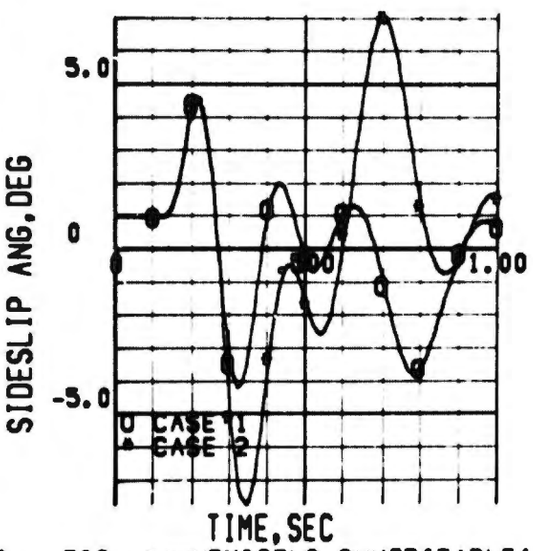

FIG 125 HEMISFLO CHUTE(TABLE1)
SEAT SIDESLIP ANGLE

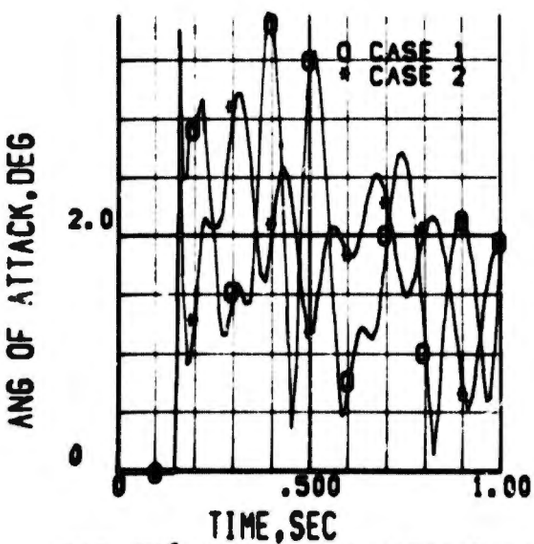

FIG 126 HEMISFLO CHUTE(TABLE1)
PARACHUTE ANGLE OF ATTACK

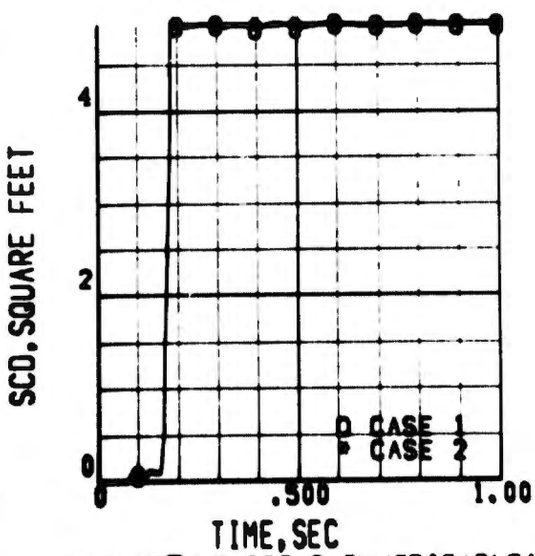

FIG 127 HEMISFLO CHUTE(TABLE1)
PARACHUTE AREA DRAG COEFF

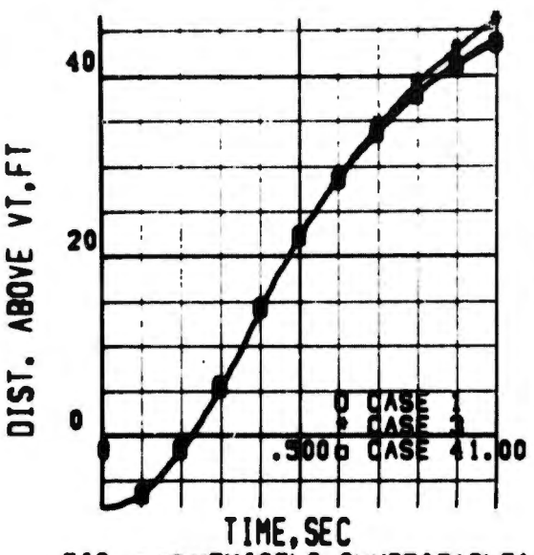

FIG 128 HEMISFLO CHUTE(TABLE1)
VERT. TAIL VERT. CLEARANCE

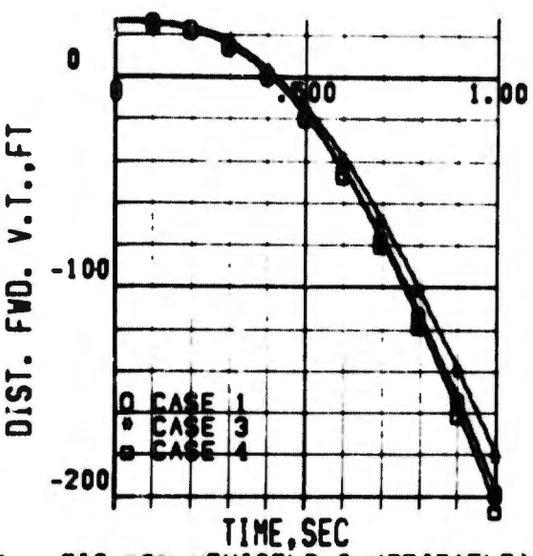

FIG 129 HEMISFLO CHUTE(TABLE1)
VERT. TAIL LONG. CLEARANCE

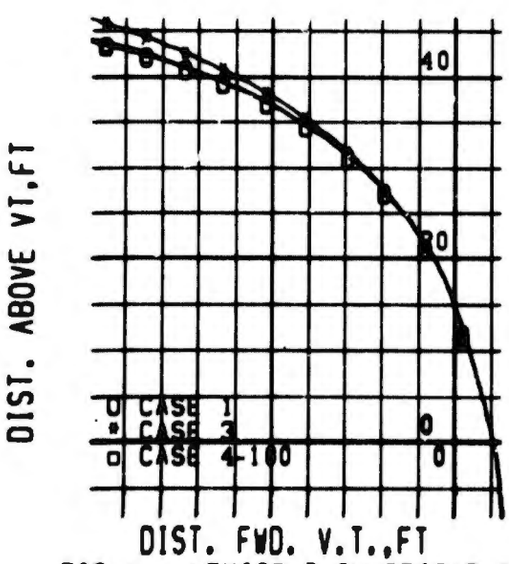

FIG 130 HEMISFLO CHUTE(TABLE1)
VERTICAL TAIL CLEARANCE

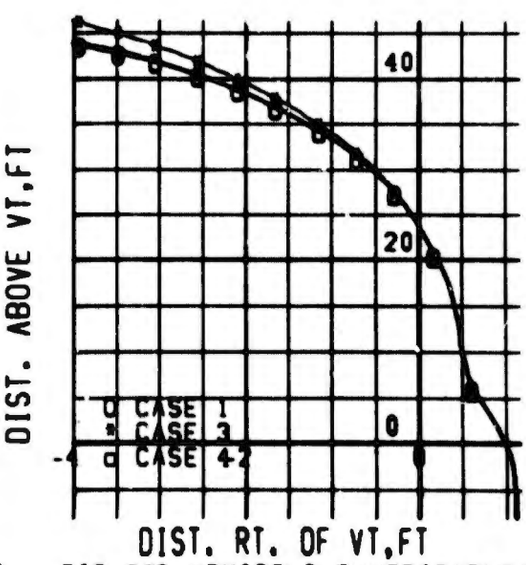

FIG 131 HEMISFLO CHUTE(TABLE1)
VERTICAL TAIL CLEARANCE

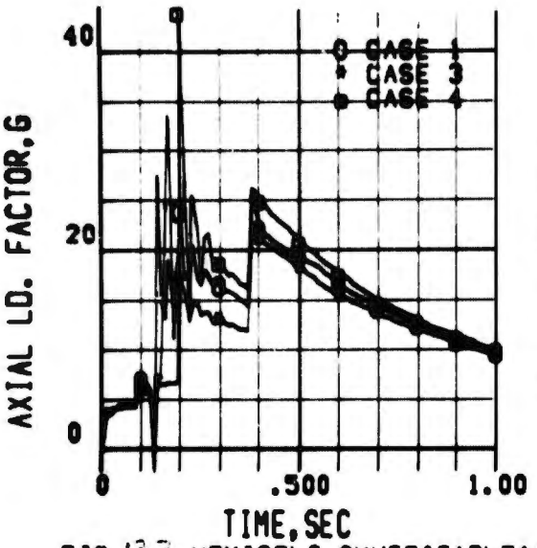

FIG 132 HEMISFLO CHUTE(TABLE1)
SEAT AXIAL LOAD FACTOR

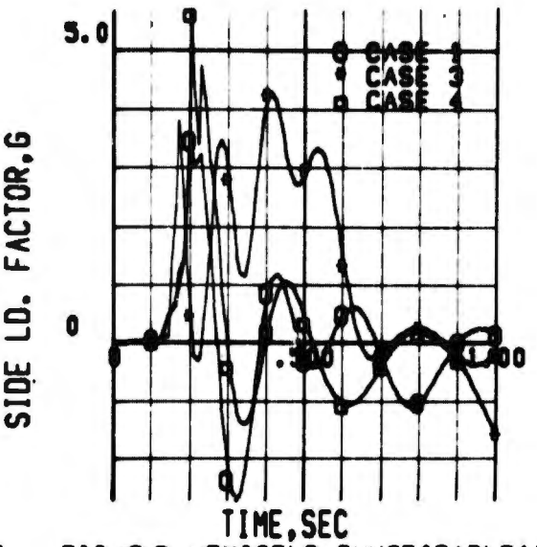

FIG 133 HEMISFLO CHUTE(TABLE1)
SEAT SIDE LOAD FACTOR

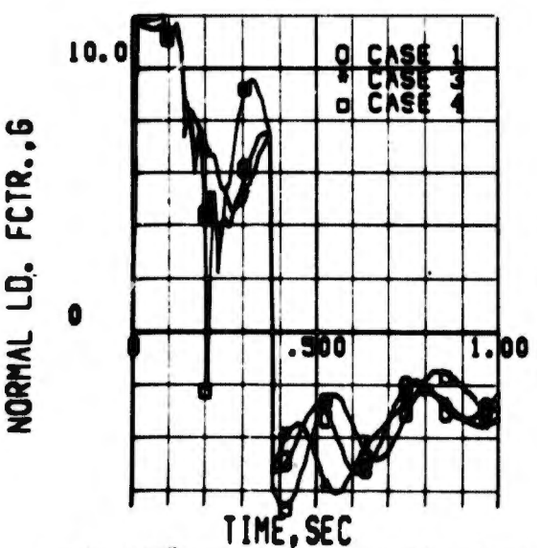

FIG 134 HEMISFLO CHUTE(TABLE1)
SEAT NORMAL LOAD FACTOR

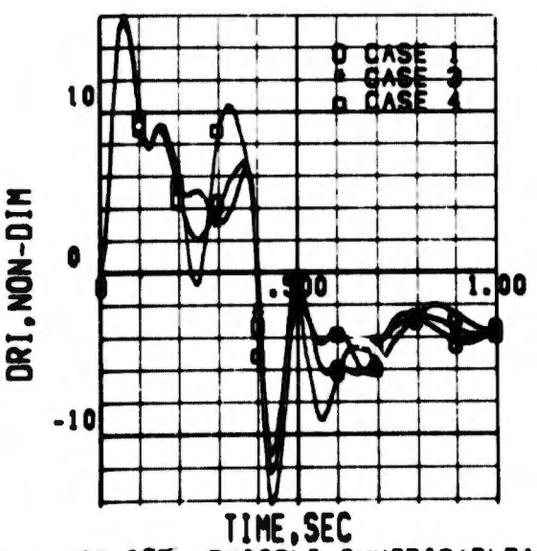

FIG 135 HEMISFLO CHUTE(TABLE1)
MAN DYNAMIC RESPONSE INDEX

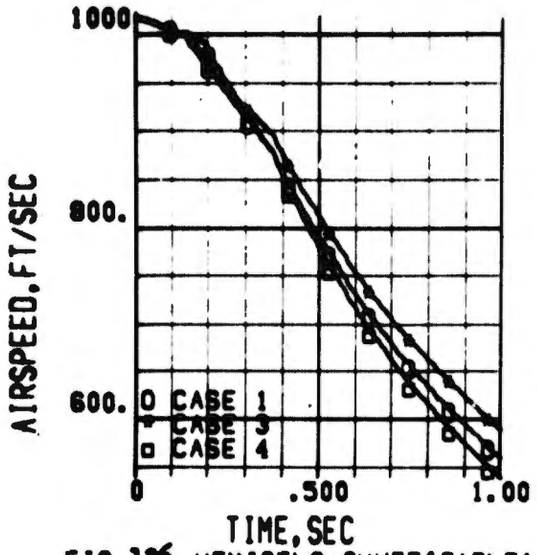

FIG 136 HEMISFLO CHUTE(TABLE1)
SEAT AIRSPEED

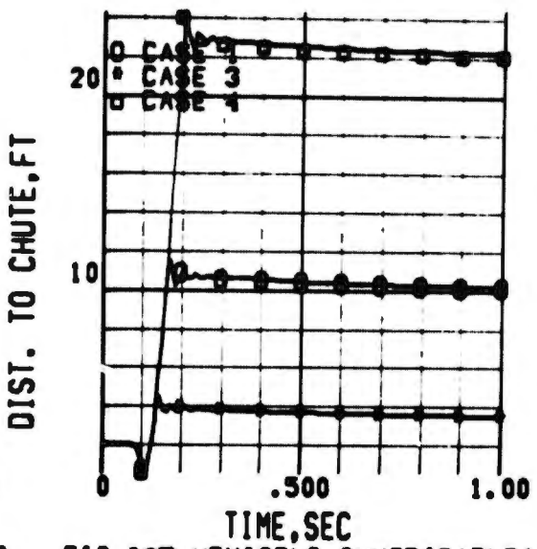

FIG 137 HEMISFLO CHUTE(TABLE1)
DIST. FROM BRIDLE TO CHUTE CG

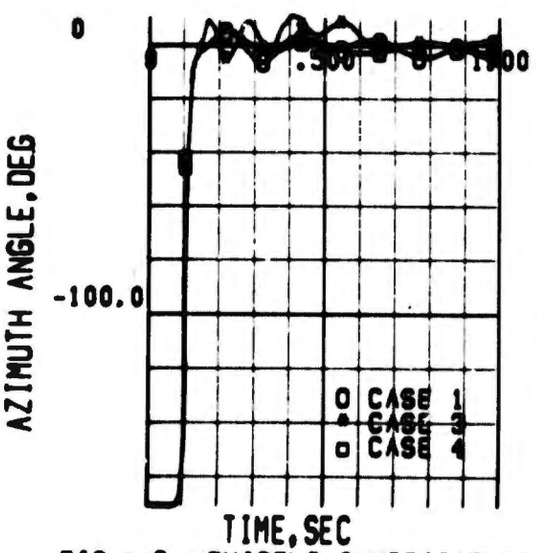

FIG 138 HEMISFLO CHUTE(TABLE1)
SEAT-PARACHUTE AZIMUTH ANGLE

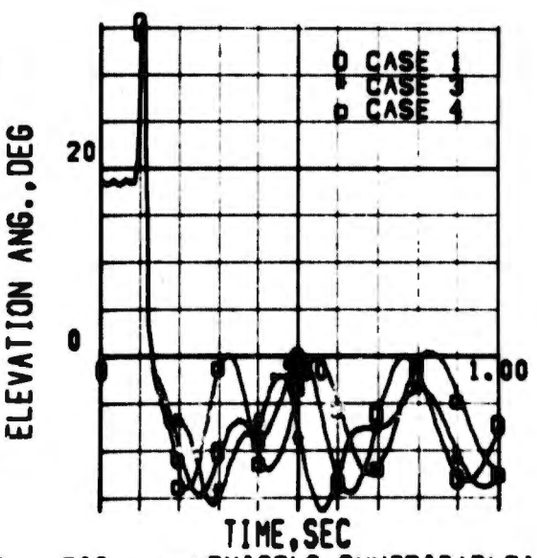

FIG 139 HEMISFLO CHUTE(TABLE1)
SEAT-PARACHUTE ELEVATION ANGLE

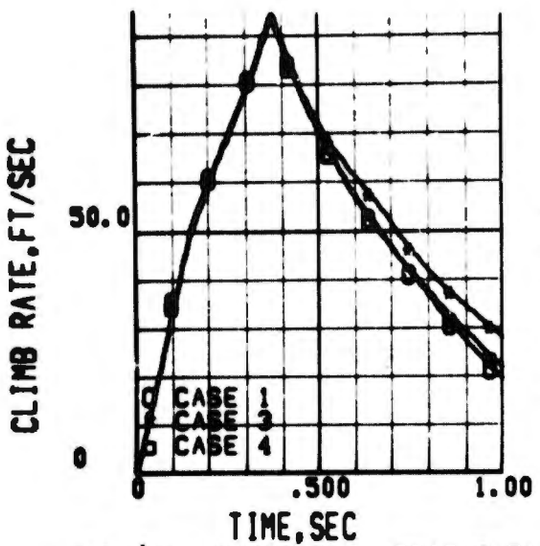

FIG 140 HEMISFLO CHUTE(TABLE1)
SEAT CLIMB RATE

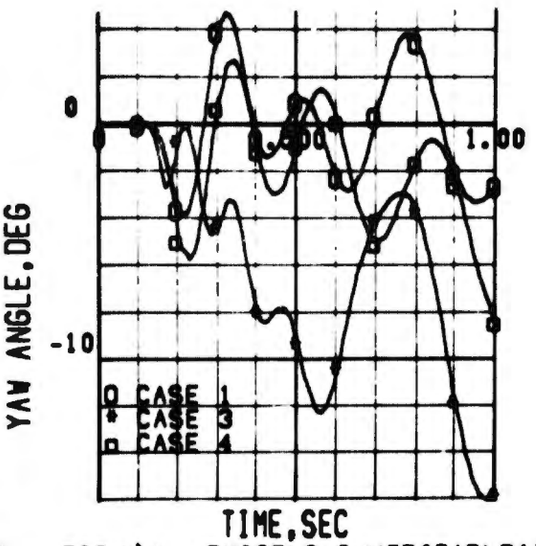

FIG 141 HEMISFLO CHUTE(TABLE1)
SEAT EARTH AXIS YAW ANGLE

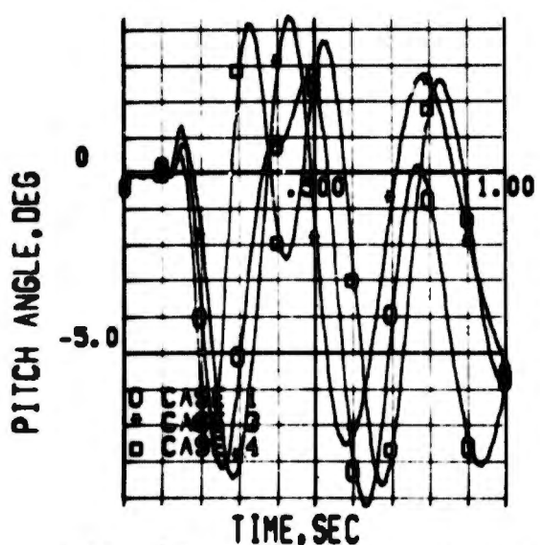

FIG 142 HEMISFLO CHUTE(TABLE1)
SEAT EARTH AXIS PITCH ANGLE

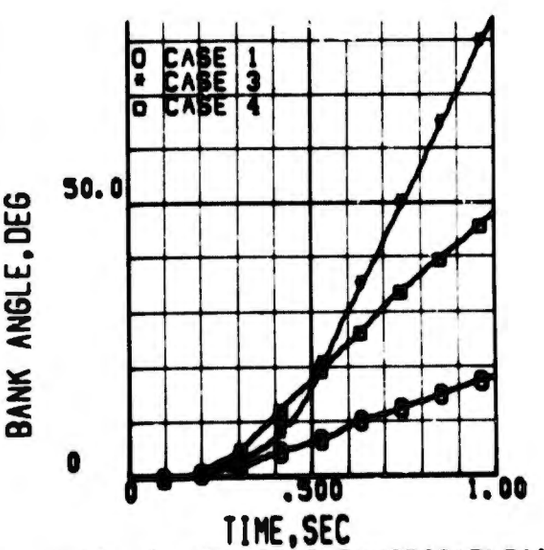

FIG 143 HEMISFLO CHUTE(TABLE1)
SEAT EARTH AXIS BANK ANGLE

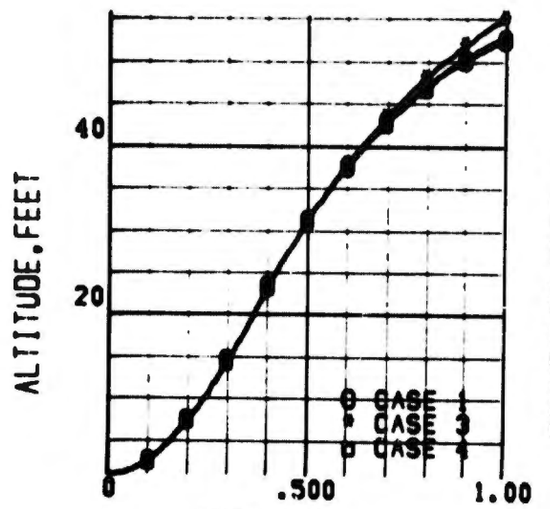

FIG 1.4 HEMISFLO CHUTE(TABLE1)
SEAT ALTITUDE

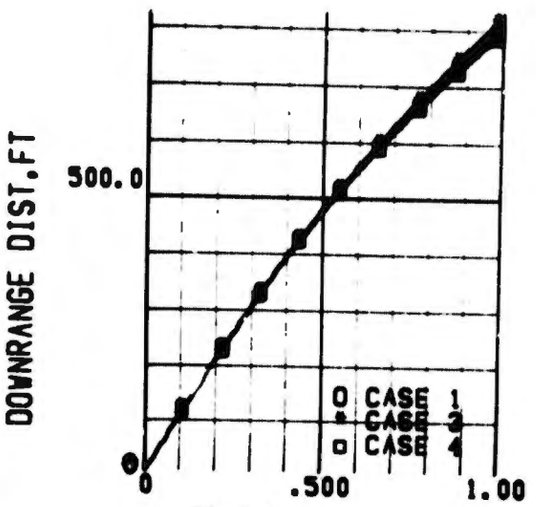

FIG 1.5 HEMISFLO CHUTE(TABLE1)
SEAT DOWNRANGE DISTANCE

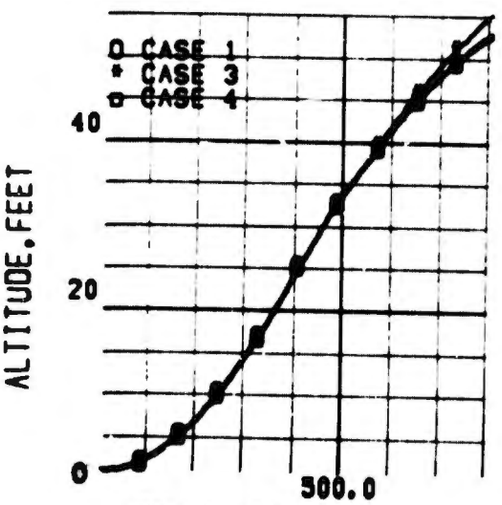

FIG 1.6 HEMISFLO CHUTE(TABLE1)
SEAT TRAJECTORY

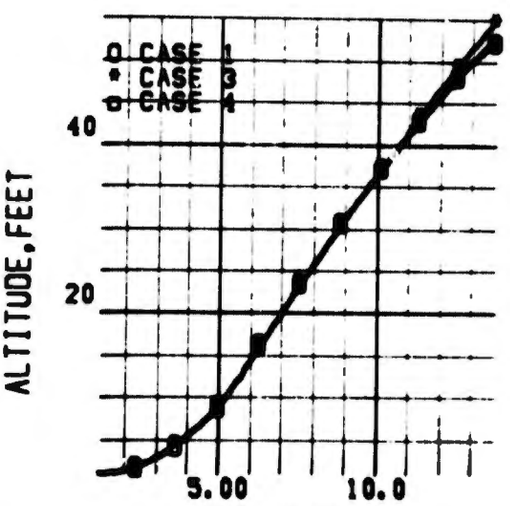

FIG 1.7 HEMISFLO CHUTE(TABLE1)
SEAT TRAJECTORY

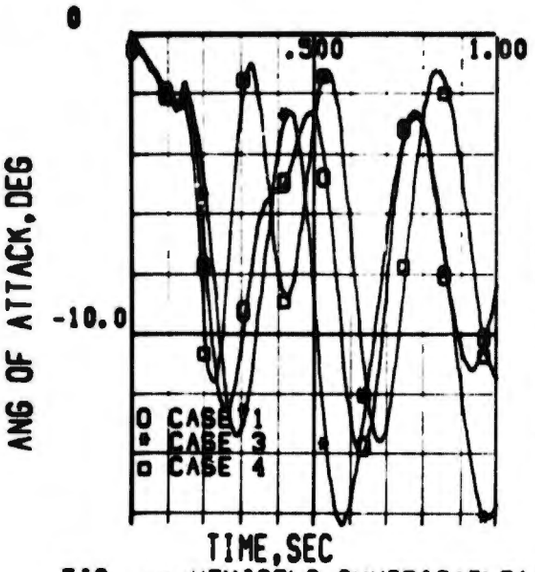

FIG 148 HEMISFLO CHUTE(TABLE1)
SEAT ANGLE OF ATTACK

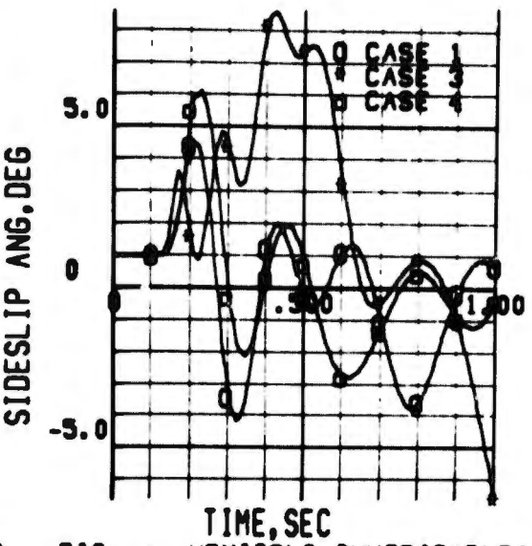

FIG 149 HEMISFLO CHUTE(TABLE1)
SEAT SIDESLIP ANGLE

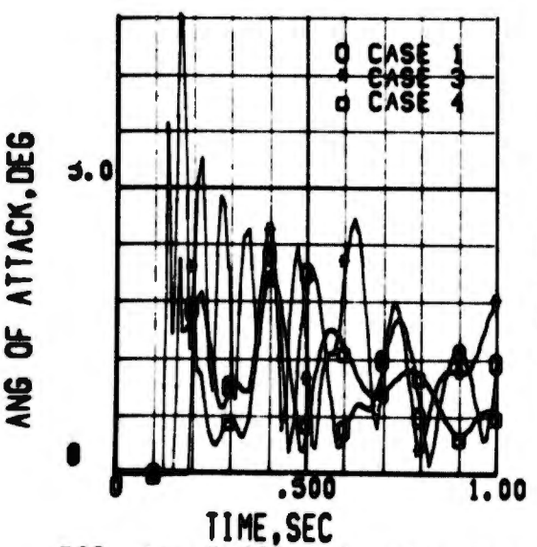

FIG 150 HEMISFLO CHUTE(TABLE1)
PARACHUTE ANGLE OF ATTACK

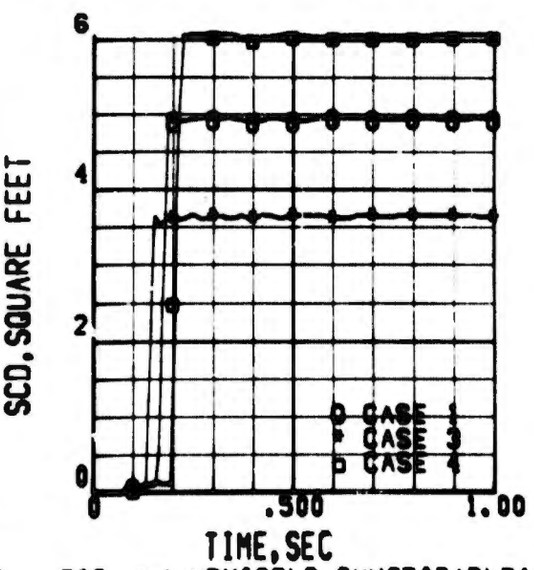

FIG 151 HEMISFLO CHUTE(TABLE1)
PARACHUTE AREA DRAG COEFF

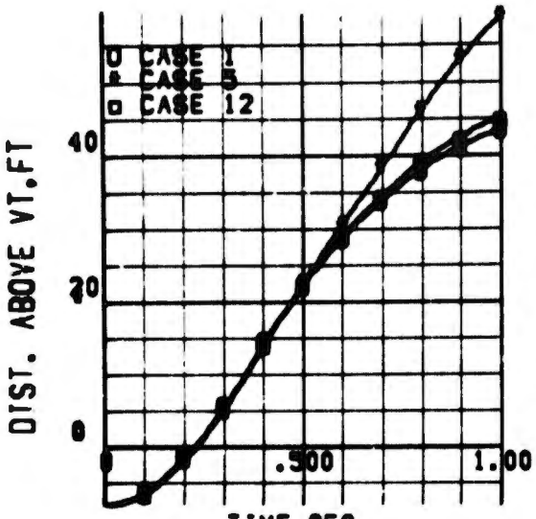

FIG 152 HEMISFLO CHUTE(TABLE1)
VERT. TAIL VERT. CLEARANCE

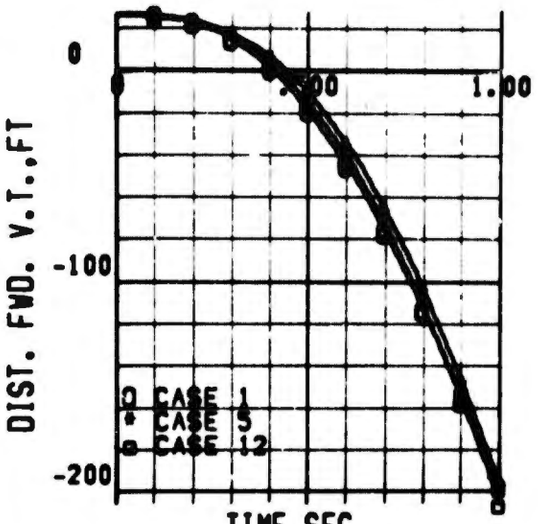

FIG 153 HEMISFLO CHUTE(TABLE1)
VERT. TAIL LONG. CLEARANCE

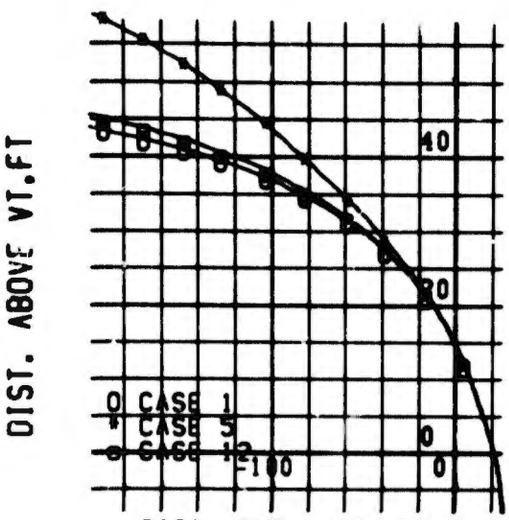

FIG 154 HEMISFLO CHUTE(TABLE1)
VERTICAL TAIL CLEARANCE

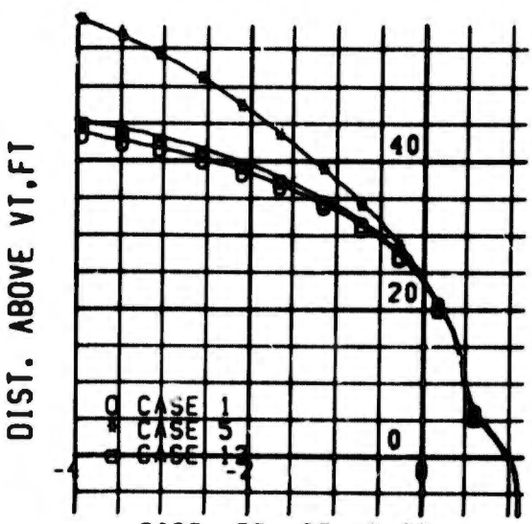

FIG 155 HEMISFLO CHUTE(TABLE1)
VERTICAL TAIL CLEARANCE

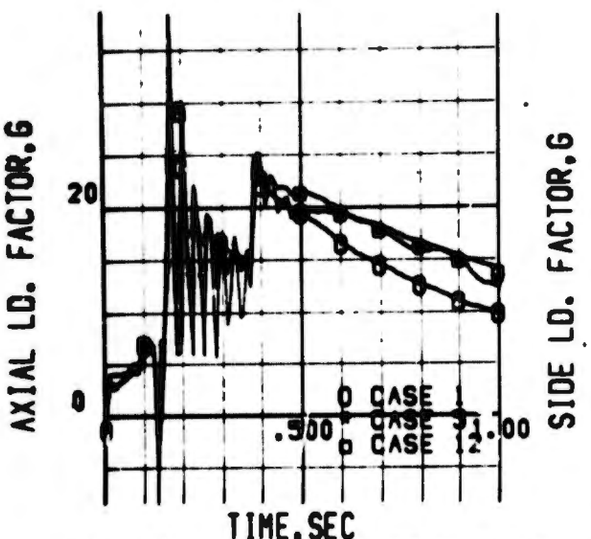

FIG 156 HEMISFLO CHUTE(TABLE1)
SEAT AXIAL LOAD FACTOR

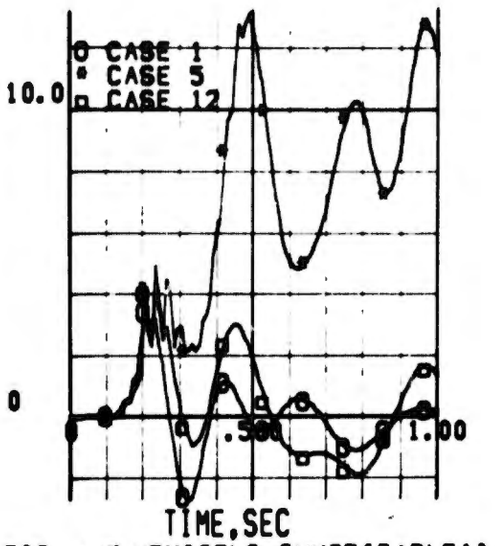

FIG 157 HEMISFLO CHUTE(TABLE1)
SEAT SIDE LOAD FACTOR

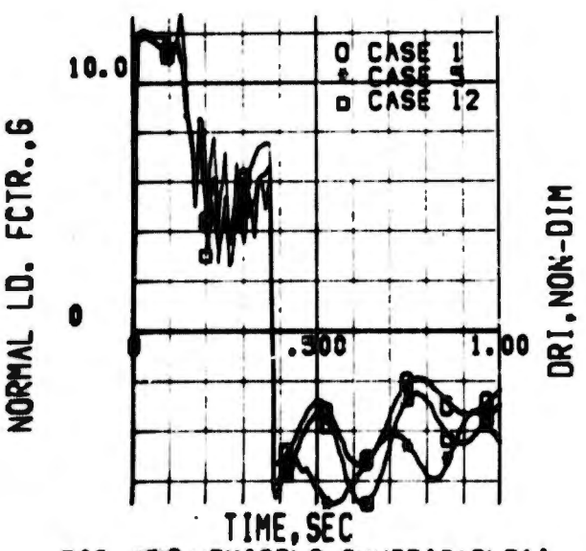

FIG 158 HEMISFLO CHUTE(TABLE1)
SEAT NORMAL LOAD FACTOR

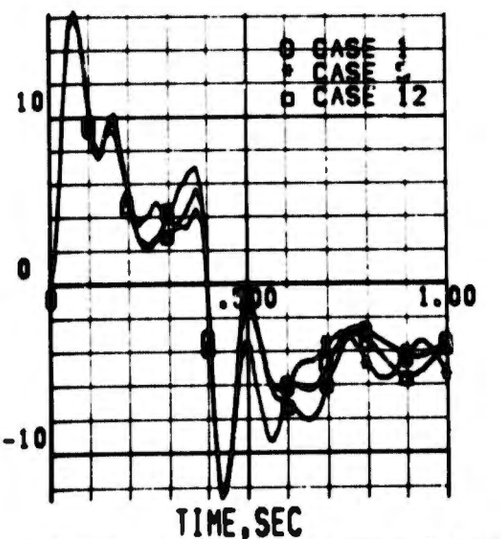

FIG 159 HEMISFLO CHUTE(TABLE1)
MAN DYNAMIC RESPONSE INDEX

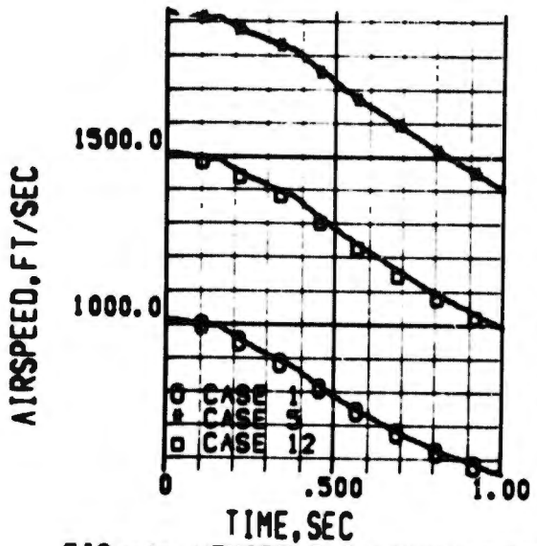

FIG 160 HEMISFLO CHUTE(TABLE1)
SEAT AIRSPEED

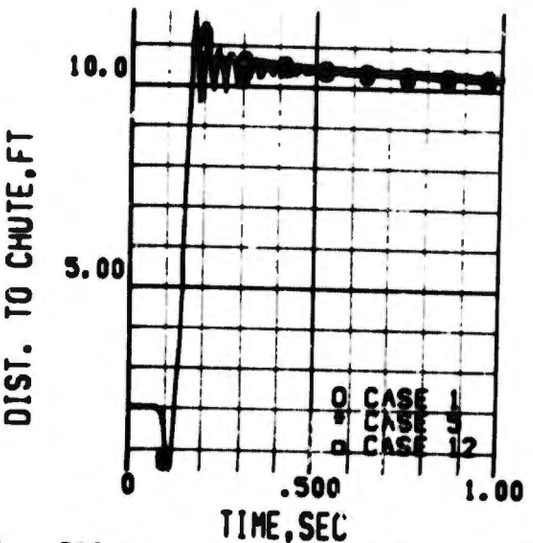

FIG 161 HEMISFLO CHUTE(TABLE1)
DIST. FROM BRIDLE TO CHUTE CG

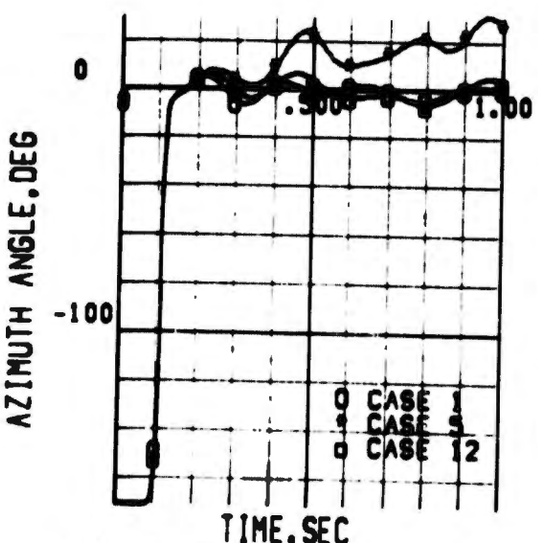

FIG 162 HEMISFLO CHUTE(TABLE1)
SEAT-PARACHUTE AZIMUTH ANGLE

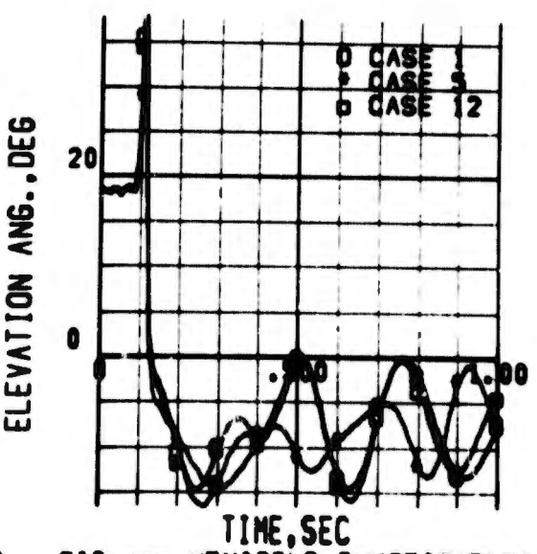

FIG 163 HEMISFLO CHUTE(TABLE1)
SEAT-PARACHUTE ELEVATION ANGLE

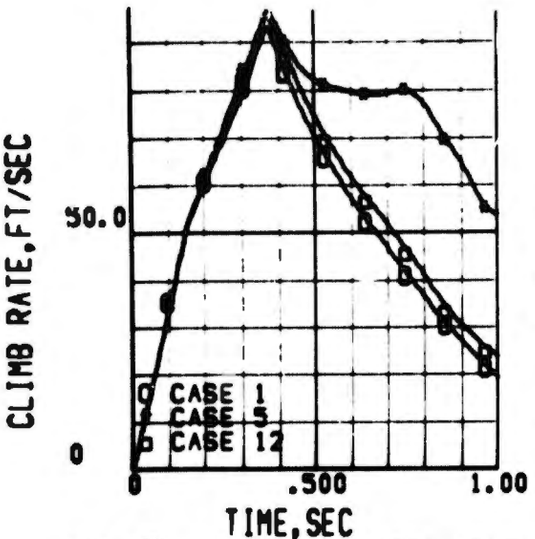

FIG 164 HEMISFLO CHUTE(TABLE1)
SEAT CLIMB RATE

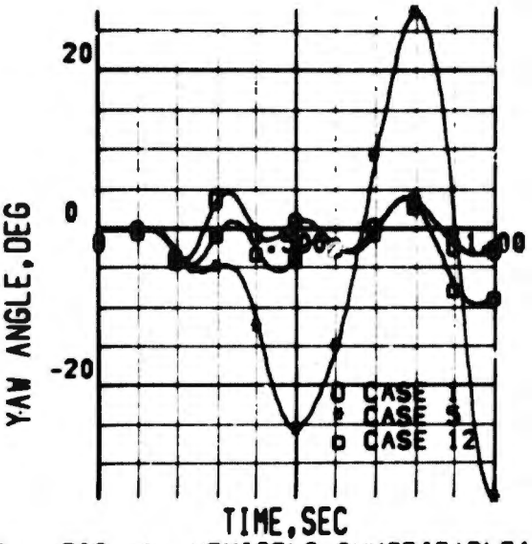

FIG 165 HEMISFLO CHUTE(TABLE1)
SEAT EARTH AXIS YAW ANGLE

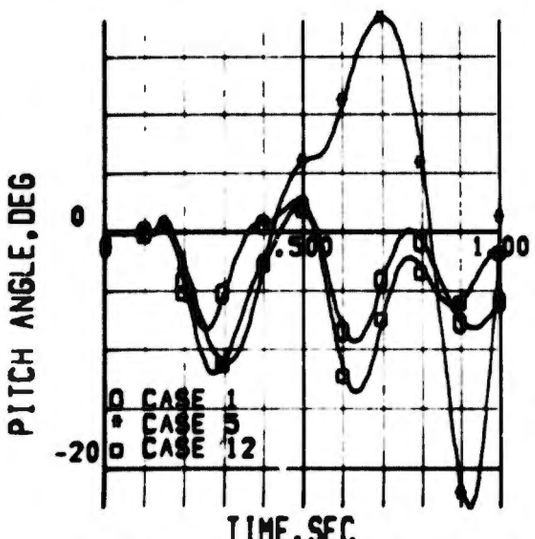

FIG 166 HEMISFLO CHUTE(TABLE1)
SEAT EARTH AXIS PITCH ANGLE

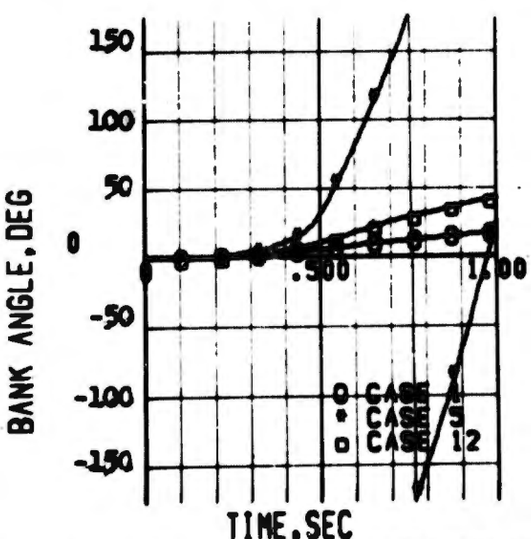

FIG 167 HEMISFLO CHUTE(TABLE1)
SEAT EARTH AXIS BANK ANGLE

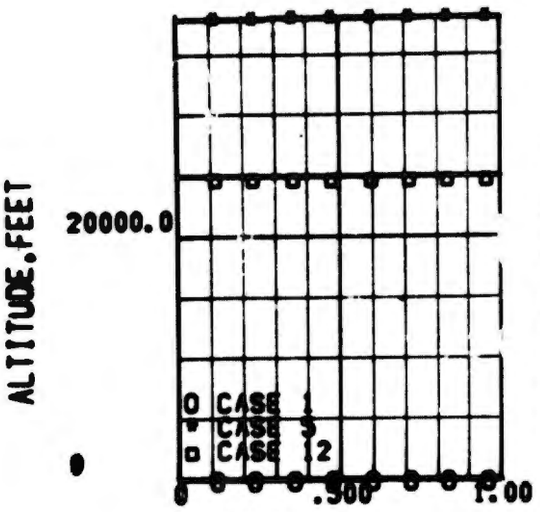

FIG 168 HEMISFLO CHUTE(TABLE1)
SEAT ALTITUDE

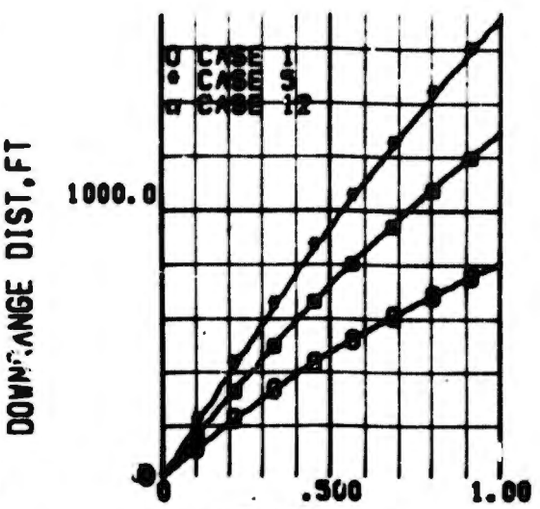

FIG 169 HEMISFLO CHUTE(TABLE1)
SEAT DOWNRANGE DISTANCE

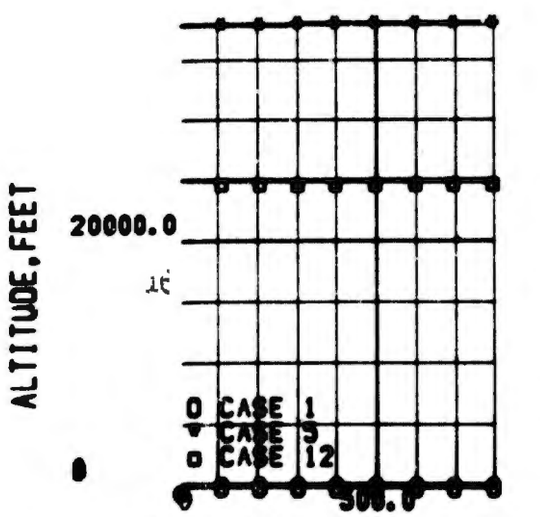

FIG 170 HEMISFLO CHUTE(TABLE1)
SEAT TRAJECTORY

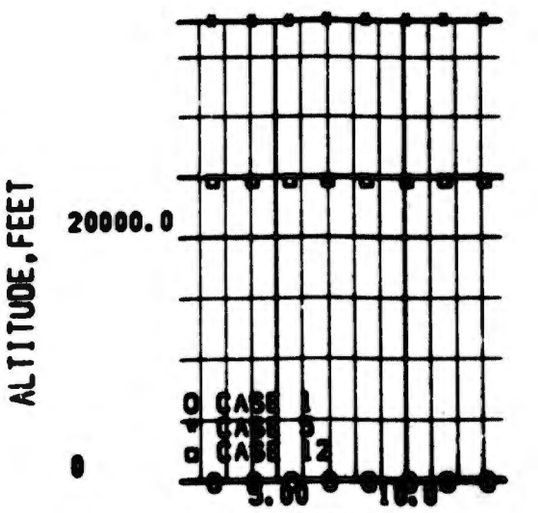

FIG 171 HEMISFLO CHUTE(TABLE1)
SEAT TRAJECTORY

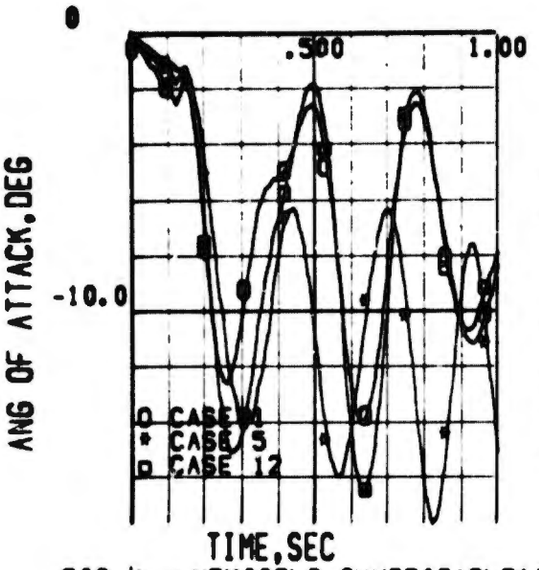

FIG 172 HEMISFLO CHUTE(TABLE1)
SEAT ANGLE OF ATTACK

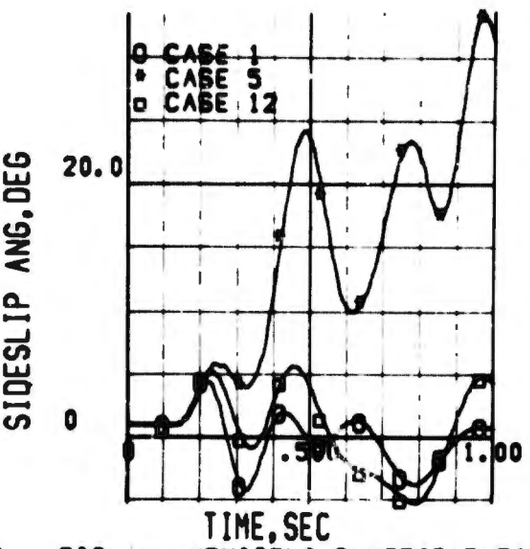

FIG 173 HEMISFLO CHUTE(TABLE1)
SEAT SIDESLIP ANGLE

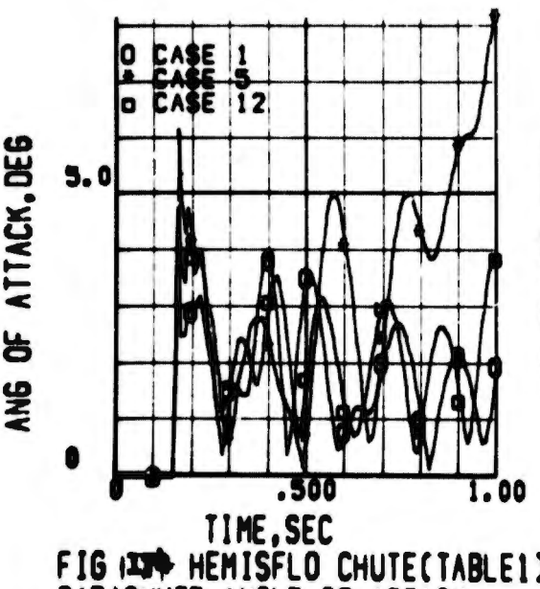

FIG 174 HEMISFLO CHUTE(TABLE1)
PARACHUTE ANGLE OF ATTACK

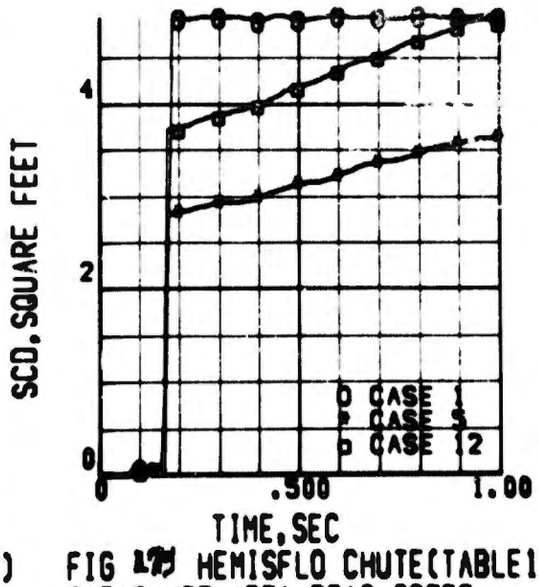

FIG 175 HEMISFLO CHUTE(TABLE1)
PARACHUTE AREA DRAG COEFF

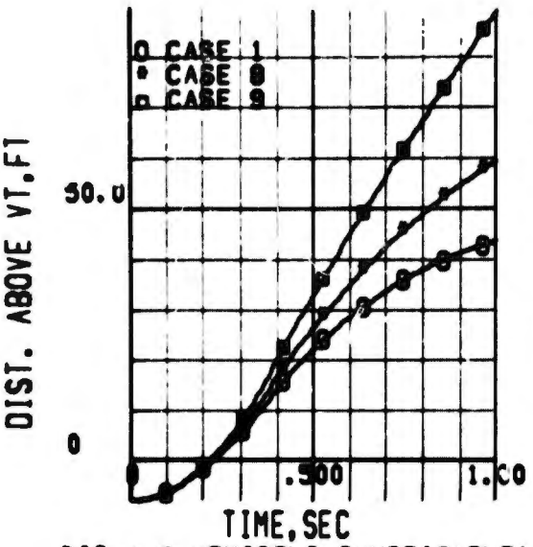

FIG 176 HEMISFLO CHUTE(TABLE1)
VERT. TAIL VERT. CLEARANCE

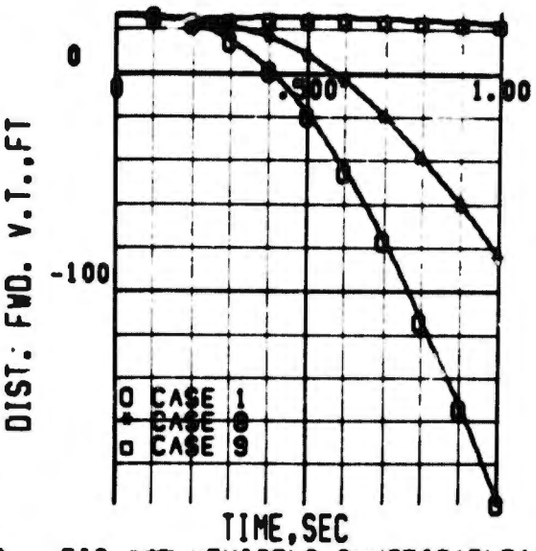

FIG 177 HEMISFLO CHUTE(TABLE1)
VERT. TAIL LONG. CLEARANCE

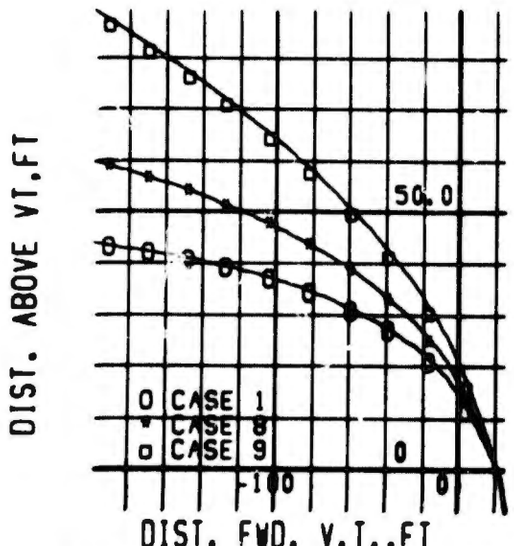

FIG 178 HEMISFLO CHUTE(TABLE1)
VERTICAL TAIL CLEARANCE

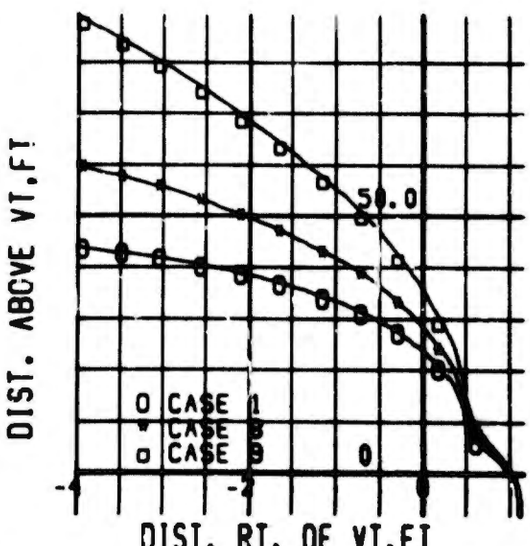

FIG 179 HEMISFLO CHUTE(TABLE1)
VERTICAL TAIL CLEARANCE

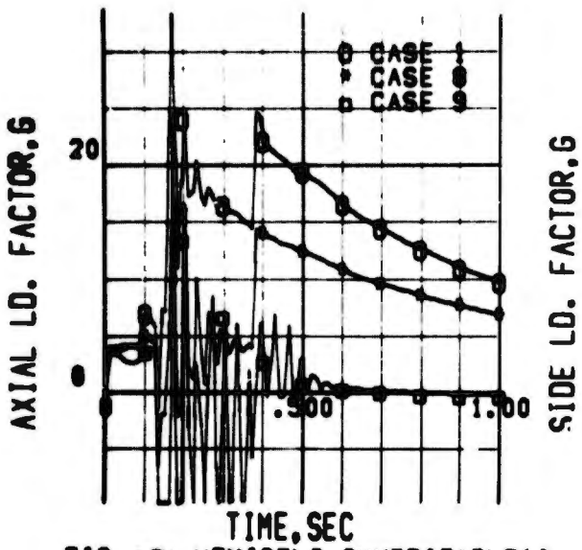

FIG 180 HEMISFLO CHUTE(TABLE1)
SEAT AXIAL LOAD FACTOR

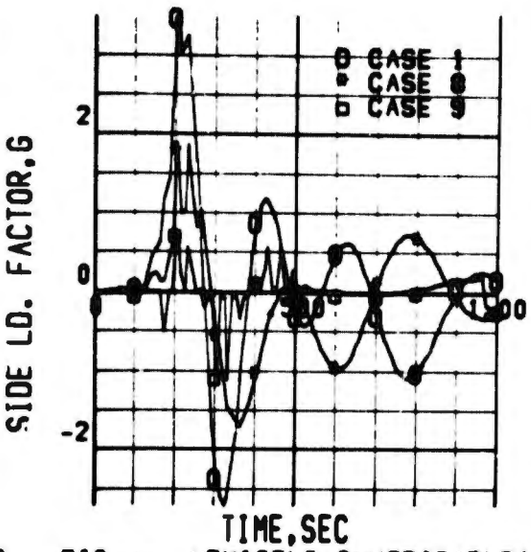

FIG 181 HEMISFLO CHUTE(TABLE1)
SEAT SIDE LOAD FACTOR

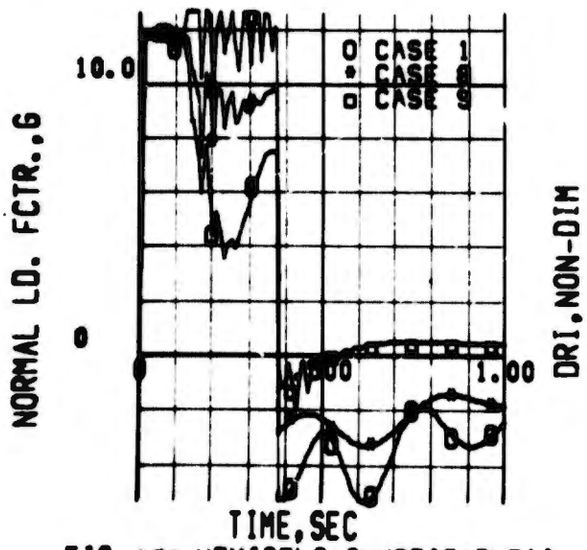

FIG 182 HEMISFLO CHUTE(TABLE1)
SEAT NORMAL LOAD FACTOR

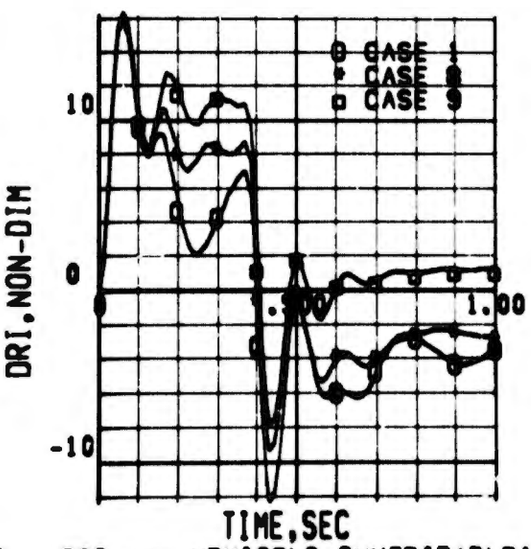

FIG 183 HEMISFLO CHUTE(TABLE1)
MAN DYNAMIC RESPONSE INDEX

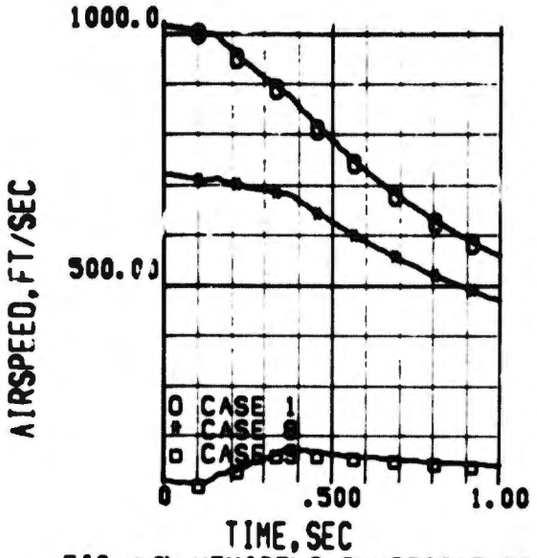

FIG 184 HEMISFLO CHUTE(TABLE1)
SEAT AIRSPEED

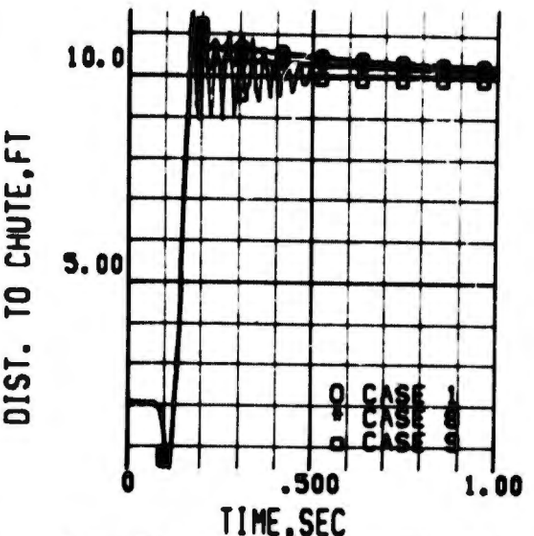

FIG 185 HEMISFLO CHUTE(TABLE1)
DIST. FROM BRIDLE TO CHUTE CG

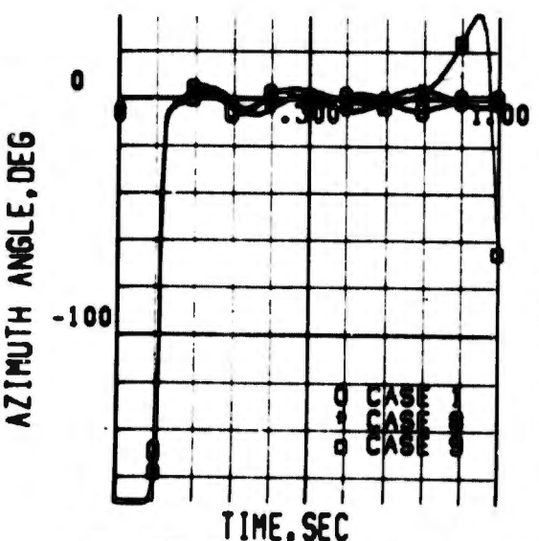

FIG 186 HEMISFLO CHUTE(TABLE1)
SEAT-PARACHUTE AZIMUTH ANGLE

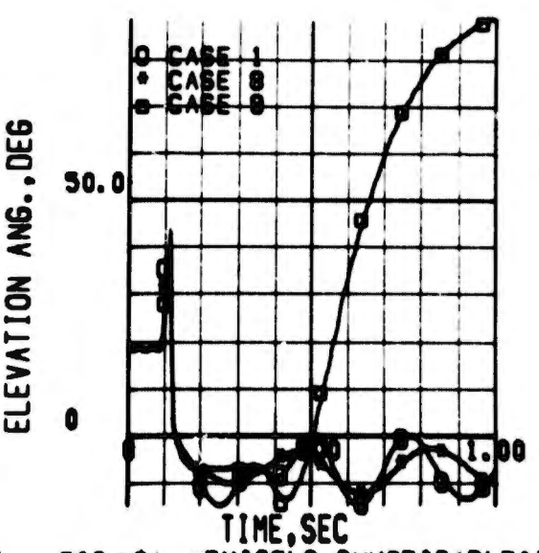

FIG 187 HEMISFLO CHUTE(TABLE1)
SEAT-PARACHUTE ELEVATION ANGLE

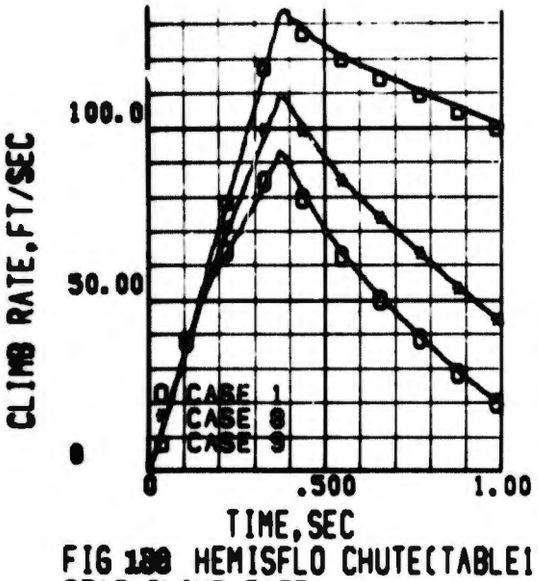

FIG 188 HEMISFLO CHUTE(TABLE1)
SEAT CLIMB RATE

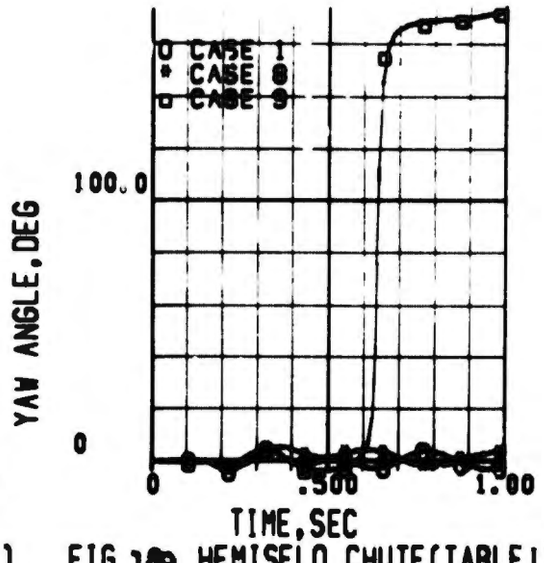

FIG 189 HEMISFLO CHUTE(TABLE1)
SEAT EARTH AXIS YAW ANGLE

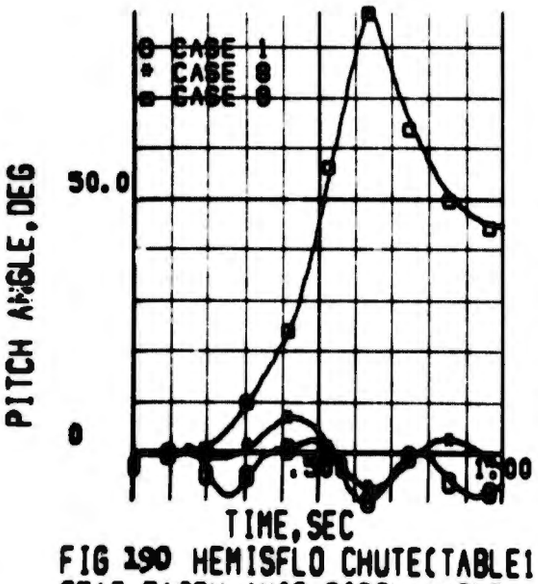

FIG 190 HEMISFLO CHUTE(TABLE1)
SEAT EARTH AXIS PITCH ANGLE

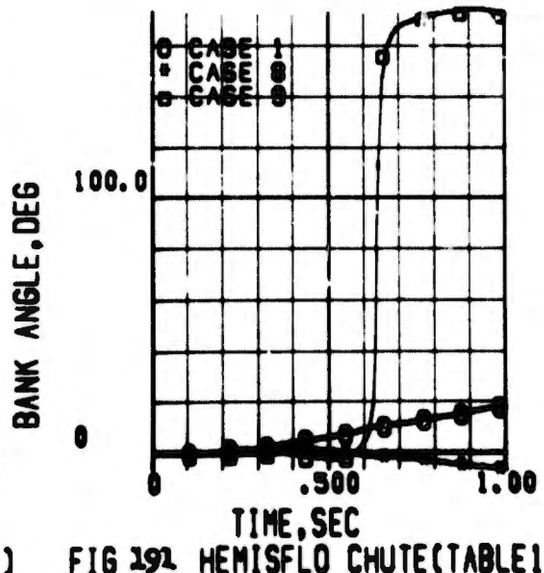

FIG 191 HEMISFLO CHUTE(TABLE1)
SEAT EARTH AXIS BANK ANGLE

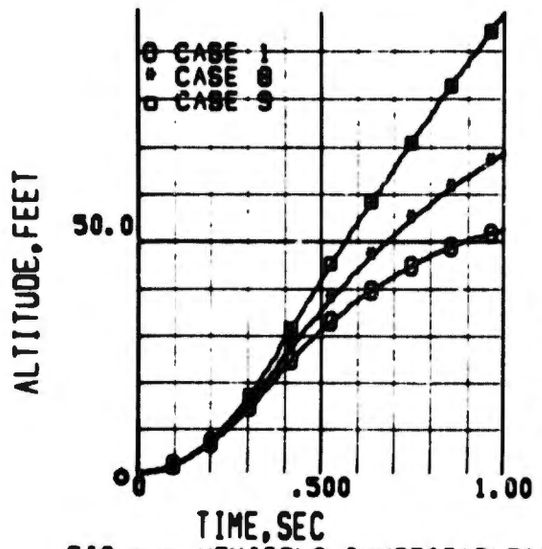

FIG 192 HEMISFLO CHUTE(TABLE1)
SEAT ALTITUDE

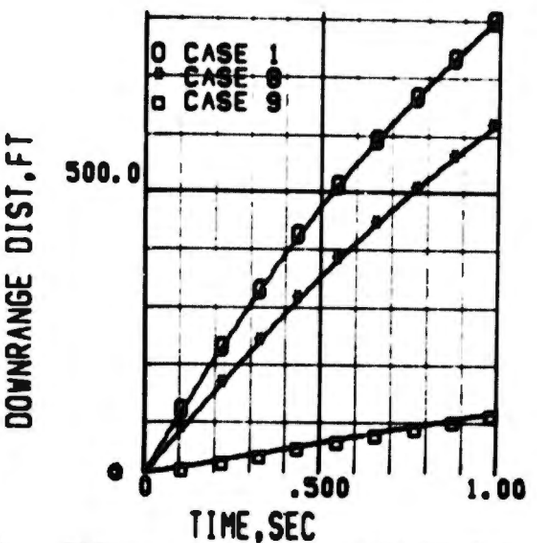

FIG193 HEMISFLO CHUTE(TABLE1)
SEAT DOWNRANGE DISTANCE

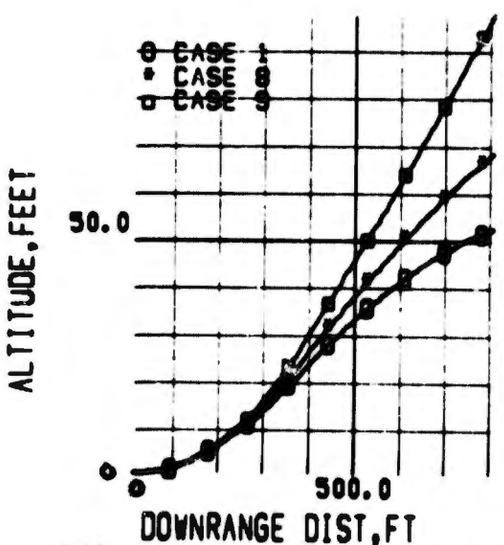

FIG 194 HEMISFLO CHUTE(TABLE1)
SEAT TRAJECTORY

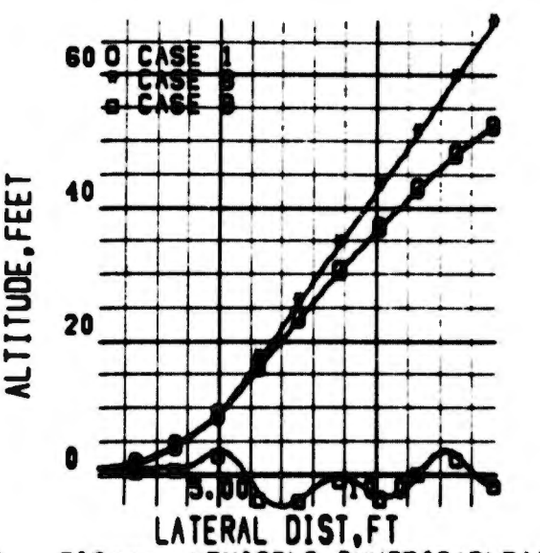

FIG195 HEMISFLO CHUTE(TABLE1)
SEAT TRAJECTORY

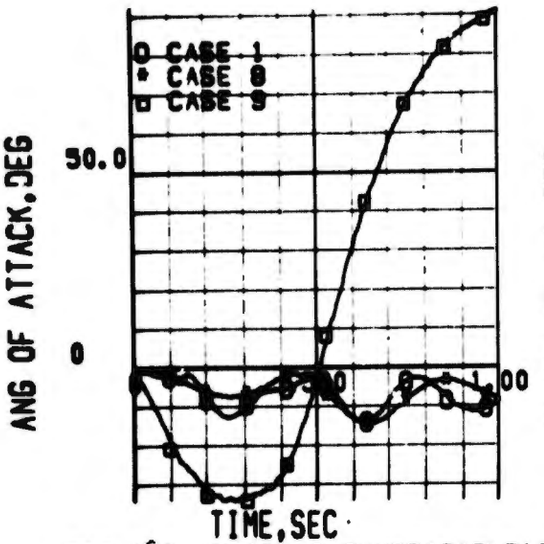

FIG 196 HEMISFLO CHUTE(TABLE1)
SEAT ANGLE OF ATTACK

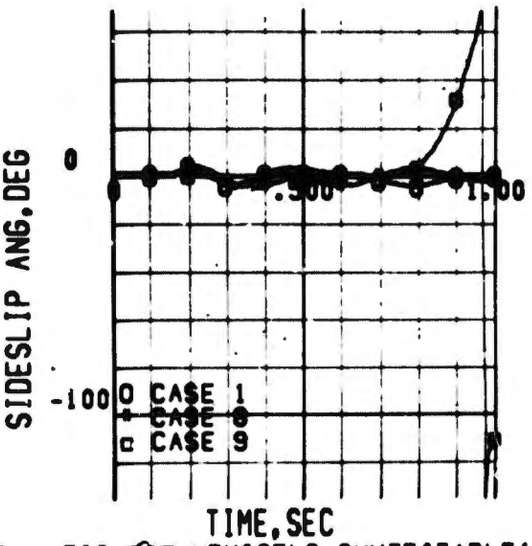

FIG 197 HEMISFLO CHUTE(TABLE1)
SEAT SIDESLIP ANGLE

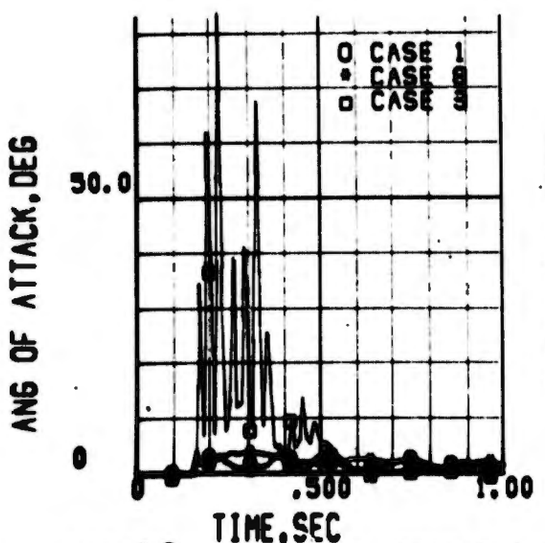

FIG 198 HEMISFLO CHUTE(TABLE1)
PARACHUTE ANGLE OF ATTACK

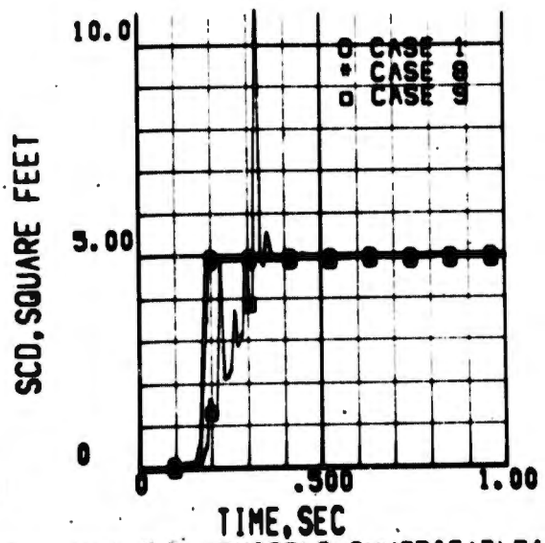

FIG 199 HEMISFLO CHUTE(TABLE1)
PARACHUTE AREA DRAG COEFF

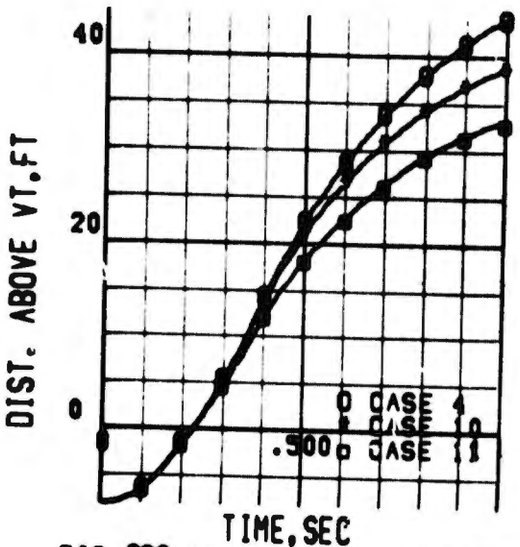

FIG 200 HEMISFLO CHUTE(TABLE1)
VERT. TAIL VERT. CLEARANCE

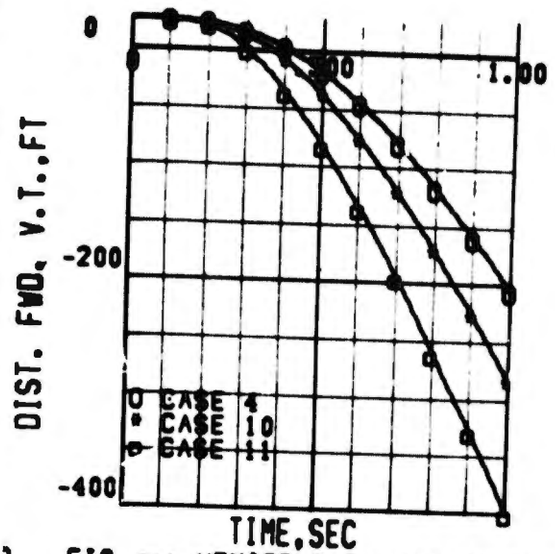

FIG 201 HEMISFLO CHUTE(TABLE1)
VERT. TAIL LONG. CLEARANCE

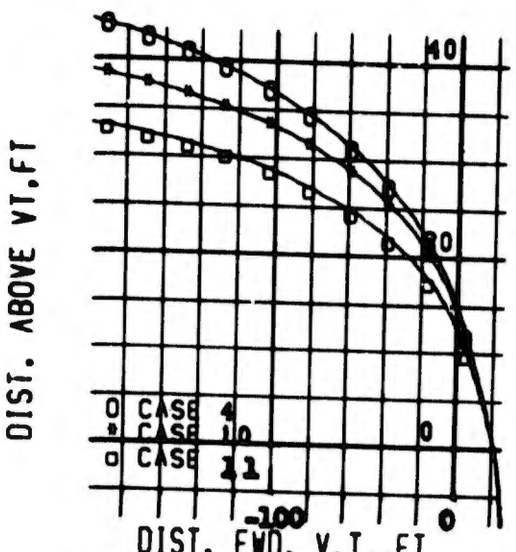

FIG 202 HEMISFLO CHUTE(TABLE1)
VERTICAL TAIL CLEARANCE

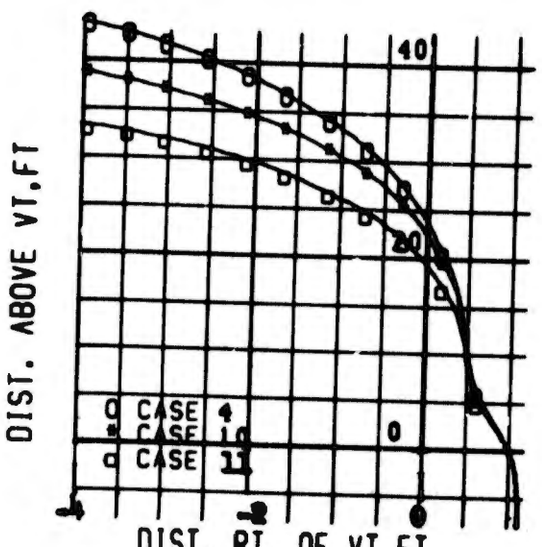

FIG 203 HEMISFLO CHUTE(TABLE1)
VERTICAL TAIL CLEARANCE

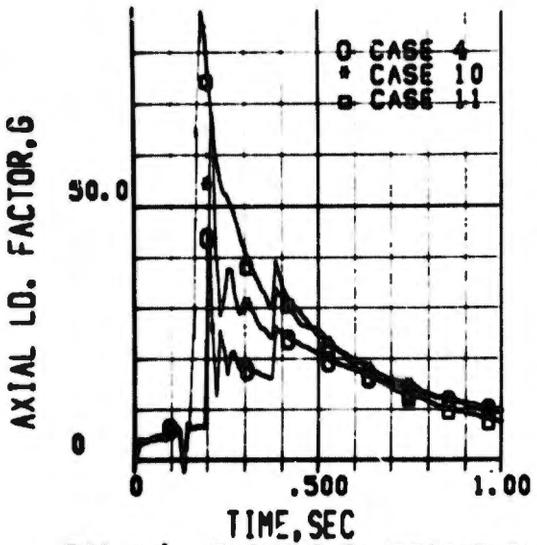

FIG 204 HEMISFLO CHUTE(TABLE1)
SEAT AXIAL LOAD FACTOR

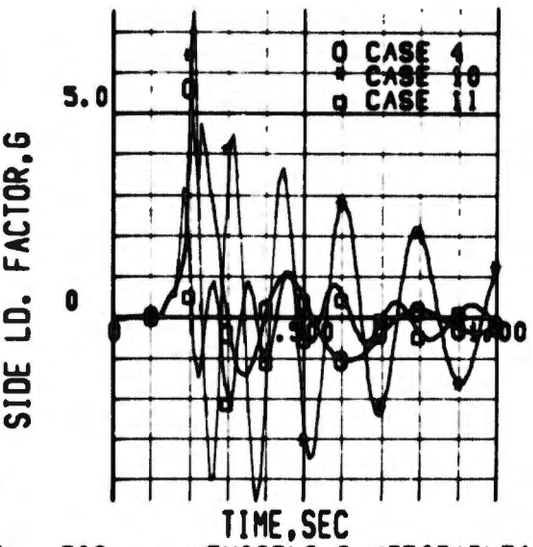

FIG 205 HEMISFLO CHUTE(TABLE1)
SEAT SIDE LOAD FACTOR

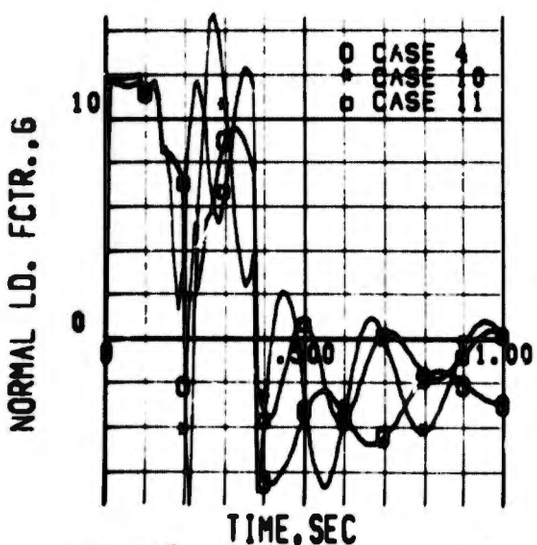

FIG 206 HEMISFLO CHUTE(TABLE1)
SEAT NORMAL LOAD FACTOR

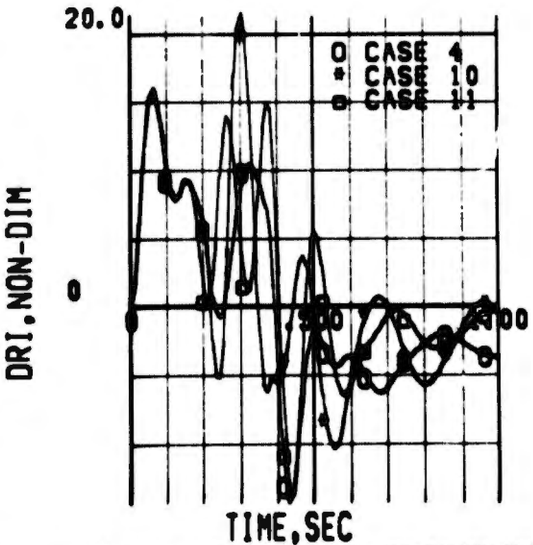

FIG 207 HEMISFLO CHUTE(TABLE1)
MAN DYNAMIC RESPONSE INDEX

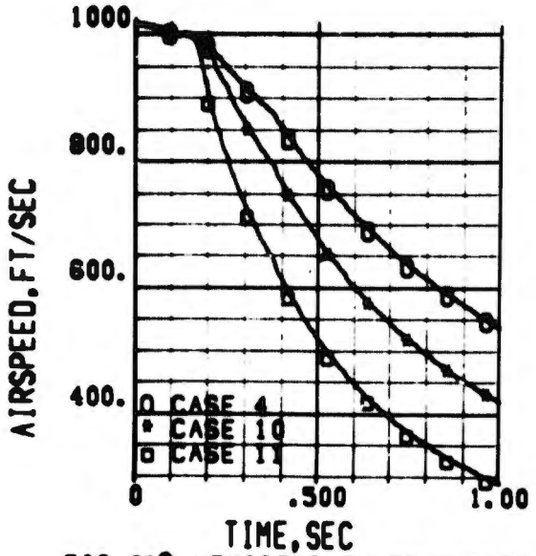

FIG 208 HEMISFLO CHUTE(TABLE1)
SEAT AIRSPEED

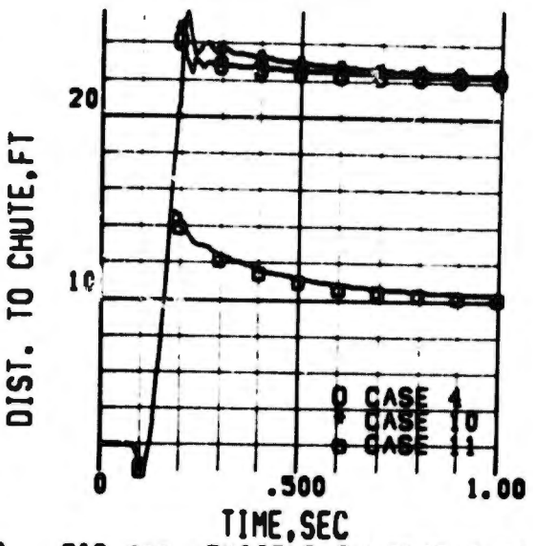

FIG 209 HEMISFLO CHUTE(TABLE1)
DIST. FROM BRIDLE TO CHUTE CG

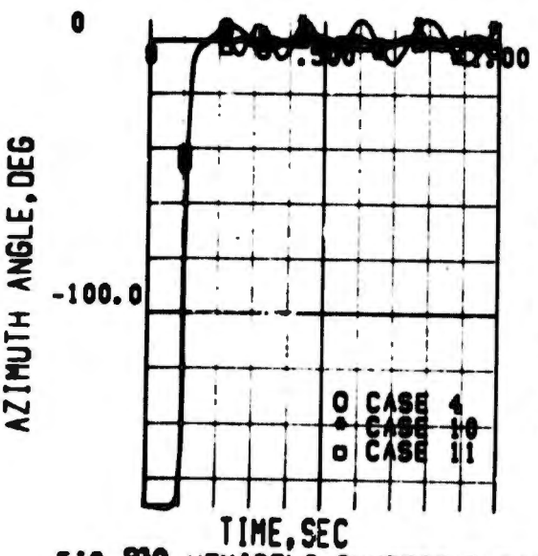

FIG 210 HEMISFLO CHUTE(TABLE1)
SEAT-PARACHUTE AZIMUTH ANGLE

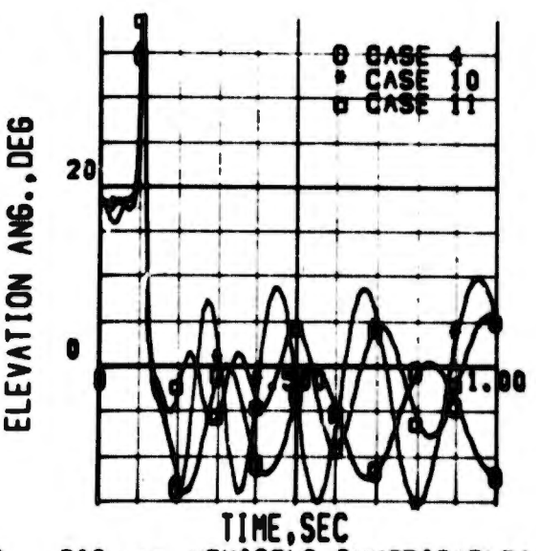

FIG 211 HEMISFLO CHUTE(TABLE1)
SEAT-PARACHUTE ELEVATION ANGLE

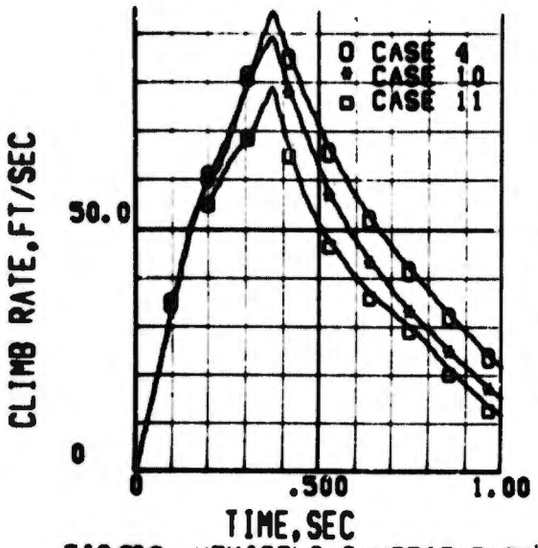

FIG 212 HEMISFLO CHUTE(TABLE1)
SEAT CLIMB RATE

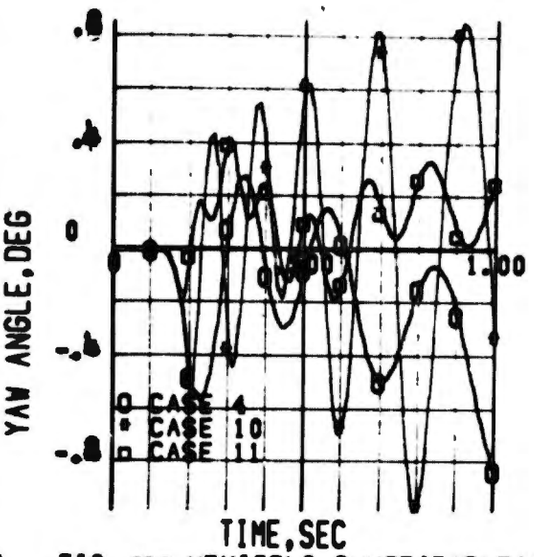

FIG 213 HEMISFLO CHUTE(TABLE1)
SEAT EARTH AXIS YAW ANGLE

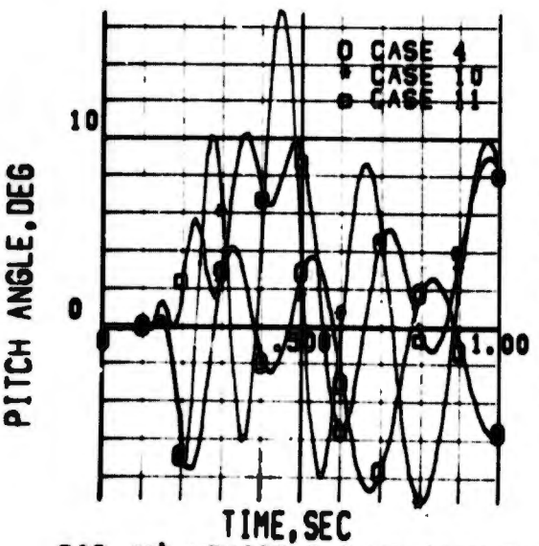

FIG 214 HEMISFLO CHUTE(TABLE1)
SEAT EARTH AXIS PITCH ANGLE

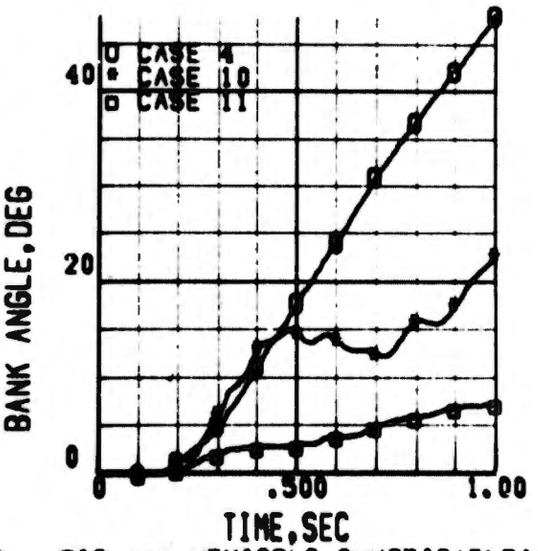

FIG 215 HEMISFLO CHUTE(TABLE1)
SEAT EARTH AXIS BANK ANGLE

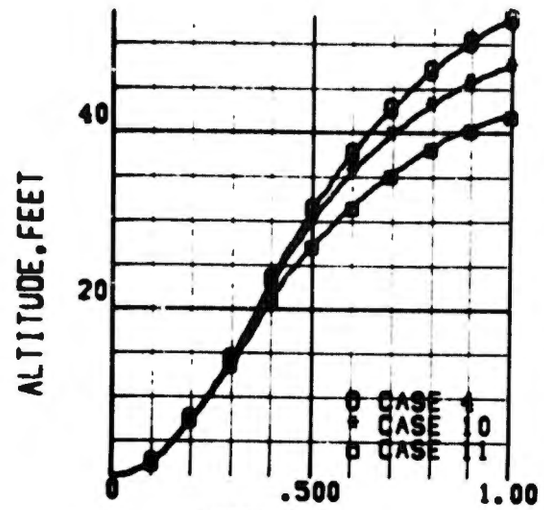

FIG 216 HEMISFLO CHUTE(TABLE1)
SEAT ALTITUDE

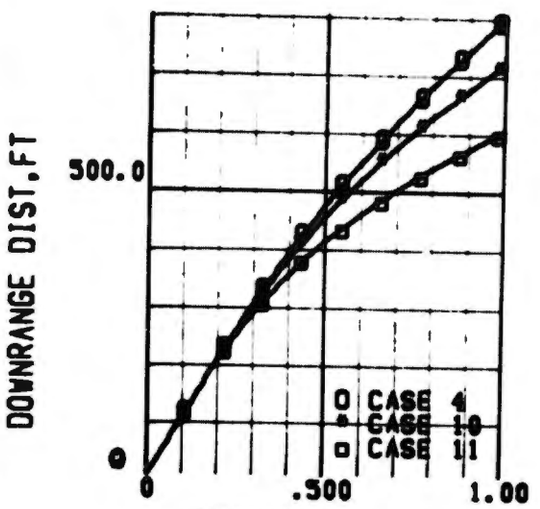

FIG 217 HEMISFLO CHUTE(TABLE1)
SEAT DOWNRANGE DISTANCE

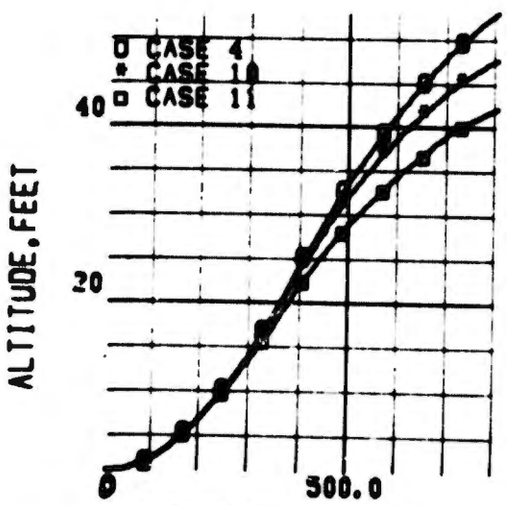

FIG 218 HEMISFLO CHUTE(TABLE1)
SEAT TRAJECTORY

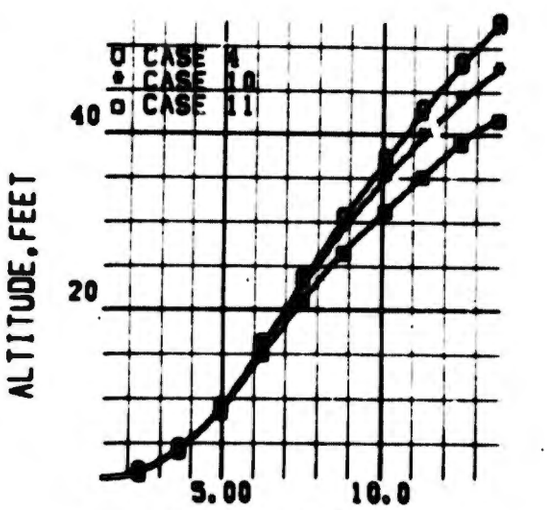

FIG 219 HEMISFLO CHUTE(TABLE1)
SEAT TRAJECTORY

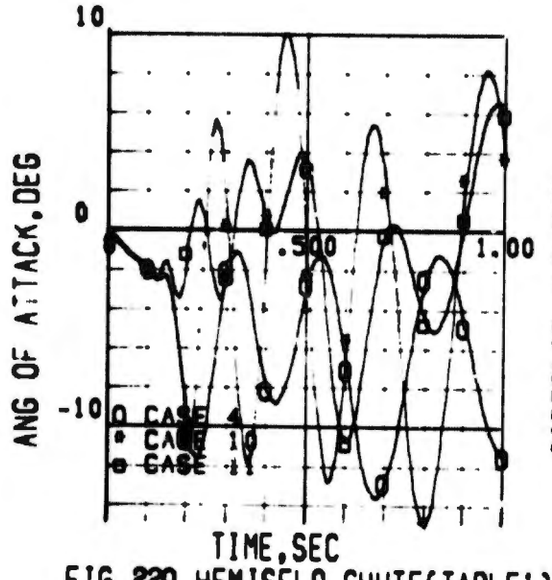

FIG 220 HEMISFLO CHUTE(TABLE1)
SEAT ANGLE OF ATTACK

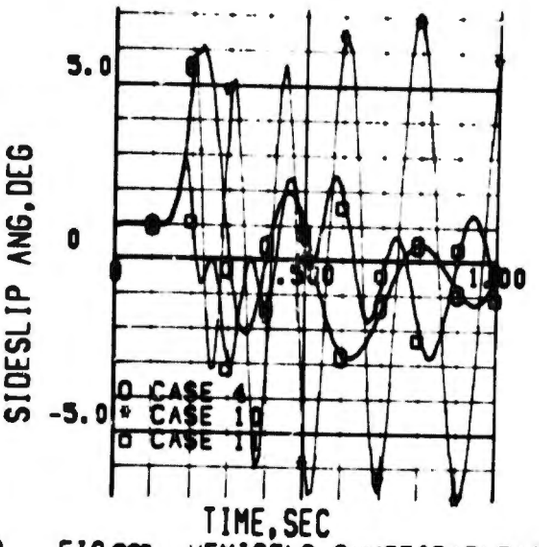

FIG 221 HEMISFLO CHUTE(TABLE1)
SEAT SIDESLIP ANGLE

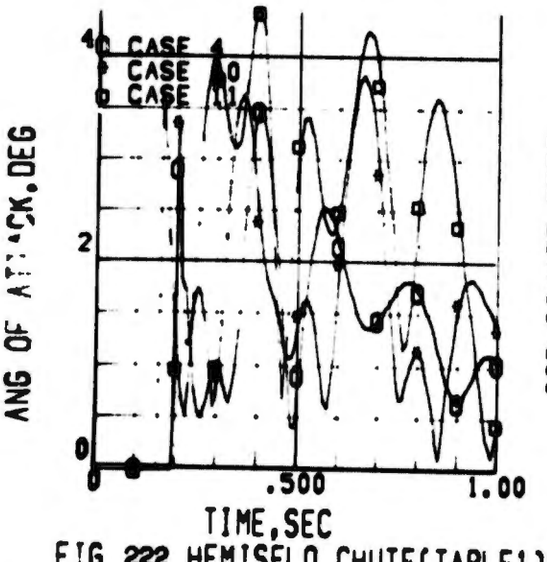

FIG 222 HEMISFLO CHUTE(TABLE1)
PARACHUTE ANGLE OF ATTACK

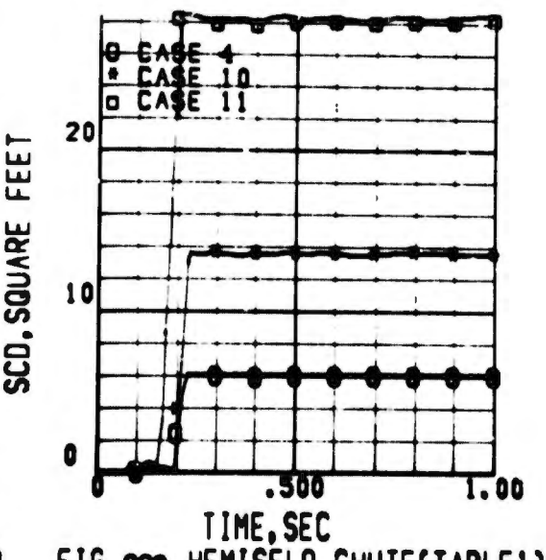

FIG 223 HEMISFLO CHUTE(TABLE1)
PARACHUTE AREA DRAG COEFF

SECTION IV

SEAT TIP-OFF EFFECTS

A critical period in the ejection sequence of an escape seat is during the tip-off portion when aircraft inputs through rail reactions have important effects on the post ejection dynamics of the seat which may be crucial in the design and timing of the seat stabilization subsystem. In the process of an escape seat ejection, the seat is guided by rails until the middle pair of slider blocks (or rollers) leaves the rails. At this point, the seat is free to rotate. From the time the catapult is fired the airplane responds by pitching down and by rolling in the case of a laterally positioned single seat ejection. These tip-off effects are functions of several ejection seat parameters such as position of slider blocks, catapult stroke, catapult thrust level, sustainer thrust level, and ejected weight and inertia. To study the effects of these parameters the ejection was initiated with the aircraft in straight and level hover.

For this study, a basic ejection seat configuration was chosen as described in Figure 224. Two values for each of the above mentioned parameters were selected in addition to the basic configuration. Six degree-of-freedom digital simulations were run using first the basic configuration and then each of the additional parameters substituted one at a time for its corresponding element in the basic data. The time histories were initiated with the same conditions described in Section III.1, but terminated at the time at which the seat became separated from the rails.

In the case of slider-block positioning, the case of no middle blocks and the case of pair of middle blocks thirteen inches above the bottom pair were compared with the basic position (eight inches above lower pair). The catapult stroke ended when the middle blocks left the rails for the basic situation. Therefore, the catapult stroke was unguided for the case of a centered pair of middle blocks and no middle blocks. This allowed the catapult to pitch the seat down relative to the rails when one pair of blocks remained on the rails.

The three catapult strokes compared were 2.9 feet (Basic case), 3.6 feet and 1.4 feet. The 3.6 foot stroke ended when the bottom pair of slider blocks left the rails and the 1.4 foot stroke ended when the top pair left. The basic stroke as well as the short stroke were completely guided and the long stroke unguided for eight inches.

The sustainer thrust levels studied were 2000, 4000, and 7000 pounds. The sustainer thrust produces a nose up moment on the seat but since it passes through the line between the bottom slider blocks it does not contribute to tip-off.

The catapult thrust levels considered were 5000, 6000, and 8000 pounds. The catapult was attached to the seat such that a nose down pitching moment was imparted to the seat. This was the catapult's contribution to tip-off. Tip-off, however, should not be a primary concern in sizing the catapult. Seat velocity at tip-off and load factors on the pilot are more restrictive on thrust levels.

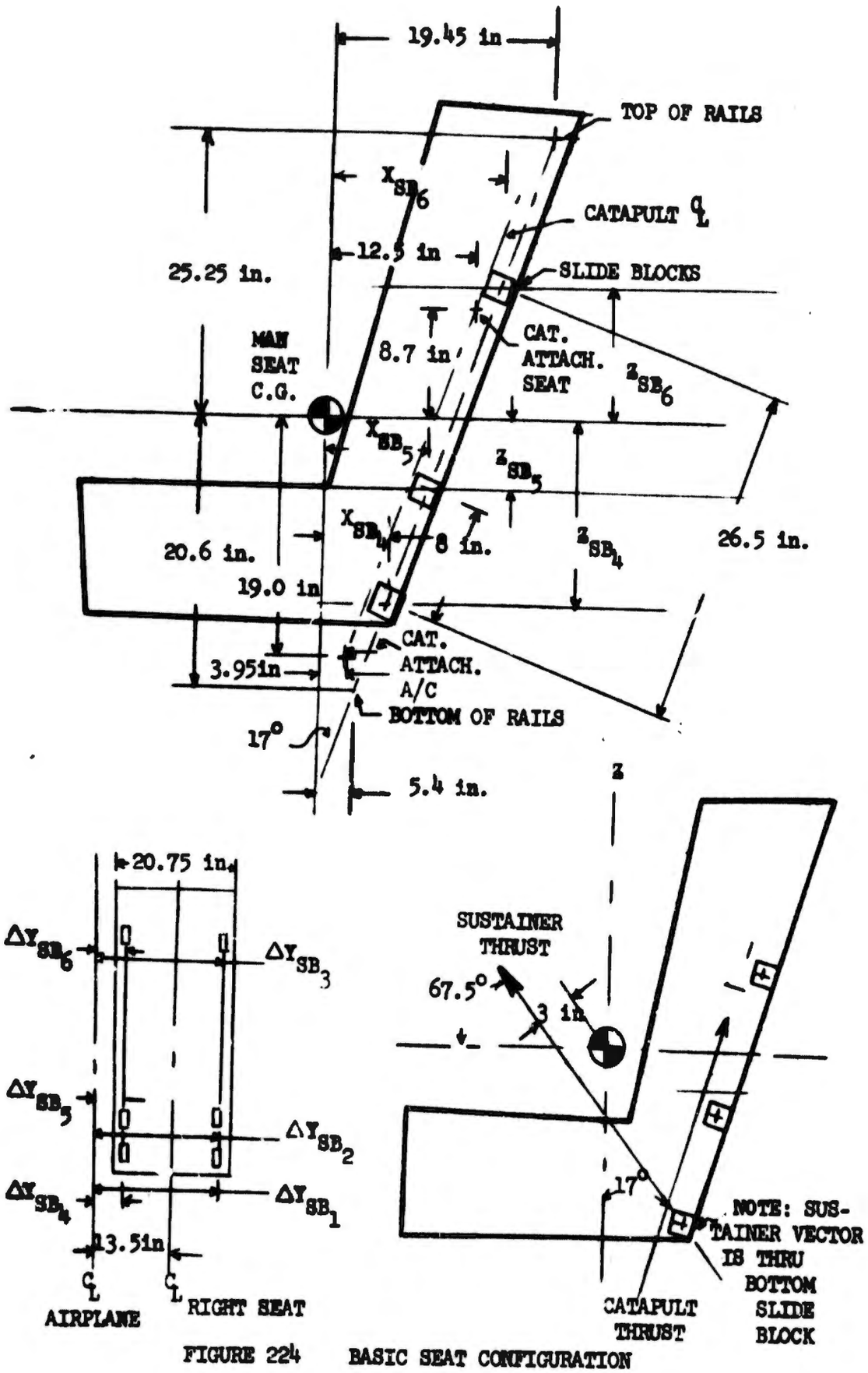

FIGURE 224 BASIC SEAT CONFIGURATION

To study the effects of ejected weights and inertias, seat-man combinations of 300, 400, and 500 pounds were used. The three hundred pound seat-man represents a weight less than that of a small man in the basic seat. The four hundred pound seat-man represents an average size man, while the five hundred pound seat-man was a weight greater than a heavy man in the basic seat. The inertias used were proportional to the seat weight. Their values can be seen in Table II.

For each of the comparisons to follow, a figure indicating the seat position on the rails as a function of time is given. These figures along with Table III are necessary for relating ejection events to the time at which they occur. After tip-off, these curves have no significance because the simulation is programmed to stop computing the rail equations while continuing the seat trajectory computations, causing the rail values to remain constant; plotting, however, continues.

1. SLIDER BLOCK LOCATION EFFECTS

Figure 225 shows the time sequence for the first set of parameters studied. It indicates the rail position of the seat for the basic case, the case with no middle block, and the case with the middle block 13 inches above the bottom block (Case 1, Case 2, and Case 3 respectively). Using Table III, the time for tip-off is .135 seconds for all three cases. Since the catapult is producing a nose down moment on the seat, as soon as the middle blocks leaves the rails, the seat begins to pitch down. Figures 226, 227, and 228 reflect this. At tip-off the seat with no middle blocks has pitched down 7.2 degrees relative to the airplane (Figure 227), while the seat with a centered middle block has pitched down only 1.0 degree relative to the airplane (Figure 228). In the basic case, the catapult stroke is completely guided so the catapult is unable to pitch the seat down relative to the rails except by deforming the structure. As the middle blocks leave the rails, the airplane pitching nose down flips the seat to a nose up pitch attitude of .3 degrees relative to the airplane at tip-off (Figure 226). For this case, the pitch attitude becomes more nose up with respect to the earth after tip-off as a result of the sustainer. In Cases 2 and 3 this did not happen. The pitch rates developed by the catapult are so large that the sustainer post tip-off moment can not overcome them in these short time histories. The pitch rates shown in Figure 229 also show the effect of an unguided stroke. At tip-off, the seat with no middle block is pitching down at 3.4 rad/sec while the seat with the largest guided stroke is pitching up 0.1 rad/sec.

A two-place cockpit was used with only the right seat being ejected. This forced the airplane to roll right. The bank angles of the airplane and seat for these three configurations are presented in Figures 230, 231, and 232. In each case the tip-off effects flip the seat to a more vertical position.

2. CATAPULT STROKE EFFECTS

Another way to change the guided stroke of the catapult is to leave the slider block positions fixed as in Case 1 and vary the length of the catapult stroke. Figure 233 along with Table III is used to relate the ejection sequence to time for this set of parameters.

(Page 86 is blank)

TABLE

SEAT TIP-OFF

Case	Case Description	Catapult Stroke	LOWER BLOCKS		MIDDLE BLOCKS		TOP BLOCKS		C T
			ΔX_{SB_1}	ΔZ_{SB_1}	ΔX_{SB_2}	ΔZ_{SB_2}	ΔX_{SB_3}	ΔZ_{SB_3}	
1	8" Mid block	2.9	-.556	1.36	-.75	.722	-1.2	-.755	5
2	No Mid block	↓	↓	↓	-1.2	-.755	↓	↓	
3	13" Mid block	↓	↓	↓	-.8845	.285	↓	↓	
4	Unguided Stroke	3.0	↓	↓	-.75	.722	↓	↓	
5	Short Stroke	1.4	↓	↓	↓	↓	↓	↓	
6	2000 Lb Sust.	2.9	↓	↓	↓	↓	↓	↓	
7	7000 Lb Sust.	↓	↓	↓	↓	↓	↓	↓	
8	6000 Lb Cat	↓	↓	↓	↓	↓	↓	↓	6
9	8000 Lb Cat.	↓	↓	↓	↓	↓	↓	↓	8
10	300 Lb Seat-Man	↓	↓	↓	↓	↓	↓	↓	5
11	500 Lb Seat-Man	↓	↓	↓	↓	↓	↓	↓	

$\Delta X_{SB_4} = \Delta X_{SB_1}$

$\Delta Z_{SB_4} = \Delta Z_{SB_1}$

$\Delta X_{SB_5} = \Delta X_{SB_2}$

$\Delta Z_{SB_5} = \Delta Z_{SB_2}$

$\Delta X_{SB_6} = \Delta X_{SB_3}$

$\Delta Z_{SB_6} = \Delta Z_{SB_3}$

$\Delta Y_{SB_1} = \Delta Y_{SB_2} = \Delta Y_{SB_3} = .86$

$\Delta Y_{SB_4} = \Delta Y_{SB_5} = \Delta Y_{SB_6} = -.86$

(All Symbols defined in Appendix III, Section II and Appendix I, Section II)

A

(Page 88 is blank)

TABLE II

SEAT TIP-OFF PARAMETERS

TOP BLOCKS ΔZ_{SB_3}	Catapult Thrust	To Sustainer	To Sustainer	Sustainer Thrust	Weight Seat & Man	I_X	I_Y	I_Z	I_{XZ}
-.755	5000.	TIME AT WHICH CAT. REACHES END OF STROKE	.25	4000.	400.	16.7	28.4	11.7	-2.03
	6000.			2000.	300.	9.7	15.0	5.3	-1.2
	8000.			7000.					
	5000.			4000.	500.	19.2	32.5	13.3	-2.4

II)

B

BLANK PAGE

TABLE III

SEAT-MAN LOCATION FOR EJECTION EVENTS

RAIL POS. OF BOTTOM SLIDER BLOCKS	EVENT
3.99 ft.	Tip-off
3.33 ft.	Middle block off (basic data)
1.78 ft.	Top block off
2.91 ft.	Middle block off (Case 3)

Figure 234 is a history of the earth axis vertical velocity of the seat for all three catapult strokes. For the basic case (completely guided stroke), the vertical velocity at tip-off is 44. ft/sec. When the catapult strokes until the bottom pair of blocks leaves the rails, the vertical velocity increases to 46.0 ft/sec (Case 4). The other catapult stroke investigated ends when the top pair of blocks left the rails (Case 5) resulting in a vertical velocity of 40. ft/sec. The reason these end velocities are nearly the same is because of the earth axis frame of reference. The longer stroking catapult pitches the airplane nose down more and the seat, being 10 ft. forward of the airplane C.G., is forced downward by the rails, reducing the seat climb rate.

When the catapult strokes until the bottom pair of blocks leaves the rails, it pitches the seat down 0.75 degrees with respect to the airplane (Figure 235). The totally guided catapult stroke (Case 5) ends when the top pair of blocks leaves the rails. The seat at tip-off has pitched down 0.6 degrees relative to the airplane (Figure 236). As stated earlier for the case of the catapult stroke ending when the middle blocks leave the rails, the seat at tip-off pitches up 0.3 degrees relative to the airplane (Figure 226).

3. SUSTAINER THRUST EFFECTS

Figure 237 is a history of the seat position on the rails for the three values of sustainer thrust. The sustainer thrust has no effect on these histories and time for tip-off is 0.135 seconds. At tip-off the seat with the 2000 pound sustainer has pitched up .25 degrees relative to the airplane and is at a pitch attitude of 1.63 degrees nose down (Figure 238). Comparing Figure 239 with Figure 238, very little change is seen until after tip-off. The seat with the 7000 pound sustainer has pitched up 0.295 degree relative to the airplane at tip-off. After tip-off, the 7000 pound sustainer continues to pitch the seat up while the 2000 pound sustainer does not pitch the seat up as much. The seat with a 4000 pound sustainer pitches up .3 degrees relative to the airplane at tip-off. From Figure 240 the pitch rate of the seat is the same for all three cases until the middle block leaves the rails. Then the pitch rates become proportional to the sustainer thrust.

4. CATAPULT THRUST EFFECTS

The catapult thrust effects were analyzed using the basic seat weight of 400 pounds. The largest effect on tip-off from catapult thrust is the time at which it occurred. As shown in Figure 241, the time at tip-off for the 5000 pound catapult is 0.135 second, for the 6000 pound catapult 0.12 second, and for the 8000 pound catapult 0.105 seconds. Figures 226, 243, and 244 reveal no significant change in pitch attitude of the seat at tip-off when the catapult thrust changes. For each case the seat is pitched down 1.5 degrees relative to the earth and up about 0.2 degree relative to the airplane. The reason for this is a completely guided catapult stroke which prevents the catapult from pitching the seat. As the catapult thrust is increased, the seat reaches slightly higher pitch rates coming up the rails (Figure 245). When the middle blocks leave the rails, the pitch velocity becomes more nose up for all the cases but at a higher rate for the larger catapult because of higher aircraft negative rate reaction, through the rails, on the bottom blocks.

5. WEIGHT AND INERTIA EFFECTS

The weight and inertia of a fixed seat configuration will change due to pilot size. The tip-off time changes with seat-man weight as shown in Figures 246. The 300 pound seat-man, Case 10, leaves the rails at .12 seconds. As the weight increases to 400 pounds, Case 9, tip-off occurs at .135 seconds while the 500 pound seat-man, Case 11, takes .15 seconds. Figure 247 indicates the obvious increase in seat velocity at tip-off as the seat-man weight is decreased. For all three of these cases the seat follows the airplane closely in pitch until the middle blocks leave the rails. The airplane then pitches the seats nose up, with respect to the airplane. Figure 226 reflects this for the 400 pound seat-man combination while Figures 248 and 249 are for the 300 and 500 pound seat-man combinations respectively. These three figures indicate that the airplane pitches the seat with the smallest weight and inertias the largest amount with respect to the airplane. These same occurences can be seen in Figure 250 with the seat pitch rate.

6. CONCLUSIONS

- Minimum tip-off effect from slider block position occurs when the middle pair of blocks are located such that the catapult stroke is completely guided.

- Changing catapult stroke does not significantly change the climb rate of the seat at tip-off, because the larger stroke pitches the airplane down more reducing the earth axis vertical rates of the seat.

- If the sustainer acts through a point half way between the bottom blocks, it does not contribute to tip-off effects. After the seat leaves the rails the larger sustainer pitches the seat up more.

- For a constant seat-man weight the climb rate of the seat-man at tip-off naturally increases as the catapult thrust increases, but not as much as would be expected. The airplane pitches down more as the catapult thrust increases which reduces the seat climb rate.

- The smaller seat-man reaches a larger velocity at tip-off in a faster time. The smaller inertia results in more pronounced tip-off effects.

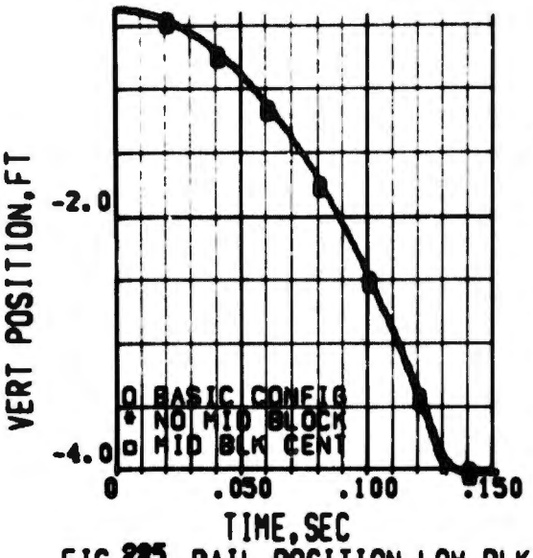

FIG 225 RAIL POSITION LOW BLK
SLIDER BLOCK (ROLLER) VARIED

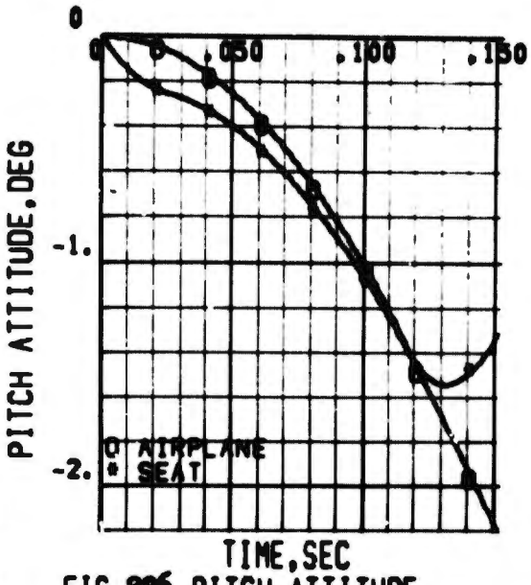

FIG 226 PITCH ATTITUDE
BASIC CONFIGURATION MIDDLE BLK

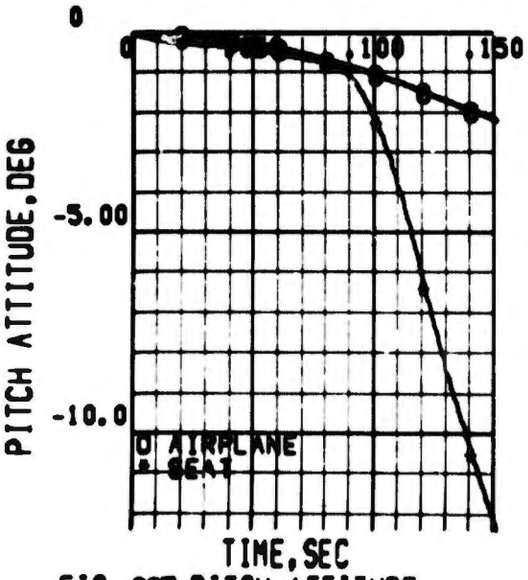

FIG 227 PITCH ATTITUDE
NO MIDDLE BLOCKS

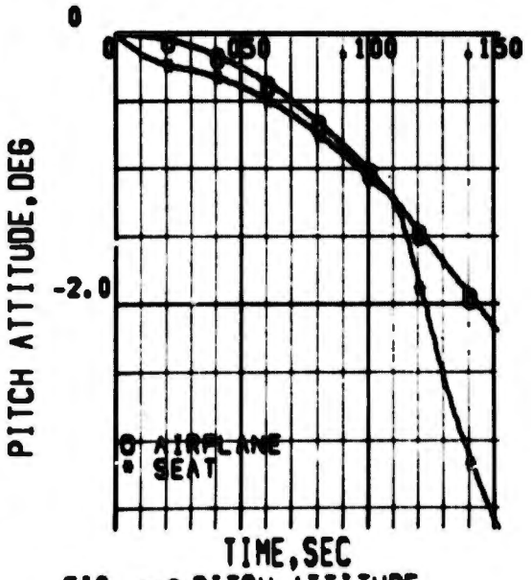

FIG 228 PITCH ATTITUDE
MIDDLE BLOCKS CENTERED

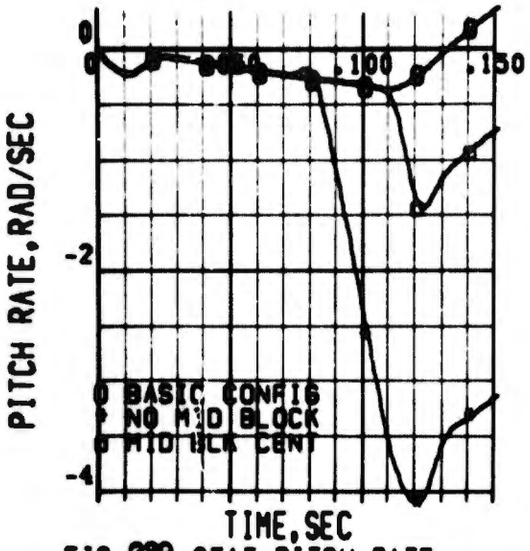

FIG 229 SEAT PITCH RATE
SLIDER BLOCK (ROLLER) VARIED

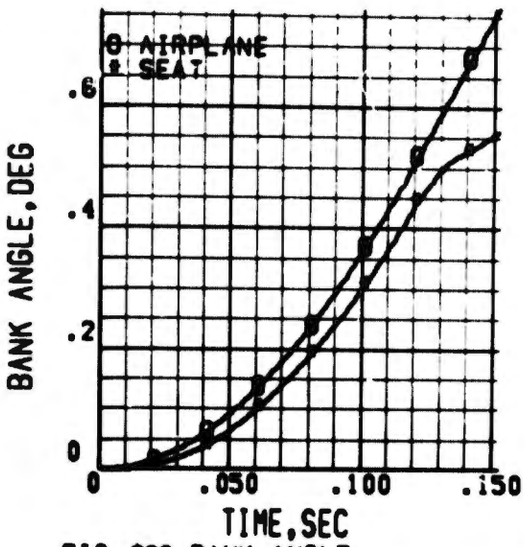

FIG 230 BANK ANGLE
BASIC CONFIGURATION MIDDLE BLK

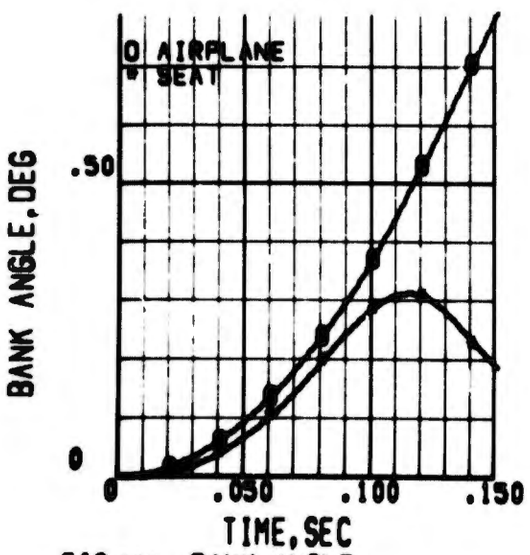

FIG 231 BANK ANGLE
NO MIDDLE BLOCKS

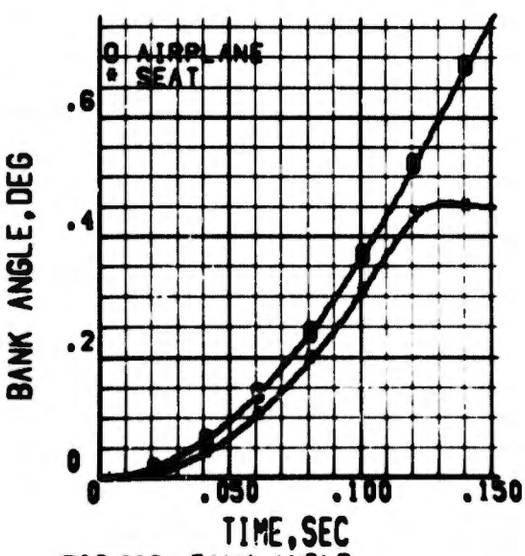

FIG 232 BANK ANGLE
MIDDLE BLOCKS CENTERED

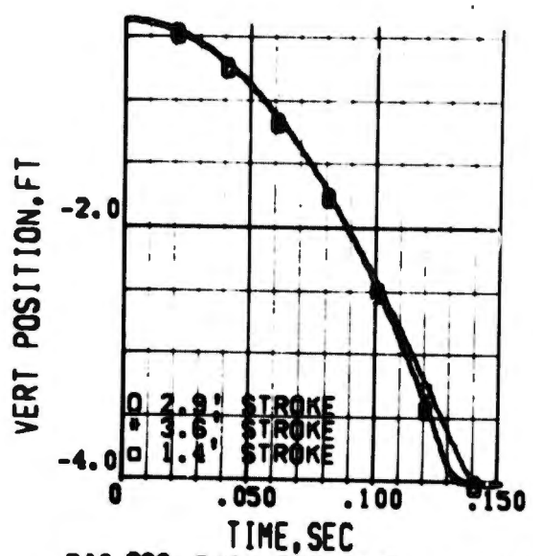

FIG 233 RAIL POSITION LOW BLK CATAPULT STROKE VARIED

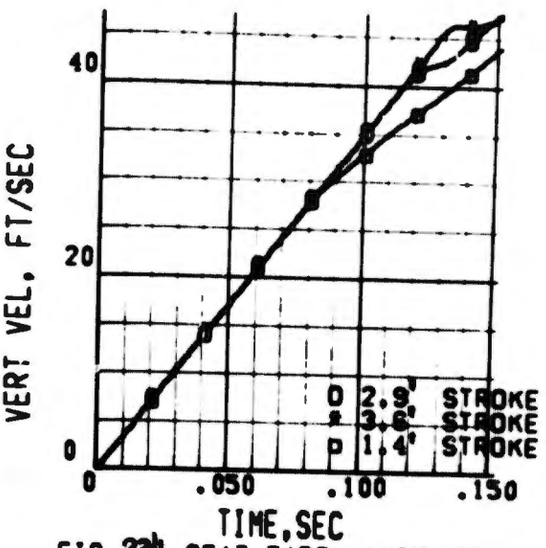

FIG 234 SEAT EARTH AXIS VEL CATAPULT STROKE VARIED

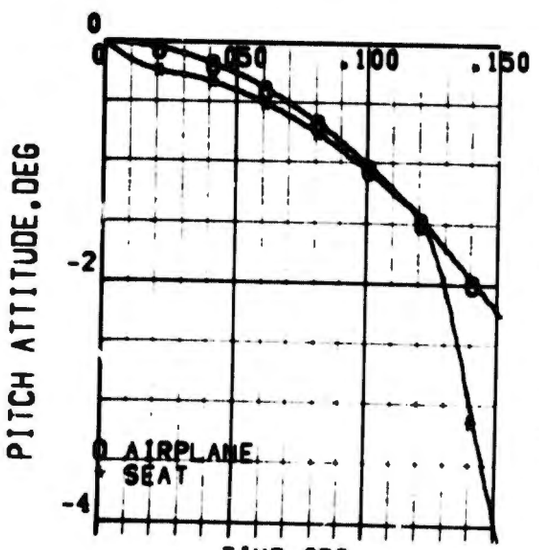

FIG 235 PITCH ATTITUDE 3.6 FT CATAPULT STROKE

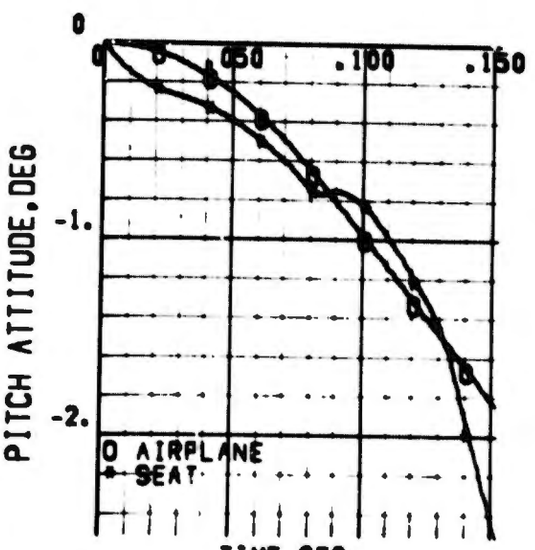

FIG 236 PITCH ATTITUDE 1.4 FT CATAPULT STROKE

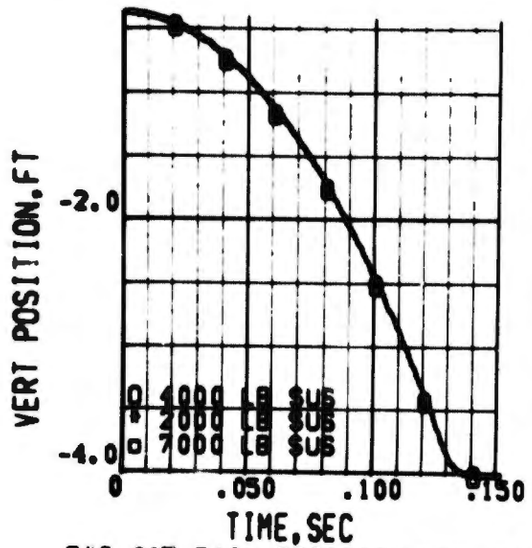

FIG 237 RAIL POSITION LOW BLK SUSTAINER THRUST VARIATION

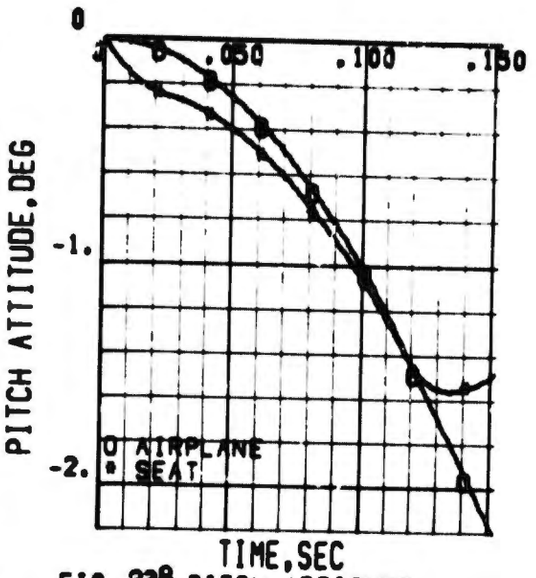

FIG 238 PITCH ATTITUDE 2000 POUND SUSTAINER THRUST

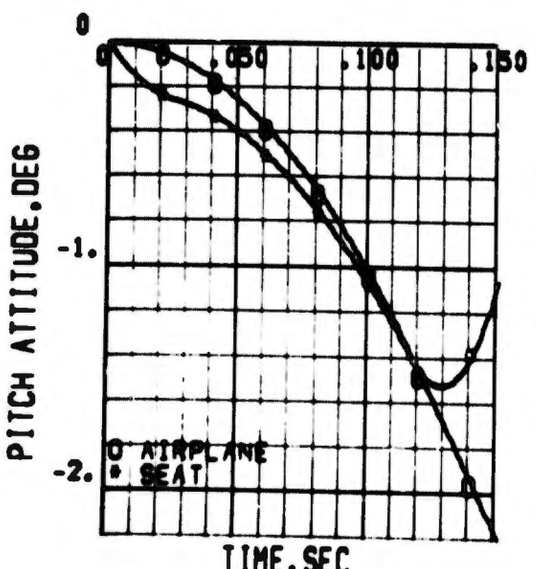

FIG 239 PITCH ATTITUDE 7000 POUND SUSTAINER THRUST

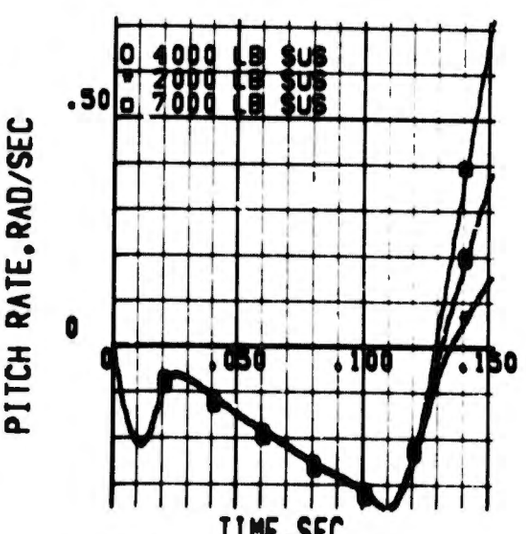

FIG 240 SEAT PITCH RATE SUSTAINER THRUST VARIATION

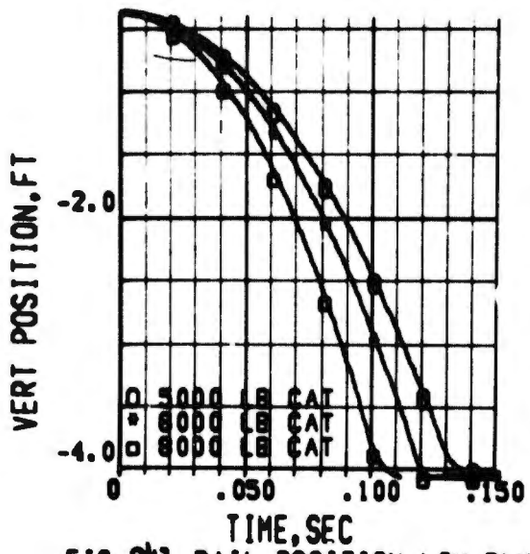

FIG 241 RAIL POSITION LOW BLK CATAPULT THRUST VARIED

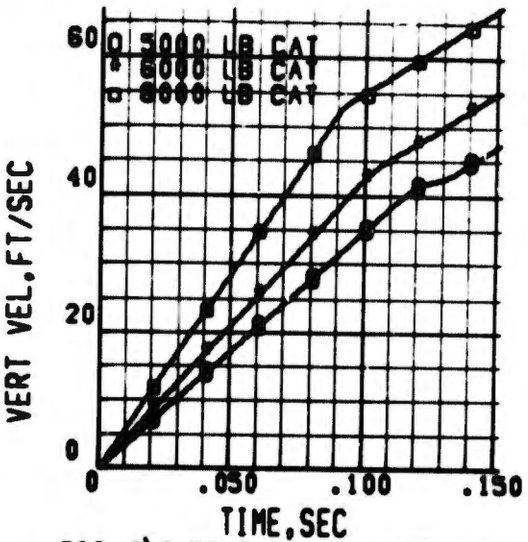

FIG 242 SEAT EARTH AXIS VEL CATAPULT THRUST VARIED

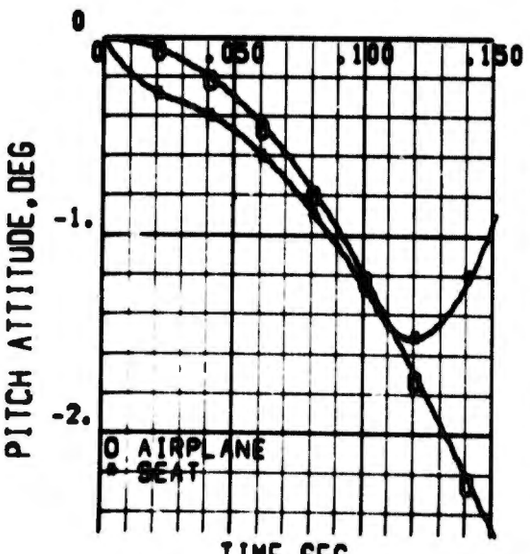

FIG 243 PITCH ATTITUDE 6000 POUND CATAPULT THRUST

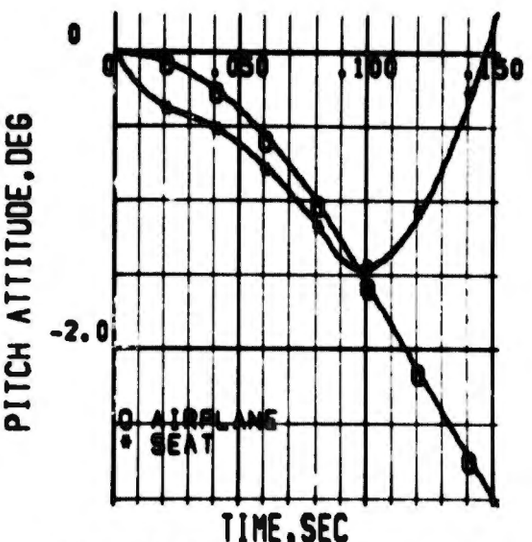

FIG 244 PITCH ATTITUDE 8000 POUND CATAPULT THRUST

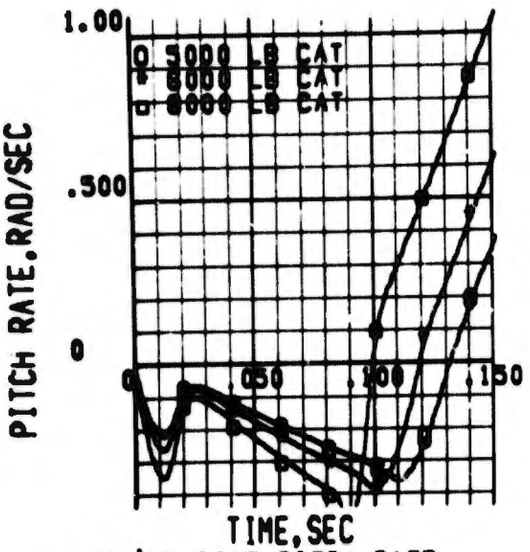

FIG 245 SEAT PITCH RATE
CATAPULT THRUST VARIATION

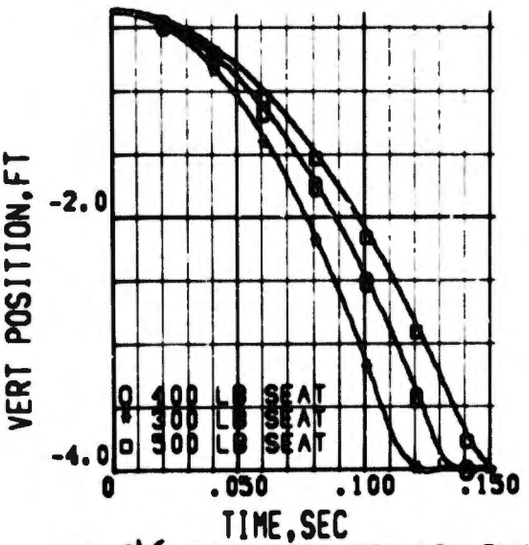

FIG 246 RAIL POSITION LOW BLK
SEAT WEIGHT AND INERTIA VARIED

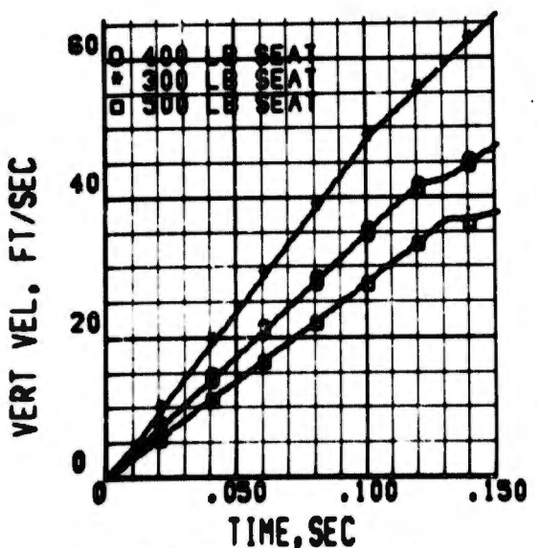

FIG 247 SEAT EARTH AXIS VEL
SEAT WEIGHT AND INERTIA VARIED

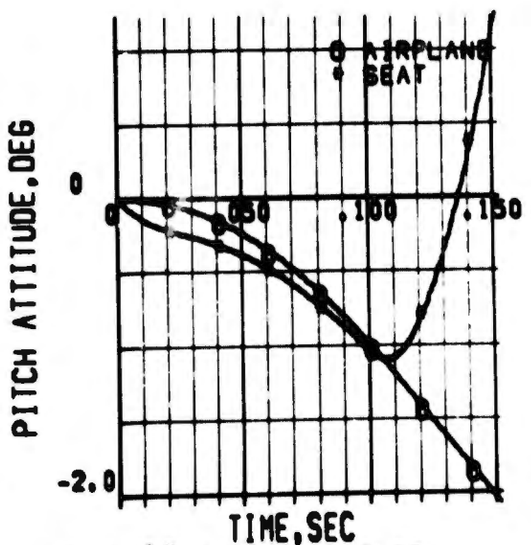

FIG 248 PITCH ATTITUDE
300 POUND SEAT

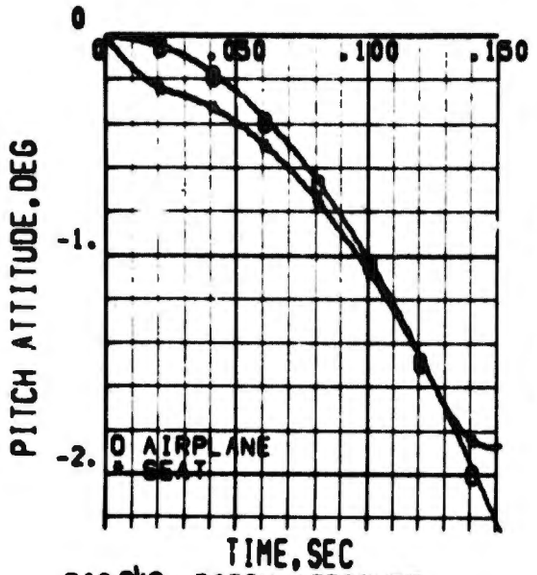

FIG 249 PITCH ATTITUDE
500 POUND SEAT

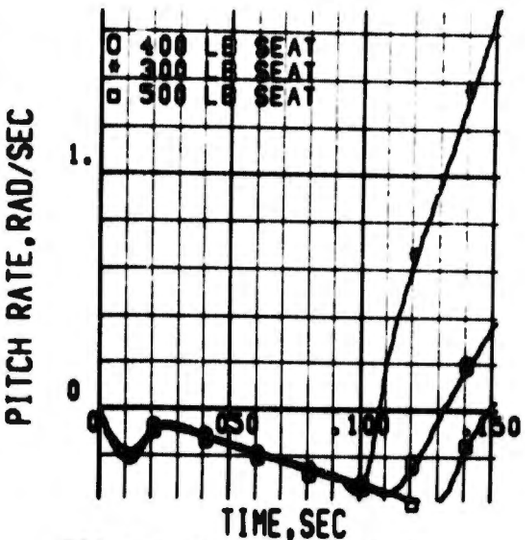

FIG 250 SEAT PITCH RATE
SEAT WEIGHT AND INERTIA VARIED

 (Page 98 is blank)

BLANK PAGE

SECTION V

EJECTION PROPULSION TECHNIQUES

1. INTRODUCTION

The problem of providing propulsion for an ejection escape system is primarily one of furnishing a propulsive force to safely separate the man/seat combination from a disabled VTOL aircraft. The extreme conditions that are encountered during emergencies in the VTOL and high speed, low altitude regimes would place the most severe performance requirements on the propulsion system and are discussed in Part I, Volume 1. The loss of one wing of the hypothetical aircraft would result in a very fast roll and a failure in the longitudinal control system would cause a rapid and excessive change in pitch.

In these two extreme conditions, two possible modes of escape were examined. In the event the aircraft were to roll or pitch to an inverted (180° from the vertical), the man/seat could be ejected upward through the floor of the aircraft. The acceleration from the propulsion system would be applied in the "eye balls up" position in accordance with MIL-C-25918. The onset rate would have to be below 125 g/sec and the maximum acceleration below 10 g. The total impulse would be less than that required for normal ejection and was considered to be a minimum of 1200 seconds. The second escape method would be to eject the man/seat downward toward the ground and after seat tip-off apply a retro force to slow the seat. Vernier motors could simultaneously turn the seat while a force from the rocket in the "eye balls down" position would carry the man/seat laterally where the full force of the rocket could be applied to carry it to a higher altitude for deployment of the personnel parachute. In this situation, the total impulse could be as high as 1800 seconds. MIL-C-25918 requires a maximum onset rate of 250 g/sec and a maximum of 20 g in the "eye balls down" situation. It was recognized that if such escape modes were to be possible, a variable thrust and variable total impulse rocket system would have to be used.

The escape modes defined by the VTOL aircraft determined the performance of the escape propulsion system. The other criteria that must be considered in the selection of a propulsion system are weight, volume, reliability, feasibility, safety, storability (environmental factors), and maintainability.

A visit was made to a representative company (Talley Industries) that manufactures solid rocket motors for ejection systems to obtain information on the latest propellants and methods of manufacture. Talley Industries and Universal Propulsion Company made two visits each to VAD to discuss the VTOL seat program. The Air Force Rocket Propulsion Laboratory was also visited as the one place where a complete survey of the potential of both the liquid and hybrid rocket motors could be obtained. In addition, information on these types of rocket motors was obtained from Rocketdyne, United Technology Center, and Aerojet General.

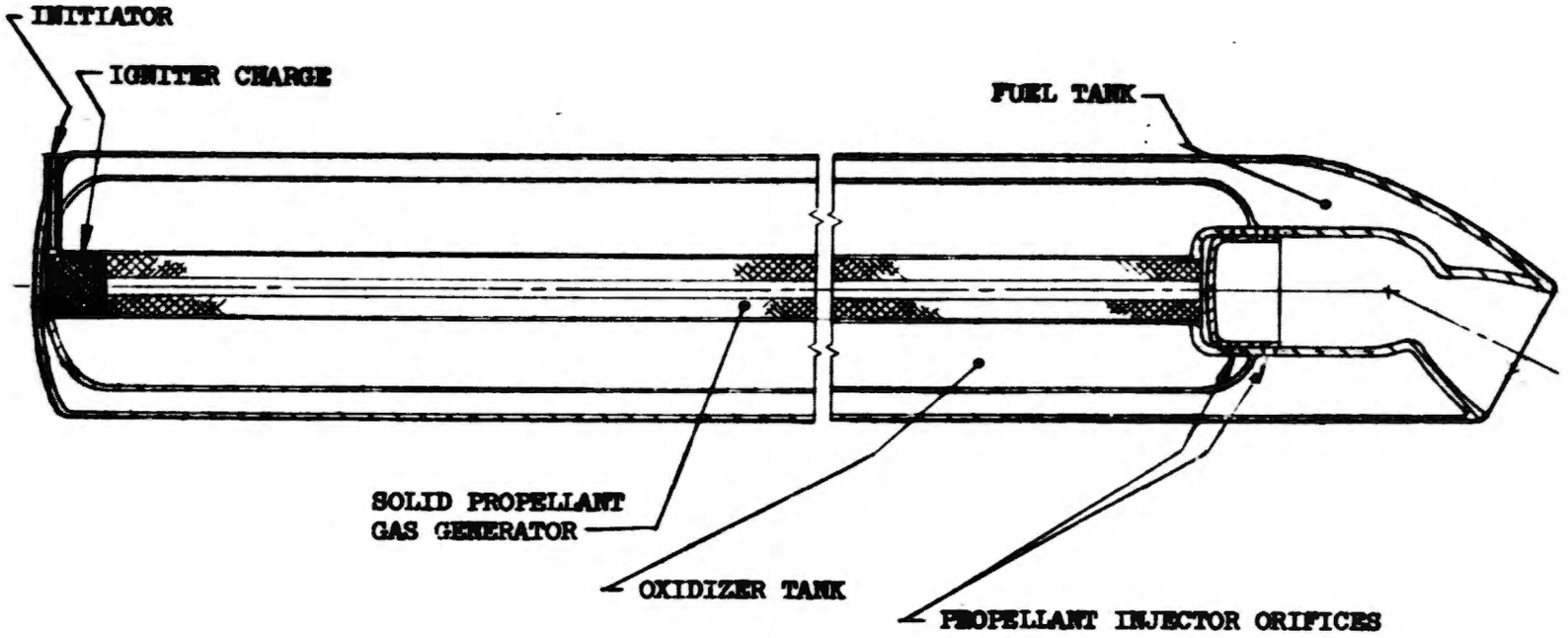

FIGURE 251 TYPICAL LIQUID PROPELLANT ROCKET

Also, a survey of the rocket motor industry was made to gather data for a comparative analysis of the propulsion methods. The following companies were contacted and provided information on solid rockets for use in an ejection system:

Quantic Ind. – Pelemoc Division
Universal Propulsion
Talley Industries
Thiokol Chemical Corp. Maryland
Northrop Carolina, Inc.
Stencel Aero Engineering

In the early stages of the program, the requirement for a variable thrust and total impulse made it appear the liquid and hybrid rocket motors would have to be considered in addition to the solids because of the variability that could be obtained by simply controlling a valve. The liquid and hybrids also could deliver a higher specific impulse than the solids and would have a lower propellant weight. The other selection criteria would have to be weighed against the high performance and controllability of these motors.

The three types of rocket motors were studied for suitability for use in the VTOL ejection seat. Each type was compared to the requirements outlined above. The solids were selected for a more detail investigation of several propulsion techniques that could satisfy the potential requirements of the failure modes envisioned.

2. LIQUID PROPELLANT ROCKETS

The liquid propellant engines are attractive for use in most applications because of their high specific impulse (300 to 457 seconds). For some liquid propellant combinations, the specific impulse (411 seconds for $F_2 + H_2$) is almost twice that of the conventional solid rocket propellants used in ejection seats. Therefore, for the same total impulse, the propellant weight for the liquid rocket would be approximately one half that of the solid propellants. Figure 252 shows how the propellant weight will vary with a change in Isp for three values of total impulse.

The advantage of the higher specific impulse has to be weighed against the disadvantages of a low density and a complex system. The liquid propellant rocket has two or more high pressure tanks, an intricate injector to provide proper mixing of the propellants in a combustion chamber, a power source for a complex feed system, and in most applications a method for controlling the flow rates into the combustion chamber (Figure 251).

The propellants are kept separated in two tanks until the rocket is fired. Some method must be used to get the propellants from the tanks and into the combustion chamber. Some large rockets use a turbo pump, whereas in smaller ones a solid fuel is burned to produce a high pressure gas. The pressure provided by the gas generator has to be higher than the chamber pressure to force the propellants from the tanks into the combustion chamber. With an oxidizer to fuel ratio (O/F) ranging from 3.0 to 7.0, the oxidizer would require the larger tank.

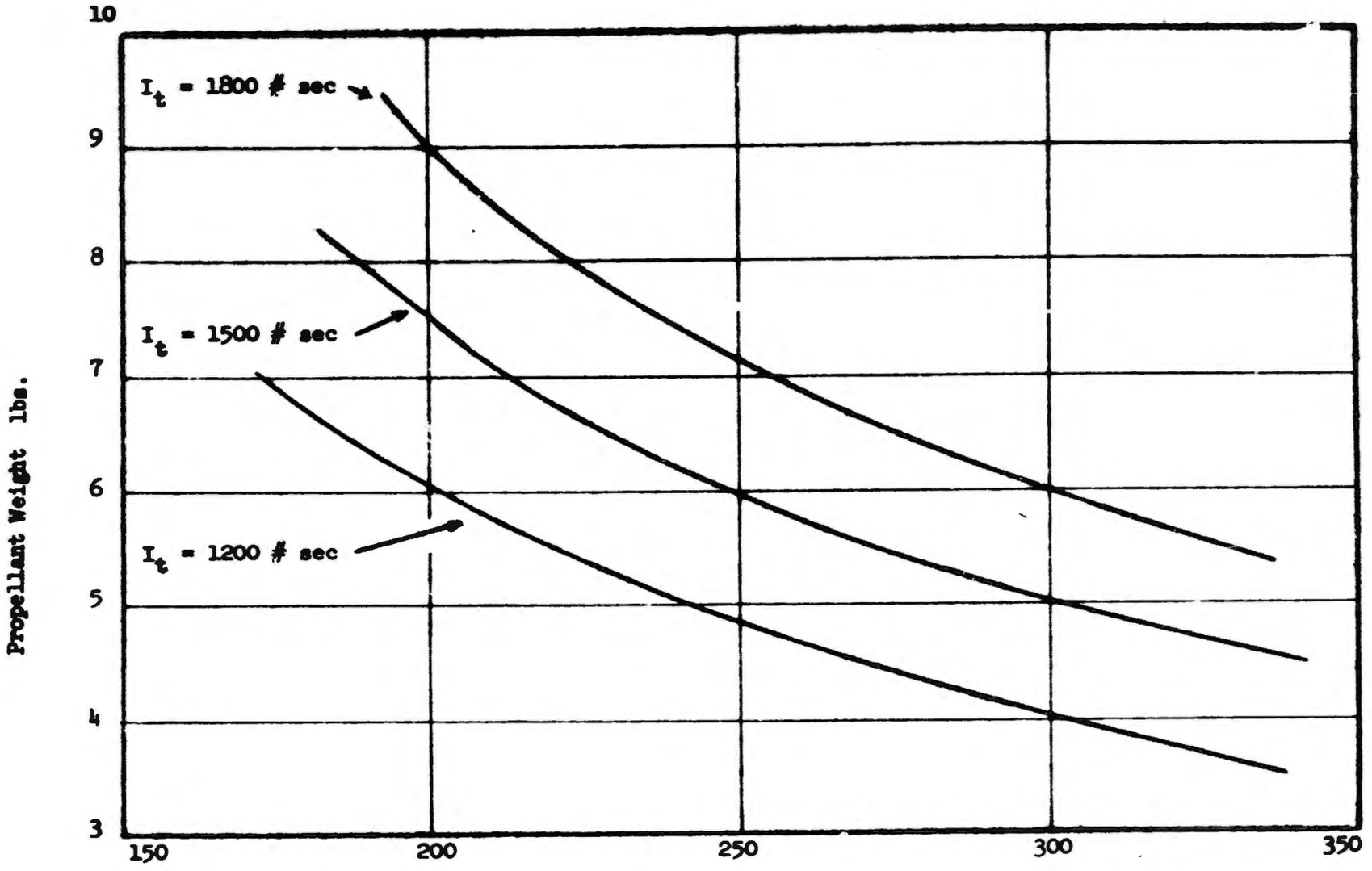

FIGURE 252 PROPELLANT WEIGHT VERSUS I_{sp}

Some of the failure modes envisioned during the early stages of the program would require the rocket to operate while undergoing acceleration in the roll direction as well as in the "up-down" directions. The acceleration of the system would make the "ullage space" go in the direction of the acceleration. If the pressurization gas were applied to fire the rocket during such acceleration, a delayed firing could occur. A piston or bladder to contain the fuel and keep it separated from the gas could alleviate this situation; however, it would be an additional complexity associated with the liquid and hybrid rockets.

In some of the escape modes examined early in the program, it appeared that it might be desirable to have thrust vector control. One method that has been experimentally investigated in the past few years is the injection of a hot gas through ports that are on an arc less than one half of the nozzle circumference and downstream of the throat. A shock wave is set up which deflects the exhaust providing a thrust vector change of about 15° maximum (Figure 253). A vector change in any one of four directions can be obtained by firing one of four gas generators. Four additional directions can also be obtained by firing a combination of two or more of the gas generators. Tabs that can be moved into the rocket exhaust can accomplish the thrust deflection and have also been experimentally investigated. These methods for thrust vector control can also be used on hybrids and solids. They do increase the complexity of the rocket motor since the hot gases will have to be bled from the combustion chamber or generated in a separate gas generator. The selection and opening of the ports would also add functions that would increase the complexity and decrease the reliability of the system.

There are many oxidizers and fuels available for use in a liquid rocket motor design; therefore, there are numerous combinations of oxidizers and fuels to give a wide choice of propellants for the design of a particular rocket motor. Table IV, provided by Rocketdyne, lists some of the possible fuel and oxidizer combinations. The Isp is given for a chamber pressure of 1000 psia expanding to sea level atmospheric pressure. Table IV indicates that the highest specific impulse (Isp) and hence the lowest propellant weight can be obtained by use of the cryogenic liquid oxidizers. This advantage is offset by the very low densities which result in a large tank weight. The cryogenic liquid propellants are not storable for any appreciable period of time and cannot be considered for use in the propulsion system of a VTOL ejection seat.

Some of the liquid propellants are storable to some degree and have found use in packaged liquid rockets for unmanned missiles. The Inhibited Red Fuming Nitric Acid (IRFNA) oxidizer is one of the more attractive storable propellants. It can be used with Mixed Amines (MAF-1), Hydrazine (N_2H_4), Unsymmetrical Dimethyl Hydrazine (UDMH) and RP-1 as fuels to provide an ejection system with some limited storage capability. Some of the fuels have low boiling points and/or high freezing temperatures. Hydrazine has a freezing temperature of 12° F; therefore, it cannot be considered as a propellant for use in an ejection seat. Unsymmetrical Dimethyl Hydrazine has a relatively high boiling point (190° F) and a low (-57° F) freezing temperature and would be used in an ejection system; however, emergency venting would be required. RP-1 also has a high boiling point and a low freezing temperature;

however, the density dictates a large volume. The liquid propellants that are storable for an appreciable length of time are hypergolic and would decrease the ignition delay time.

Inhibited Red Fuming Nitric Acid has a high oxygen content and reacts violently with organic materials such as paper, wood, cloth, and leather. It is hypergolic with the fuels of interest which cuts down the ignition delay time. It combines readily with petroleum products to form a highly explosive mixture which is sensitive to small shocks or sparks. It has a low vapor pressure and can be stored for long periods of time. It could withstand the vibration and shock normally encountered by an ejection seat. It would be a hazard in the cockpit of an airplane for if it were struck by a projectile or the container broken open in case of an accident, the fumes as well as the liquid would probably be fatal to the pilot. It would also be a hazard in handling and servicing because if any breakage or leakage occurred, the oxidizer would ignite any organic material with which it came in contact.

The use of Hydrogen Peroxide (H_2O_2) and RP-1 makes a system that is storable for approximately one year. A 90% concentration of H_2O_2 is a clear, colorless liquid and is slightly acidic with a Ph of about 5. It has a freezing point of about 13°F and is subject to decomposition which limits its storage life to approximately one year without venting. The relatively high freezing temperature and limited storage life make it undesirable for an ejection seat propulsion system.

The liquid rocket motors have several features that make them undesirable for use in an ejection seat. The sequence of events from the initiation of the signal which fires the initiator for the gas generator, ignition and combustion of the solid fuel, the pressure rise in the propellant tanks and the flow of the propellants through an injector into the combustor, and the burning of the propellants requires appreciable time. The numerous events that must take place sequentially make the liquid rocket motor more complex and less reliable than the simple solid rocket. The oxidizers generally have relatively high freezing points, disassociate with time, and are extremely reactive with organic materials which make them a hazard in the cockpit of a VTOL aircraft.

3. HYBRID PROPELLANT ROCKETS

The hybrid propellant rocket motor normally uses solid fuel with a liquid oxidizer. This combination can take advantage of the high density of the solid fuel and the controllability of the liquid oxidizer. The thrust level of the hybrid can be varied by controlling the oxidizer flow rate while the total impulse can be selected by metering a certain amount of oxidizer. Thrust can be terminated by stopping the oxidizer flow and restarted at a later time by starting the flow of oxidizer.

The hybrid rocket motor has four major components: fuel tanks, a high pressure gas generator, a combustor, and a nozzle with the solid fuel chamber also serving as a combustion chamber. The fuel for the hybrid can be a metal hybrid or a rubber base which can be loaded with metal particles. The fuel density can be quite high, which results in a relatively small fuel tank and combustion chamber. The gas generator is sized by the amount of oxidizer used

TABLE IV
SOME POSSIBLE FUEL AND OXIDIZER COMBINATIONS

OXIDIZER	FUEL	Isp SPECIFIC IMPULSE	DENSITY Lb/In.^{3}
Liquid Oxygen (O_2)	Liquid Hydrogen (H_2)	391	.0101
	Hydrogen Beryllium (H_2Be)	457	.0080
	RP-1 (Kerosene)	300	.0368
	Hydrazine (N_2H_4)	312	.0386
Fluorine (F_2)	H_2	411	.0162
	H_2Li (Hydrogen-Lithium)	432	.0060
	RP-1	318	.0437
	MMH*	346	.0450
Chlorine Trifluoride (ClF_3)	MMH*	286	.0509
	N_2H_4	293	.0541
Nitrogen Tetroxide (N_2O_4)	MMH*	288	.0433
	N_2H_4 - UDMH**	289	.0433
Inhibited Red Fuming Nitric Acid (IRFNA)	MAF-1 (Mixed Amine)	243	.0373
	MMH*	275	.0448
	UDMH**	243	.0440
	RP-1	220	.0438
Hydrogen Peroxide (H_2O_2)	MMH*	285	.0458
	N_2H_4	287	.0458

* MMH = Monomethyl Hydrazine
** UDMH = Unsymmetrical Dimethyl Hydrazine

and hence can be smaller than the liquid rocket motor where the fuel tank also has to be pressurized. The specific impulse of the hybrid can be in the range of 240 to 250 seconds which results in a relatively low propellant weight. Some propellants for hybrids are shown in Table V.

TABLE V SOME PROPELLANTS FOR HYBRIDS

		DENSITY Lbs/In.^{3}
OXIDIZER		
Nitrogen Tetroxide	N_2O_4	0.052
Hydrogen Peroxide	H_2O_2	0.053
Chlorine Trifluoride	ClF_3	0.064
FUEL		
Beryllium Hydride	BeH_2	0.061
Aluminized Rubber		0.067
Titanium Hydride	TiH_2	0.136
Zirconium Hydride	ZrH_2	0.203

Nitrogen tetroxide (N_2O_4), because of its high oxygen content, could be used as the oxidizer. It is hypergolic with solid fuels, and its density is relatively high. When it is used with the high density fuels, a lower volume is realized than with all the liquified propellants. Nitrogen tetroxide has to be stored in steel cylinders but can be used in aluminum (6061) for short periods of time. It has a relatively high freezing point of 11.7°F and a relatively low boiling point of 69.8°F. It will spontaneously ignite in contact with paper, cloth, wood, leather, and other organic materials. It is highly toxic and does not give an adequate warning of a high gas concentration. Because of its high oxygen content, it will readily support combustion. It is insensitive to mechanical vibration and shock as well as heat and does not deteriorate with time. This oxidizer would constitute a safety hazard in the cockpit of an airplane because of its high reactivity with numerous materials.

Chlorine trifluoride, because of its high density, would provide a relatively small volume rocket motor when used with the very high density fuels such as zirconium hydride. It is a very pale green-yellow liquid that is ten times as toxic as elemental chlorine and is highly corrosive to metals. The vapors are so noxious that the threshold of perception is very low (approximately 0.1 to 2.0 ppm) and any contaminated area is usually evacuated before damage is done. It is the second most reactive chemical substance known with elemental fluorine being first. It is such a vigorous oxidizer that it will react explosively with almost all organic materials. The oxidizers for use in the hybrid rocket motor are so toxic and reactive that they would present a hazard for use in the cockpit of an aircraft and would also present a safety problem in handling, servicing, and storage.

The hybrid has the problem of pressurization of the oxidizer tank and the movement of the oxidizer from its tank into the solid fuel-combustion chamber. It is more complex than the all-solid but does provide flexibility in total impulse, thrust level, and a stop-start capability. The reliability of the hybrid would fall between that of all all-liquid and all-solid rocket motors because of its complexity. The hybrid rocket motor has not been experimentally investigated as extensively as the all-liquid and all-solid rocket motors. The hybrid rocket motor has the same undesirable characteristics as the all-liquid motor because of the liquid oxidizer.

4. SOLID PROPELLANT ROCKET MOTORS

The conventional solid propellant rocket motors are being successfully used in existing ejection seats; however, they have fixed thrust and total impulse. Since some of the original escape modes envisioned required variable impulse and thrust, methods for accomplishing this for solid rockets were of interest. In the past few years, several techniques for providing variable thrust and total impulse as well as stop-start capability and methods for thrust vector control have been experimentally investigated.

One concept has a wafer design where two or more grains are separated by a frangible barrier. When only one grain is fired, one level of thrust is provided. With two or more grains being fired simultaneously, still other levels of thrust could be provided. This method of achieving variable thrust and total impulse also provides a way to have a start-stop capability in a solid rocket.

The propellant for a solid rocket must have a chamber pressure above a certain value to support combustion. The burning rate of the propellant and the rate of formation of the products of combustion are a function of the chamber pressure (reference 14). Therefore, the chamber pressure can be controlled by varying the nozzle area. This can be accomplished by moving a plug in and out of the throat. The burning rate could be controlled which would result in a control of the thrust level. The rocket could be so designed that a rapid movement of the plug to give maximum throat area would extinguish the burning of the propellant because of the decrease of pressure below the critical value required for combustion. One technique for terminating the thrust would be to have blow out ports on the rocket end as shown in Figure 254. The blow out ports would provide a rapid decrease in pressure which would extinguish the combustion of the propellant and provide an additional escape position for the gases in the chamber. This would provide some thrust in the opposite direction and counteract that provided by the nozzle.

The solid propellant rocket has a relatively high density (0.06 lbs/in.^{3}). Therefore, the volume required for a given impulse is relatively low. Figure 255 shows a typical drawing of a solid rocket. The delivered specific impulse for these rockets is about 210 seconds, which gives an acceptable rocket weight. The propellant is a solid that can withstand vibration and shock as well as extremes of temperature and is storable for up to five years.

Although there are numerous solid propellant combinations, the family of polysulfide and ammonium perchlorate with metal additives are of interest for use in the VTOL ejection system. These propellants provide theoretical

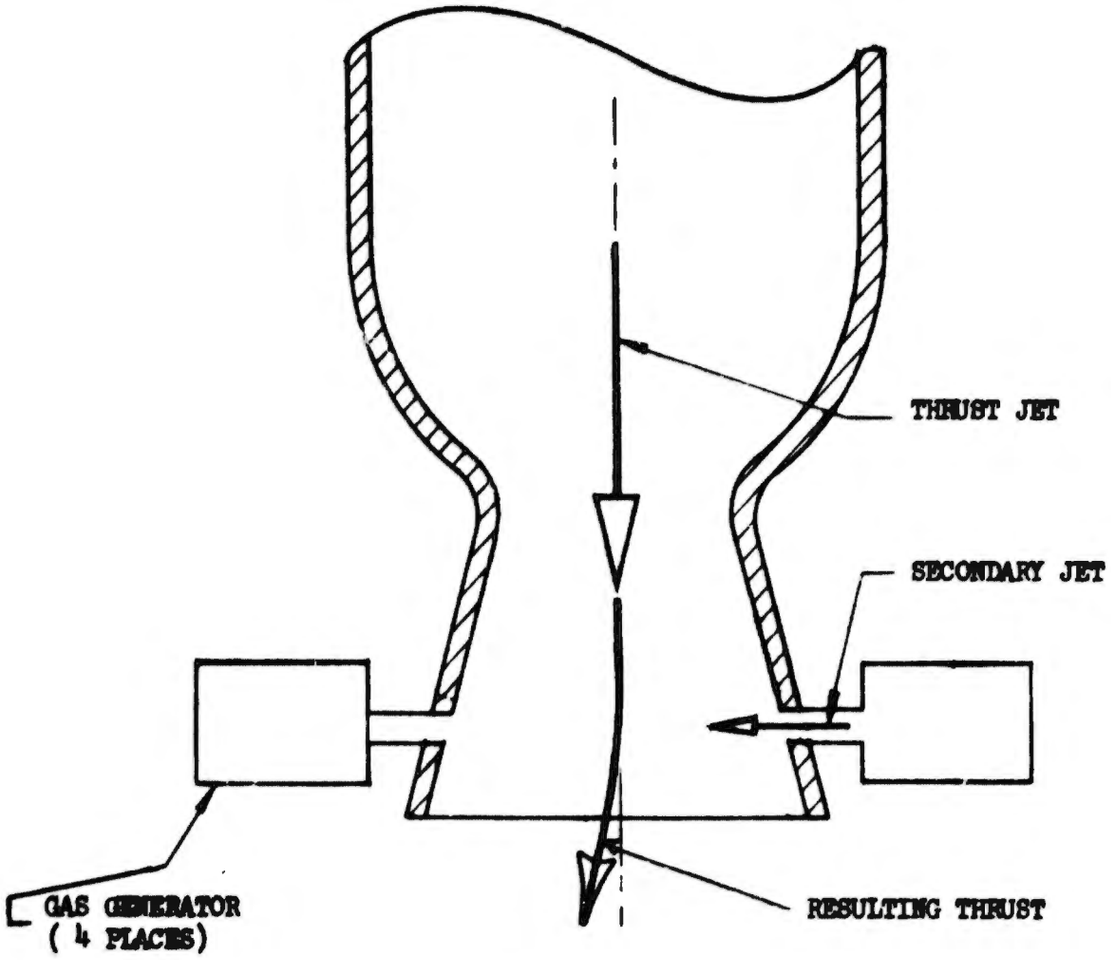

FIGURE 253 THRUST VECTOR CONTROL CONCEPT

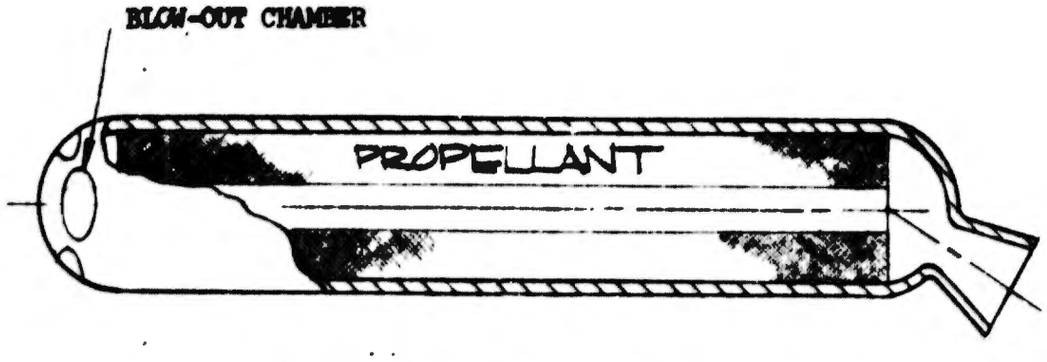

FIGURE 254 BLOW-OUT PORT CONCEPT

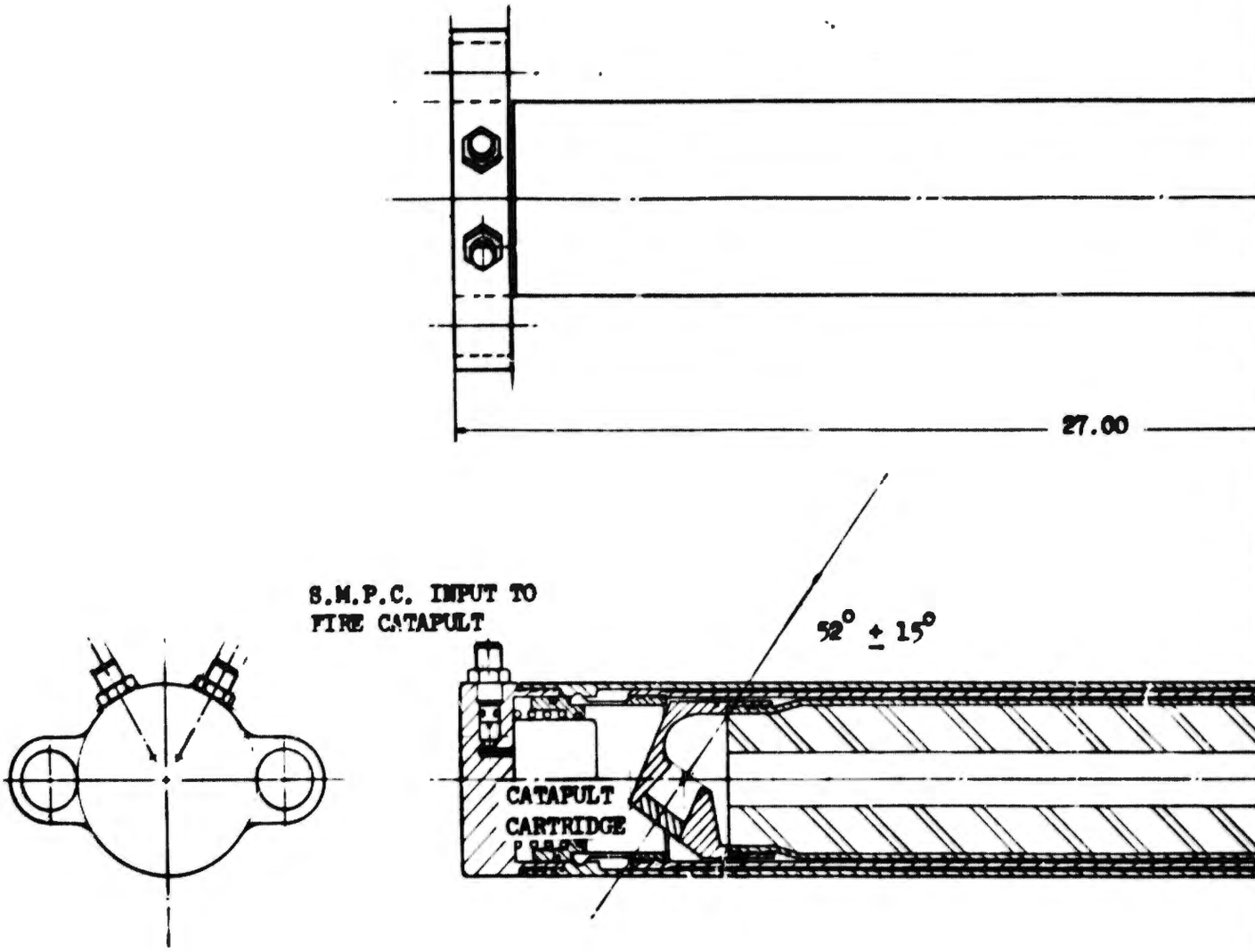

FIGURE 255 TYPICAL SOLID ROCKET

(Page 110 is blank)

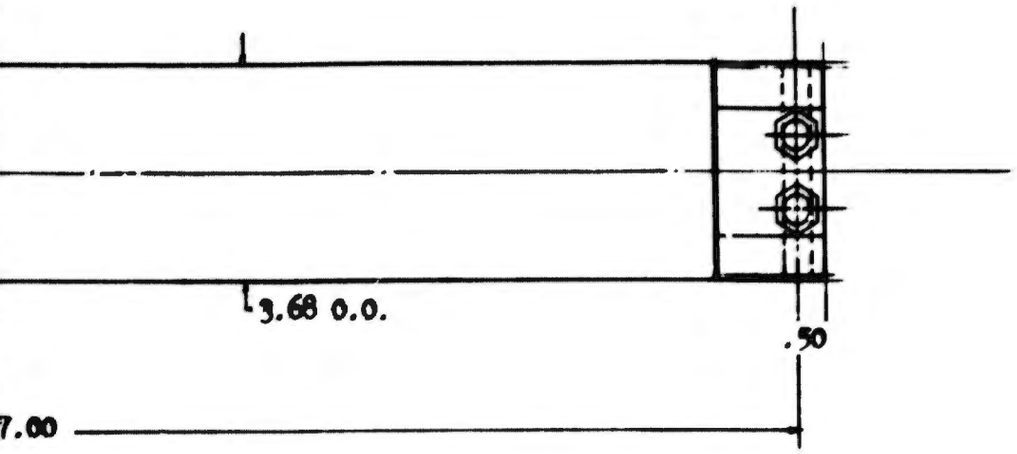
3.68 O.D.
.50
7.00

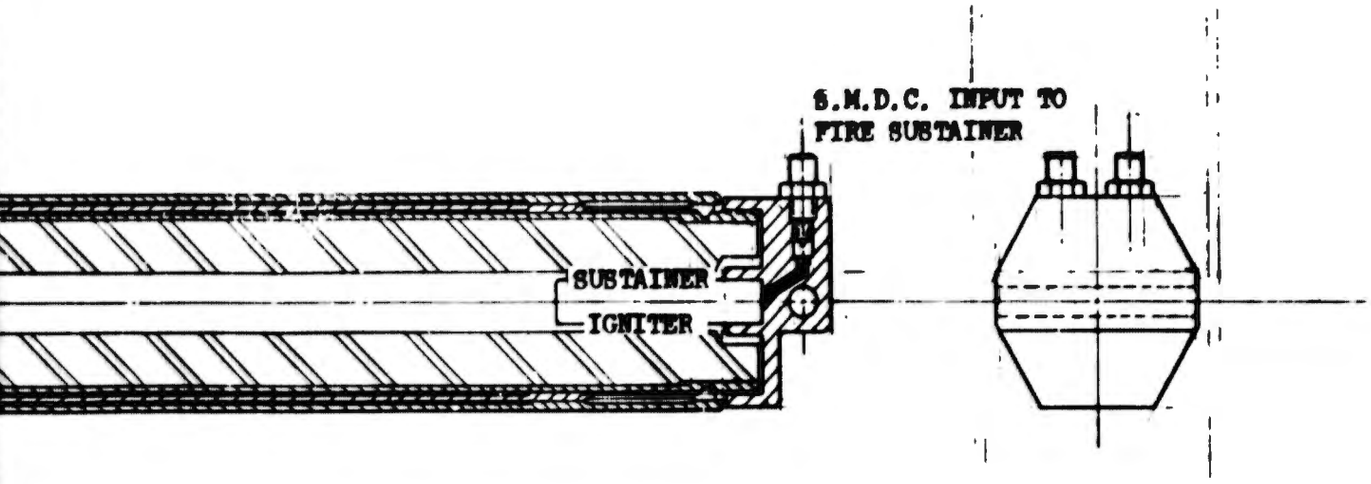
S.M.D.C. INPUT TO
FIRE SUSTAINER
SUSTAINER
IGNITER

B

impulses up to 230 seconds and have a density of over 0.06 lb/in.^{3}. The Carboxy Terminated Polybutadiene with Ammonium Perchlorate promises to provide higher density propellant. This propellant can be developed to have a lower temperature storage capability and a higher density at the expense of a lower specific impulse. Thus a rocket sustainer with a weight and volume somewhat lower than those presently being produced is possible.

Unlike the hypergolic liquid and hybrid propellants, the solid propellants must have an ignition source. In some integral catapult-rocket escape systems, the hot gas from the catapult is used to ignite the rocket propellant grain; however, in some escape modes of the VTOL seat, ignition is withheld until after seat tip-off. Any potential improvement in the ejection system performance lies in tailoring the trajectory for the initial conditions and reducing the elapsed time to a fully inflated personnel parachute. In an attempt to reduce this elapsed time, the ignition delay time should be reduced to a minimum. The ignitor for the solid rocket would be of the pyrotechnic type. It usually consists of a primer that is sensitive to temperature and will easily ignite. Black powder or one of the chlorates or perchlorates is usually used as the main igniter charge. The main ignitor charge is ignited by the primer and provides a hot flame which ignites the solid rocket grain. In an attempt to reduce the delay time from receiving a signal to full thrust, the amount of energy in the signal, the amount and type of primer, and amount and type of main igniter charge were investigated. The amount of main primer charge is usually taken, as a rule of thumb, to be about 40 grams for each pound or rocket grain to be ignited. The exact amount of main igniter and primer charge is usually optimized during the development of the rocket and the ignition time delay is usually from 20 to 30 milliseconds with a minimum of 10 and a maximum of 50 milliseconds. The signal to the catapult or rocket can be mechanical (firing pin), electrical, gas pressure, and shielded mild detonating cord (SMDC) since each method can produce the energy required to ignite the primer. Very low activation energies should not be used for safety reasons. This is important in aircraft since they are operated near modern high-power electronic installations (radar). The use of the SMDC is especially attractive since it is "hard" to a nuclear burst which could generate a large current in an electrical signal system and fire the catapult and rocket.

The solid rocket appears to be attractive for use in the VTOL ejection seat because of its acceptable weight and volume. It also has the best safety features and is storable under the expected environment.

The ballistic catapult is an efficient and proven way to eject the man/seat system from the airplane and has been selected for use in the design. The use of a rocket only to provide the impulse for ejection was studied, but no acceptable way was found to divert the exhaust gases outside the two-place cockpit without airframe penalties.

5. COMPARISON OF LIQUIDS, HYBRIDS, AND SOLID PROPELLANT ROCKET MOTOR

A comparative analysis of the three types of propulsion systems (liquids, hybrids, and solids) gives their relative standing for possible use in a propulsion system (Table VI). The liquids deliver a higher specific impulse

(Page 112 is blank)

TABL
TRADI
EVALUATION OF TYPES O

	CONVENTIONAL SOLID PROPELLANT MOTORS WITH FIXED TOTAL IMPULSE (1)	SOLID PROPELLANT MOTORS WITH VARIABLE TOTAL IMPULSE (2)	HI
Performance	Grain design may be tailored to provide required performance.	Same as (1)	Pe ar co
Simplicity of Function	Extreme simplicity	Fairly simple	Co of ar
Feasibility	Many configurations presently being used. Qualified.	Requires careful selection of grain design and composition. Greater testing required.	Pr co ab
Ignition System	a. Spring loaded firing mechanisms b. Gas pressure actuated firing mechanisms c. Electrical firing mechanisms	Same as (1)	Nc pc va
Method of Ignition	Relatively high heats and flame produced by use of explosive powders and grain.	Same as (1)	Hy
Time Delay (Ignition to Design Thrust)	0-50 milliseconds depending upon grain design and requirements	Same as (1)	At lo
Reliability	0.999	Less than (1)	Le
I_{sp} (sec)	210	210	2l
Storage Temperature	Insensitive	Insensitive	Se
No. of Pressure Vessels	1	1	2
Fuel or Oxidizer Pressurized?	No	No	Ye
Storage Life	Long	Long	Sl
System Weight vs Total Impulse	Least	Least	Co
Thrust Modulation	Fixed	Requires dual or variable nozzle. Multiple grains	Re mi
Safety	Safest	Safest	Le

A

(Page 114 is blank)

TABLE VI
TRADE STUDY
UATION OF TYPES OF EJECTION PROPULSION

TORS WITH MPULSE	HYBRID MOTORS WITH VARIABLE THRUST LEVEL AND TOTAL IMPULSE (3)	PACKAGED STORABLE LIQUID PROPELLANT MOTORS WITH VARIABLE THRUST LEVEL AND TOTAL IMPULSE (4)
	Performance parameter lower than anticipated for preliminary tests conducted by Hercules Power Co.	High specific impulse possible.
	Complex. Requires close control of injecting and mixing of fuel and oxidizer.	Complex. Same as (3).
tion of sition. ed.	Preliminary investigations only conducted on small motors suitable for escape system use.	Feasible but weight and safety would be a problem.
	Not fully explored. Indications point to fairly complex system of valves for precise mixing.	Complex system of valves, etc. to provide proper propellant flow.
	Hypergolic ignition and electrical	Pyrotechnic, hypergolic, electric, hot gas, additives, catalytic
	At present 100 milliseconds or longer	100 milliseconds or longer
	Less than (1)	Less than (1)
	240	260
	Sensitive	Sensitive
	2	3
	Yes	Yes
	Short	Short
	Comparable to solids	Greatest
ble ns	Requires precise metering and mixing. Stop-Start capability.	Requires precise metering and mixing. Stop-Start capability.
	Less safe than solids	Least safe

B

than the solids or hybrids but are handicapped by a relatively low density. The density impulse (the pounds of thrust delivered for each cubic inch of volume) would be highest for the hybrid since the solid fuel can have a very high density. The density impulse is a measure of the volume efficiency of the propellants.

The hybrid has not been completely developed and would have a problem in attaining a high combustion efficiency. The liquids can achieve a combustion efficiency of 96 to 98%; however, a small amount (1 to 2%) of the propellants cannot be expelled from the tanks. The solids also have about 2% of the propellant that is not burned. In all types of rocket motors, the mixture of propellants is oxidizer rich to assure all of the fuel can be oxidized. A propellant combination for each of the three types of propellants is compared on a weight and volume basis in Figures 256 and 257 respectively. The propellants were chosen because of their storability; however, with few exceptions, they also have lower weight and volume than other available combinations. The majority of the other propellant combinations for each of the three types of rocket motors would fall in a band above the combinations plotted in Figures 256 and 257.

In the total impulse range of interest for VTOL seats, the curves are straight lines; however, at lower total impulses, the curves would level out and reach a minimum. The inert weight which is comprised of the nozzle, tanks, and combustion chamber (for liquids) would then comprise a major portion of the rocket weight. At larger values of total impulse, the propellants become a larger fraction of the total weight and for very large rockets the solid can achieve a propellant mass fraction as high as 0.92. Each of the three types of propulsion systems could provide sufficient performance for an ejection seat.

The need for a pressurization system, separate propellant tanks, and a combustion chamber in the liquid rockets makes the process of producing thrust a relatively complex process when compared with the simplicity of the solid rocket. Although each of the types is feasible with proper development, the solid provides an already proven technology. The complexity of the liquid and hybrid and the number of events necessary to produce thrust make them less reliable than the solid rocket motor.

The liquid and hybrids present a safety problem in that the highly reactive oxidizer is toxic, reacts with organic materials and is corrosive to most metals. In the event of an aircraft accident and a rupture of the oxidizer tanks, the toxic vapors could be fatal not only to the pilot but also to any rescue workers. In combat, a rupture of the oxidizer tank by a projectile could prove fatal to the pilot. However, the liquid and solid rockets can be handled, serviced, and stored if proper precautions are taken.

The escape modes finally selected for intensive investigation did not require the unique variable thrust, total impulse, and stop-start capability of the liquids and hybrid rocket motor. The solid rocket gives a relatively low weight and volume, is relatively simple, reliable, and can be safely handled, serviced, and stored.

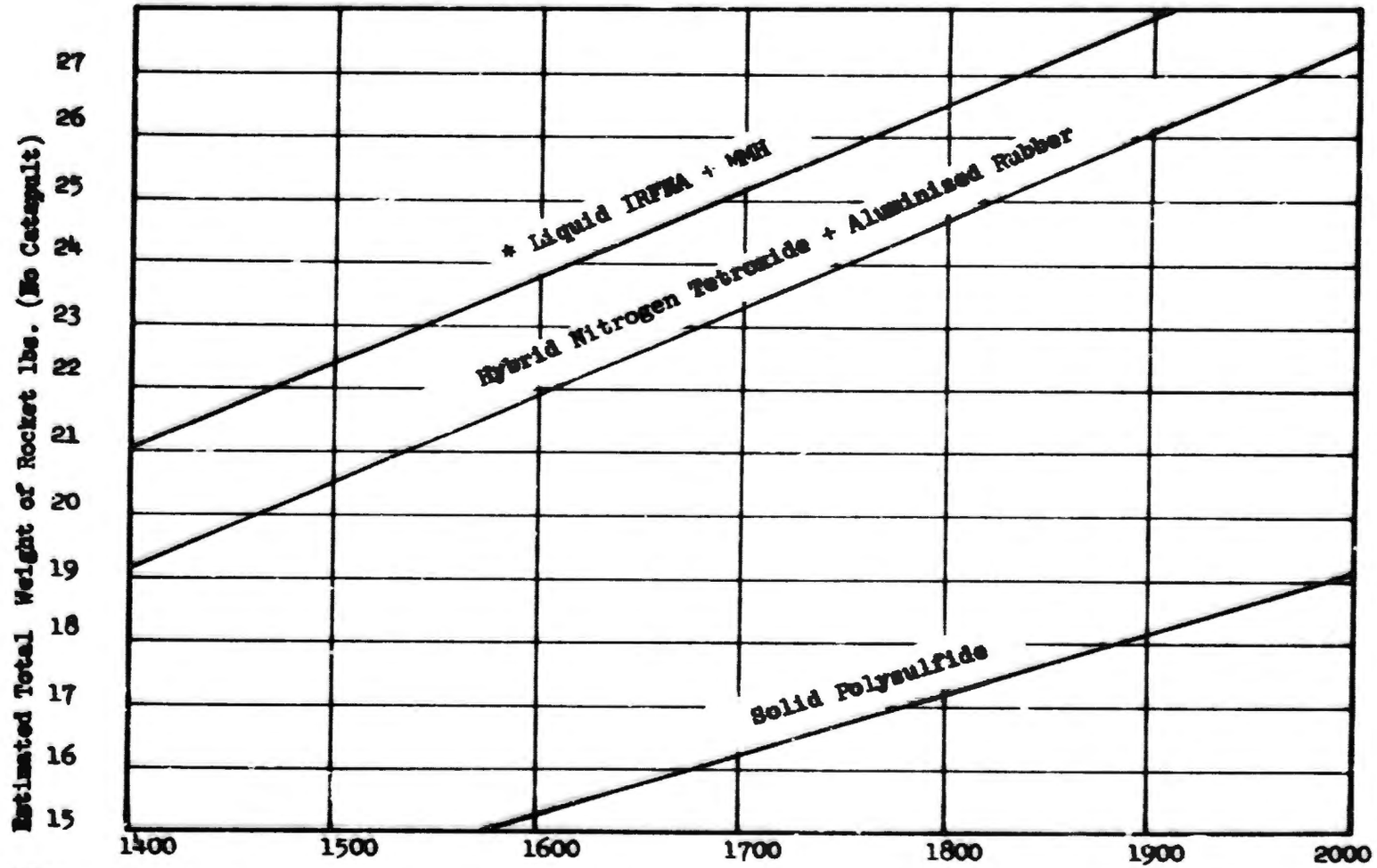

* IRFNA - Inhibited Red Fuming Nitric Acid
MMH - Monomethyl Hydrazine

FIGURE 256 ROCKET WEIGHT VERSUS TOTAL IMPULSE

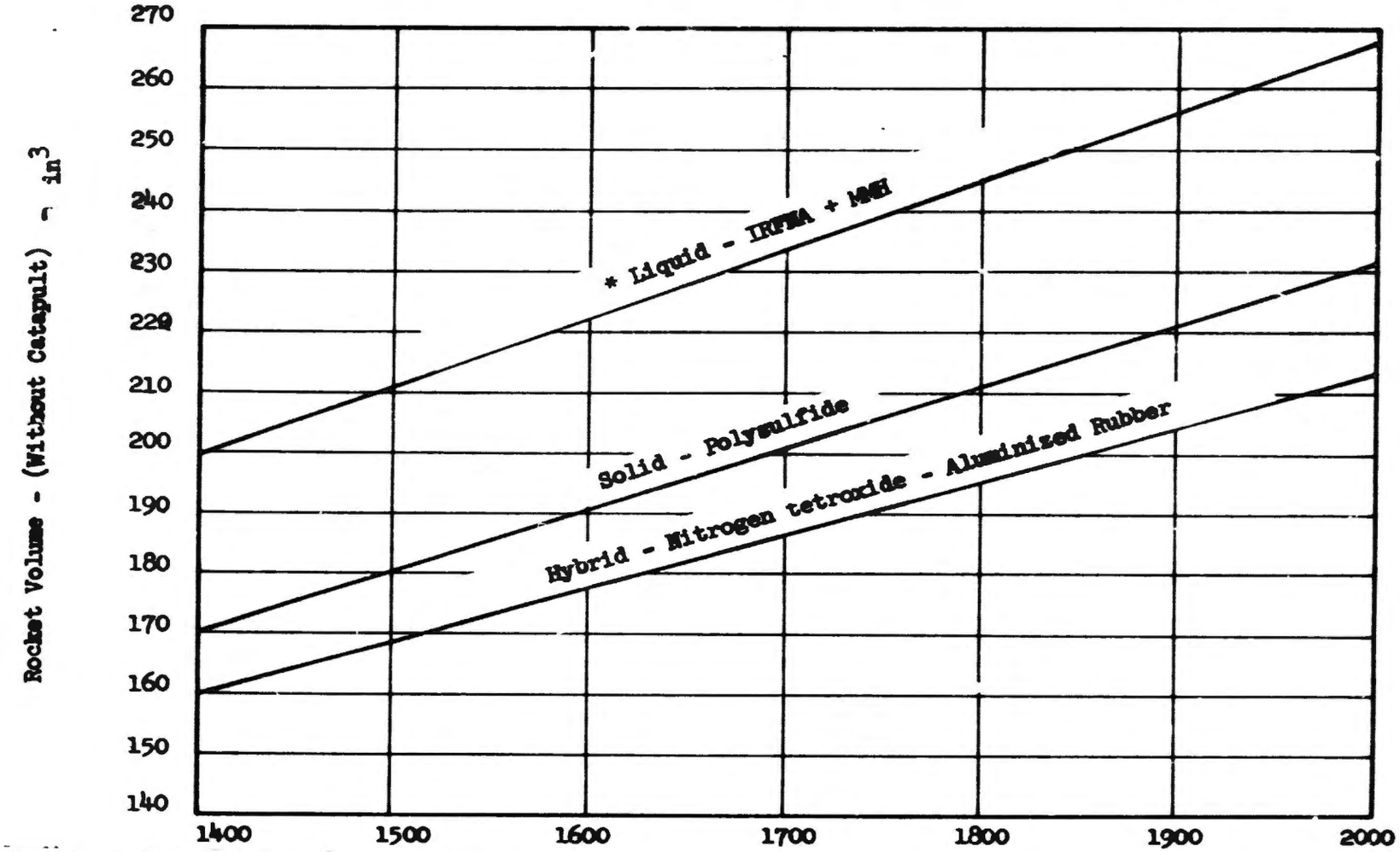

*IRFNA - Inhibited Red Fuming Nitric Acid
MMH - Monomethylhydrazine

FIGURE 257 ROCKET VOLUME VERSUS TOTAL IMPULSE

6. SOLID ROCKET MOTOR PROPULSION TECHNIQUES

The solid rocket propulsion techniques investigated were concerned with providing a simple, safe, reliable, and low volume and weight system. The different escape modes investigated placed different requirements on the propulsion system; therefore, propulsion techniques were investigated for varying the thrust and total impulse as well as up and down capability. Table VII gives a comparison of several propulsion techniques.

a. Rocket Cluster

A technique for providing different thrust levels and total impulse while at the same time giving some steering to the seat involved a cluster of rockets (Figure 258). The cluster would involve two or more rockets on the back of the seat and spaced around a conventional catapult on the centerline. Two or more rockets could be fired to give a given impulse. If steering were needed, two or more could be fired on one side of the centerline with one or more on the other side of the centerline. The mass fraction of the inert parts would be greater for these smaller rockets; therefore, the weight and volume would be greater for a given impulse than single rocket. The reliability would be less because of having to provide signals for several rockets and the lowered probability of the multiple rockets firing. The safety, handling, servicing, and storage would be more complex than a single rocket because of the number of rocket motors involved.

b. Up-Down Capability

An up or down capability appeared to be necessary in some of the escape modes looked at during the early part of the program. A technique for providing an up or down capability was to have a single motor with a nozzle on each end of the rocket. In an inverted position, the catapult would eject the seat, the retro nozzle at the top of the rocket would be opened and the thrust would slow the seat down for parachute deployment (Figures 259 and 260). The nozzle throat for the retro-nozzle would be approximately twice that of the nozzle at the other end. This larger throat nozzle would have less thrust since the permissible acceleration for the man in the "eye balls up" direction is one half that in the normal direction. The burn time would be approximately twice that of the upward case since the burn rate is a function of pressure which in turn is proportional to the throat area. This propulsion technique would, however, give the required performance. The weight and volume would be approximately 10% higher than the single nozzle because of the weight of the additional nozzle at the top end of the rocket case.

The reliability of the two nozzle concept would be the same as the single rocket in the normal ejection mode, but as an overall system, the reliability would be lower because of the complexity of selecting up or down, and then sending a signal to the desired rocket nozzle. The two nozzle concept could be serviced and stored the same as a single nozzle. The safety of the two nozzle concept would be the same as the one nozzle.

c. Dual Rocket, Single Catapult

The use of dual rockets with a single catapult provides an ejection propulsion technique that would give the necessary performance (Figure 261). The catapult would be a conventional catapult with a telescoping sleeve to

TABLE VII

PROPULSION CONCEPT COMPARISONS

	INTEGRAL CATAPULT ROCKET (1)	CLUSTER OF ROCKETS SINGLE CATAPULT (2)	SINGLE CATAPULT & ROCKET UP & DOWN CAPABILITY (3)	SI
Performance	Propellant Formulation tailored to give required performance	Number of rockets needed to give required performance	Propellant formulation tailored to provide required Isp. Nozzle thrust tailored to give required thrust level	P t
Feasibility	Many configurations presently being used. Qualified.	Would require some development testing.	Would require some development testing to tailor the propellant and nozzle.	F
Simplicity of Function	Simplest	Most complex.	More complex than 1 but less than 2.	S
Ignition System Design	a. Spring loaded firing mechanisms b. Gas pressure actuated firing mechanisms c. Electrical firing device	Same as (1)	Same as (1)	S
Method of Ignition	High temperature flame produced by explosive powders and grains	Same as (1)	Same as (1)	S
Time Delay(Ignition to Design Thrust)	0-50 milliseconds. Depending on propellant formulation	Same as (1)	0-50 milliseconds in normal up ejection. 50-100 millisecond for retro nozzle.	S
Reliability Isp. (sec.)	.999 210	Much less than (1) 210	Less than (1) but greater than (2) 210	L g
Storage Temp.	Insensitive	Insensitive	Insensitive	I
No. of Pressure Vessles	1	Three or more	1	3
Storage Life	Long	Long	Long	L
System Wt.	Least	Highest	Low but more than (1)	M b
System Volume	Least	Highest	Low but more than (1)	H b
Thrust Modulation	Fixed	Step changes depending on number of rockets fired	A fixed thrust for up-ejection. A fixed thrust for down-ejection	F
Safety	Safest	Much less than (1)	Safe but less than (1)	S
Servicing & Handling	Easiest	Complex. Numerous rockets to service	Easy, but additional problems with extra nozzle	E s c

A

(Page 120 is blank)

LE VII

NCEPT COMPARISONS

TAPULT & ROCKET N CAPABILITY(3)	DUAL ROCKET SINGLE CATAPULT (4)	DUAL CATAPULT SINGLE ROCKET (5)	TWIN CHAMBERS - ONE NOZZLE ONE CATAPULT (6)
nt formulation to provide Isp. Nozzle ailored to give thrust level	Propellant formulation tailored to performance	Same as (1)	Same as (1)
quire some ent testing to he propellant le.	Feasible	Feasible	Feasible
plex than 1 but n 2.	Simple	Simple	Simple
(1)	Same as (1)	Same as (1)	Same as (1)
(1)	Same as (1)	Same as (1)	Same as (1)
liseconds in p ejection. illisecond for zzle.	Same as (1)	Same as (1)	0-75 millisecond
n (1) but than (2) 210	Less than (1) but greater than (2) 210	Less than (1) but greater than (2) 210	High but less than (1) 210
ive	Insensitive	Insensitive	Insensitive
	3	3	3
	Long	Long	Long
more than (1)	More than (1) and (3) but less than (2)	More than (1) and (3) but less than (4)	More than (1) but less than (2), (4), & (5)
more than (1)	Higher than (1) or (3) but less than (2)	Higher than (1), (3), & (4) but less than (2)	More than (1) but less than (2), (4), & (5)
thrust for up- . A fixed or down-ejection	Fixed	Fixed	Fixed
less than (1)	Safe	Safe	Safe
t additional with extra	Easy, additional & separate rocket complicates procedures.	Same as (4)	Complicated by twin chambers on bottom of seat

B

BLANK PAGE

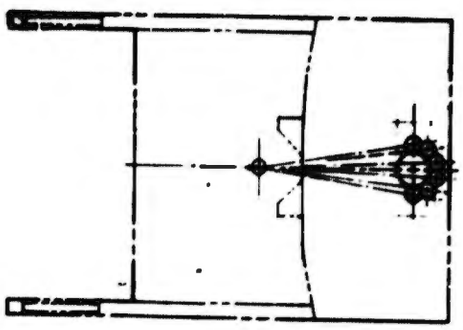

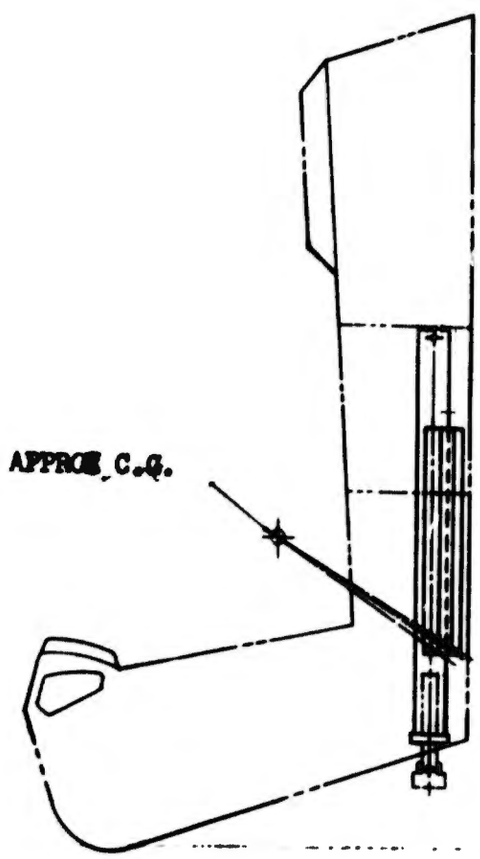

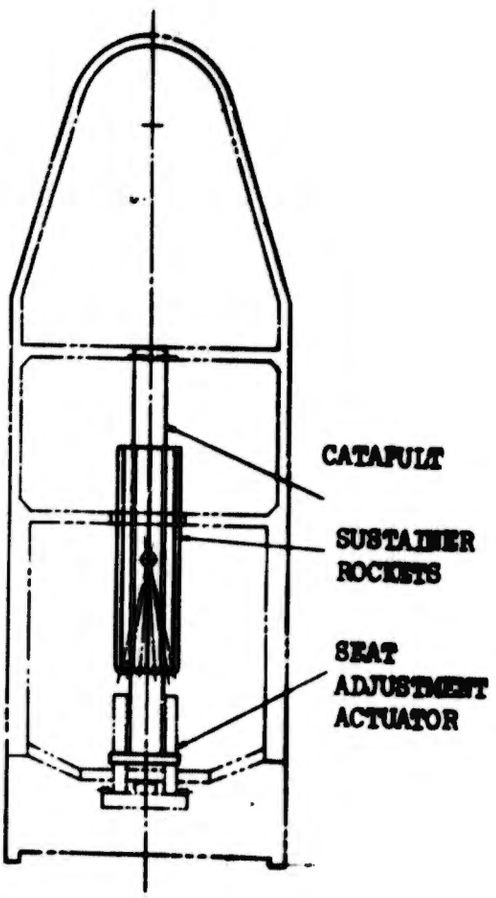

FIGURE 258 ROCKET CLUSTER

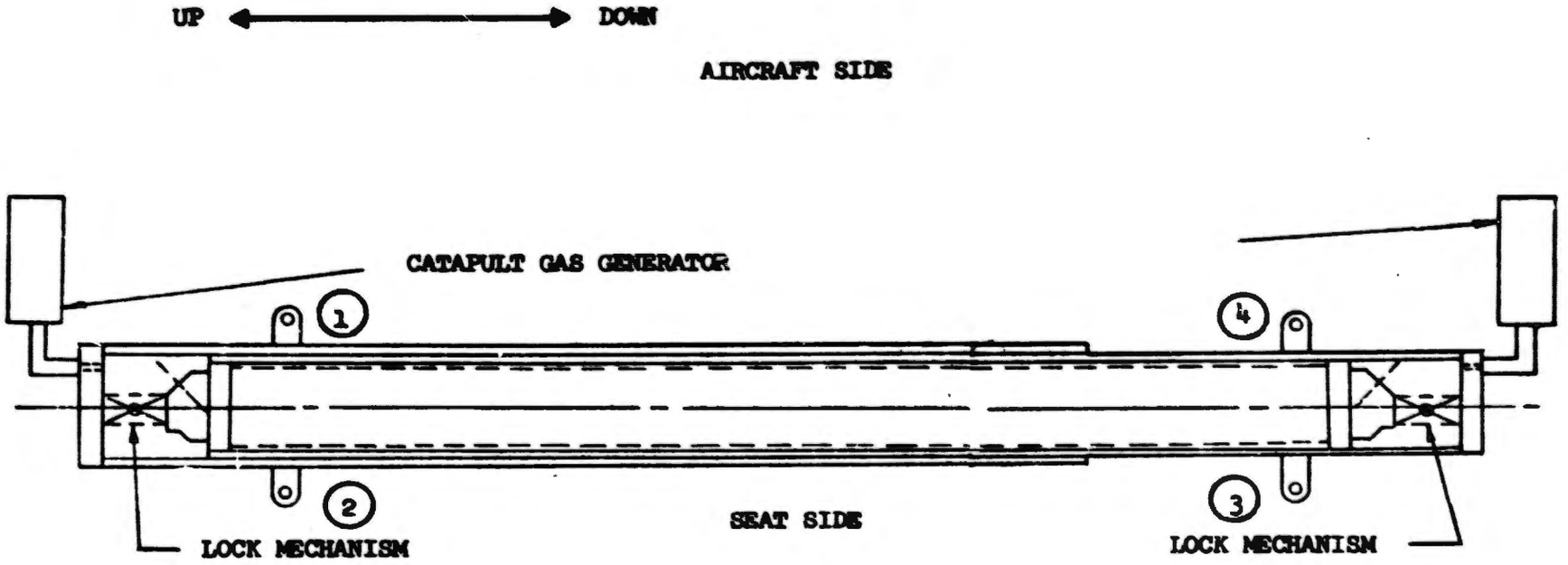

FIGURE 25 ROCKET CATAPULT FOR UP AND DOWN EJECTIONS

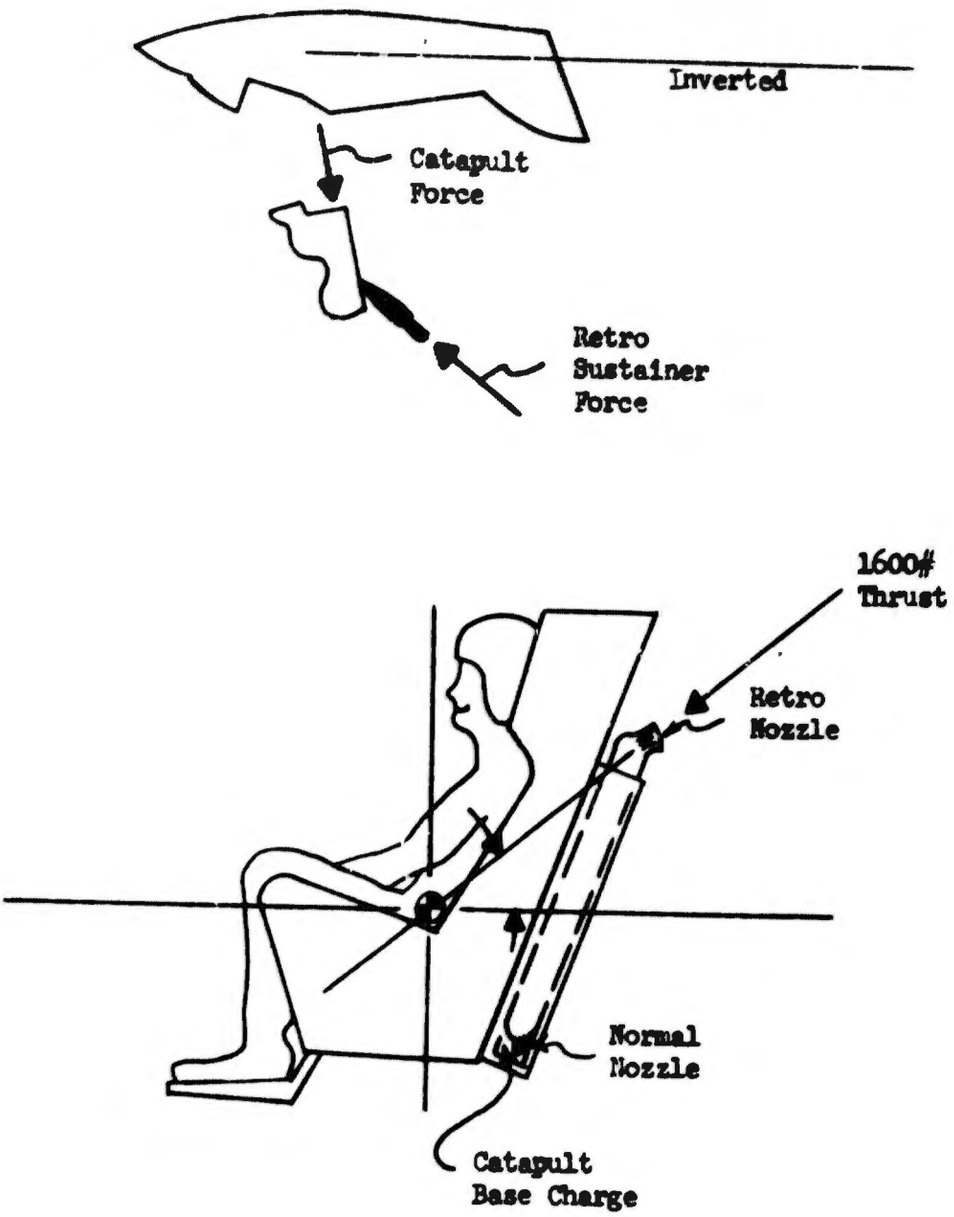

FIGURE 260 UP-DOWN ROCKET

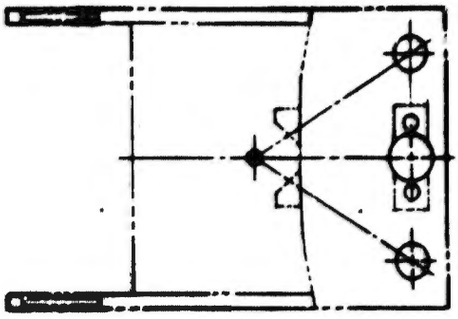

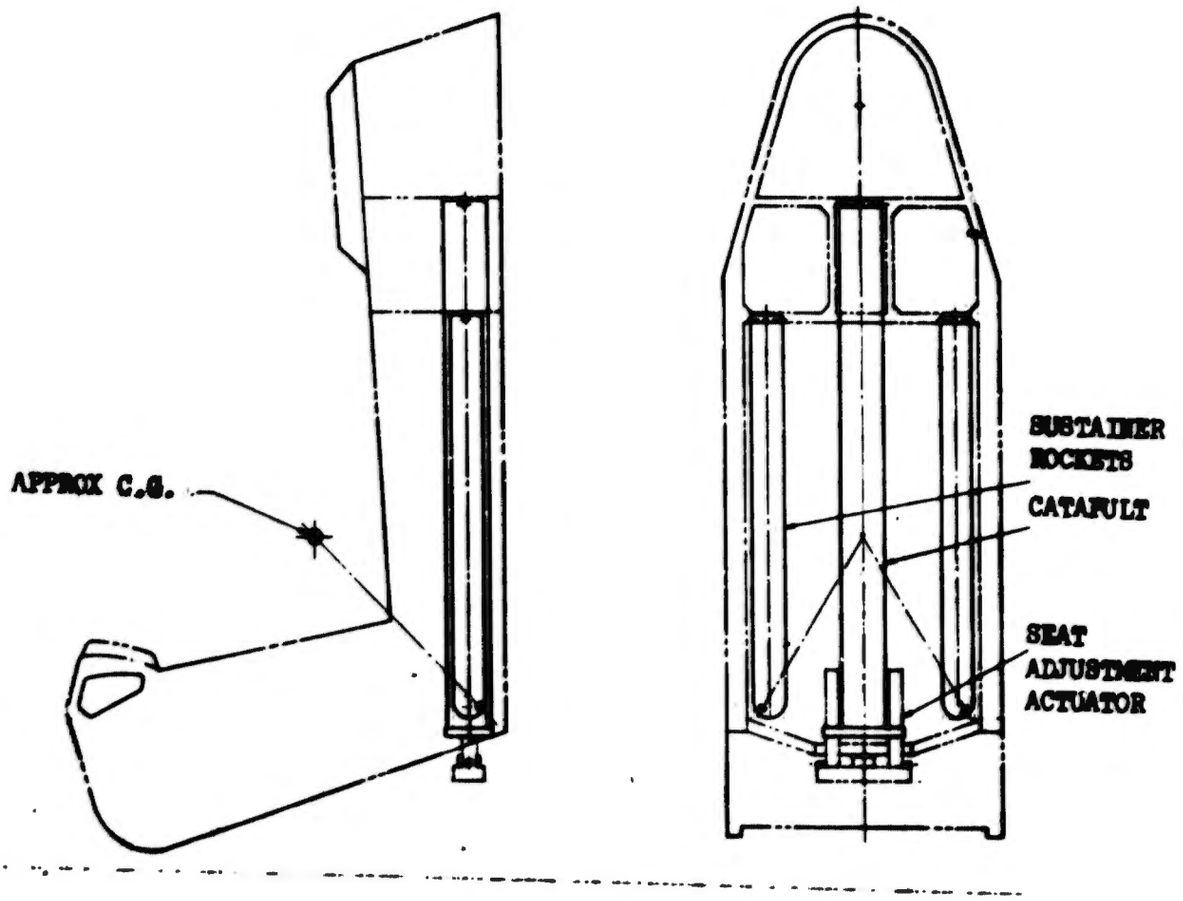

FIGURE 261 DUAL ROCKETS - SINGLE CATAPULT

give the required stroke distance of 36 inches. The use of two rockets would permit using shorter overall rockets since each would have only one half of the total propellant volume; however, because two rockets would be used, the inert parts of the two rockets combined would weight approximately 15% more than a single rocket. The overall volume of the two rockets and the catapult would be about 1.9 times that of the single rocket. The reliability of the twin rocket concept would be less because two rocket motors would have to receive a signal instead of one. The seat would receive a translation force if one rocket fired at a different time or generated a different amount of thrust. The twin rocket is not as simple as the single rocket but is a feasible concept. The servicing and storage problem of the two rockets would be almost doubled that of a single rocket. The twin rockets could have a retro rocket at the top as described under the previous concept, however, this would have the effect of increasing the volume and weight, while decreasing the reliability.

d. Single Rocket, Dual Catapult

A single rocket concept was investigated which would have two catapults (Figure 262). The use of two catapults decreases the diameter of the cases, but the total stroke length remains the same because of the"g" limitation imposed on the man. Therefore, the two catapults would weigh more than the one catapult design. The total volume on the back of the seat would be greater by a factor of approximately 1.7. The reliability would be less for the two catapult design because two "fire" signals would have to be sent and two initiators and two motor grains would have to be ignited. The servicing and storage problem would be complicated by having the catapults separate from the rocket. There would also be two catapults for each rocket instead of being an integral part of the rocket. The two catapults would have to be initiated at the same time and have very similar pressures-time curves in order not to impart a torque to the seat which would place a binding force on the rollers. A central cartridge chamber vented to both catapults would solve this problem.

e. Single Rocket, Single Catapult

An arrangement of catapult and sustainer motor as shown in Figure 263 was considered to provide a capability to orient the thrust vector vertically through the center of gravity. The weight of the total system would be approximately 15% greater than that of the integral catapult rocket. The catapult for this concept would have to be on the back of the seat and have the 90% of the volume of the integral catapult rocket. The weight would also be greater because of the separate propellant chambers. The mass fraction of the inert parts would be greater because of the smaller amount of propellants. The reliability could be less because a signal would have to be sent to each of the propellant chambers. The two chambers are interconnected, and if one chamber fails to "fire" from the signal, the hot gases from the other chamber would provide sufficient energy to ignite the second one; however, this would result in a delay to full thrust. The safety and storage of the rocket and catapult would not impose any additional problems over the single rocket-catapult, other than that there would be two separate units for each seat instead of one.

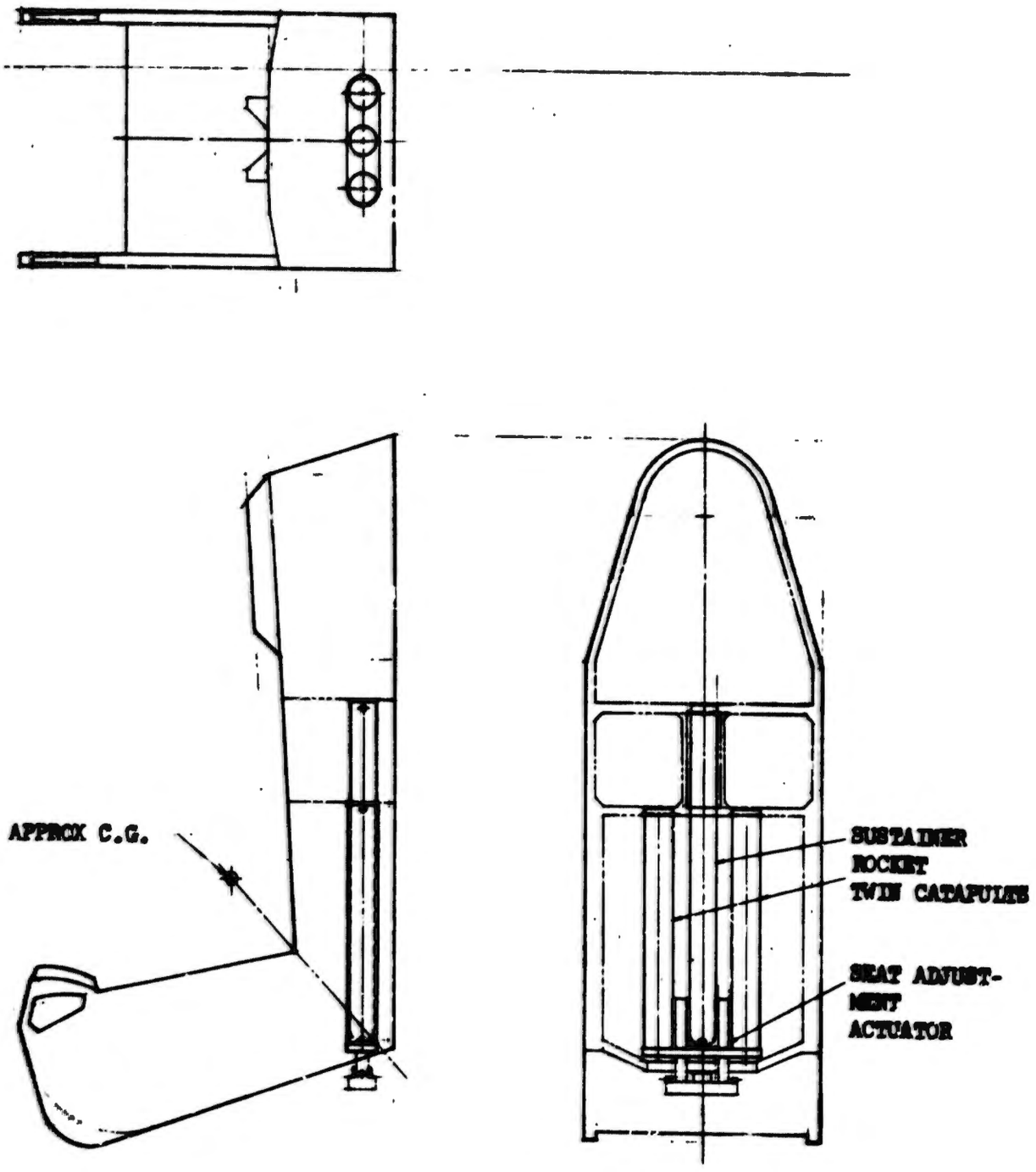

FIGURE 262 SINGLE ROCKET - TWIN CATAPULTS

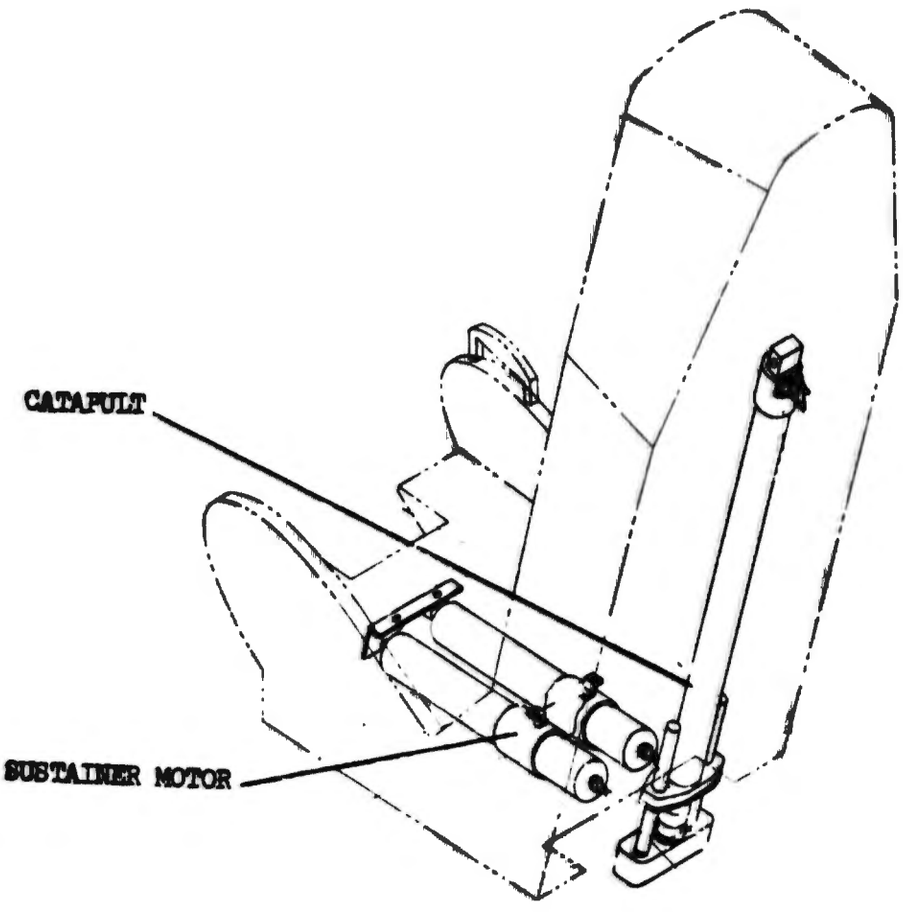

FIGURE 263 SINGLE ROCKET - SINGLE CATAPULT

f. Tractor Rocket

The tractor rockets provide an ejection seat propuslion technique that could provide the required performance. The tractor rocket is "fired" out of the cockpit by a catapult. A line is attached to the rocket that ignites the rocket at line stretch. The man/seat is then pulled up the rails and clear of the aircraft. An attitude control system is incorporated in the rocket that seeks the vertical in the upside-down mode. This concept would have a larger weight and volume than the integral catapult because of the attitude control system, and it would also be more complex and less reliable. The storage and handling would also be more involved.

g. Integral Rocket-Catapult

The integral rocket-catapult is a simple, reliable and proven propulsion system (Figure 255). This system could provide variable thrust and total impulse if the escape method dictated such a capability. However, the increased complexity would decrease the reliability. The integral catapult and rocket requires less volume than the other concepts examined. The catapult has a piston which acts through a distance (stroke) to give the man/seat the needed velocity. Since the rocket can occupy the space inside the catapult cylinder, the overall propulsion system volume is reduced. The mounting provision for the integral catapult and rocket gives a lower weight than the mounting for the dual rockets and catapults. In addition, this concept would require only one signal to the catapult and if ignition of the rocket was delayed only one additional signal would be needed. The simplicity of only one catapult integral with one rocket would result in a higher reliability. The storage, handling and maintenance of this compact propulsion system would be simpler because of the fewer number of propulsion devices involved. The conclusion is made that the integral rocket catapult is the most suitable seat ejection propulsion technique investigated.

7. EFFECTS OF PROPULSION CONFIGURATION ON SYSTEM PERFORMANCE

Six different propulsion configurations were evaluated to determine their respective effects on system performance. The configurations considered were:

No.	Configuration
1	Separate single catapult and sustainer rocket
2	Conventional rocket catapult
3	Single tractor rocket
4	Separate rocket catapult with single retro rocket
5	Separate rocket catapult with special dual energy catapult

6. Up-down system consisting of separate rocket catapult stages tailored to the respective ejection directions

Configuration 1, as initially evaluated, consisted of a conventional 50 fps and velocity upward ejecting catapult and a seat-bucket-mounted 1700 lb/sec sustainer rocket thrusting vertically through the system center of gravity. Figure 264 illustrates this configuration.

Figure 265 is the plot of a computer-calculated trajectory of this configuration with all aircraft conditions being zero except for a 50°/sec pitch down condition. In the system analyzed here, the parachute is forcibly projected aft from the seat. This plot illustrates how the 17° rearward ejection angle combined with the vertical thrust vector results in a rearward seat trajectory. Hence, the seat moves toward the projected parachute causing the parachute riser lines to go slack, resulting nn additional altitude required for recovery.

Configuration 2 was evaluated with a 1700 lb/sec sustainer thrusting forward and upward at 50 degrees above horizontal. Figure 266 illustrates this configuration. Ejection under the same conditions as Configuration 1 resulted in a forward trajectory which aids in achieving rapid and repeatable line stretch and canopy inflation. Figure 267 illustrates this trajectory.

Configurations 1 and 2 were subjected to further evaluation to determine if either had any advantages over the other under 600 KEAS ejection conditions. The vertical thrust sustainer obviously provides a higher trajectory as can be seen by comparing Figures 268 and 269. The "eyeballs-out" acceleration of the system center of gravity is likewise greater for the vertical thrust configuration. However, the peak acceleration achieved in either case with a 36 inch diameter drogue chute is within the recognized limits for the human body. Figures 270 and 271 illustrate the acceleration time histories of these two configurations. A variation of Configuration 2 is discussed later when inverted performance is considered.

The effect of propulsion on inverted ejection was investigated. Table VIII summarizes the results giving the recovery height for each configuration considered.

Configuration 3 consists of a 1700 lb/sec steerable tractor rocket and no catapult. The rocket is attached to the seat by a flexible pendant and is launched above the seat. Line stretch forces ignite the rocket. After tip-off, during an inverted ejection, the rocket is steered to rotate about the roll axis in an attempt to correct the vertical component of the seat trajectory from a downward to an upward direction. Motor rotational rates of 180 degrees/second and 360 degrees/second were analyzed with the motor rotating at the given rate until burnout. Recovery heights for these conditions were respectively 122 and 18 feet below the ejection altitude. Figures 272 and 273 illustrate these trajectories.

TABLE VIII

INVERTED EJECTION PROPULSION SUMMARY

INVERTED EJECTION PROPULSION CONFIGURATION	RECOVERY ALTITUDE - FEET (+) INDICATES RECOVERY ABOVE EJECTION ALTITUDE, (-) BELOW
Steerable Tractor Rocket	
180°/sec Rotation Rate	-122
360°/sec Rotation Rate	- 18
Conventional Rocket Catapult	-146
w/o Sustainer	- 96
Conventional Rocket Catapult w/retro rocket, 1600 lb.	- 90
3200 lb.	- 75
Conventional Rocket with 25 fps Catapult	- 77
Up-Down System	+ 12

An advantage of this type of propulsion system is its inherent stability with regard to center of gravity thrust line induced instabilities. A disadvantage is the fact that the seat remains in the aircraft approximately 0.1 second longer while the rocket is traveling out to the required line stretch point (rocket ignition). Figure 274 illustrates this configuration.

Figures 275 and 276 are computer plots of head accelerations induced under inverted ejection conditions using the tractor rocket rotated at 360 deg/sec. The high lateral acceleration is the result of the seat "whipping" at the end of the tractor rocket pendant.

A variation of Configuration 2 was considered. Under inverted ejection conditions, it was proposed that the sustainer not be fired. The resultant trajectory, shown in Figure 277, shows recovery 96 feet below the ejection altitude. For comparison purposes, the inverted performance of the same system with the sustainer fired is illustrated in Figure 278. Recovery was achieved at 146 feet below the ejection altitude.

Configuration 4 consists of a conventional 50 fps upward ejecting catapult and 1700 lb/sec sustainer. In addition, a retro-rocket with a downward and forward directed thrust vector (40 degrees below horizontal) is provided. If the retro-rocket is fired instead of the sustainer and it has 1600 lbs thrust for 0.25 sec., recovery can be achieved at 90 feet below the ejection altitude. Figure 279 is a plot of the resultant trajectory. If the retro rocket thrust is increased to 3200 lbs., recovery can be achieved 75 feet below ejection altitude as illustrated in Figure 280. Figure 281 shows the retro-rocket configuration.

Configuration 5 is similar to Configuration 4 except that the retro-rocket is deleted and the conventional catapult is replaced with a dual energy catapult which can provide either a 25 fps or a 50 fps end velocity. In the inverted case, the sustainer is withheld and only the 25 fps catapult is ignited. Figure 282 shows recovery at 77 feet below ejection altitude. Figure 283 illustrates the system configuration.

Another configuration investigated consists of two separate propulsion systems, one tailored for the upward ejection and one tailored to the downward (relative to the aircraft) ejection. In this configuration, an inverted ejection would actually be upward through the floor of the aircraft. The sustainer thrust vector is 40 degrees off the horizontal, and the motor has 400 lb/sec of impulse. The catapult imparts an end velocity to the seat of 25 fps. With this configuration, Figure 284 shows recovery 12 feet above the ejection altitude. Figure 285 shows this configuration.

It is concluded from this study of the effect of propulsion system configuration on performance and trajectory that:

- Vertical orientation of the sustainer motor thrust vector results in more altitude required for safe escape because the rearward velocity component of the catapult causes a longer period of slack parachute risers.

- Withholding sustainer motor ignition after ejection from an inverted altitude results in substantially less altitude required for safe recovery.

- The "dead-beat" altitude control system which rotates the seat/man at 360 degrees per second imparts unacceptable high lateral accelerations to the head. Rotational rates lower than 360 degrees per second do not result in significantly improved performance.

- The Up-Down system gives the best performance of the configurations investigated when ejection occurs from the 180° roll attitude.

8. INFLUENCE OF THRUST VECTOR STABILITY, ACCURACY, AND REPEATABILITY

A major cause of ejection seat instability during sustainer burn is the eccentricity between the thrust vector and the dynamic center of gravity of the system. The larger this eccentricity, the higher the rates of rotation achieved by the seat. These rotational rates decrease trajectory height and affect recovery capability. Hence, it is desirable to eliminate or reduce them to an acceptable level. To do this requires a thorough knowledge of what causes the eccentricities. A large factor, of course, is the variation in system center of gravity due to the variation in the center of gravity of the human body. References 19 and 20 indicate that the most eccentricity to be expected due to this factor is in the neighborhood of 2.0 inches. Another factor is the variation in sustainer thrust angle. The following discussion pertains to this factor.

The eccentricity between the system dynamic center of gravity and the sustainer thrust line due to variations in the thrust angle is a function of the tangent of the angle between the designed thrust line and the actual thrust line as illustrated in Figure 286. Thus, the change in eccentricity due to thrust angle variation is a function of both the distance of the center of gravity from the nozzle and the angle of variation. An increase in either will increase the change in eccentricity for a given center of gravity.

Stabilization devices are available to overcome the adverse effects of the human body induced eccentricities. The same devices can correct for thrust angle variations provided the resultant eccentricities are not too large; i.e., at least one degree less magnitude than the human body induced eccentricities and preferably smaller. In other words, within reasonable limits, a stabilization system can be designed to accommodate the effects of variations in thrust angle.

The repeatability of the thrust angle is a function of the stability of the angle during rocket burn, and the accuracy with which the nozzle is manufactured. Stability, in turn, is a function of nozzle erosion and distortion. Accuracy depends upon the tolerances involved in machining the nozzle.

In order to design a stabilization system which will accommodate the total eccentricity to be encountered, the repeatability of the nozzle angle must be known. Reference 21 reports the results of a test program which was conducted to confirm the repeatability of the nozzle angle of the Rocket Power Incorporated P/N 2174-520 rocket catapult. In this test, six rocket motors were fired in a precision 3-axis test fixture. The mechanical nozzle angle in the pitch plane of each rocket was within the prescribed $53^{\circ} \pm 0^{\circ}$ 15' prior to firing. The angles measured during firing measured from 53° + 15' to 53° + 37'. Thus, the maximum variation could have been + 0 52'. The results of this test series are tabulated in Table IX.

9. MOUNTING AND INSTALLATION REQUIREMENTS FOR PROPULSION SYSTEMS

The mounting and installation requirements for the escape system propulsion units are dependent upon many factors. Some of these factors are:

a. Seat configuration - one-piece vs two-piece

b. Volume and form factor available for propulsion

c. Center of gravity envelope

The seat structural arrangement has the most influence on propulsion mounting and installation. The two basic seat configurations are:

a. Two-piece, fixed headrest, adjustable bucket

b. One-piece, integral headrest and bucket

The two-piece seat configuration places special requirements on the propulsion system installation. The need to maintain the sustainer thrust line passing through the system center of gravity necessitates that the sustainer be attached to the adjustable bucket since the system center of gravity tends to move with the bucket. On the other hand, the catapult need not be attached directly to the bucket, and may be attached to the seat headrest. Thus, the two-piece seat justifies separate catapult and sustainer packages.

The one-piece seat is adaptable to all propulsion configurations. The center of gravity of the system moves with the seat so the sustainer rocket can be attached to the seat structure. The catapult can likewise be attached to the entire seat. Hence, the one-piece seat is adaptable to either the single unit rocket catapult in common use today or to the separate sustainer and catapult components.

One configuration in common use today is the one-piece seat combined with the single unit rocket catapult mounted to the airframe and attached to the seat by the screwjack seat adjustment actuator. This means that the nozzle position and angle are fixed and that the system center of gravity moves perpendicular to the thrust line approximately five inches. This results in a less than optimum center of gravity thrust line relationship under the conditions where the seat is adjusted to its extremes of vertical travel.

TABLE IX - NOZZLE ANGLE REPEATABILITY DATA

FIRING NUMBER	ROCKET MOTOR PERFORMANCE													
	IGNITION TIME (SEC)	BURNOUT TIME (SEC)	ACTION TIME (SEC)	MAX. PRESSURE (PSIA)	Pdt. (PSIA. SEC)	MAX. LONGITUDINAL THRUST (LB)	MAX. NORMAL THRUST (LB)	MAX RESULTANT THRUST (LB)	RESULTANT THRUST AT BURNOUT (LB)	TOTAL IMPULSE (LB.SEC)	* IMPULSE ANGLE (DEGREE)	SPECIFIC IMPULSE (LB.SEC/LB)	AVERAGE PRESSURE (PSIA)	AVERAGE RESULTANT THRUST (LB)
1	.007	.398	.536	4440	1946	4505	55	4505	4360	1961	+0°15'	200	3630	3660
2	.005	.400	.517	4510	1905	4560	65	4560	4305	1959	+0°26'	202	3685	3790
3	.005	.389	.515	4740	1893	4990	50	4990	4680	2103	+0°28'	213	3675	4085
4	.005	.437	.570	4395	1912	4095	55	4095	3910	1956	+0°23'	204	3480	3430
5	.005	.426	.558	4670	2010	4305	55	4305	3930	1973	+0°26'	201	3600	3535
6	.005	.425	.548	4610	1946	4470	80	4470	3930	2003	+0°37'	201	3550	3655

Note This data obtained from Reference (3)

** This angle is the actual deviation from the nozzle's mechanical angle of 53°

Another consideration governing propulsion mounting and installation is the volume and form factor of the various propulsion configurations. The need to provide high exit velocity of the seat from the cockpit within the physical tolerances of the human body has prescribed the form factor of the catapult. Variations, including telescoping, have altered the form factor very little; the catapult still remains basically a long cylindrical tube. Hence, the seat backrest area is the universal mounting area since it is the only area in the seat which can provide for the long installed length of the catapult.

In contrast to the catapult, the sustainer motor (if a separate unit from the catapult) can adopt almost any shape including complex, if necessary. Consequently, the sustainer motor can be mounted in the backrest area along the seat centerline, in the backrest area outboard of the seat centerline, underneath the seat bucket, or a combination of these. Hence, the sustainer motor can more readily be configured to match the volume and form factor available rather than requiring configuration of the seat around the sustainer.

The ejected center of gravity of the system has overriding influence on mounting and installation requirements for the propulsion system. The sustainer thrust vector must pass through or very close to the c.g. in order to assure repeatable performance; however, the c.g. location is variable as a function of the individual crewman. An approximate correlation exists between the crewman's selected seat position and the system c.g. Hence, provided the sustainer is separate from the catapult, the sustainer can be flexibly mounted so that seat position changes nozzle angle. As an alternate, the flexible mount could be dedigned so that the individual crewman can manually select a nozzle angle in accordance with his weight, sitting height percentile, etc.

It is concluded from this study of seat propulsion systems mounting and installation requirements that:

- The two-piece type seat (adjustable bucket, fixed headrest) will benefit performance-wise from a propulsion system configuration which allows the sustainer motor thrust vector to move with the pilot adjustable seat bucket.

- The optimum propulsion system for the single piece seat (integral bucket and headrest) allows the sustainer motor to move with the seat as it is adjusted to the flight eye position.

The above conclusions are based on the overriding propulsion system installation requirement to minimize the eccentricity between the ejected mass and the thrust vector.

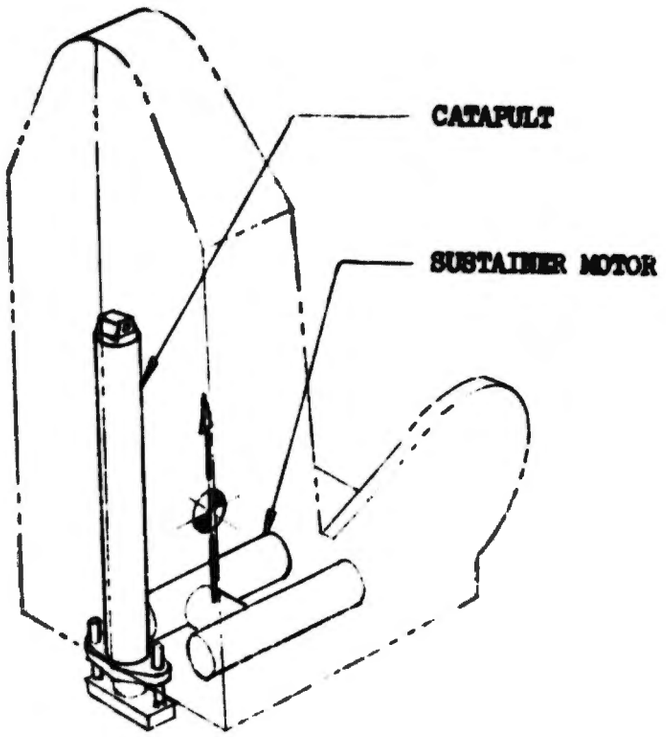

FIGURE 264 SEPARATE SINGLE CATAPULT AND SUSTAINER ROCKET PROPULSION CONFIGURATION

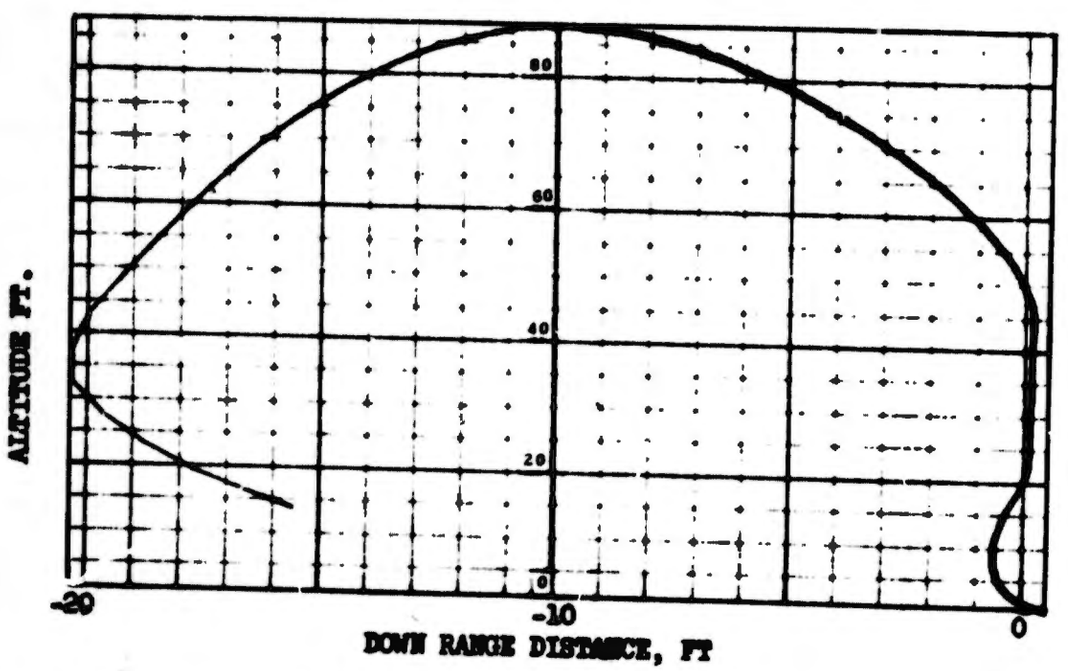

FIGURE 265 VERTICAL THRUST SUSTAINER - SEAT TRAJECTORY AT ZERO SPEED

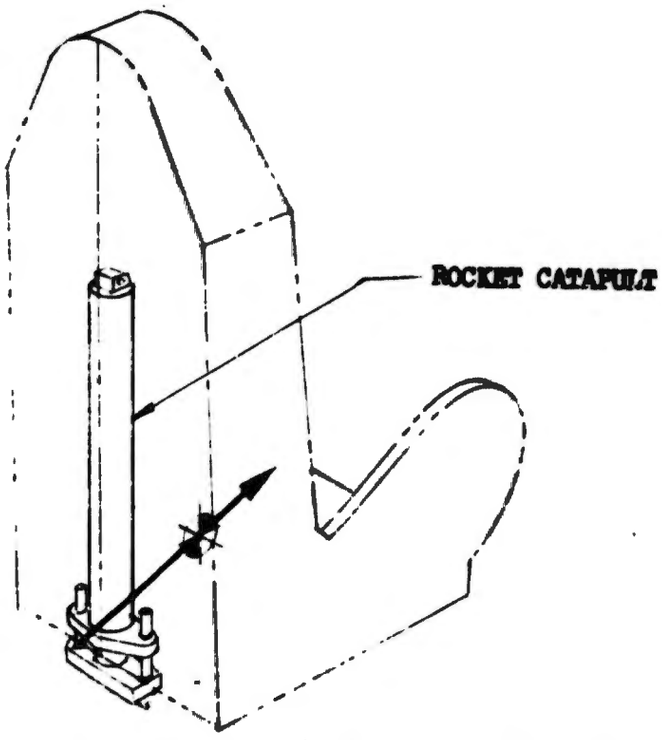

FIGURE 266 CONVENTIONAL ROCKET CATAPULT PROPULSION CONFIGURATION

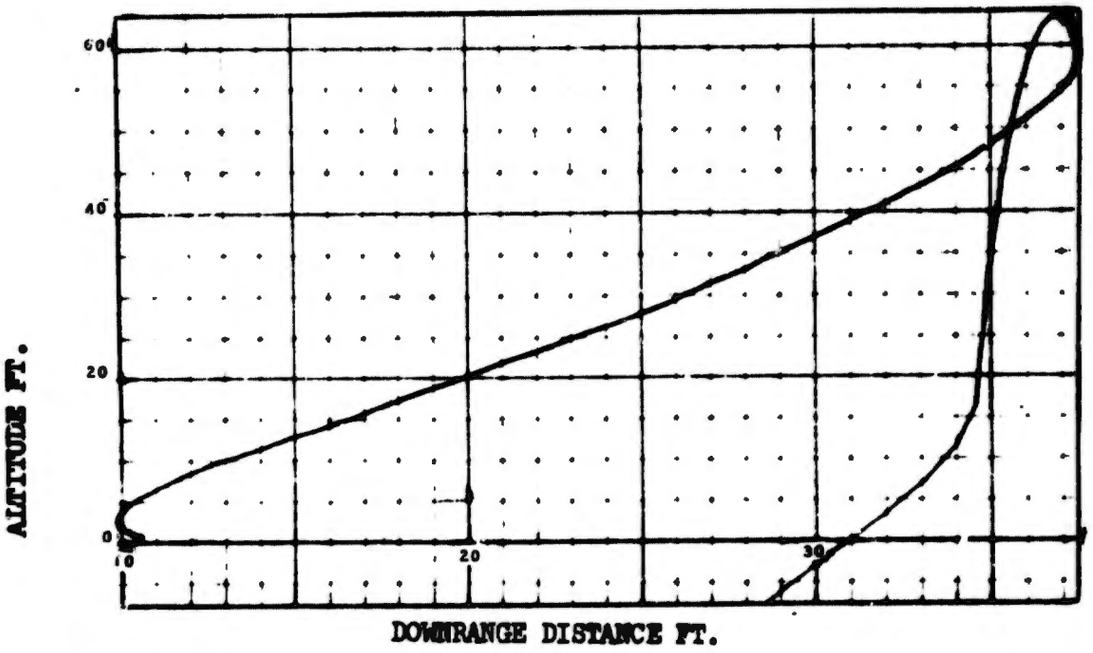

FIGURE 267 SUSTAINER WITH FWD THRUST COMPONENT-SEAT TRAJECTORY AT ZERO SPEED

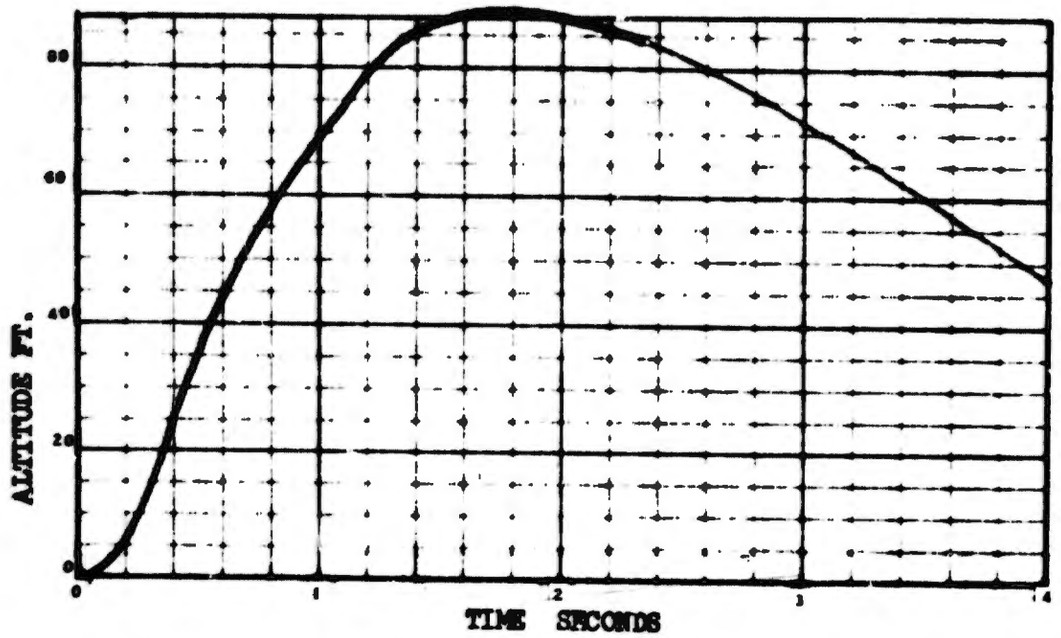

FIGURE 268 VERTICAL THRUST SUSTAINER - SEAT TRAJECTORY, 600 KEAS

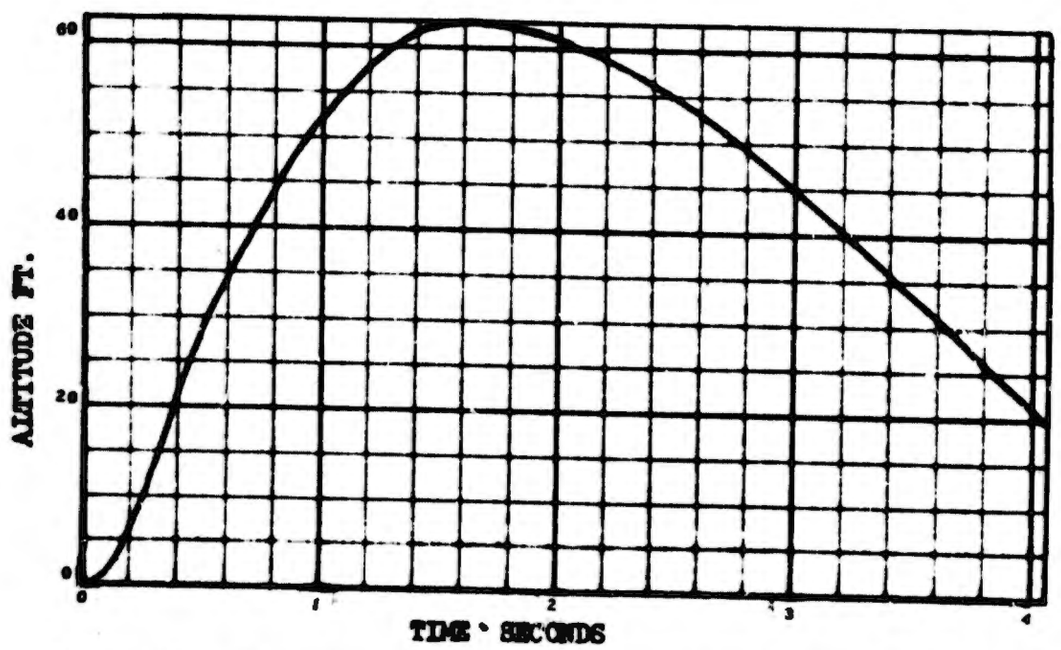

FIGURE 269 SUSTAINER WITH FWD THRUST COMPONENT - SEAT TRAJECTORY, 600 KEAS

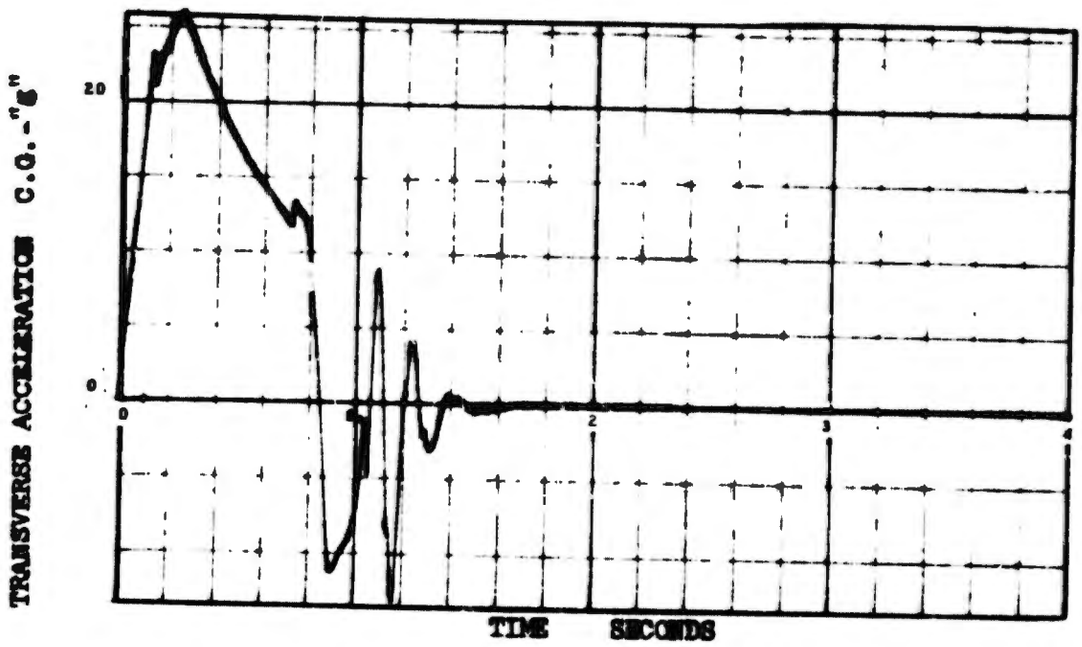

FIGURE 270 VERTICAL THRUST SUSTAINER - EYEBALLS OUT ACCEL., 600 KEAS

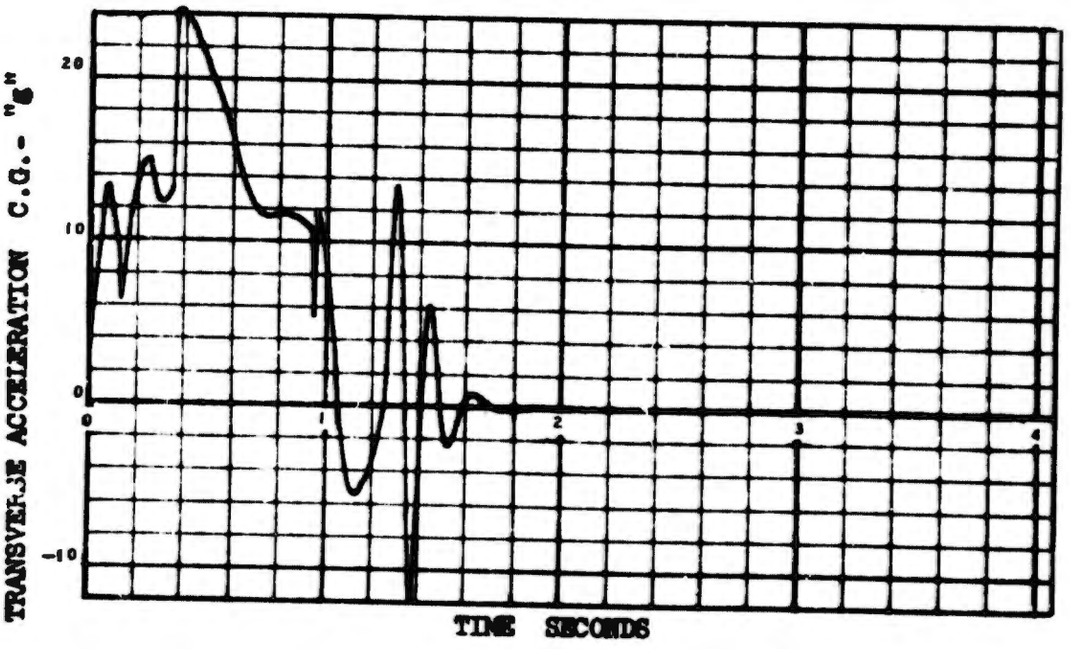

FIGURE 271 SUSTAINER WITH FWD THRUST COMPONENT - SEAT TRAJECTORY, 600 KEAS

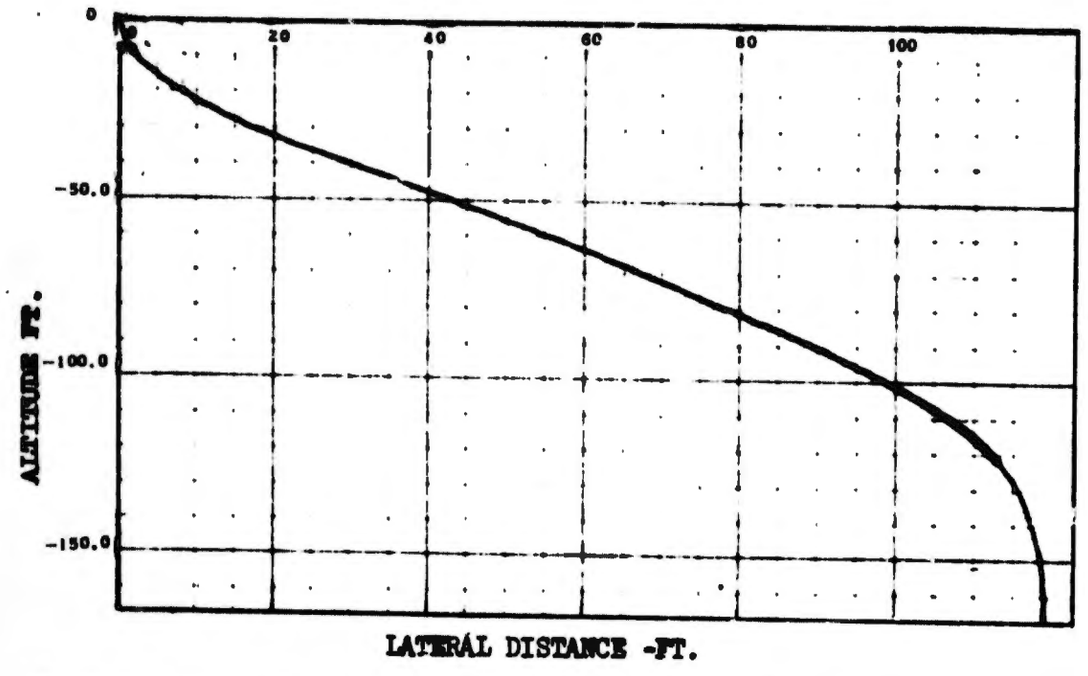

FIGURE 272 STEERABLE TRACTOR ROCKET ROTATED AT 180 DEG/SEC - SEAT TRAJECTORY AT ZERO SPEED, INVERTED

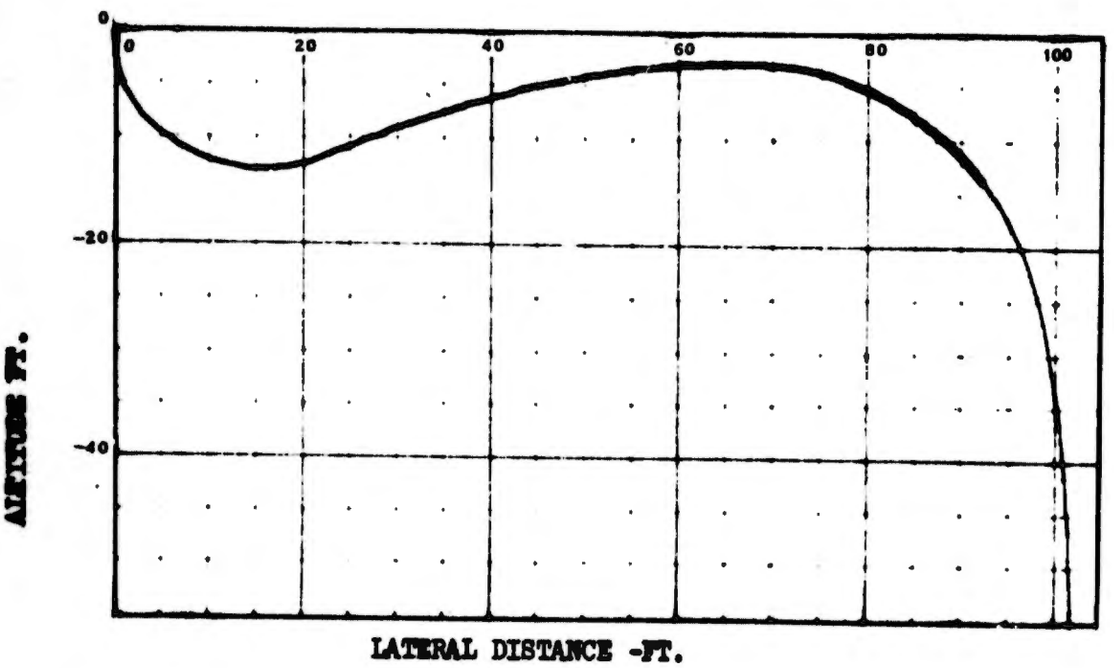

FIGURE 273 STEERABLE TRACTOR ROCKET ROTATED AT 360 DEG/SEC - SEAT TRAJECTORY AT ZERO SPEED , INVERTED

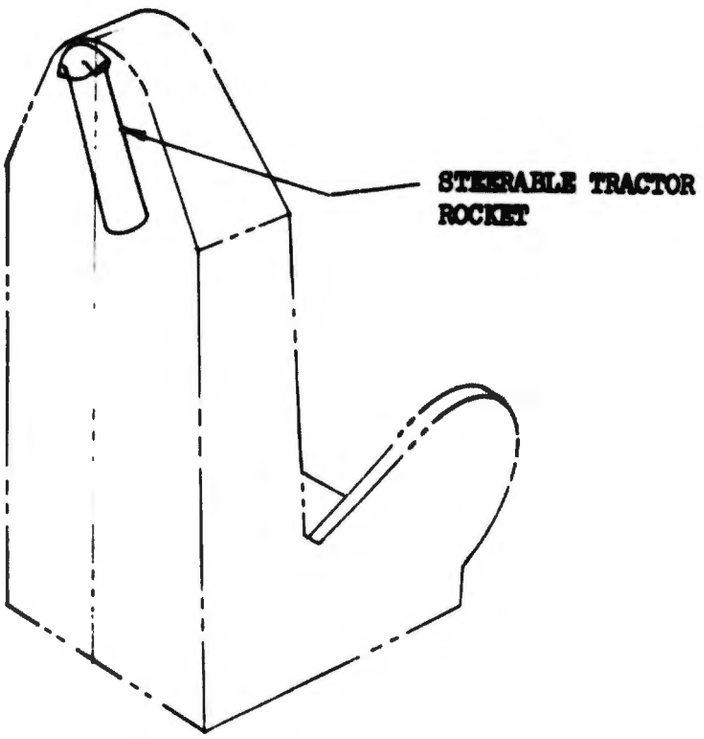

FIGURE 274 STEERABLE TRACTOR ROCKET PROPULSION CONFIGURATION

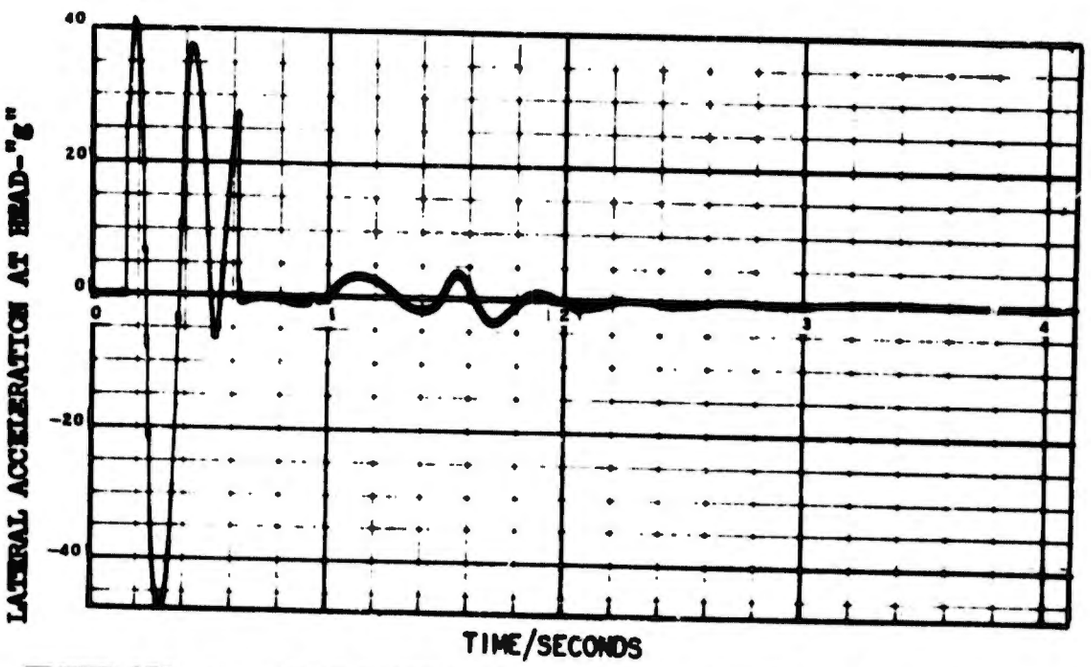

FIGURE 275 STEERABLE TRACTOR ROCKET ROTATED AT 360 DEG/SEC - HEAD ACCELERATION AT ZERO SPEED, INVERTED

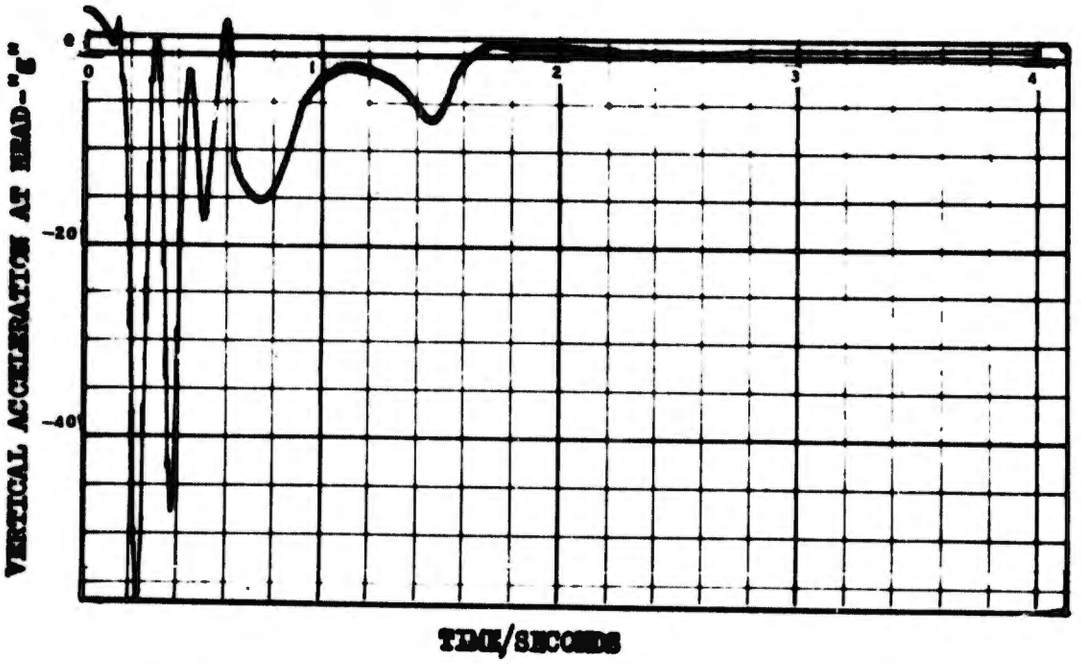

FIGURE 276 STEERABLE TRACTOR ROCKET ROTATED AT 36 DEG/SEC - HEAD ACCELERATION AT ZERO SPEED, INVERTED

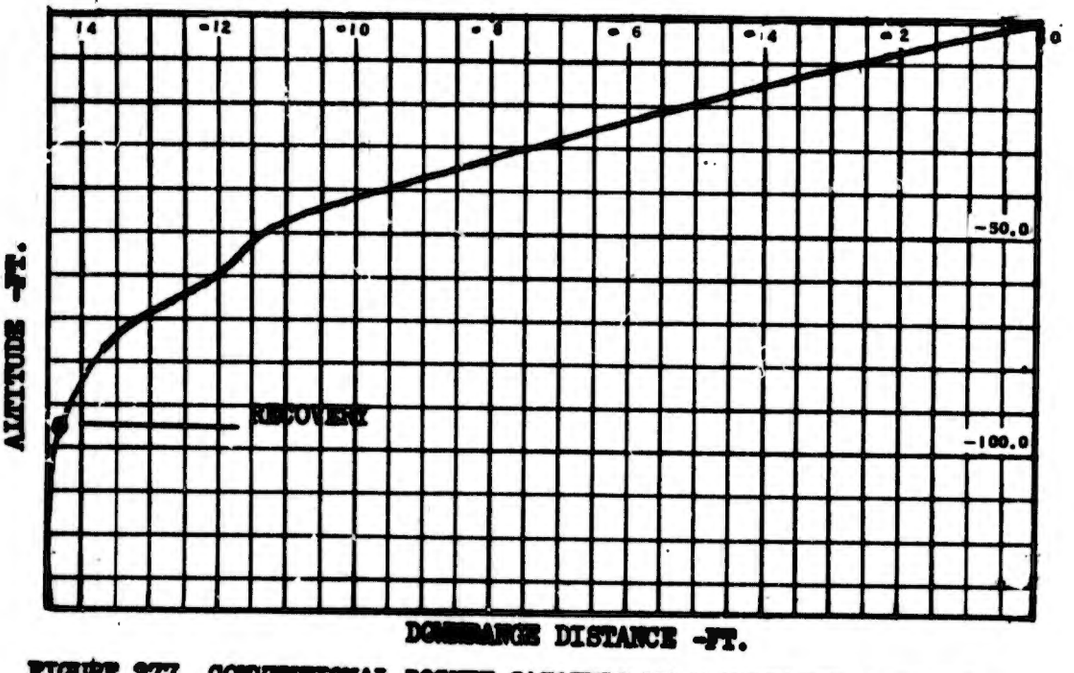

FIGURE 277 CONVENTIONAL ROCKET CATAPULT WITH SUSTAINER WITHELD- SEAT TRAJECTORY AT ZERO SPEED, INVERTED

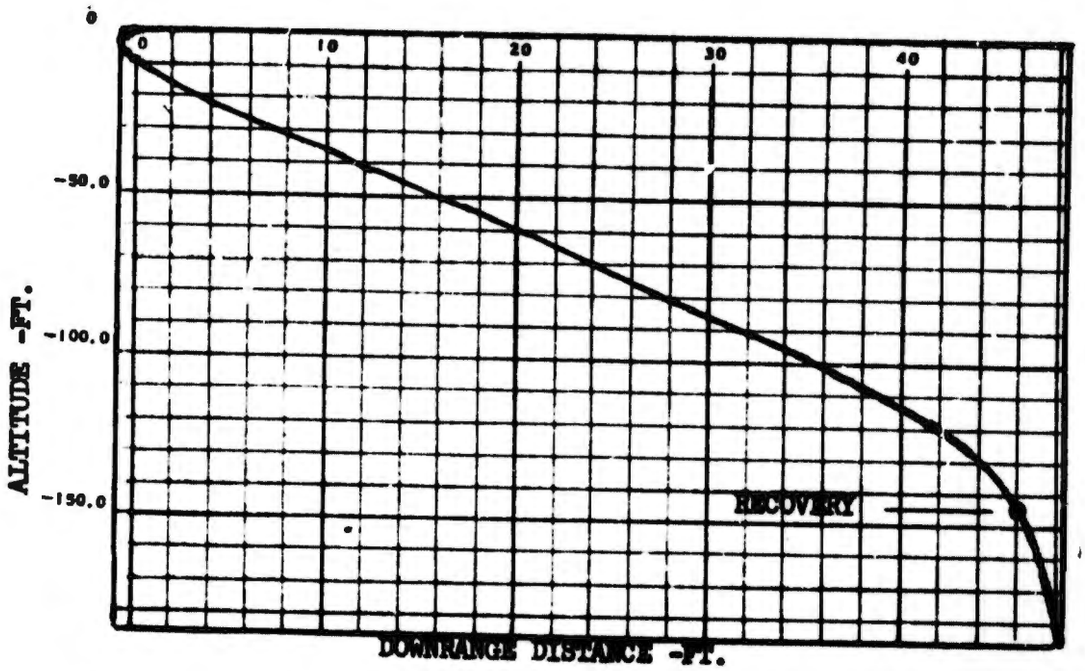

FIGURE 278 CONVENTIONAL ROCKET CATAPULT-SEAT TRAJECTORY AT ZERO SPEED, INVERTED

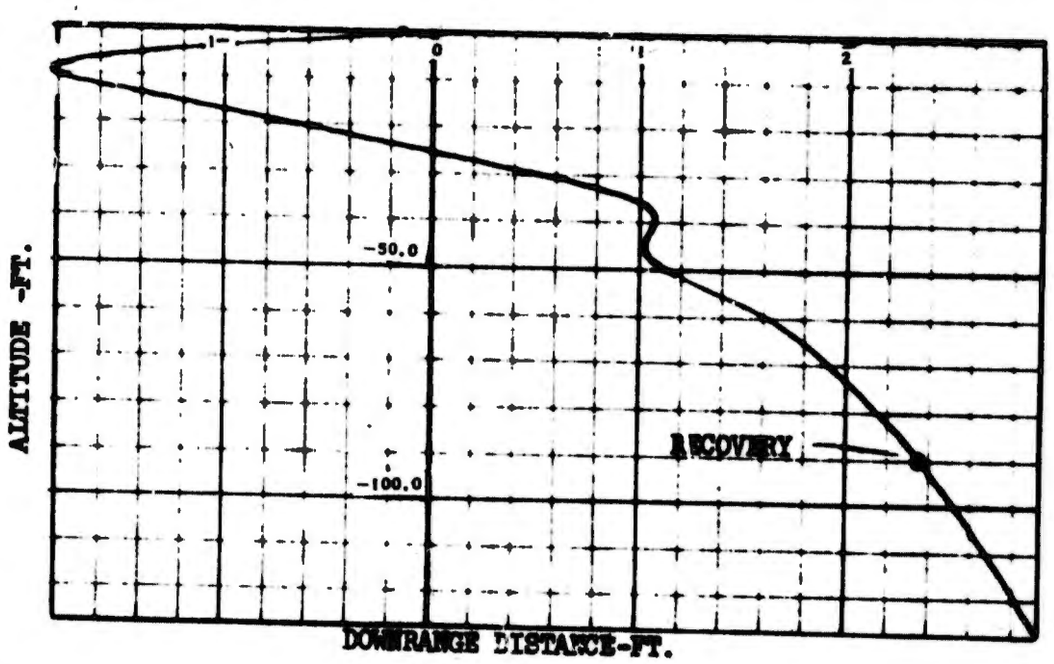

FIGURE 279 NO SUSTAINER; 1600 LB THRUST RETRO-ROCKET - INVERTED TRAJECTORY ZERO SPEED

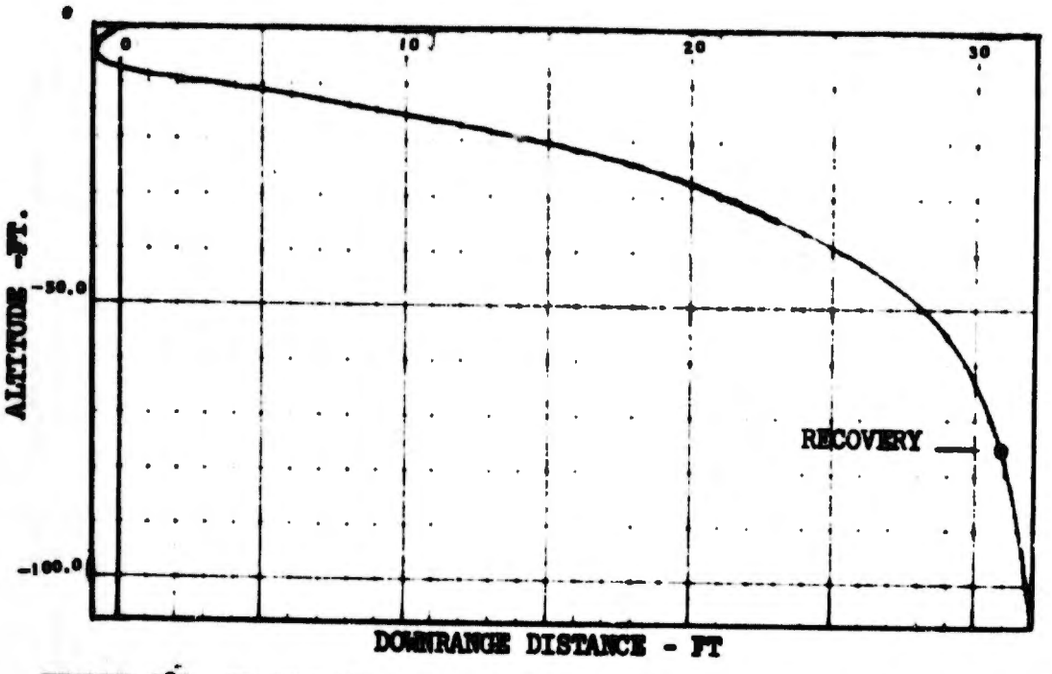

FIGURE 260 NO SUSTAINER, 3200 LB. THRUST - RETRO ROCKET - INVERTED TRAJECTORY ZERO SPEED

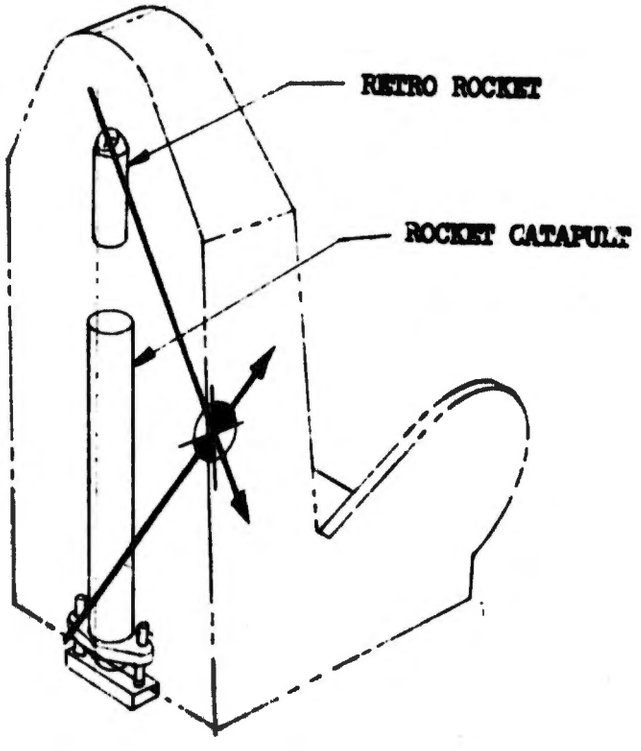

FIGURE 261 CONVENTIONAL ROCKET CATAPULT WITH RETRO ROCKET PROPULSION CONFIGURATION

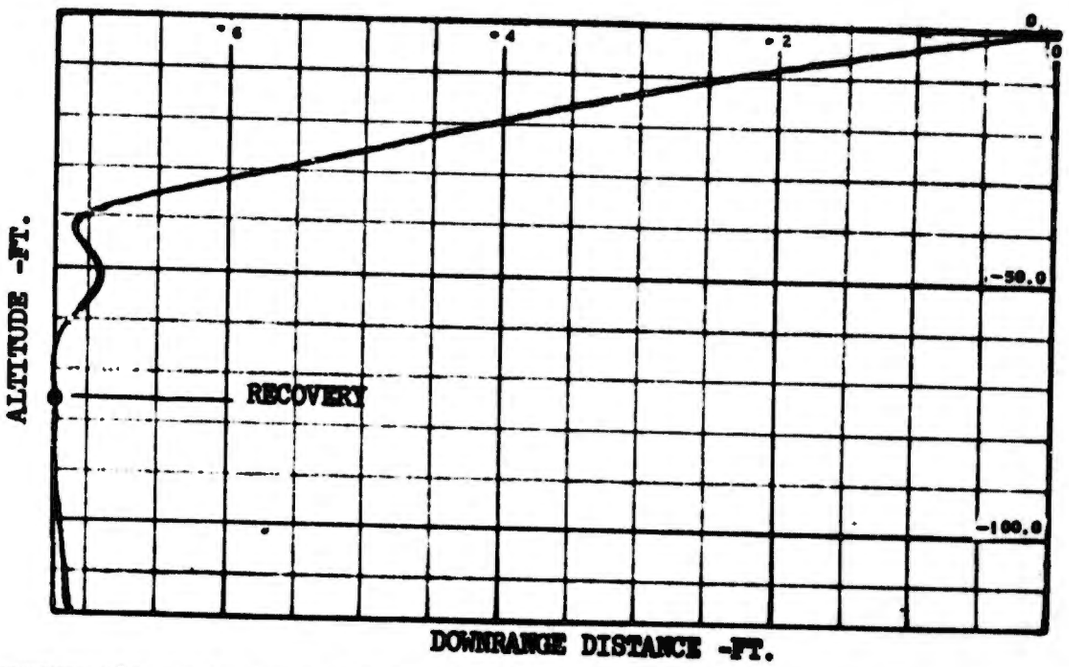

FIGURE 282 DUAL ENERGY CATAPULT, 25 FPS TIP OFF VELOCITY ,INVERTED TRAJECTORY WITH ZERO SPEED

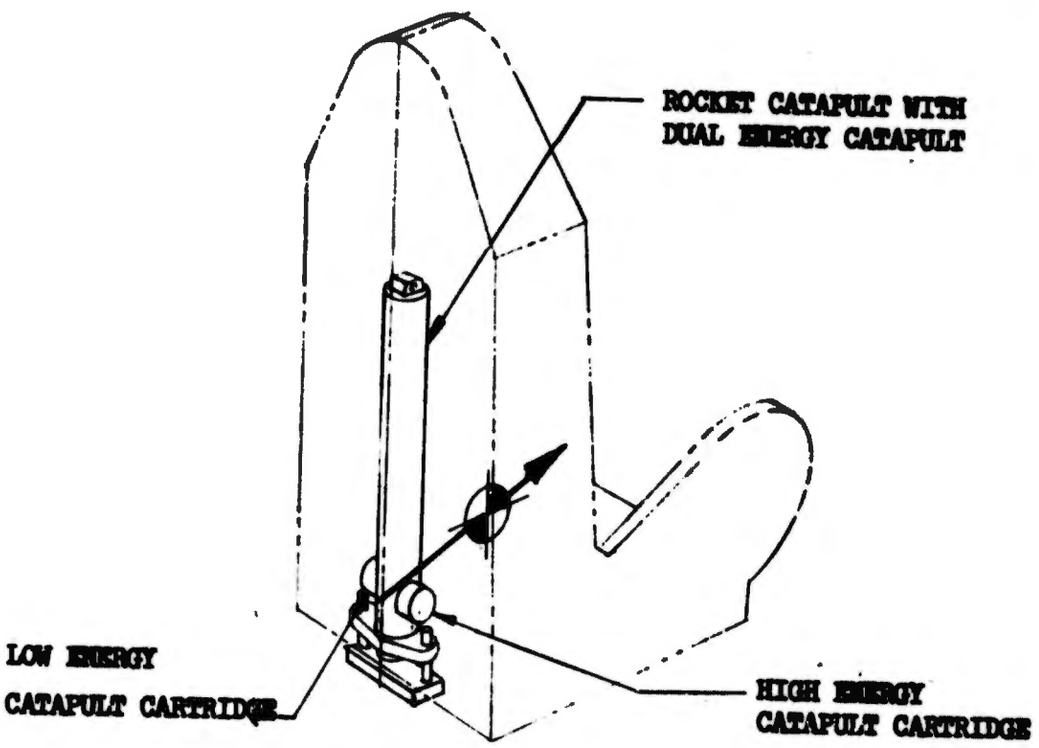

FIGURE 283 CONVENTIONAL ROCKET CATAPULT WITH DUAL ENERGY CATAPULT PROPULSION CONFIGURATION

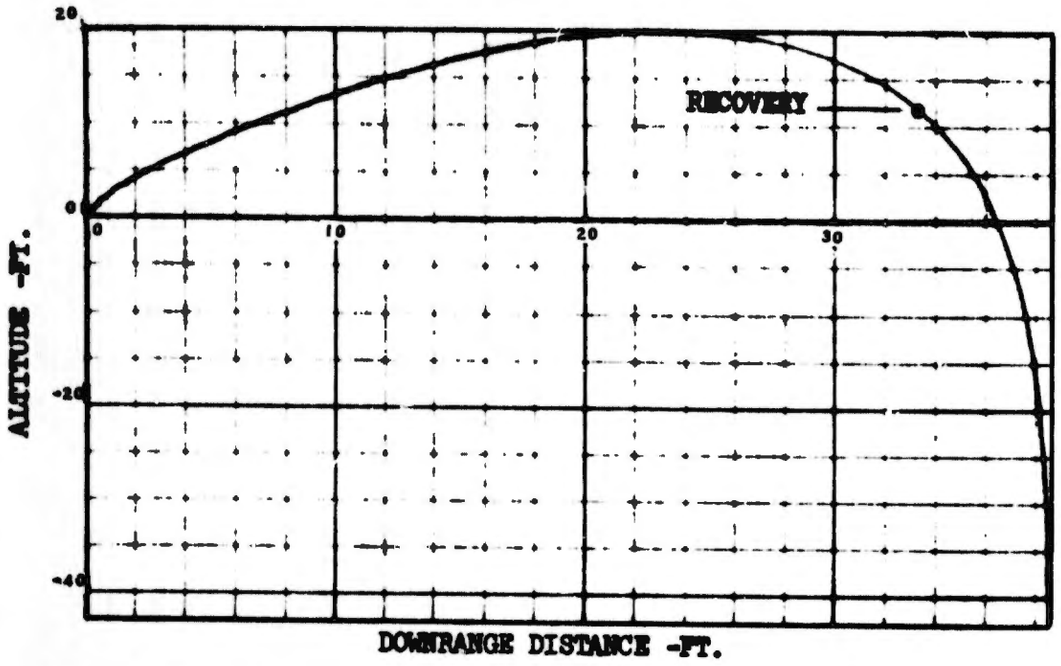

FIGURE 284 UP-DOWN SYSTEM - INVERTED EJECTION, ZERO SPEED

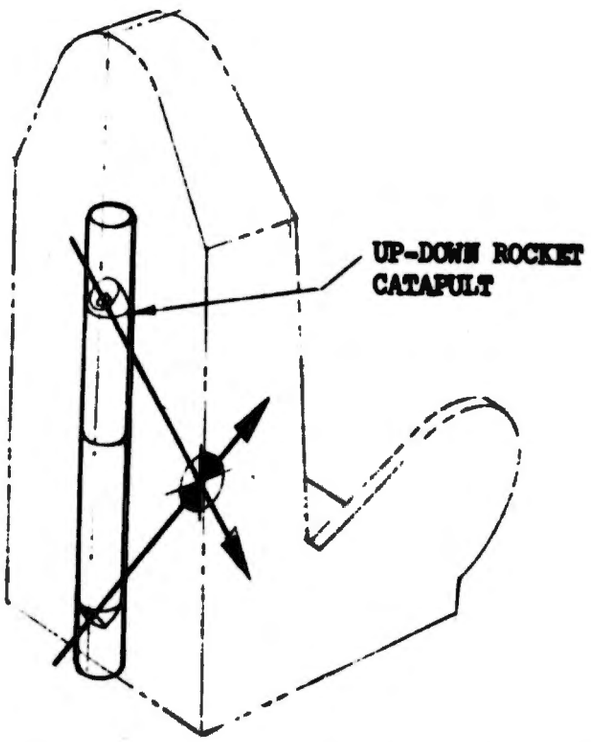

FIGURE 285 UP-DOWN ROCKET CATAPULT PROPULSION CONFIGURATION

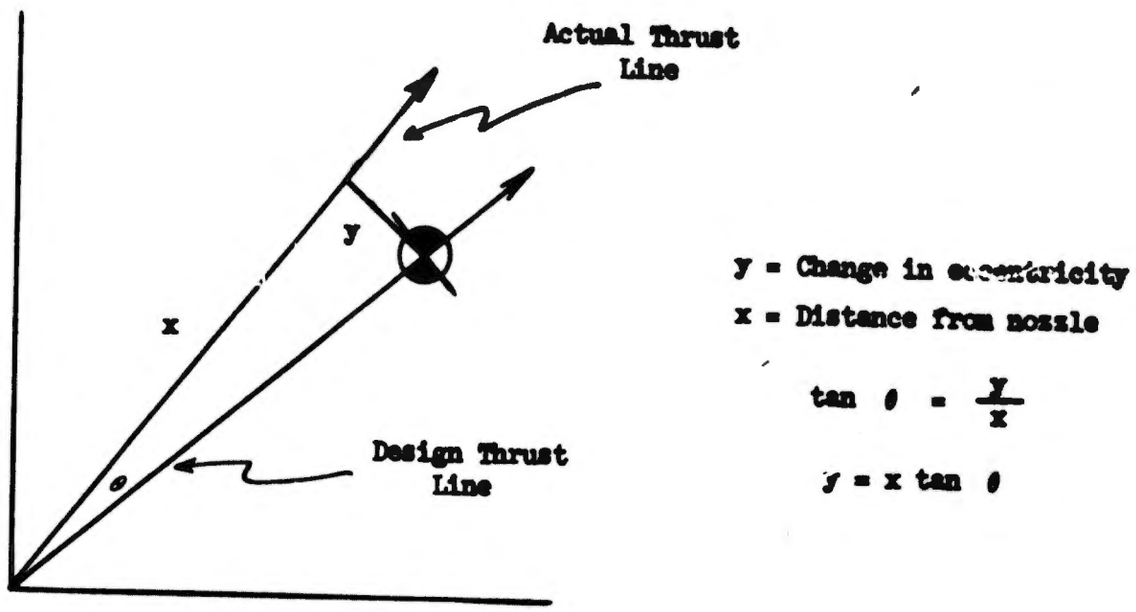

FIGURE 286 CENTER OF GRAVITY THRUST LINE RELATIONSHIP

(Page 148 is blank)

BLANK PAGE

APPENDIX I

SEAT-MAN EQUATIONS OF MOTION AND DATA

TABLE OF CONTENTS

APPENDIX I

SECTION I

GENERAL

The six degree-of-freedom body axis equations for the seat-man system are presented in this section, without derivation, in the sequential form necessary for digital computer solution. The equations were derived from basic physical laws in a manner identical to the formulation in Part I, Volume I, Appendix I of this five volume report.

For the seat-man equations, no plane of mass symmetry was assumed; therefore, products of inertia appear in the inertia tensor that are traditionally found to be negligible in aircraft equations. In addition, unlike the airplane equations, the acceleration dependent aeroelastic coefficients were assumed to be infinitesimal. Consequently, an alternative development is used in the conversion of the coupled acceleration components to the first order differential equation form integrable by digital computer. There is no fundamental difference in the form of the final, canonical equations or the solution algorithm, consequently, re-derivation of the equations would serve no tutorial purpose.

The conventional aerodynamic coefficients are presented for any seat-mind orientation to provide simulation fidelity during seat tumbling. In the computer simulation, accurate coefficients are acquired by double-table-look-up employing an efficient bi-quadratic LaGrange interpolation technique.

The seat attitude with respect to the earth is computed by integrating six of the nine direction cosine rates. The remaining three direction cosines are determined through an orthogonal relationship involving the six integrated rates. The Euler angles are computed from the direction cosines.

The Dynamic Response Index (DRI) of the human spine is computed by describing the human body in terms of an analogous, lumped parameter, mechanical model consisting of a mass, spring, and damper - as required by Paragraph 6.4.1, Reference 5.

APPENDIX I

SECTION II

SYMBOLS

GW	LB	Gross weight
S	FT^2	Seat aerodynamic reference area
c	FT	Seat aerodynamic reference length
b	FT	Seat aerodynamic reference length
F_{x_o}	LB	Axial force summation
F_{y_o}	LB	Lateral force summation
F_{z_o}	LB	Vertical force summation
r_{x_o}	FT-LB	Rolling moment summation
r_{y_o}	FT-LB	Pitching moment summation
r_{z_o}	FT-LB	Yawing moment summation
$\dot{m}$	SLUGS/SEC	Propellant mass flow rate
m	SLUGS	Propellant mass
I_{xx}, I_{yy}, I_{zz}	SLUG-FT^2	Moments of inertia of seat

I_{xy}, I_{xz}, I_{yz}	SLUG-FT^2	Products of inertia of seat
Δx_{cg}, Δy_{cg}, Δz_{cg}	FT	C.G. shift from base C.G.
$\mathcal{M}_{x_{is}}$	FT-LB	Rolling moment from rockets and catapults
$\mathcal{M}_{y_{is}}$	FT-LB	Pitching moment from rockets and catapults
$\mathcal{M}_{z_{is}}$	FT-LB	Yawing moment from rockets and catapults
$\mathcal{M}_{x_{ps}}$	FT-LB	Rolling moment from parachute line stretch
$\mathcal{M}_{y_{ps}}$	FT-LB	Pitching moment from parachute line stretch
$\mathcal{M}_{z_{ps}}$	FT-LB	Yawing moment from parachute line stretch
C_A	NON-DIM	Seat axial force coefficient
C_y	NON-DIM	Seat lateral force coefficient
C_N	NON-DIM	Seat vertical force coefficient
C_l	NON-DIM	Seat rolling moment coefficient
C_m	NON-DIM	Seat pitching moment coefficient
C_n	NON-DIM	Seat yawing moment coefficient
$\dot{x}_s$	FT/SEC	Downrange earth axis velocity component

$\dot{y}_s$	FT/SEC	Lateral earth axis velocity component
$\dot{z}_s$	FT/SEC	Vertical earth axis velocity component
$F_{x_{i_s}}$	LB	Axial seat axis component of rockets and catapults
$F_{y_{i_s}}$	LB	Lateral seat axis component of rockets and catapults
$F_{z_{i_s}}$	LB	Vertical seat axis component of rockets and catapults
$F_{x_{ps}}$	LB	Axial force component on seat due to parachute line stretch
$F_{y_{ps}}$	LB	Lateral force component on seat due to parachute line stretch
$F_{z_{ps}}$	LB	Vertical force component on seat due to parachute line stretch
F_{ps}	LB	Magnitude of force from parachute on seat
$\dot{u}$	FT/SEC^2	Axial seat axis acceleration component of the seat
$\dot{v}$	FT/SEC^2	Lateral seat axis acceleration component of the seat
$\dot{w}$	FT/SEC^2	Vertical seat axis acceleration component of the seat
u	FT/SEC	Axial seat axis velocity component of the seat
v	FT/SEC	Lateral seat axis velocity component of the seat
w	FT/SEC	Vertical seat axis velocity component of the seat
x_s	FT	Downrange earth axis position component of seat
y_s	FT	Lateral earth axis position component of seat
z_s	FT	Vertical earth axis position component of seat

p	RAD/SEC	Angular velocity component of seat about axial seat axis
q	RAD/SEC	Angular velocity component of seat about lateral seat axis
r	RAD/SEC	Angular velocity component of seat about vertical seat axis
$\dot{p}$	RAD/SEC^2	Angular acceleration component of seat about axial seat axis
$\dot{q}$	RAD/SEC^2	Angular acceleration component of seat about lateral seat axis
$\dot{r}$	RAD/SEC^2	Angular acceleration component of seat about vertical seat axis
a_{11} ... a_{33}	NON-DIM	Direction cosines relating the seat to the earth
V_s	FT/SEC	Total speed of seat
ρ	SL/FT^3	Ambient air density
δ	FT	Human spinal compression
b_s	SEC^{-1}	Vibration damping of the human spine
k_s	SEC^{-2}	Spring constant of the human spine

APPENDIX I

SECTION III

EQUATIONS OF MOTION

(1) Axial Load Factor

$$n_{x_{cg}} = -F_{x_o}/GW$$

(2) Side Load Factor

$$n_{y_{cg}} = -F_{y_o}/GW$$

(3) Normal Load Factor

$$n_{z_{cg}} = -F_{z_o}/GW$$

(4) Axial Acceleration

$$\dot{u} = r\,v - q\,w + 32.17(a_{31} - n_{x_{cg}}) - (\dot{m}/m)\,u$$

(5) Side Acceleration

$$\dot{v} = p\,w - r\,u + 32.17(a_{32} - n_{y_{cg}}) - (\dot{m}/m)\,v$$

(6) Normal Acceleration

$$\dot{w} = q\,u - p\,v + 32.17(a_{33} - n_{z_{cg}}) - (\dot{m}/m)\,w$$

(7) Angular Momentum Component, Roll Axis

$$H_x = I_{xx}p - I_{xy}q - I_{xz}r$$

(8) Angular Momentum Component, Pitch Axis

$$H_y = -I_{xy}p + I_{yy}q - I_{yz}r$$

(9) Angular Momentum Component, Yaw Axis

$$H_z = -I_{xz}p - I_{yz}q + I_{zz}r$$

(10) Pitching Acceleration

$$r_{x_1} = rH_y - qH_z + r_{x_0} + GW(n_{y_{cg}}\Delta z_{cg} - n_{z_{cg}}\Delta y_{cg})$$

$$r_{y_1} = pH_z - rH_x + r_{y_0} + GW(n_{z_{cg}}\Delta x_{cg} - n_{x_{cg}}\Delta z_{cg})$$

$$r_{z_1} = qH_x - pH_y + r_{z_0} + GW(n_{x_{cg}}\Delta y_{cg} - n_{y_{cg}}\Delta x_{cg})$$

$$\Delta m_1 = I_{xy}I_{zz} + I_{xz}I_{yz}$$

$$\Delta m_2 = I_{xx}I_{zz} - I_{xz}I_{xz}$$

$$\Delta m_3 = I_{xx}I_{yz} + I_{xy}I_{xz}$$

$$\dot{q} = (r_{x_1}\Delta m_1 + r_{y_1}\Delta m_2 + r_{z_1}\Delta m_3) / (-I_{xy}\Delta m_1 + I_{yy}\Delta m_2 - I_{yz}\Delta m_3)$$

(11) Rolling Acceleration

$$\dot{p} = (I_{zz}(r_{x_1} + I_{xy}\dot{q}) + I_{xz}(r_{z_1} + I_{yz}\dot{q})) / \Delta m_2$$

(12) Yawing Acceleration

$$\dot{r} = (r_{z_1} + I_{yz}\dot{q} + I_{xz}\dot{p}) / I_{zz}$$

(13) Direction Cosine Rates

$$\dot{a}_{11} = a_{12}r - a_{13}q$$

$$\dot{a}_{12} = a_{13}p - a_{11}r$$

$$\dot{a}_{13} = a_{11}q - a_{12}p$$

$$\dot{a}_{21} = a_{22}r - a_{23}q$$

$$\dot{a}_{22} = a_{23}\, p - a_{21}\, r$$

$$\dot{a}_{23} = a_{21}\, q - a_{22}\, p$$

(14) Direction Cosines

$$a_{ij} = \int \dot{a}_{ij}\, dt$$

$$a_{31} = a_{12}\, a_{23} - a_{13}\, a_{22}$$

$$a_{32} = a_{13}\, a_{21} - a_{11}\, a_{23}$$

$$a_{33} = a_{11}\, a_{22} - a_{12}\, a_{21}$$

(15) Euler Angles

$$\psi = \mathrm{Tan}^{-1}(a_{21}/a_{11})$$

$$\theta = \mathrm{Sin}^{-1}(-a_{31})$$

$$\Phi = \mathrm{Tan}^{-1}(a_{32}/a_{33})$$

(16) Earth Axis Velocity Components

$$\dot{x}_s = a_{11}\, u + a_{12}\, v + a_{13}\, w$$

$$\dot{y}_s = a_{21}\, u + a_{22}\, v + a_{23}\, w$$

$$\dot{z}_s = a_{31}\, u + a_{32}\, v + a_{33}\, w$$

(17) Seat Total Speed

$$V_s = (u^2 + v^2 + w^2)\ 1/2$$

(18) Dynamic Pressure

$$q_a = .5\rho V_s^2$$

(19) Axial Force Summation

$$F_{x_a} = -q_a S C_A + F_{x_{i_s}} + F_{x_{ps}}$$

(20) Lateral Force Summation

$$F_{y_a} = q_a S C_y + F_{y_{i_s}} + F_{y_{ps}}$$

(21) Vertical Force Summation

$$F_{z_a} = -q_a S C_N + F_{z_{i_s}} + F_{z_{ps}}$$

(22) Rolling Moment Summation

$$r_{x_a} = q_a S b C_l + r_{z_{i_s}} + r_{z_{ps}}$$

(23) Pitching Moment Summation

$$r_{y_a} = q_a S c C_m + r_{y_{i_s}} + r_{y_{ps}}$$

(24) Yawing Moment Summation

$$r_{z_a} = q_a S b C_n + r_{z_{i_s}} + r_{z_{ps}}$$

The seat-man aerodynamic coefficients are computed by a double-table-look-up numerical technique using angles of attack and sideslip angles given by--

(25) Sideslip Angle

$$\beta = \text{Tan}^{-1}(v/u)$$

(26) Angle of Attack

$$\alpha = \text{Tan}^{-1}(w|\text{Cos}\beta|/u)$$

The arctangent function is evaluated for all four quadrants for valid angular computation during seat tumbling. For this reason, the angle of attack equation is different from the conventional small angle expression.

(27) Dynamic Compression of the Human Spine

$$d^2\delta/dt^2 = -b_s(d\delta/dt) - k_s\delta + 32.17(n_{z_{cg}} - a_{33})$$

$$d\delta/dt = \int(d^2\delta/dt)\,dt$$

$$\delta = \int(d\delta/dt)\,dt$$

APPENDIX I

SECTION IV

The six degree-of-freedom aerodynamic coefficients for the seat-man combination are presented in Figures 288 through 293. The data were taken from Reference 1 and extrapolated where necessary to sideslip and angle-of-attack ranges from -180 deg. to 180 deg.

Figures 294 through 299 are the aerodynamic coefficients used for the man-alone equations. The coefficients were computed employing Newtonian flow and a flat plate analogy. The values were compared with those of Reference 2 and determined to be sufficiently accurate for man-parachute dynamic simulation, considering the overwhelming parachute forces which obscure the effects of man-alone aerodynamic coefficient variations.

The following figure shows the right-hand axis system used in all equations in this report for the seat, the man, the rails, the earth axis and all force and moment inputs.

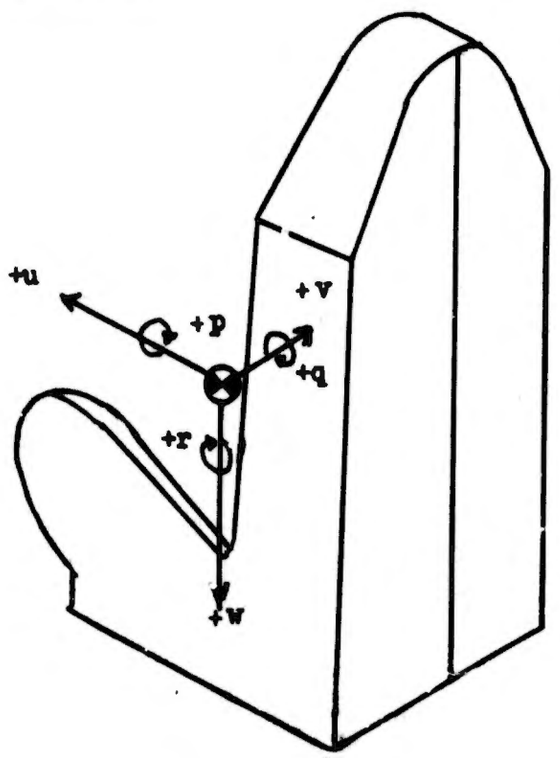

FIGURE 287 AXIS SYSTEM CONVENTION

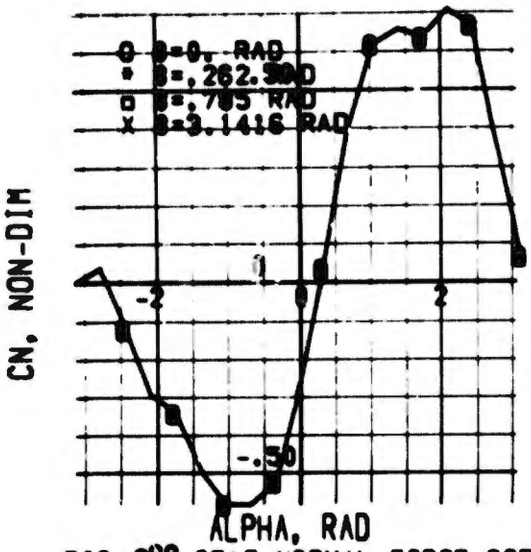

FIG 288 SEAT NORMAL FORCE COEF

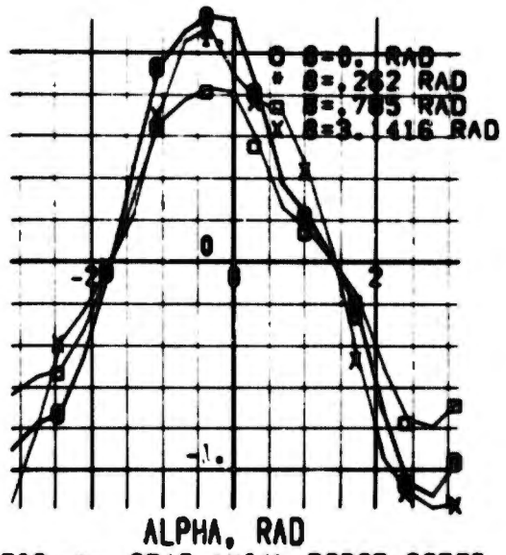

FIG 289 SEAT AXIAL FORCE COEFF

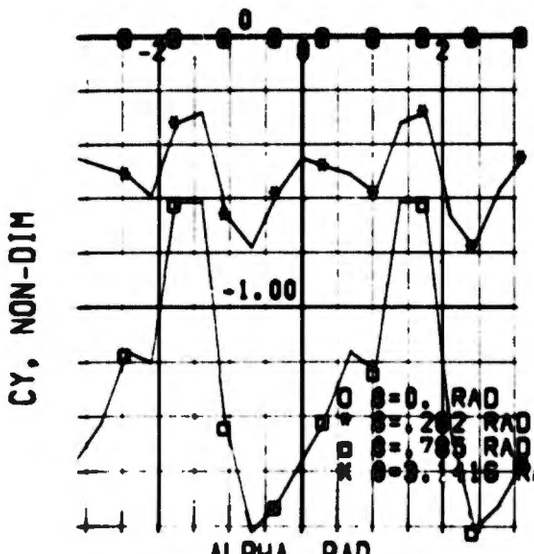

FIG 290 SEAT SIDE FORCE COEFF

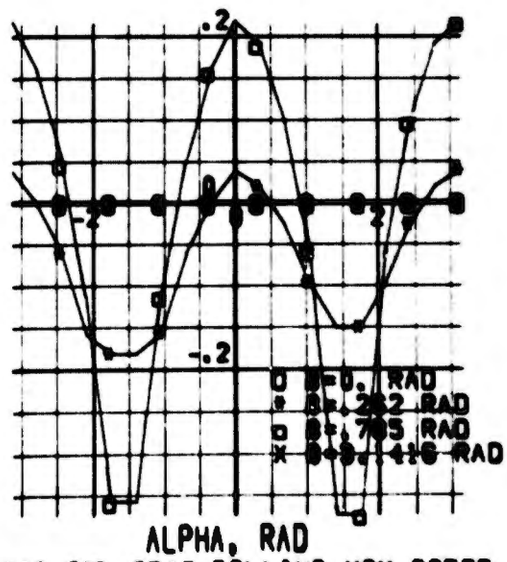

FIG 291 SEAT ROLLING MOM COEFF

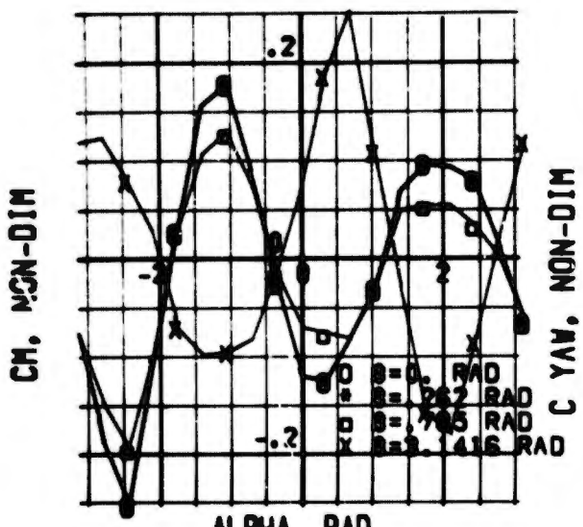

FIG 292 SEAT PITCHING MOM COEF

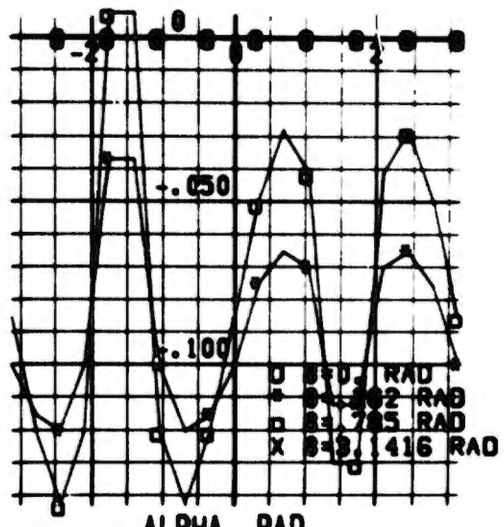

FIG 293 SEAT YAWING MOM COEFF

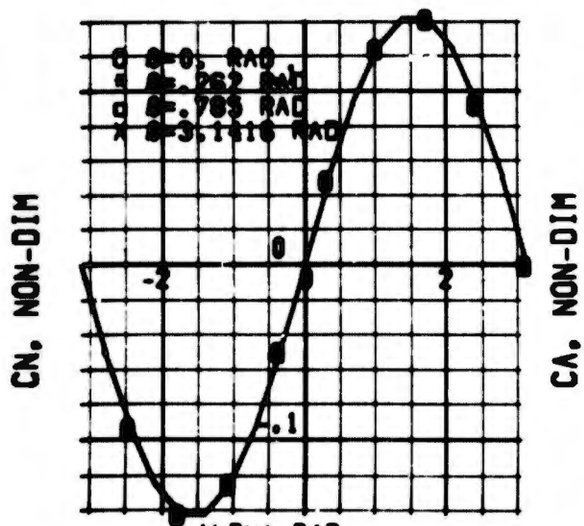

FIG 294 MAN NORMAL FORCE COEF

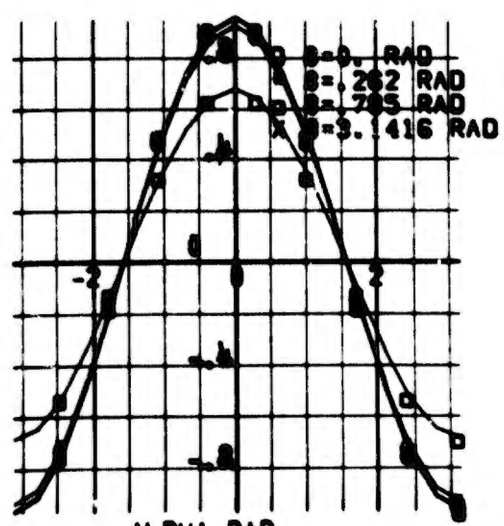

FIG 295 MAN AXIAL FORCE COEFF

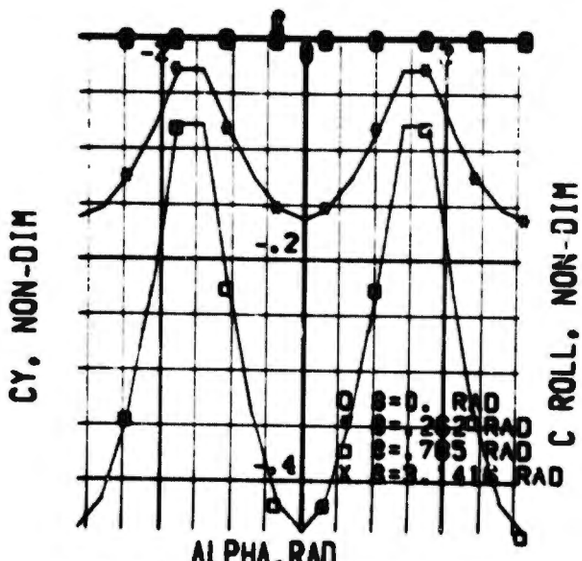

FIG 296 MAN SIDE FORCE COEFF

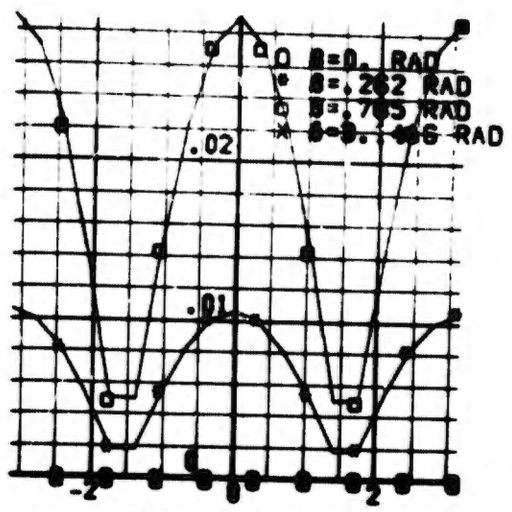

FIG 297 MAN ROLLING MOM COEFF

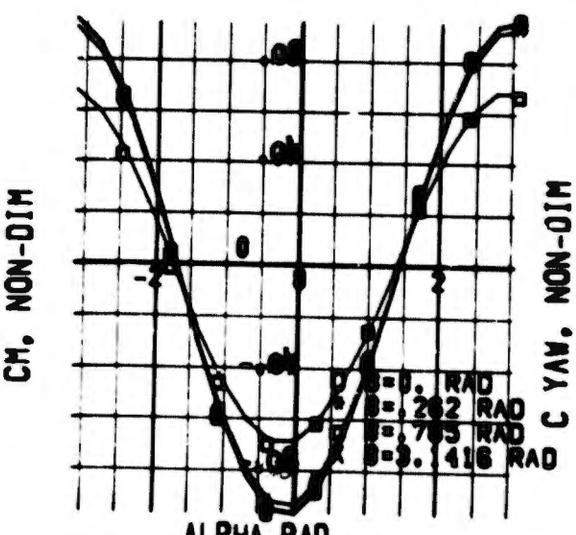

FIG 298 MAN PITCHING MOM COEF

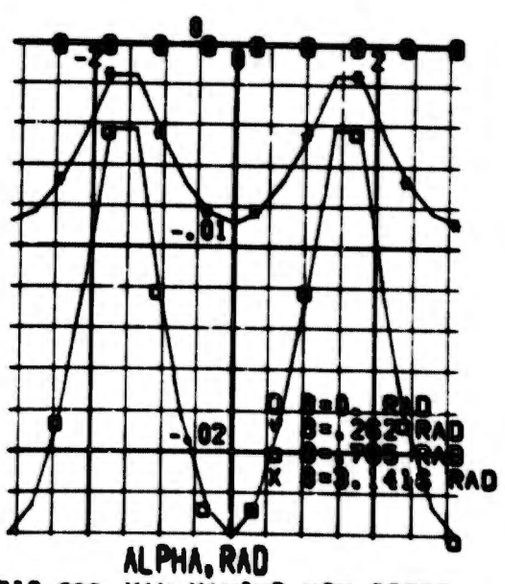

FIG 299 MAN YAWING MOM COEFF

The aerodynamic reference lengths and areas for the seat-man combination and the man alone are:

SEAT-MAN

S = 5.05
b = 3.82
c = 3.82

MAN-ALONE

S = 6.0
b = 1.375
c = .9

SPINAL COMPRESSION CONSTANTS

b_s = 23.7
k_s = 2795.00

The inertial properties of the seat-man are given in Table II, Section IV.

The man-alone (with survival gear) inertial properties are, for a 95% man in a standing position:

GW = 294.0
I_{xx} = 13.0
I_{yy} = 15.0
I_{zz} = 6.0

A completely symmetrical man is assumed, with all products of inertia set to zero.

APPENDIX I

SECTION V

NON-AERODYNAMIC FORCES AND MOMENTS

The external forces and moments, excluding gravity, on the seat and/or man are from the catapult and sustainer-control rockets (Appendix IV), parachutes and parachute ejection guns (Appendix II), rail deformation and slider block friction (Appendix III).

A separate section is required for the equations representing each of the external inputs because of the detailed treatment given each element of the system.

APPENDIX II

PARACHUTE EQUATIONS OF MOTION AND DATA

TABLE OF CONTENTS

APPENDIX II

SECTION I

GENERAL

The parachute equations developed in this section represent any parachute translating in three degrees of freedom with respect to the earth and rotating with respect to attach points moving in the earth reference axes. The differential equations describe the parachute accelerations from an initial stowed position to full inflation. The accelerations are expressed in a form required for numerical integration by digital computer and the forces are general enough to allow evaluation of parachute stability, opening reliability and performance while operating in the vicinity of a seat or man.

From the stowed position the equations allow the parachute to be projected either aerodynamically or pyrotechnically. From projection time to line stretch the parachute accelerations are simulated as functions of mortar impulse, rocket force, reefed lift-drag force and deployment bag strip-off force. At line-stretch time, shroud-line-bridle-riser elastic forces become operative, a mass acquisition term is determined and the growth of lift-drag forces during inflation is computed. Line reaction forces and moments are projected on the seat/man axis system portraying the loads resulting from snatch forces and opening shocks.

APPENDIX II

SECTION II

SYMBOLS

$\dot{x}_p$	FT/SEC	Downrange earth axis velocity component
$\dot{y}_p$	FT/SEC	Lateral earth axis velocity component
$\dot{z}_p$	FT/SEC	Vertical earth axis velocity component
x_p	FT	Downrange earth axis position component
y_p	FT	Lateral earth axis position component
z_p	FT	Vertical earth axis position component
$F_{x_{sp}}$	LB	Axial force component on parachute due to seat
$F_{y_{sp}}$	LB	Lateral force component on parachute due to seat
$F_{z_{sp}}$	LB	Vertical force component on parachute due to seat
$F_{x_{i_s}}$	LB	Axial seat axis component of rockets and catapults
$F_{y_{i_s}}$	LB	Lateral seat axis component of rockets and catapults
$F_{z_{i_s}}$	LB	Vertical seat axis component of rockets and catapults
F_{x_m}	LB	Air mass acquisition axial force component
F_{y_m}	LB	Air mass acquisition lateral force component
F_{z_m}	LB	Air mass acquisition vertical force component
F_{x_i}	LB	Axial earth axis component of rockets and catapults

F_{y_i}	LB	Lateral earth axis component of rockets and catapults
F_{z_i}	LB	Vertical earth axis component of rockets and catapults
$F_{x_{ps}}$	LB	Axial force component on seat due to parachute line stretch
$F_{y_{ps}}$	LB	Lateral force component on seat due to parachute line stretch
$F_{z_{ps}}$	LB	Vertical force component on seat due to parachute line stretch
F_{ps}	LB	Magnitude of force from parachute on seat
u_s	FT/SEC	Axial seat axis velocity component of the seat
v_s	FT/SEC	Lateral seat axis velocity component of the seat
w_s	FT/SEC	Vertical seat axis velocity component of the seat
x_s	FT	Downrange earth axis position component of seat
y_s	FT	Lateral earth axis position component of seat
z_s	FT	Vertical earth axis position component of seat
p	RAD/SEC	Angular velocity component of seat about axial seat axis
q	RAD/SEC	Angular velocity component of seat about lateral seat axis
r	RAD/SEC	Angular velocity component of seat about vertical seat axis
a_{11} ⋮ a_{33}	NON-DIM	Direction cosines relating the seat to the earth

V_p	FT/SEC	Total speed of parachute
V_s	FT/SEC	Total speed of seat
t_e	SEC	Parachute ejection time
t_{LS}	SEC	Time at line stretch
Δt_{gun}	SEC	Decrease in the chute spreading time due to spreading gun
Δt_i	SEC	Mass acquisition time
m_p	SLUG	Mass of parachute
$\dot{m}_a$	SL/SEC	Air mass acquisition rate
α	RAD	Parachute angle of attack
Vol	FT^3	Volume of air acquired by parachute
ρ_s	SL/FT^3	Compressed air density
ρ	SL/FT^3	Ambient air density
Δx_a	FT	Axial seat axis component from apex of attachment bridle to chute
Δy_a	FT	Lateral seat axis component from apex of attachment bridle to chute
Δz_a	FT	Vertical seat axis component from apex of attachment bridle to chute
Δx_{ap}	FT	Axial seat axis component of packed parachute location
Δy_{ap}	FT	Lateral seat axis component nf packed parachute location
Δz_{ap}	FT	Vertical seat axis component of packed parachute location

R_{lines}	FT	Riser length
R_L	FT	Distance from apex of bridle to parachute cg
R_{x_L}	FT	Downrange component of R_L in earth axis system
R_{y_L}	FT	Lateral component of R_L in earth axis system
R_{z_L}	FT	Vertical component of R_L in earth axis system
R_{L_o}	FT	R_L at full inflation
R_{sc}	FT	Length of the skirt and canopy quarter circumference
R_{in}	FT	Inlet radius of the parachute
R_m	FT	Canopy circumference
K	LB/FT	Line elastic modulus
B_o	FT^2	Constants in equation for SC_D of reefed parachute
B_1	FT	
B_2	NON-DIM	
B_3	FT^{-1}	
V_{p_o}	FT/SEC	Velocity associated with SC_D/SC_{D_i} vs R_L/R_{L_o}
C_1	FT-SEC	Constants on equation for SC_D
C_2	SEC^2	
k_1, k_2, k_3	NON-DIM	Constants in equation for Δt_i

$SC_{D_{LS}}$	FT^2	Product of reference area and drag coef. at line stretch
SC_{D_i}	FT^2	SC_D at full inflation
F_{x_L}	LB	Downrange lift force
F_{y_L}	LB	Lateral lift force
F_{z_L}	LB	Vertical lift force
F_L	LB	Lift force
F_{DB}	LB	Deployment bag strip out force
F_{x_D}	LB	Downrange drag force
F_{y_D}	LB	Lateral drag force
F_{z_D}	LB	Vertical drag force
F_D	LB	Drag force magnitude
$SC_{T_{(\alpha=0)}}$, SC_{T_α}, $SC_{T_{\alpha^2}}$, $SC_{T_{\alpha^3}}$	NON-DIM	Curve fit coefficients for SC_T as f(α)
SC_{N_α}, $SC_{N_{\alpha^2}}$, $SC_{N_{\alpha^3}}$	NON-DIM	Curve fit coefficients for SC_N as f(α)

m_x	NON-DIM	Downrange lift unit vector
m_y	NON-DIM	Lateral lift unit vector
m_z	NON-DIM	Vertical lift unit vector
u_p	FT/SEC	Axial earth axis velocity component of parachute
v_p	FT/SEC	Lateral earth axis velocity component of parachute
w_p	FT/SEC	Vertical earth axis component of parachute
$\dot{v}_{p_x}$	FT/SEC^2	Downrange earth axis acceleration component
$\dot{v}_{p_y}$	FT/SEC^2	Lateral earth axis acceleration component
$\dot{v}_{p_z}$	FT/SEC^2	Vertical earth axis acceleration component
F_c	NON-DIM	Mach dependent compressibility function
F_d	NON-DIM	Wake lift and drag coefficient ratio
M	NON-DIM	Mach number

γ	NON-DIM	Ratio of specific heats
C	NON-DIM	Effective porosity
F_x	LB	Axial component of force applied at apex of bridle
F_y	LB	Lateral component of force applied at apex of bridle
F_z	LB	Vertical component of force applied at apex of bridle
x_1 . x_4	FT	Axial seat axis coordinates of bridle attach points
y_1 . y_4	FT	Lateral seat axis coordinates of bridle attach points
z_1 . z_4	FT	Vertical seat axis coordinates of bridle attach points

x_a y_a z_a	FT	Seat axis coordinates of apex of bridle
NLINES	NON-DIM	Number of lines in bridle
r_x r_y r_z	FT-LB	Moments on seat due to parachute acting through bridle
x_f y_f z_f	FT	Seat axis coordinates of force application point
A, B, C, D	NON-DIM	Coefficients in the equation of the plane of bridle attach points
F	LB	Magnitude of force applied at apex of bridle

APPENDIX II

SECTION III

PARACHUTE EQUATIONS OF MOTION

A trivial application of Newton's laws produces the earth axis acceleration of the parachute, consequently, the derivation is not presented. The equations for the forces and geometry, however, are more complex and the development details are fully explained.

(1) Downrange Earth Axis Acceleration Component

$$\dot{v}_{p_x} = (F_{x_D} + F_{x_L} + F_{x_m} + F_{x_i} + F_{x_{sp}}) / m_p$$

(2) Lateral Earth Axis Acceleration Component

$$\dot{v}_{p_y} = (F_{y_D} + F_{y_L} + F_{y_m} + F_{y_i} + F_{y_{sp}}) / m_p$$

(3) Vertical Earth Axis Acceleration Component

$$\dot{v}_{p_z} = (F_{z_D} + F_{z_L} + F_{z_m} + F_{z_i} + F_{z_{sp}}) / m_p + 32.17$$

(4) Downrange Earth Axis Velocity Component

$$\dot{x}_p = \dot{x}_{p_0} + \int \dot{v}_{p_x} dt$$

(5) Lateral Earth Axis Velocity Component

$$\dot{y}_p = \dot{y}_{p_0} + \int \dot{v}_{p_y} dt$$

(6) Vertical Earth Axis Velocity Component

$$\dot{z}_p = \dot{z}_{p_0} + \int \dot{v}_{p_z} dt$$

(7) Downrange Earth Axis Position

$$x_p = x_{p_0} + \int \dot{x}_p dt$$

(8) Lateral Earth Axis Position

$$y_p = y_{p_0} + \int \dot{y}_p dt$$

(9) Vertical Earth Axis Position

$$z_p = z_{p_0} + \int \dot{z}_p dt$$

F_{x_m}, F_{y_m}, F_{z_m} are force components resulting from parachute air mass acquisition in the interval from first line stretch to full parachute inflation.

$F_{x_{sp}}$, $F_{y_{sp}}$, $F_{z_{sp}}$ are force components from the seat (or man) pull through the parachute risers and bridle.

At first line stretch, the parachute is assumed to acquire an air mass which is accelerated to a speed equal to the parachute speed during the inflation period, Δt_i. The compressed air density can be computed as a function of stagnation pressure.

(10) Compressed Air Density

$$\rho_s = \rho(\rho_s/\rho) = \rho[1 + M^2(\gamma - 1) / 2)^{-1/(\gamma-1)}$$

With the density known, the acquired mass can be computed if a volume is known or assumed. The chosen volume should result in snatch loads and opening shock loads that agree with the available flight test data.

(11) Air Mass Acquisition Rate

$$\dot{m}_a = Vol\ \rho_s / \Delta t_i, \quad t_{LS} \le t \le t_{LS} + \Delta t_i$$

$$= 0, \text{ otherwise}$$

where t_{LS} is time at first line stretch and Δt_i is computed as follows.

(12) Time for Full Parachute Inflation

$$\Delta t_i = 2k_1 R_{sc} / (V_s(k_2 - k_3 C)) - \Delta t_{gun}$$

(13) Force Components Due to Mass Acquisition

$$F_{x_m} = -\dot{m}_a \dot{x}_p$$

$$F_{y_m} = -\dot{m}_a \dot{y}_p$$

$$F_{z_m} = -\dot{m}_a \dot{z}_p$$

Figure 300 shows the geometry from which the radius, R_m, of the spherical mass is derived.

$$Vol = 4/3\ \pi R_m^3$$

$$R_m = (R_L + R_{sc}) / (R_L/R_{in} + \pi/2)$$

To compute the line forces on the parachute mass, the distance from the parachute attach point on the seat (or man) is needed. The components of the vector $\mathbf{R}_L$, Figure 301, are given by the following matrix equation.

(14) Distance Components from Parachute CG to Bridle Apex

$$R_L = R_{sp} - A\ R_a$$

expanding,

$$\begin{bmatrix} R_{x_L} \\ R_{y_L} \\ R_{z_L} \end{bmatrix} = \begin{bmatrix} x_p - x_s \\ y_p - y_s \\ z_p - z_s \end{bmatrix} - \begin{bmatrix} a_{11} & a_{12} & a_{13} \\ a_{21} & a_{22} & a_{23} \\ a_{31} & a_{23} & a_{33} \end{bmatrix} \begin{bmatrix} \Delta x_a \\ \Delta y_a \\ \Delta z_a \end{bmatrix}$$

(15) Elastic Line Force on Parachute

$$F_{sp} = -K (R_L - R_{L_o}) \qquad R_L > R_{L_o}$$

$$= 0, \text{ otherwise}$$

(16) Distance from Parachute CG to Bridle Apex

$$R_L = (R_{x_L}^2 + R_{y_L}^2 + R_{z_L}^2)^{1/2}$$

Projecting the line force on the earth axis is necessary for solution of the parachute trajectory.

(17) Force Components from Line Stretch

$$F_{x_{sp}} = F_{sp} R_{x_L} / R_L$$

$$F_{y_{sp}} = F_{sp} R_{y_L} / R_L$$

$$F_{z_{sp}} = F_{sp} R_{z_L} / R_L$$

The reaction force on the seat from line stretch is given by the vector

$$F_{ps} = -F_{sp}$$

with seat (or man) body axis components given by the following equation

(18) Components of Reaction Force

$$F_{ps} = -A^T F_{sp}$$

$$\begin{bmatrix} F_{x_{ps}} \\ F_{y_{ps}} \\ F_{z_{ps}} \end{bmatrix} = \begin{bmatrix} a_{11} & a_{21} & a_{31} \\ a_{12} & a_{22} & a_{32} \\ a_{13} & a_{23} & a_{33} \end{bmatrix} \begin{bmatrix} -F_{x_{sp}} \\ -F_{y_{sp}} \\ -F_{z_{sp}} \end{bmatrix}$$

Reference 9

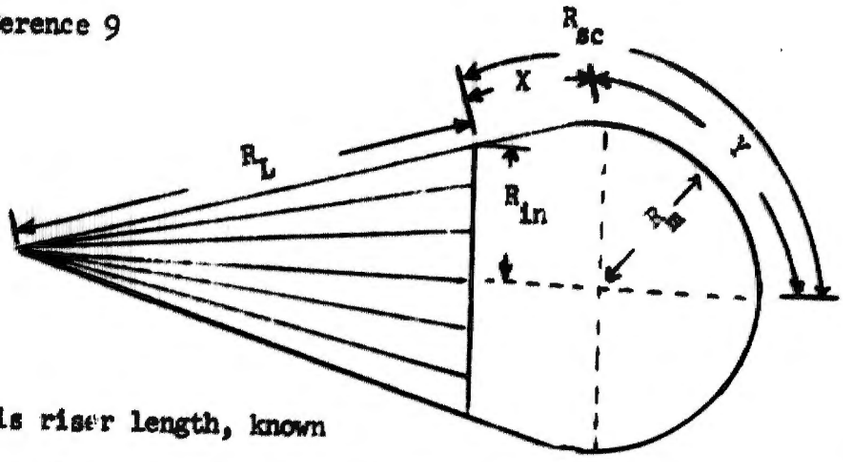

R_L is riser length, known

R_{sc} is length of the skirt and canopy quarter circumference, known

R_{in} is inlet radius, assumed

Solve for R_m by triangle similarity.

$$\frac{R_L}{R_{in}} = \frac{(X + R_L)}{R_m}$$

therefore,

$$X = R_m R_L/R_{in} - R_L$$

$$Y = 2\pi R_m/4 = \pi R_m/2$$

$$X + Y = R_m R_L/R_{in} - R_L + \pi R_m/2$$

$$= (R_L/R_{in} + \pi/2)\ R_m - R_L$$

$$X + Y = R_{sc}$$

$$R_{sc} = (R_L/R_{in} + \pi/2)\ R_m - R_L$$

$$R_m = (R_L + R_{sc})/(R_L/R_{in} + \pi/2)$$

FIGURE 300 MASS ACQUISITION GEOMETRY

VECTOR DEFINITIONS

$$\vec{R}_{es} = i_e X_s + j_e Y_s + k_e Z_s \qquad \text{known}$$

$$\vec{R}_{ep} = i_e X_p + j_e Y_p + k_e Z_p \qquad \text{known}$$

$$\vec{R}_a = i\Delta X_a + j\Delta Y_a + k\Delta Z_a \qquad \text{known}$$

$$\vec{R}_{ap} = i\Delta X_{ap} + j\Delta Y_{ap} + k\Delta Z_{ap} \qquad \text{known}$$

$$* \quad \vec{R}_{sp} = \vec{R}_{ep} - \vec{R}_{es} = i_e (X_p - X_s) + j_e (Y_p - Y_s) + k_e (Z_p - Z_s)$$

$$* \quad \vec{R}_L = \vec{R}_{sp} - \vec{R}_a = i_e R_{x_L} + j_e R_{y_L} + k_e R_{z_L}$$

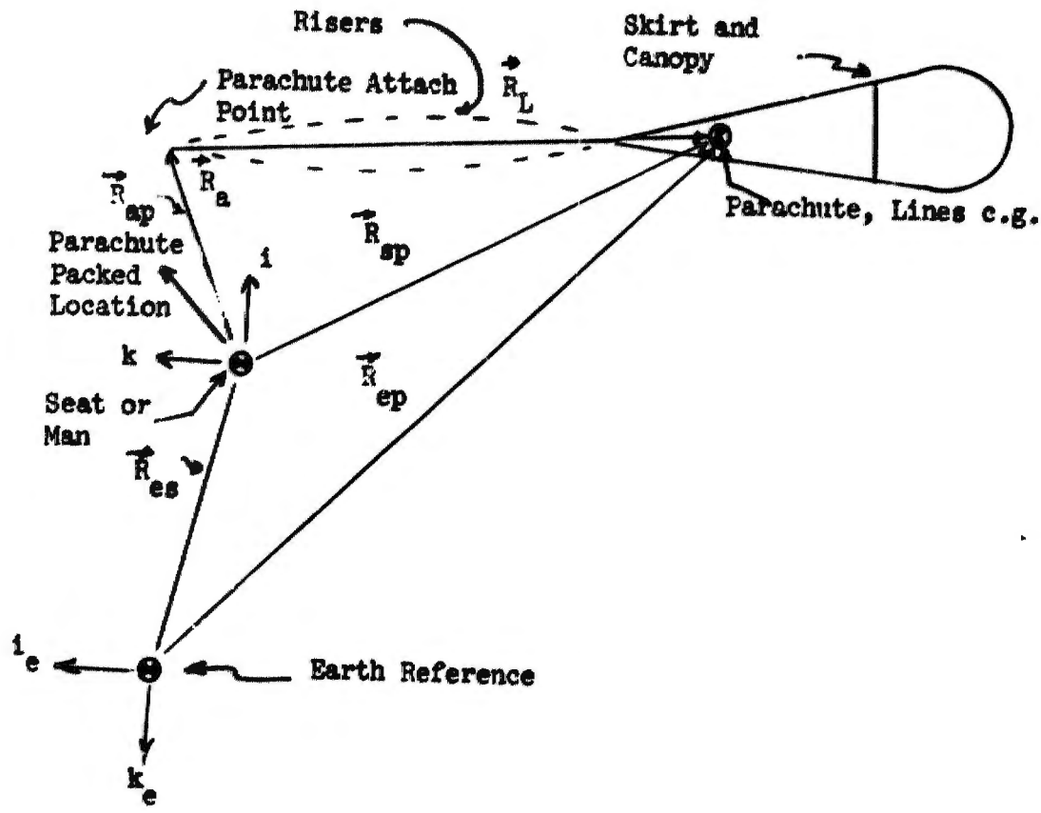

* Calculated from known vectors

FIGURE 301 ESCAPE SYSTEM GEOMETRY

The parachute drag area, SC_D, in the reefed condition is nearly a cubic function of distance aft of the man (or seat), with the maximum drag area at about 40% of line stretch, according to available wind tunnel data. Furthermore, the maximum reefed drag area is usually from 2% to 5% of the fully inflated drag area. With these traits as a guide, SC_D before line stretch can be expressed as follows.

(19) Drag Force Area before Line Stretch

$$SC_D = (B_0 + B_1R + B_2R^2 + B_3R^3)\, SC_{T(\alpha = 0)}$$

where $R = R_L / R_{L_0}$

The lift force area, SC_L, is assumed to be negligible before first line stretch.

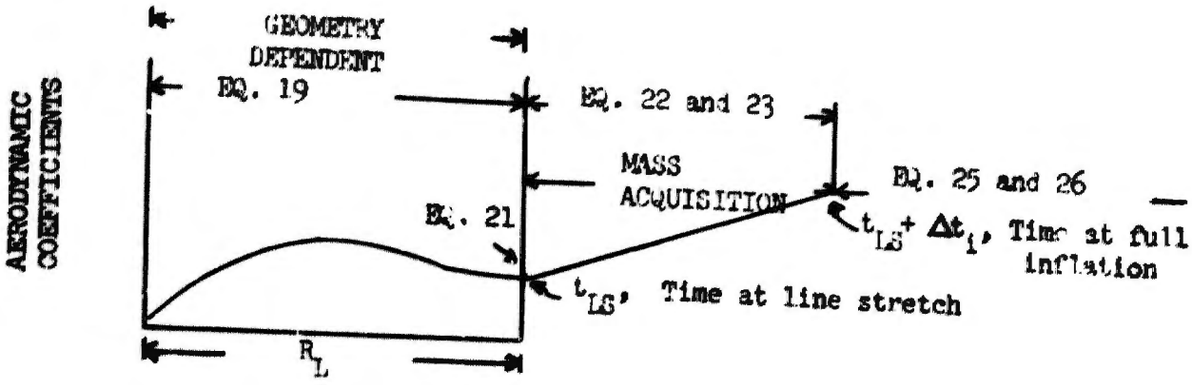

FIGURE 302 DRAG FORCE AREA

During parachute inflation (from $t = t_{LS}$ to $t = t_{LS} + \Delta t_i$) linear interpolation is used to calculate SC_T and SC_N as a function of the parachute angle of attack.

(20) Tangential Area Force Coefficient at Full Inflation

$$SC_{T_{i\alpha}} = SC_{T_{(\alpha = 0)}} + SC_{T_\alpha}\alpha + SC_{T_{\alpha^2}}\alpha^2 + SC_{T_{\alpha^3}}\alpha^3$$

(21) Tangential Area Force Coefficient at Line Stretch

$$SC_{T_{LS}} = (B_0 + B_1 + B_2 + B_3)\, SC_{T_{i\alpha}}$$

(22) Tangential Area Force Coefficient during Inflation

$$SC_T = SC_{T_{LS}} + (SC_{T_{i\alpha}} - SC_{T_{LS}})\,(t - t_{LS}) / (\Delta t_i)$$

(23) Normal Area Force Coefficient during Inflation

$$SC_N = (SC_{N_\alpha}\alpha + SC_{N_{\alpha^2}}\alpha^2 + SC_{N_{\alpha^3}}\alpha^3)\,(t - t_{LS}) / (\Delta t_i)$$

The aerodynamic forces on the fully deployed parachute are functions of lift and drag coefficients. These aerodynamic coefficients for each canopy type vary with angle of attack, Mach number, effective porosity and parachute-seat relative positions. The equations for the parachute angle of attack are fundamental to a dynamic stability simulation and are developed first.

(24) Angle of Attack, by Scalar Product

$$\alpha = \left|\mathrm{Cos}^{-1}(\mathbf{R}_L \cdot \mathbf{V}_p / (R_L V_p))\right|$$

$$= \left|\mathrm{Cos}^{-1}(R_{x_L}\dot{x}_p + R_{y_L}\dot{y}_p + R_{z_L}\dot{z}_p / R_L V_p)\right|$$

The tangential and normal force coefficients are cubic functions of angle of attack, with curve-fit coefficients dependent upon porosity, Mach number, and distance behind the seat.

(25) Tangential Area Force Coefficient

$$SC_T = SC_{T_{(\alpha=0)}} + SC_{T_\alpha}\alpha + SC_{T_{\alpha^2}}\alpha^2 + SC_{T_{\alpha^3}}\alpha^3$$

(26) Normal Area Force Coefficient

$$SC_N = SC_{N_\alpha}\alpha + SC_{N_{\alpha^2}}\alpha^2 + SC_{N_{\alpha^3}}\alpha^3$$

(27) Lift Force Area

$$SC_L = (SC_N\mathrm{Cos}\alpha - SC_T\mathrm{Sin}\alpha)\,F_c F_d$$

(28) Drag Force Area

$$SC_D = (SC_N\mathrm{Sin}\alpha + SC_T\mathrm{Cos}\alpha)\,F_c F_d$$

(29) Drag Force Magnitude

$$F_D = .5\rho V_p^2 SC_D$$

The drag force in the earth axis system is computed by projection through the earth axis velocity direction cosines.

(30) Velocity Direction Cosines

$$\mathbf{V}_p/V_p = i_e\dot{x}_p/V_p + j_e\dot{y}_p/V_p + k_e\dot{z}_p/V_p$$

(31) Downrange Drag Force

$$F_{xD} = -.5\rho V_p^2 SC_D \dot{x}_p / V_p$$

$$= -.5\rho V_p SC_D \dot{x}_p$$

(32) Lateral Drag Force

$$F_{yD} = -.5\rho V_p SC_D \dot{y}_p$$

(33) Vertical Drag Force

$$F_{zD} = -.5\rho V_p SC_D \dot{z}_p$$

Next, the lift forces are projected on the earth axis system.

(34) Lift Force Magnitude

$$F_L = .5\rho V_p^2 (SC_L)$$

The lift components in the earth axis system are projected through a unit vector developed through the requirements that the lift vector is normal to the parachute velocity vector and lies in the plane formed by the parachute velocity vector and the position vector from the bridle attach point to the parachute center of gravity. These conditions determine the direction of the lift force, while the sense is specified by the sign of (SC_L). A lift stable parachute will be characterized by a positive (SC_L) slope versus α, α carrying no sign because of parachute symmetry.

Developing the unit vector normal to $\mathbf{V}_p$ in the plane of $\mathbf{R}_L$ and $\mathbf{V}_p$ through the triple vector product,

$$\mathbf{m} = \mathbf{V}_p \times \mathbf{V}_p \times \mathbf{R}_L \; / \; |\mathbf{V}_p \times \mathbf{V}_p \times \mathbf{R}_L|$$

$$= i_e m_x + j_e m_y + k_e m_z$$

$$\mathbf{V}_p \times \mathbf{R}_L = \begin{bmatrix} i_e & j_e & k_e \\ \dot{x}_p & \dot{y}_p & \dot{z}_p \\ R_{x_L} & R_{y_L} & R_{z_L} \end{bmatrix}$$

$$= i_e u_p + j_e v_p + k_e w_p$$

Where,

$$u_p = \dot{y}_p R_{z_L} - \dot{z}_p R_{y_L}$$

$$v_p = \dot{z}_p R_{x_L} - \dot{x}_p R_{z_L}$$

$$w_p = \dot{x}_p R_{y_L} - \dot{y}_p R_{x_L}$$

$$\mathbf{V}_p \times \mathbf{V}_p \times \mathbf{R}_L = \begin{bmatrix} i_e & j_e & k_e \\ \dot{x}_p & \dot{y}_p & \dot{z}_p \\ u_p & v_p & w_p \end{bmatrix}$$

$$= i_e a_x + j_e a_y + k_e a_z$$

Where,

$$a_x = \dot{y}_p w_p - \dot{z}_p v_p$$

$$a_y = \dot{z}_p u_p - \dot{x}_p w_p$$

$$a_z = \dot{x}_p v_p - \dot{y}_p u_p$$

$$a = (a_x^2 + a_y^2 + a_z^2)^{1/2}$$

(35) Downrange Lift Unit Vector

$$m_x = a_x / a$$

(36) Lateral Lift Unit Vector

$$m_y = a_y / a$$

(37) Vertical Lift Unit Vector

$$m_z = a_z / a$$

(38) Downrange Lift Force

$$F_{x_L} = F_L m_x$$

(39) Lateral Lift Force

$$F_{y_L} = F_L m_y$$

(40) Vertical Lift Force

$$F_{z_L} = F_L m_z$$

APPENDIX II

SECTION IV

AERODYNAMIC FORCES

The aerodynamic coefficients of the five canopy types are presented in Figures 303 through 312. The tangential force and normal force curve-fit coefficients are tabulated in Table XI.

The following Table shows the relationship between the notes on the graphs and the porosities.

TABLE X

PARACHUTE POROSITY PARAMETERS

POROSITY	SOLID CLOTH	RIBBON
1	.01	.221
2	.0085	.188
3	.0077	.17
4	.0064	.14

TABLE XI
PARACHUTE PARAMETER EFFECTS

Canopy Type	Case	Porosity	C_D/C_{D_∞}*	SC_T (α =0)	SC_{T_α}	$SC_{T_{\alpha^2}}$
Ribless	1	.01	.71	7.00	1.495	3.65
Guide	2	↓	↓	↓	↓	↓
Surface	3		.525			
↓	4	↓	.87	↓	↓	↓
	5	.0077	.71	6.80	2.00	0.
	6	.0064	↓	6.70	.437	3.57
	7,(12)	.0085		6.90	2.29	0.
	8	.01		7.00	1.495	3.65
	9	↓	↓	↓	↓	↓
	10		.91	15.0	3.204	7.94
	11	↓	.95	30.0	6.41	15.82
Flat Circ.	1	.01	.71	7.00	.690	4.58
Cloth	2	↓	↓	↓	↓	↓
↓	3		.525			
	4	↓	.87	↓	↓	↓
	5	.0077	.71	7.15	1.440	0.0
	6	.0064	↓	7.24	2.522	0.0
	7,(12)	.0085		7.08	1.440	0.0
	8	.01		7.00	.690	4.58
	9	↓	↓	↓	↓	↓
	10		.91	15.0	1.371	9.10
	11	↓	.95	30.0	2.745	18.20
Flat Circ.	1	.221	.71	7.00	.1359	-14.41
Ribbon	2	↓	↓	↓	↓	↓
↓	3		.525			
	4	↓	.87	↓	↓	↓
	5	.17	.71	7.00	.293	-30.9
	6	.14	↓	7.00	.293	-30.9
	7,(12)	.188		7.00	.293	-30.9
	8	.221		7.00	.293	-30.9
	9	↓	↓	↓	↓	↓
	10		.91	15.0	.293	-30.9
	11	↓	.95	30.0	.586	-61.5
Equiflo	1	.221	.71	7.00	-.327	-14.6
↓	2	↓	↓	↓	↓	↓
	3		.525			
	4	↓	.87	↓	↓	↓
	5	.17	.71	7.00	-.327	-14.6
	6	.14	↓	7.00	-.327	-14.6
	7,(12)	.188		7.00	-.327	-14.6
	8	.221		7.00	-.327	-14.6
	9	↓	↓	↓	↓	↓
	10		.91	15.0	-.701	-31.4
	11	↓	.95	30.0	-1.402	-62.6
Hemisflo	1	.221	.71	7.00	-.362	-16.18
↓	2	↓	↓	↓	↓	↓
	3		.525			
	4	↓	.87	↓	↓	↓
	5	.17	.71	7.00	-.362	-16.18
	6	.14	↓	7.00	-.362	-16.18
	7,(12)	.188		7.00	-.362	-16.18
	8	.221		7.00	-.362	-16.18
	9	↓	↓	↓	↓	↓
	10		.91	15.0	-.775	-34.6
	11	↓	.95	30.0	-1.55	-69.2

* Wake drag coefficient ratio

(Page 188 is blank)

TABLE XI
PARACHUTE PARAMETER EFFECTS

C_T (r =0)	SC_{T_α}	$SC_{T_\alpha}{}^2$	$SC_{T_\alpha}{}^3$	SC_{N_α}	$SC_{N_\alpha}{}^2$	$SC_{N_\alpha}{}^3$
7.00	1.495	3.69	-7.38	2.86	-0.054	-0.524
6.80	2.00	0.	-2.52			
6.70	.437	3.57	-4.90			
6.90	2.29	0.	-2.70			
7.00	1.495	3.69	-7.38			
15.0	3.204	7.94	-15.85	6.11	-0.116	-1.121
30.0	6.41	15.82	-31.60	12.25	-0.232	-2.25
7.00	.690	4.58	-8.82	-1.962	1.902	2.04
7.15	1.440	0.0	-2.4			
7.24	2.522	0.0	-2.88			
7.08	1.440	0.0	-2.4			
7.00	.690	4.58	-7.00			
15.0	1.371	9.10	-13.92	-3.90	3.78	4.04
30.0	2.745	18.20	-27.80	-7.80	7.55	8.08
7.00	.1359	-14.41	8.05	2.865	8.85	-4.2
15.0	.293	-30.9	17.24	6.14	19.0	-9.00
30.0	.586	-61.5	34.50	12.28	38.0	-18.0
7.00	-.327	-14.6	8.81	18.72	-1.861	-1.185
15.0	-.701	-31.4	18.9	40.1	-3.98	-2.54
30.0	-1.402	-62.6	37.8	80.3	-7.99	-5.08
7.00	-.352	-16.18	9.75	20.7	-2.06	-1.31
15.0	-.775	-34.6	20.85	44.3	-4.41	-2.80
30.0	-1.55	-69.2	41.70	88.6	-8.84	-5.62

B

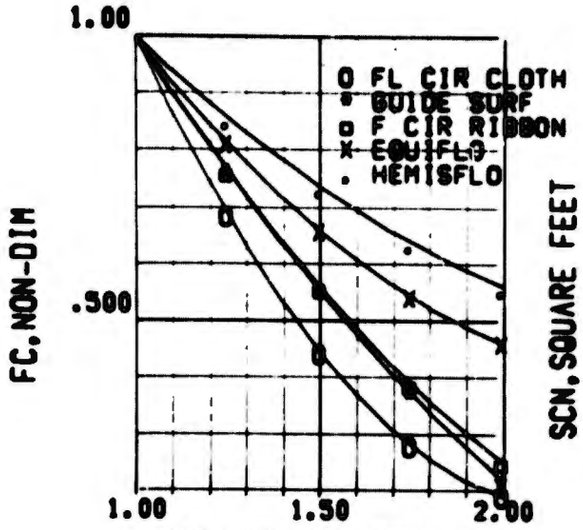

FIG 303 PARACHUTE COMPRESSIBILITY FUNCTIONS

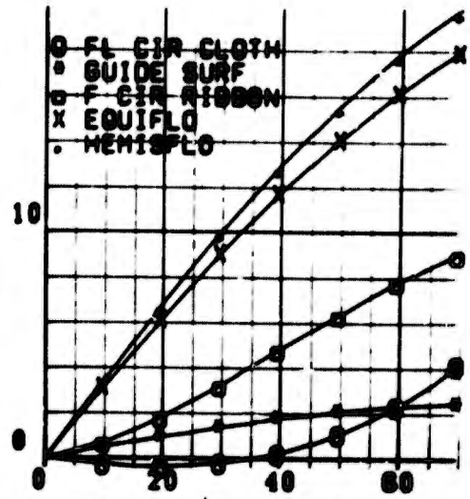

FIG 304 CHUTE NORMAL FORCE AREA COEFF, POROSITY 1

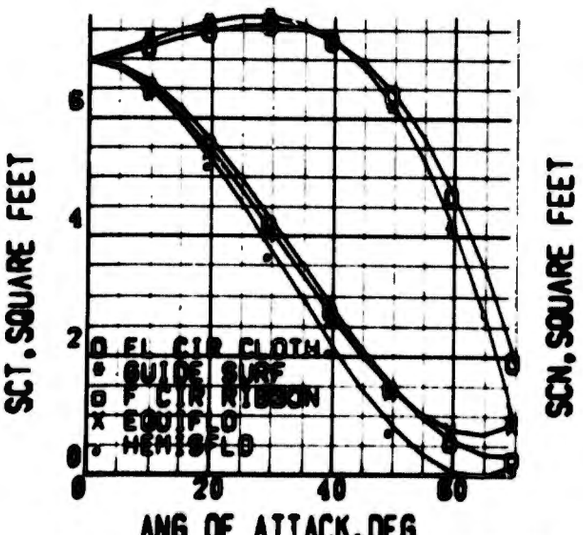

FIG 305 CHUTE TANGENTIAL FORCE AREA COEFF, POROSITY 1

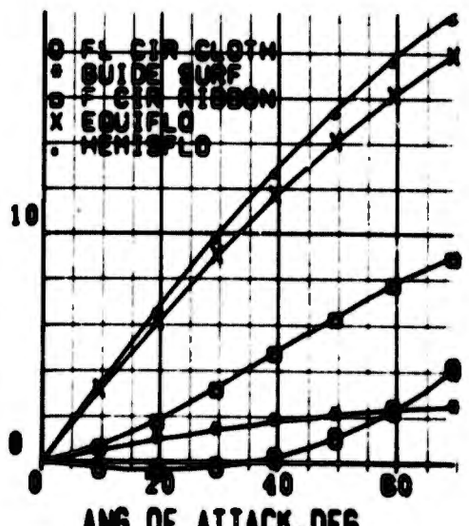

FIG 306 CHUTE NORMAL FORCE AREA COEFF, POROSITY 2

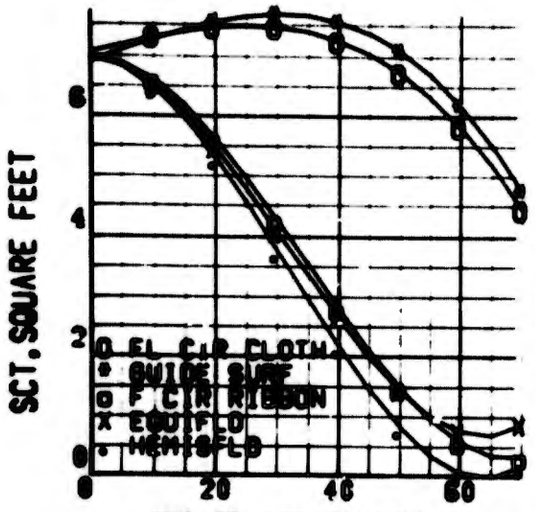

FIG 307 CHUTE TANGENTIAL FORCE AREA COEFF, POROSITY 2

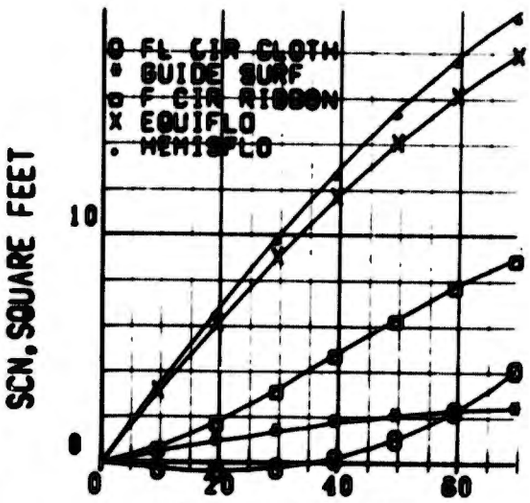

FIG 308 CHUTE NORMAL FORCE AREA COEFF, POROSITY 3

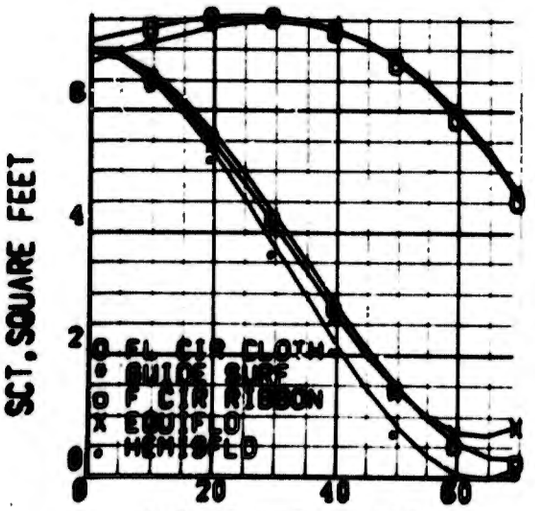

FIG 309 CHUTE TANGENTIAL FORCE AREA COEFF, POROSITY 3

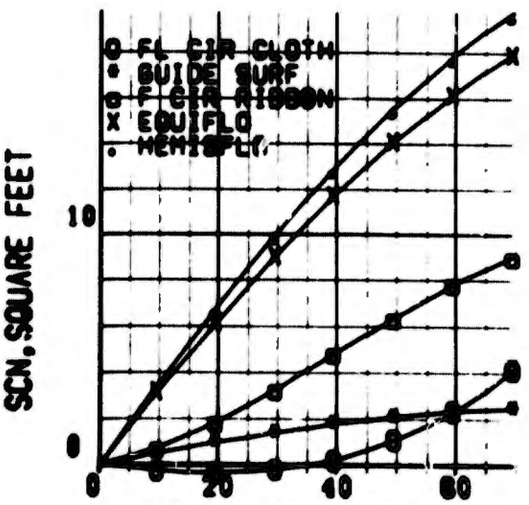

FIG 310 CHUTE NORMAL FORCE AREA COEFF, POROSITY 4

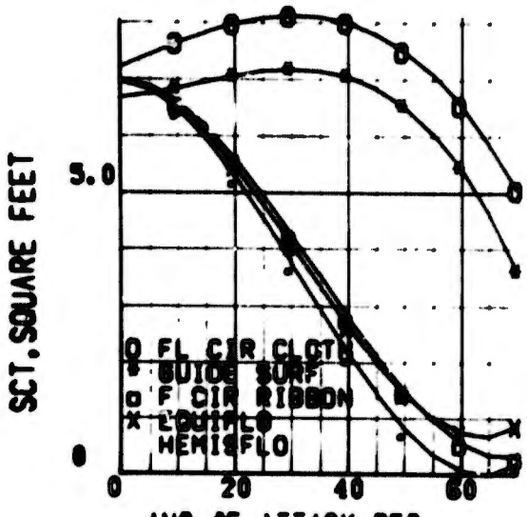

FIG 311 CHUTE TANGENTIAL FORCE AREA COEFF, POROSITY 4

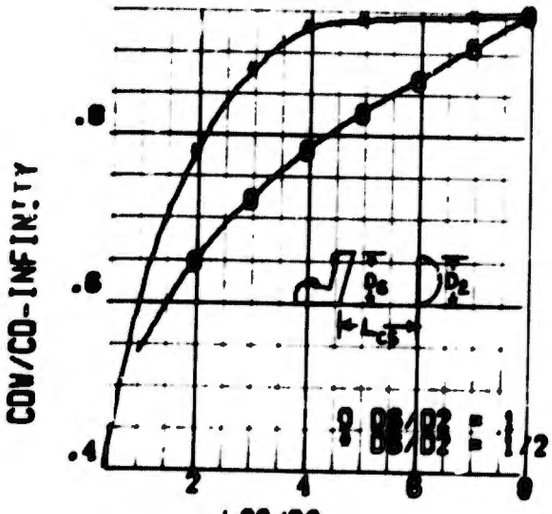

FIG 312 WAKE DRAG COEFFICIENT RATIO

APPENDIX II

SECTION V

NON-AERODYNAMIC FORCES

The non-aerodynamic forces operating on the parachute are: the deployment rocket (or gun) with an impulse/weight ratio of approximately 1.0 lb-sec/lb; the deployment bag strip-off force of about 10.0 lb; line elasticity through a combined Young's Modulus and "squidding" constant of 7000.00 lb/ft. These are all nominal values which will change with the parachute configuration.

APPENDIX II

SECTION VI

BRIDLE EQUATIONS

The parachute is assumed to be attached to the apex of a bridle which may be constructed of one, two, three or four lines which do not support compression. The equations for a multiple line bridle are developed modularly so that any number of lines is represented as an assemblage of simpler bridles. Each line of the bridle is tested for compression and, if compression exists, that line is eliminated from load carrying. The bridle apex position is adjusted for force vector and geometric compatibility with each line elimination until all lines are in tension.

1. Equation of the plane which contains bridle attach points

Four points in the same plane with $(x,y,z,)$ unknown

$$\begin{bmatrix} 1 & x_1 & y_1 & z_1 \\ 1 & x_2 & y_2 & z_2 \\ 1 & x_3 & y_3 & z_3 \\ 1 & x & y & z \end{bmatrix} = 0.$$

Expanding

$$\begin{bmatrix} 1 & y_1 & z_1 \\ 1 & y_2 & z_2 \\ 1 & y_3 & z_3 \end{bmatrix} x - \begin{bmatrix} 1 & x_1 & z_1 \\ 1 & x_2 & z_2 \\ 1 & x_3 & z_3 \end{bmatrix} y + \begin{bmatrix} 1 & x_1 & y_1 \\ 1 & x_2 & y_2 \\ 1 & x_3 & y_3 \end{bmatrix} z - \begin{bmatrix} x_1 & y_1 & z_1 \\ x_2 & y_2 & z_2 \\ x_3 & y_3 & z_3 \end{bmatrix} = 0.$$

For

$Ax + By + Cz + D = 0.$

$$A = \begin{bmatrix} 1 & y_1 & z_1 \\ 1 & y_2 & z_2 \\ 1 & y_3 & z_3 \end{bmatrix} \quad B = \begin{bmatrix} x_1 & 1 & z_1 \\ x_2 & 1 & z_2 \\ x_3 & 1 & z_3 \end{bmatrix} \quad C = \begin{bmatrix} 1 & x_1 & y_1 \\ 1 & x_2 & y_2 \\ 1 & x_3 & y_3 \end{bmatrix} \quad D = \begin{bmatrix} y_1 & x_1 & z_1 \\ y_2 & x_2 & z_2 \\ y_3 & x_3 & z_3 \end{bmatrix}$$

2. Direction cosines of force applied to apex of bridle

$$C\alpha_f = F_{x_{sp}}/F_{sp}$$

$$C\beta_f = F_{y_{sp}}/F_{sp}$$

$$C\gamma_f = F_{z_{sp}}/F_{sp}$$

3. Intersection (x_i, y_i, z_i) of force applied to bridle apex with plane of bridle attach points

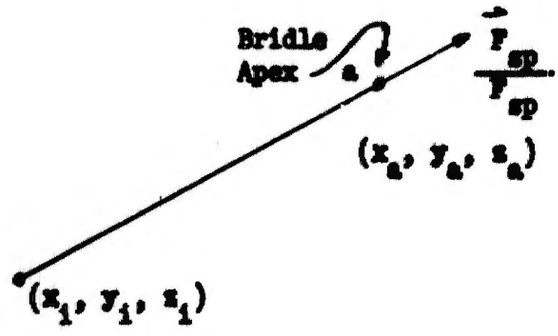

(a) $x_a - x_i = R_{ia} C\alpha_f$

(b) $y_a - y_i = R_{ia} C\beta_f$

(c) $z_a - z_i = R_{ia} C\gamma_f$

Since (x_i, y_i, z_i) lies in the plane of the bridle attach points

(d) $Ax_i + By_i + Cz_i + D = 0.$

To make this equation a function of only x_i

Divide (b) by (a)

$$y_a - y_i = C\beta_f / C\alpha_f \, (x_a - x_i)$$

(e) $y_i = y_a + C\beta_f / C\alpha_f \, (x_i - x_a)$

Divide (c) by (a)

$$z_a - z_i = C\gamma_f / C\alpha_f \, (x_a - x_i)$$

(f) $z_i = z_a + C\gamma_f / C\alpha_f \, (x_i - x_a)$

Substituting (e) and (f) into (d) for $C\alpha_f \neq 0$

$$Ax_i + B[y_a + (C\beta_f / C\alpha_f)(x_i - x_a)] + C[z_a + (C\gamma_f / C\alpha_f)(x_i - x_a)] + D = 0.$$

$$[A + B(C\beta_f / C\alpha_f) + C(C\gamma_f / C\alpha_f)]x_i + B[y_a - (C\beta_f / C\alpha_f)x_a] + C[z_a - (C\gamma_f / C\alpha_f)x_a] + D = 0.$$

$$x_i = \frac{B[(C\beta_f / C\alpha_f)x_a - y_a] + C[(C\gamma_f / C\alpha_f)x_a - z_a] - D}{A + B(C\beta_f / C\alpha_f) + C(C\gamma_f / C\alpha_f)}$$

$$y_i = y_a + (C\beta_f/C\alpha_f)(x_i - x_a)$$

$$z_i = z_a + (C\gamma_f/C\alpha_f)(x_i - x_a)$$

A solution in terms of y_i for $C\beta_f \neq 0$.

$$y_i = \frac{A[(C\alpha_f/C\beta_f)y_a - x_a] + C[(C\gamma_f/C\beta_f)y_a - z_a] - D}{A(C\alpha_f/C\beta_f) + B + C(C\gamma_f/C\beta_f)}$$

$$x_i = x_a + (C\alpha_f/C\beta_f)(y_i - y_a)$$

$$z_i = z_a + (C\gamma_f/C\beta_f)(y_i - y_a)$$

A solution in terms of z_i for $C\gamma_f \neq 0$.

$$z_i = \frac{A[(C\alpha_f/C\gamma_f)z_a - x_a] + B[(C\beta_f/C\gamma_f)z_a - y_a] - D}{A(C\alpha_f/C\gamma_f) + B(C\beta_f/C\gamma_f) + C}$$

$$y_i = y_a + (C\beta_f/C\gamma_f)(z_i - z_a)$$

$$x_i = x_a + (C\alpha_f/C\gamma_f)(z_i - z_a)$$

The set of equations with the largest direction cosine in the denominator is used.

4. Four line bridle

The attach points of the four line bridle are numbered in a counterclockwise direction 1, 2, 3, and 4.

The four line bridle is reduced to a three line bridle by determining on which side of line 2,4 the force-plane intersection point lies.

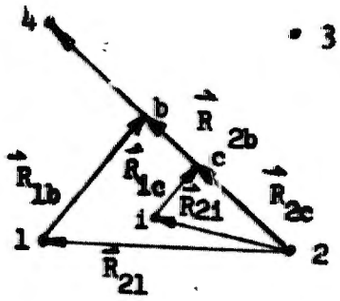

Direction cosines of $\vec{R}_{24}$

$$R_{24} = [(x_4 - x_2)^2 + (y_4 - y_2)^2 + (z_4 - z_2)^2]^{1/2}$$

$$C\alpha_{24} = (x_4 - x_2) / R_{24}$$

$$C\beta_{24} = (y_4 - y_2) / R_{24}$$

$$C\gamma_{24} = (z_4 - z_2) / R_{24}$$

Coordinates of point c

$$\vec{R}_{2c} = R_{2c}\,\vec{R}_{24}/R_{24} = (\vec{R}_{2i} \cdot \vec{R}_{24}/R_{24})\,\vec{R}_{24}/R_{24}$$

$$R_{24} = \vec{R}_{2i} \cdot \vec{R}_{24}/R_{24} = (x_i - x_2)C\alpha_{24} + (y_i - y_2)C\beta_{24} + (z_i - z_2)C\gamma_{24}$$

$$x_c = x_2 + R_{2c}(C\alpha_{24})$$

$$y_c = y_2 + R_{2c}(C\beta_{24})$$

$$z_c = z_2 + R_{2c}(C\gamma_{24})$$

Direction cosines of $\mathbf{R}_{ic}$

$$R_{ic} = [(x_c - x_i)^2 + (y_c - y_i)^2 + (z_c - z_i)^2]^{1/2}$$

$$C\alpha_{ic} = (x_c - x_i) / R_{ic}$$

$$C\beta_{ic} = (y_c - y_i) / R_{ic}$$

$$C\gamma_{ic} = (z_c - z_i) / R_{ic}$$

The same procedure is used to determine coordinates of point b and direction cosines of $\mathbf{R}_{1b}$

$$x_b = x_2 + R_{2b}(C\alpha_{24})$$

$$y_b = y_2 + R_{2b}(C\beta_{24})$$

$$z_b = z_2 + R_{2b}(C\gamma_{24})$$

$$C\alpha_{1b} = (x_b - x_1) / R_{1b}$$

$$C\beta_{1b} = (y_b - y_1) / R_{1b}$$

$$C\gamma_{1b} = (z_b - z_1) / R_{1b}$$

Determine position of force-plane intersection point relative to line 2,4.

$$\text{IF} \quad \frac{\mathbf{R}_{1b} \cdot \mathbf{R}_{ic}}{R_{1b} R_{ic}} = +1.$$

Points i and 1 are on the same side of line 2,4.

$$\text{IF} \quad \frac{\mathbf{R}_{1b} \cdot \mathbf{R}_{ic}}{R_{1b}R_{ic}} = -1.$$

Points i and 1 are on opposite sides of line 2,4.

$$\frac{\mathbf{R}_{1b} \cdot \mathbf{R}_{ic}}{R_{1b}R_{ic}} = C\alpha_{1b}C\alpha_{ic} + C\beta_{1b}C\beta_{ic} + C\gamma_{1b}C\gamma_{ic}$$

5. Three line bridle

If points 1 and i are on the same side of line 2,4, the four line bridle becomes a three line bridle with attach points of 1, 2, and 4. For points 1 and i on opposite sides of line 2,4, the three line bridle attach points are 2, 3, and 4.

To develop the equations for a three line bridle, points 1, 2, and 4 will be used, but the development holds for the other case.

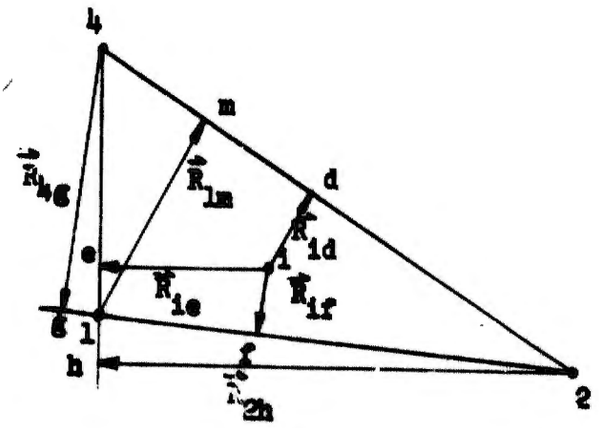

Each bridle line is checked to see if it is in compression. When the first line in compression is found, a two line bridle using the other two lines is considered.

For the bridle line attached at point 1.

$$\text{IF} \quad \frac{R_{1m} \cdot R_{id}}{R_{1m} R_{id}} = -1.$$

This line is slack and a two line bridle attached at points 2 and 4 is investigated.

$$\text{IF} \quad \frac{R_{1m} \cdot R_{id}}{R_{1m} R_{id}} = +1.$$

The line attached at point 1 is in tension and the line attached at point 2 is then checked.

These dot products are computed the same as those in the check with line 2,4.

Checking line attached at point 2.

$$\text{IF} \quad \frac{\mathbf{R}_{2h} \cdot \mathbf{R}_{ie}}{R_{2h} R_{ie}} = -1.$$

This line is slack and a two line bridle attached at points 4 and 1 is investigated.

$$\text{IF} \quad \frac{\mathbf{R}_{2h} \cdot \mathbf{R}_{ie}}{R_{2h} R_{ie}} = +1.$$

The line attached at point 2 is in tension and the line attached at point 4 is then checked.

Checking the line attached at point 4.

$$\text{IF} \quad \frac{\mathbf{R}_{4g} \cdot \mathbf{R}_{if}}{R_{4g} R_{if}} = -1.$$

This line is slack and a two line bridle attached at points 1 and 2 is investigated.

$$\text{IF} \quad \frac{\mathbf{R}_{4g} \cdot \mathbf{R}_{if}}{R_{4g} R_{if}} = +1.$$

All the bridle lines are in tension and the force application point is the orginal bridle apex location.

6. Two line bridle

A two line bridle is left when one of the lines of the three line bridle becomes slack. The following development will use points 1 and 2 for attach points but is valid regardless of the numbers of the attach points.

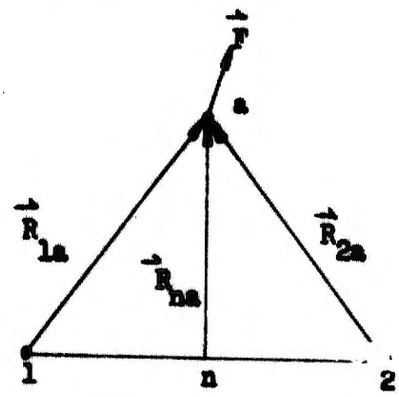

A new axis system is defined as follows.

$$i_0 = R_{na} / R_{na}$$

$$j_0 = R_{2a} \times R_{1a} / |R_{2a} \times R_{1a}|$$

$$k_0 = i_0 \times j_0$$

The direction cosines of R_{na} and the coordinates of n are found as before; i.e. by projecting the known vector R_{1a} on the known vector R_{12} by the scalar product.

Therefore

$$i_o = \vec{R}_{na} / R_{na} = C\alpha_{na} i_s + C\beta_{na} j_s + C\gamma_{na} k_s = i_s D_{11} + j_s D_{21} + k_s D_{31}$$

$$j_o = \begin{bmatrix} i_s & j_s & k_s \\ x_a - x_2 & y_a - y_2 & z_a - z_2 \\ x_a - x_1 & y_a - y_1 & z_a - z_1 \end{bmatrix} / |\vec{R}_{1a} \times \vec{R}_{2a}|$$

$$\begin{aligned} &= i_s[((y_a - y_2) / R_{2a})((z_a - z_1) / R_{1a}) - ((z_a - z_2) / R_{2a})((y_a - y_1) / R_{1a})] \\ &+ j_s[((z_a - z_2) / R_{2a})((x_a - x_1) / R_{1a}) - ((x_a - x_2) / R_{2a})((z_a - z_1) / R_{1a})] \\ &+ k_s[((x_a - x_2) / R_{2a})((y_a - y_1) / R_{1a}) - ((y_a - y_2) / R_{2a})((x_a - x_1) / R_{1a})] \\ &= i_s D_{12} + j_s D_{22} + k_s D_{32} \end{aligned}$$

$k_o = i_o \times j_o$, however it will not be needed

$$\begin{pmatrix} i_o \\ j_o \\ k_o \end{pmatrix} = \begin{bmatrix} D_{11} & D_{21} & D_{31} \\ D_{12} & D_{22} & D_{32} \\ D_{13} & D_{23} & D_{33} \end{bmatrix} \begin{pmatrix} i_s \\ j_s \\ k_s \end{pmatrix} = D^T \begin{pmatrix} i_s \\ j_s \\ k_s \end{pmatrix}$$

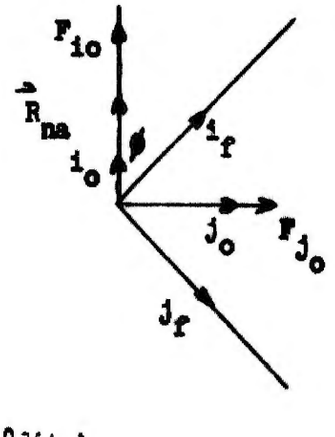

$$\begin{pmatrix} i_o \\ j_o \\ k_o \end{pmatrix} = \begin{bmatrix} \text{Cos } \phi & -\text{Sin } \phi & 0 \\ \text{Sin } \phi & \text{Cos } \phi & 1 \\ 0 & 0 & 1 \end{bmatrix} \begin{pmatrix} i_f \\ j_f \\ k_f \end{pmatrix}$$

The two line bridle rotates through the angle Φ until it and the force applied at the apex lie in the same plane.
Therefore

$$\text{Tan } \Phi = F_{j_o} / F_{i_o}$$

$$\vec{F} = i_s F_x + j_s F_y + k_s F_z$$

$$F_o = \begin{pmatrix} F_{i_o} \\ F_{j_o} \\ F_{k_o} \end{pmatrix} = D^T F$$

$$\text{Tan } \Phi = (D_{12} F_x + D_{22} F_y + D_{32} F_z) / (D_{11} F_x + D_{21} F_y + D_{31} F_z)$$

New normal vector orientation

$$\vec{R}_{na} = R_{na}\, i_f = R_{na}(i_o \text{ Cos } \Phi + j_o \text{ Sin } \Phi)$$

$$= R_{na} \text{ Cos } \Phi\, (D_{11} i_s + D_{21} j_s + D_{31} k_s) + R_{na} \text{ Sin } \Phi\, (D_{12} i_s + D_{22} j_s + D_{32} k_s)$$

The new location of the bridle apex (x_f, y_f, z_f) then becomes

$$x_f = x_n + R_{na}(D_{11} \text{ Cos } \Phi + D_{12} \text{ Sin } \Phi)$$
$$y_f = y_n + R_{na}(D_{21} \text{ Cos } \Phi + D_{22} \text{ Sin } \Phi)$$
$$z_f = z_n + R_{na}(D_{31} \text{ Cos } \Phi + D_{32} \text{ Sin } \Phi)$$

The new bridle apex is the force application point if both lines of the bridle are in tension. A check must be made to determine if one of the lines is slack. The bridle apex has dropped such that $\vec{F}$ passes through line 1,2. If it intersects between points 1 and 2 then both lines are in tension. This new intersection (x_{in}, y_{in}, z_{in}) is now determined.

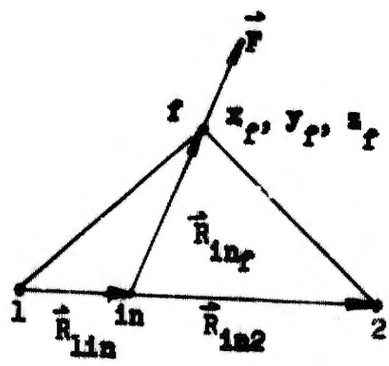

$$R_{in_f} = i_s(x_f - x_{in}) + j_s(y_f - y_{in}) + k_s(z_f - z_{in})$$

$$= i_s(R_{inf}\, C\alpha_f) + j_s(R_{inf}\, C\beta_f) + k_s(R_{inf}\, C\gamma_f)$$

$$R_{in_2} = i_s(x_2 - x_{in}) + j_s(y_2 - y_{in}) + k_s(z_2 - z_{in})$$

$$= i_s(R_{in2}\, C\alpha_{12}) + j_s(R_{in2}\, C\beta_{12}) + k_s(R_{in2}\, C\gamma_{12})$$

Solving for x_{in}, y_{in}, z_{in}

(1) $x_f - x_{in} = R_{inf}\, C\alpha_f$
(2) $y_f - y_{in} = R_{inf}\, C\beta_f$
(3) $z_f - z_{in} = R_{inf}\, C\gamma_f$
(4) $x_2 - x_{in} = R_{in2}\, C\alpha_{12}$
(5) $y_2 - y_{in} = R_{in2}\, C\beta_{12}$
(6) $z_2 - z_{in} = R_{in2}\, C\gamma_{12}$

(2) / (1)
(7) $y_f - y_{in} = C\beta_f / C\alpha_f (x_f - x_{in})$

(3) / (1)

(8) $z_f - z_{in} = C\gamma_f/C\alpha_f(x_f - x_{in})$

(5) / (4)

(9) $y_2 - y_{in} = C\beta_{12}/C\alpha_{12}(x_2 - x_{in})$

(6) / (4)

(10) $z_2 - z_{in} = C\gamma_{12}/C\alpha_{12}(x_2 - x_{in})$

Therefore

$$y_f + C\beta_f/C\alpha_f(x_{in} - x_f) = y_2 + C\beta_{12}/C\alpha_{12}(x_{in} - x_2)$$

$$(C\beta_f/C\alpha_f - C\beta_{12}/C\alpha_{12})\, x_{in} = y_2 - y_f + C\beta_f/C\alpha_f\, x_f - C\beta_{12}/C\alpha_{12}\, x_2$$

For $\Delta = (C\beta_f/C\alpha_f)\, C\alpha_{12} - C\beta_{12} \neq 0$

$$x_{in} = [(y_2 - y_f + C\beta_f/C\alpha_f\ x_f)\, C\alpha_{12} - C\beta_{12}\, x_2] / \Delta$$
$$y_{in} = y_f + C\beta_f/C\alpha_f\ (x_{in} - x_f)$$
$$z_{in} = z_f + C\gamma_f/C\alpha_f\ (x_{in} - x_f)$$

The three equations above are used when $C\alpha_f > C\beta_f$ and $C\gamma_f$

For $C\beta_f > C\alpha_f$ and $C\gamma_f$ the following equations derived in the same manner are used.

For $\Delta = (C\alpha_f/C\beta_f)\, C\beta_{12} - C\alpha_{12} \neq 0$

$$y_{in} = [(x_2 - x_f + (C\alpha_f/C\beta_f)\, y_f)\, C\beta_{12} - C\alpha_{12}\, y_2] / \Delta$$

$$x_{in} = x_f + C\alpha_f/C\beta_f\ (y_{in} - y_f)$$

$$z_{in} = z_f + C\gamma_f/C\beta_f\ (y_{in} - y_f)$$

For $C\gamma_f > C\alpha_f$ and $C\beta_f$ the following equations are used.

$$\Delta = (C\alpha_f/C\gamma_f)\, C\gamma_{12} - C\alpha_{12} \neq 0$$

$$z_{in} = [(x_2 - x_f + C\alpha_f/C\gamma_f\, z_f)\, C\gamma_{12} - C\alpha_{12}\, z_2\,]/\,\Delta$$

$$x_{in} = x_f + C\alpha_f/C\gamma_f\, (z_{in} - z_f)$$

$$y_{in} = y_f + C\beta_f/C\gamma_f\, (z_{in} - z_f)$$

With the coordinate of point in known, R_{1in} is known.

If $R_{1in} \cdot R_{12} < 0$, the line attached at point 2 is slack and the force application point is then point 1.

If $R_{1in} \cdot R_{12} \geq 0$ and $R_{1in} > R_{12}$, the line attached at point 1 is slack and the force application point is then point 2.

If $R_{1in} \cdot R_{12} \geq 0$ and $R_{1in} \leq R_{12}$, both bridle lines are in tension and the force application point is the new bridle apex location.

APPENDIX III

RAIL EQUATIONS AND DATA

TABLE OF CONTENTS

APPENDIX III

SECTION I

GENERAL

The seat equations of motion and the airplane equations are referenced to inertial space and, consequently, represent two completely independent systems when catapult and rail inputs are nulled. In this section the equations for the rail forces and moments on the seat and reactions on the airplane are developed, completing the escape system analytical description.

Seat rail elasticity and contact friction through sliders or rollers are considered to be the only rail parameters linking the seat and airplane. Elastic forces are transmitted to the seat computationally through a stiffness matrix relating the force at each design contact to the translation of the contact from a rail. The translation is computed by integrating the seat and aircraft differential equations independently, transforming the resulting inertial space positions to the rail axis system and attributing the displacements to seat deformations. The friction forces parallel to a rail are presumed to be proportional to the elastic restoring force components normal to the rails. The forces and associated moments from each contact point are projected back on the seat and aircraft axes to complete the interaction cycle.

Invariance of the seat rail stiffness matrix elements is assured by hypothesizing a rigid airplane rail and a flexible seat rail.

APPENDIX III

SECTION II

SYMBOLS

x_s	FT	Downrange earth axis position of seat
y_s	FT	Lateral earth axis position of seat
z_s	FT	Vertical earth axis position of seat
x_a	FT	Downrange earth axis position of airplane
y_a	FT	Lateral earth axis position of airplane
z_a	FT	Vertical earth axis position of airplane
Δx_{sb}	FT	Axial seat axis component of i^{th} slider-block
Δy_{sb}	FT	Lateral seat axis component of i^{th} slider-block
Δz_{sb}	FT	Vertical seat axis component of i^{th} slider-block
x_{ar_0}	FT	Axial airplane axis component of bottom of j^{th} rail
y_{ar_0}	FT	Lateral airplane axis component of bottom of j^{th} rail
z_{ar_0}	FT	Vertical airplane axis component of bottom of j^{th} rail
$z_{sb_{r_{01}}}$	FT	Rail axis vertical position of lower slider block for undeflected rails
Δx_{sb_r}	FT	Axial rail axis component of i^{th} slider-block
Δy_{sb_r}	FT	Lateral rail axis component of i^{th} slider-block

Δz_{sb_r}	FT	Vertical rail axis component of i^{th} slider-block
S_x	LB/FT	Axial rail stiffness
S_y	LB/FT	Lateral rail stiffness
S_z	LB/FT	Vertical rail stiffness
A_{ea}	NON-DIM	Direction cosine matrix relating A/P to earth
A_{es}	NON-DIM	Direction cosine matrix relating seat to earth
D_{ac}	NON-DIM	Direction cosine matrix relating rails to A/P
D_{cs}	NON-DIM	Direction cosine matrix relating seat to deformed rails
C_{cs}	NON-DIM	Direction cosine matrix relating seat to undeformed rails
ΔF_{x_c}	LB	Axial force component on rail due to one slider block
ΔF_{y_c}	LB	Lateral force component on rail due to one slider block
ΔF_{z_c}	LB	Vertical force component on rail due to one slider block
ΔF_{x_s}	LB	Axial seat axis force component on seat due to a slider block
ΔF_{y_s}	LB	Lateral seat axis force component on seat due to a slider block
ΔF_{z_s}	LB	Vertical seat axis force component on seat due to a slider block
ΔF_{x_a}	LB	Axial a/p axis force component on a/p due to a slider block

ΔF_{y_a}	LB	Lateral a/p axis force component on a/p due to a slider block
ΔF_{z_a}	LB	Vertical a/p axis force component on a/p due to a slider block
Δx_{ab}	LB	Axial a/p axis component of a slider block
Δy_{ab}	LB	Lateral a/p axis component of a slider block
Δz_{ab}	LB	Vertical a/p axis component of a slider block
Δr_{x_s}	FT-LB	Rolling moment on seat due to a slider block
Δr_{y_s}	FT-LB	Pitching moment on seat due to a slider block
Δr_{z_s}	FT-LB	Yawing moment on seat due to a slider block
Δr_{x_a}	FT-LB	Rolling moment on airplane due to a slider block
Δr_{y_a}	FT-LB	Pitching moment on airplane due to a slider block
Δr_{z_a}	FT-LB	Yawing moment on airplane due to a slider block
Δr_{x_g}	FT-LB	Rolling moment component in rail axis system required to deform rails
Δr_{y_g}	FT-LB	Pitching moment component in rail axis system required to deform rails
Δr_{z_g}	FT-LB	Yawing moment component in rail axis system required to deform rails
$\Delta r_{x_{sg}}$	FT-LB	Rolling moment on seat from rail deformation
$\Delta r_{y_{sg}}$	FT-LB	Pitching moment on seat from rail deformation
$\Delta r_{z_{sg}}$	FT-LB	Yawing moment on seat from rail deformation

$\Delta r_{x_{a_g}}$	FT-LB	Rolling moment on A/P from rail deformation
$\Delta r_{y_{a_g}}$	FT-LB	Pitching moment on A/P from rail deformation
$\Delta r_{z_{a_g}}$	FT-LB	Yawing moment on A/P from rail deformation
UP	NON-DIM	+ 1 for upward, - 1 for downward ejection
B_F	NON-DIM	Slider block friction coefficient
G_x	FT-LB/RAD	Rail rigidity about axial rail axis
G_y	FT-LB/RAD	Rail rigidity about lateral rail axis
G_z	FT-LB/RAD	Rail rigidity about vertical rail axis

APPENDIX III

SECTION III

SEAT-RAIL-AIRPLANE INTERACTION EQUATIONS

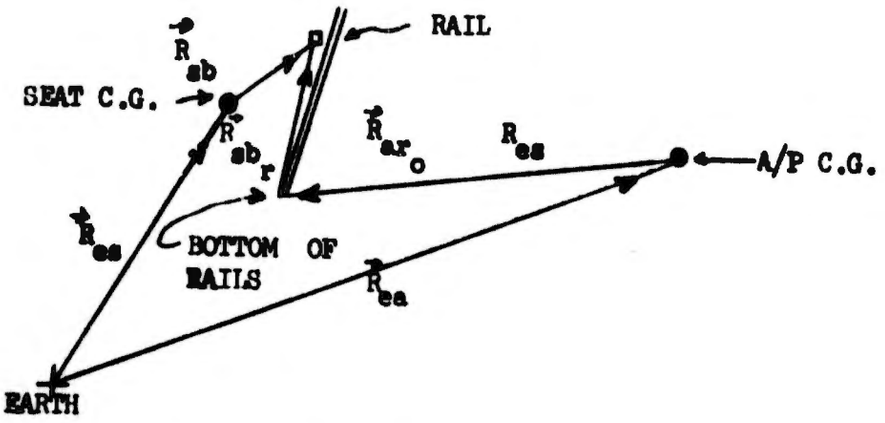

FIGURE 313 SEAT-RAIL-AIRPLANE-EARTH GEOMETRY

The following equations represent the contribution of each individual slider-block.

(1) Vector from Bottom of Rail to Slider-block

$$\vec{R}_{sb_r} = \vec{R}_{es} + \vec{R}_{sb} - \vec{R}_{ea} - \vec{R}_{ar_o}$$

(2) Direction Cosines Relating A/P to Earth

$$\begin{bmatrix} i_e \\ j_e \\ k_e \end{bmatrix} = A_{ea} \begin{bmatrix} i_a \\ j_a \\ k_a \end{bmatrix}$$

(3) Direction Cosines Relating Seat to Earth

$$\begin{bmatrix} i_e \\ j_e \\ k_e \end{bmatrix} = A_{es} \begin{bmatrix} i_s \\ j_s \\ k_s \end{bmatrix}$$

(4) Direction Cosines Relating Rail to A/P

$$\begin{bmatrix} i_e \\ j_e \\ k_e \end{bmatrix} = D_{ac} \begin{bmatrix} i_c \\ j_c \\ k_c \end{bmatrix}$$

(5) Vector from Earth to Seat C.G.

$$R_{es} = i_e x_s + j_e y_s + k_e z_s$$

(6) Vector from Earth to A/P C.G.

$$R_{ea} = i_e x_a + j_e y_a + k_e z_a$$

(7) Vector from Seat C.G. to Slider-block

$$R_{sb} = i_s \Delta x_{sb} + j_s \Delta y_{sb} + k_s \Delta z_{sb}$$

(8) Vector from A/P C.G. to Bottom of Rail

$$R_{ar_0} = i_e x_{ar_0} + j_e y_{ar_0} + k_e z_{ar_0}$$, constant for each rail

(9) Seat Position Relative to Aircraft in Rail Axis System

$$R_{es_c} - R_{ea_c} = (A_{ea}D_{ac})^T(R_{es} - R_{ea})$$

(10) R_{sb} in Rail Axes

$$R_{sb_c} = (A_{ea}D_{ac})^T A_{es}R_{sb}$$

$$= D_{cs}R_{sb}$$

(11) R_{ar_o} in Rail Axes

$$R_{ar_{o_c}} = D_{ac}{}^T R_{ar_o}$$

(12) Expansion of Equation (1)

$$R_{sb_r} = (A_{ea}D_{ac})^T(R_{es} - R_{ea} + A_{es}R_{sb}) - D_{ac}{}^T R_{ar_o}$$

$$\begin{bmatrix} \Delta x_{sb_r} \\ \Delta y_{sb_r} \\ \Delta z_{sb_r} \end{bmatrix} = (A_{ea}D_{ac})^T \left[\begin{bmatrix} x_s - x_a \\ y_s - y_a \\ z_s - z_a \end{bmatrix} + A_{es} \begin{bmatrix} \Delta x_{sb} \\ \Delta y_{sb} \\ \Delta z_{sb} \end{bmatrix} \right] - D_{ac}{}^T \begin{bmatrix} x_{ar_o} \\ y_{ar_o} \\ z_{ar_o} \end{bmatrix}$$

(13) Force Components Required to Deflect Rails in Rail Axis System

$$\Delta F_c = i_c \Delta F_{x_c} + j_c \Delta F_{y_c} + k_c \Delta F_{z_c}$$

$$\Delta F_{x_c} = S_x \Delta x_{sb_r}$$

$$\Delta F_{y_c} = S_y \Delta y_{sb_r}$$

$$\Delta F_{z_c} = S_z(\Delta z_{sb_r} - z_{sb_{r_{u1}}}) \text{ , for seat below normal resting place}$$

$$\Delta F_{z_c} = 0. \text{, for moving seat}$$

(14) Friction Force

$$\Delta F_{z_c} = -B_f \, UP \, (\Delta F_{x_c}{}^2 + \Delta F_{y_c}{}^2)\, 1/2$$

(15) Force Components on Seat in Seat Axis System

$$\Delta F_s = i_s \Delta F_{x_s} + j_s \Delta F_{y_s} + k_s \Delta F_{z_s}$$

$$\begin{bmatrix} \Delta F_{x_s} \\ \Delta F_{y_s} \\ \Delta F_{z_s} \end{bmatrix} = -D_{cs}{}^T \begin{bmatrix} \Delta F_{x_c} \\ \Delta F_{y_c} \\ \Delta F_{z_c} \end{bmatrix}$$

(16) Force Components on A/P in A/P Axis System

$$\Delta F_a = i_a \Delta F_{x_a} + j_a \Delta F_{y_a} + k_a \Delta F_{z_a}$$

$$\begin{bmatrix} \Delta F_{x_a} \\ \Delta F_{y_a} \\ \Delta F_{z_a} \end{bmatrix} = D_{ac} \begin{bmatrix} \Delta F_{x_c} \\ \Delta F_{y_c} \\ \Delta F_{z_c} \end{bmatrix}$$

(17) Slider Block Moment Arm in A/P Axis System

$$R_{ab} = D_{ac} R_{sb} + R_{ar_a}$$

$$\begin{bmatrix} \Delta x_{ab} \\ \Delta y_{ab} \\ \Delta z_{ab} \end{bmatrix} = D_{ac} \begin{bmatrix} \Delta x_{sb} \\ \Delta y_{sb} \\ \Delta z_{sb} \end{bmatrix} + \begin{bmatrix} x_{ar_a} \\ y_{ar_a} \\ z_{ar_a} \end{bmatrix}$$

(18) Moment Components on Seat from Slider Block Reaction

$$\Delta r_s = R_{sb} \times \Delta F_s = i_s \Delta r_{x_s} + j_s \Delta r_{y_s} + k_s \Delta r_{z_s}$$

(19) Moment Components on Airplane from Slider Block Reaction

$$\Delta r_a = R_{ab} \times \Delta F_a = i_a \Delta r_{x_a} + j_a \Delta r_{y_a} + k_a \Delta r_{z_a}$$

(20) Direction Cosines Relating Seat to Undeformed Rails

$$\begin{bmatrix} i_{\&c} \\ j_{\&c} \\ k_{\&c} \end{bmatrix} = C_{cs} \begin{bmatrix} i_s \\ j_s \\ k_s \end{bmatrix}$$

(21) Direction Cosines Relating Deformed Rails to Undeformed Rails

$$\begin{bmatrix} i_c \\ j_c \\ k_c \end{bmatrix} = A_{cc} \begin{bmatrix} i_{\&c} \\ j_{\&c} \\ k_{\&c} \end{bmatrix}$$

where

$$A_{cc} = (A_{ea} D_{ac})^T A_{es} C_{cs}^T = \begin{bmatrix} A_{11} & A_{12} & A_{13} \\ A_{21} & A_{22} & A_{23} \\ A_{31} & A_{32} & A_{33} \end{bmatrix}$$

(22) Rail Angular Deformation

$$\begin{bmatrix} \Delta\phi_c \\ \Delta\theta_c \\ \Delta\psi_c \end{bmatrix} = \begin{matrix} \text{Tan}^{-1}(A_{32}/A_{33}) \\ \text{Sin}^{-1}(-A_{31}) \\ \text{Tan}^{-1}(A_{21}/A_{11}) \end{matrix}$$

(23) Moment Components in Rail Axis System Required to Deform Rails

$$\begin{bmatrix} \Delta r_{x_g} \\ \Delta r_{y_g} \\ \Delta r_{z_g} \end{bmatrix} = \begin{bmatrix} G_x \Delta\theta_c \\ G_y \Delta\theta_c \\ G_z \Delta\psi_c \end{bmatrix}$$

(24) Moment Components on Seat from Rail Deformation

$$\begin{bmatrix} \Delta r_{x_{sg}} \\ \Delta r_{y_{sg}} \\ \Delta r_{z_{sg}} \end{bmatrix} = -D_{cs}^T \begin{bmatrix} \Delta r_{x_g} \\ \Delta r_{y_g} \\ \Delta r_{z_g} \end{bmatrix}$$

(25) Moment Components on A/P from Rail Deformation

$$\begin{bmatrix} \Delta r_{x_{a_g}} \\ \Delta r_{y_{a_g}} \\ \Delta r_{z_{a_g}} \end{bmatrix} = D_{ac} \begin{bmatrix} \Delta r_{x_g} \\ \Delta r_{y_g} \\ \Delta r_{z_g} \end{bmatrix}$$

APPENDIX IV

ROCKET AND CATAPULT EQUATIONS AND DATA

TABLE OF CONTENTS

APPENDIX IV

SECTION I

GENERAL

Differential equations are presented in this section describing the thrust available from catapults and rockets. The thrusts and resulting moments are transformed to a seat axis system through thrust-to-seat direction cosine matrices and catapult reactions are similarly transformed to the airplane axis system.

The equations account for the thrust variations with propellant burn rate, internal pressure, piston friction, heat loss and grain geometry.

The data used in the equations were obtained from Reference 6, 7, and 8.

APPENDIX IV

SECTION II

SYMBOLS

dL_j/dt	IN/SEC	Burn rate of propellant at time j
b	IN/SEC/(LB/IN^2)^n	Burn rate proportionality constant
p_j	LB/IN^2	Pressure on piston base
n	Non-dim	Burn rate exponent of burn rate power law
c_j	SLUG	Mass of propellant burned at time j
c	SLUG	Mass of total propellant
L_j	IN	Length of propellant burned at time j
a_1	1/IN	Coefficients of the propellant grain cubic form function
a_2	1/IN^2	
a_3	1/IN^3	
R	FT-LB/MOLE ^oK	Universal gas constant
T_j	^{o}kelvin	Space average gas temperature at time j
M	MOLES	Molecular weight of propellant
V_o	IN^3	Initial free volume available to the propellant gases
A	IN^2	Piston area

x	IN	Distance piston has traveled
P_B	LB/IN^2	Booster pressure
F_c	LB	Force transmitted to seat
k_1	LB/LB/FT^2	Friction proportionality constant
$P_{(tang\ lock)}$	LB/IN^2	Pressure actuating the tang which allows the piston to move
$D_{11_{cs}}$ ⋮ $D_{33_{cs}}$	NON-DIM	Direction cosines relating seat to catapult
$D_{11_{ac}}$ ⋮ $D_{33_{ac}}$	NON-DIM	Direction cosines relating catapult to airplane
$F_{x_{cs}}$	LB	Seat axial force from catapult
$F_{y_{cs}}$	LB	Seat lateral force from catapult
$F_{z_{cs}}$	LB	Seat vertical force from catapult
$M_{x_{cs}}$	FT-LB	Seat rolling moment from catapult
$M_{y_{cs}}$	FT-LB	Seat pitching moment from catapult
$M_{z_{cs}}$	FT-LB	Seat yawing moment from catapult
$F_{x_{ca}}$	LB	Airplane axial force from catapult

$F_{y_{ca}}$	LB	Airplane lateral force from catapult
$F_{z_{ca}}$	LB	Airplane vertical force from catapult
$r_{x_{ca}}$	FT-LB	Airplane rolling moment from catapult
$r_{y_{ca}}$	FT-LB	Airplane pitching moment from catapult
$r_{z_{ca}}$	FT-LB	Airplane yawing moment from catapult
Δx_{cs}	FT	Axial seat axis coordinate of catapult to seat attach point
Δy_{cs}	FT	Lateral seat axis coordinate of catapult to seat attach point
Δz_{cs}	FT	Vertical seat axis coordinate of catapult to seat attach point
$x_{a_{r_o}}$	FT	Axial airplane axis coordinate of catapult to airplane attach point
$y_{a_{r_o}}$	FT	Lateral airplane axis coordinate of catapult to airplane attach point
$z_{a_{r_o}}$	FT	Vertical airplane axis coordinate of catapult to airplane attach point
k_3	NON-DIM	Heat loss constant
T_v	°Kelvin	Constant volume flame temperature
c_v	CAL/SLUG °K	Constant volume specific heat
c_o	SLUG	Booster propellant mass

γ	NON-DIM	Ratio of specific heats
$\dot{x}$	IN/SEC	Piston speed
m	SLUGS	Ejected mass

APPENDIX IV

SECTION III

CATAPULT FORCES AND MOMENTS ON THE SEAT

The thrust available from a cartridge actuated device with a specified grain configuration and chemical composition is primarily a function of the propellant burn rate which depends upon the internal pressure which, in turn, varies with the free volume changes. The free volume available to the expanding gases is solely a function of the seat-cylinder relative position which is computed by integrating the seat-rail differential equations. The seat-rail accelerations are formulated in Appendices I and III, therefore, only the burn rate differential equation and associated pressure-force relationship are needed to complete the system description.

The following equations were extracted from Reference 6.

(1) Propellant Burn Rate at Time t_j

$$dL_j/dt = b\, p_j^n \quad , \quad c_j \leq c$$

$$= 0. \quad , \quad c_j > c$$

(2) Propellant Burned at Time t_j

$$c_j = (a_1 L_j + a_2 L_j^2 + a_3 L_j^3)\, c \quad , \quad c_j \leq c$$

$$= c \quad , \quad c_j > c$$

(3) Space Average Gas Temperature

$$T_j = (1 - k_3)\, T_v - .5(1 + k_1)\, (\dot{x})^2 m \,/\, (c_v\, (c_j + c_0))$$

(4) Pressure at Time t_j

$$p_j = (R/M)\, T_j\, (c_j + c_0) \,/\, (V_0 + Ax)$$

Where c_0 and c_v are given by

$$c_0 = p_0 V_0 \,/\, ((R/M)\, T_v\, (1 - k_3))$$

$$c_v = R \,/\, (M(\gamma - 1))$$

(5) Force Transmitted to the Seat

$$F_c = A\, p_j \,/\, (1 + k_1) \quad , \quad p_j \geq p(\text{tang lock})$$

$$= 0. \quad , \quad p_j < p(\text{tang lock})$$

The catapult force is applied to the seat at a point off the seat center of gravity, resulting in moment components as well as force components. The component axis transformation is accomplished through the direction cosines expressed by the unit vectors--

$$\begin{bmatrix} i_c \\ j_c \\ k_c \end{bmatrix} = \begin{bmatrix} D_{11_{cs}} & D_{12_{cs}} & D_{13_{cs}} \\ D_{21_{cs}} & D_{22_{cs}} & D_{23_{cs}} \\ D_{31_{cs}} & D_{32_{cs}} & D_{33_{cs}} \end{bmatrix} \begin{bmatrix} i_s \\ j_s \\ k_s \end{bmatrix}$$

The catapult force vector is parallel to the rail and, for headward ejection, in the negative rail Z-direction.

$$\mathbf{F}_c = -F_c k_c$$

Projecting this force on the seat axis system results in the three force components,

$$F_{x_{cs}} = \mathbf{F}_c \cdot i_s = -F_c D_{31_{cs}}$$

$$F_{y_{cs}} = \mathbf{F}_c \cdot j_s = -F_c D_{32_{cs}}$$

$$F_{z_{cs}} = \mathbf{F}_c \cdot k_s = -F_c D_{33_{cs}}$$

With these force components and known moment arms, the standard vector product is used to compute moments. Recapitulating below.

(6) Seat Axial Force from the Catapult

$$F_{x_{cs}} = -D_{31_{cs}} F_c$$

(7) Seat Side Force from the Catapult

$$F_{y_{cs}} = -D_{32_{cs}} F_c$$

(8) Seat Normal Force from the Catapult

$$F_{z_{cs}} = -D_{33_{cs}} F_c$$

(9) Seat Rolling Moment from the Catapult

$$r_{x_{cs}} = \Delta y_{cs} F_{z_{cs}} - \Delta z_{cs} F_{y_{cs}}$$

(10) Seat Pitching Moment from the Catapult

$$r_{y_{cs}} = \Delta z_{cs} F_{x_{cs}} - \Delta x_{cs} F_{z_{cs}}$$

(11) Seat Yawing Moment from the Catapult

$$r_{z_{cs}} = \Delta x_{cs} F_{y_{cs}} - \Delta y_{cs} F_{x_{cs}}$$

TABLE XII
CATAPULT THERODYNAMIC CONSTANTS

T_v	=	2653.00
b	=	.0316
n	=	.44
c	=	.0053
R	=	1.08×10^6
M	=	25.47
V_o	=	5.9
A	=	5.9
a_1	=	.05
a_2	=	130.0
a_3	=	1500.0
C_v	=	$.231 \times 10^6$
k_1	=	.09
k_3	=	.3
c_o	=	$.5 \times 10^{-5}$

APPENDIX IV

SECTION IV

CATAPULT FORCES AND MOMENTS ON THE AIRPLANE

The known catapult force reaction projected on the airplane axis system is computed in the same way as the seat calculation, through the airplane to rail relationship,

$$\begin{bmatrix} i_a \\ j_a \\ k_a \end{bmatrix} = \begin{bmatrix} D_{11_{ac}} & D_{12_{ac}} & D_{13_{ac}} \\ D_{21_{ac}} & D_{22_{ac}} & D_{23_{ac}} \\ D_{31_{ac}} & D_{32_{ac}} & D_{33_{ac}} \end{bmatrix} \begin{bmatrix} i_c \\ j_c \\ k_c \end{bmatrix}$$

resulting in,

(12) Airplane Axial Force from the Catapult

$$F_{x_{ca}} = -F_c D_{13_{ac}}$$

(13) Airplane Side Force from the Catapult

$$F_{y_{ca}} = -F_c D_{23_{ac}}$$

(14) Airplane Normal Force from the Catapult

$$F_{z_{ca}} = -F_c D_{33_{ac}}$$

(15) Airplane Rolling Moment from the Catapult

$$\mathcal{M}_{x_{ca}} = y_{a_{r_0}} F_{z_{ca}} - z_{a_{r_0}} F_{y_{ca}}$$

(16) Airplane Pitching Moment from the Catapult

$$\mathcal{M}_{y_{ca}} = z_{a_{r_0}} F_{x_{ca}} - x_{a_{r_0}} F_{z_{ca}}$$

(17) Airplane Yawing Moment from the Catapult

$$r_{z_{ca}} = x_{a_{r_o}} F_{y_{ca}} - y_{a_{r_o}} F_{x_{ca}}$$

APPENDIX IV

SECTION V

SUSTAINER ROCKET FORCES AND MOMENTS ON THE SEAT

Except for the volume change equations and a test for sonic flow at the throat, the rocket force can be expressed by a set of equations analogous to those for the catapult in Section IV of this appendix. During the burning of the propellant grain, a variation of the area on which the pressure operates is given by an equation which is of the same form as the burn rate law, equation (1). The energy balance equation (3) and pressure equation (4), along with Piobert's form factor [equation (2)] are identical to the catapult equations when the piston travel terms, x and $\dot{x}$, are set to zero. With these modifications, the rocket and catapult equations are interchangeable. The full details of the rocket equations are given in Part I, Volume 3.

APPENDIX IV

SECTION VI

PARACHUTE EJECTION MORTAR REACTION ON THE SEAT

When an ejection mortar is used instead of a rocket to deploy the parachute, a reaction on the seat results, with reaction force and moment equations identical in form to those of Section III of this appendix. The magnitude of the mortar reaction is a parameter, given in Appendix II, Section V - with a sign reversal on the force sense.

REFERENCES

1. Wind Tunnel Report 69, "Transonic and Supersonic Tests of a 0.096 Scale Man-Seat Jettisonable Capsule Model," Massachusetts Institute of Technology, Contract AF 33(616)-369, December 1953 - January 1954.

2. "Full Scale Subsonic Wind Tunnel Tests on Fully Equipped 75 and 5 Percentile Dummies," Technical Report AFFDL-TR-67-44, August 1967.

3. "United States Air Force Parachute Handbook," WADC TR 55-265, Dec 1958 ASTIA No. AD 118036.

4. "Performance and Design Criteria for Deployable Aerodynamic Decelerators," American Power Jet Company, TR No. ASD-TR-61-579, Dec 1963.

5. Military Specification MIL-S-9479 (USAF) Amendment 1, 27 Nov 1967, "Seat System: Upward Ejection, Aircraft, General Specifications for"

6. "An Evaluation of the High-Low Ballistic Principle for Cartridge Actuated Devices," NWL Report No. 1964, U.S. Naval Weapons Laboratory, Dahlgren, Va.

7. Talley Industries - Product Data Sheet.

8. "Propellant Actuated Devices, Engineering Manual", IEP 65-6370-8, U.S. Army Munitions Command, Frankford Arsenal, Philadelphia, Pa., 19137, April 1965.

9. "Aerodynamic Deployable Decelerator Performance - Evaluation Program, Phase III", FDL-TR-67-60, Oct. 1967, F. Bloetscher, W. V. Arnold.

10. Report No. FDL-TDR-64-31 Feasibility Investigation of a Hybrid Rocket for Crew Escape Capsule Applications, March 1964.

11. C. T. Morgan et al, Human Engineering Guide to Equipment Design, McGraw-Hill, New York, 1963.

12. A. Leone, Survey of Methods for Deflecting Exhaust in Missile Control, U.S. Naval Air Rocket Station Report No. 60.

13. Department of the Air Force Technical Order, TO 11P-14, Propellant Actuated Devices, November 1965.

14. George P. Sutton, Rocket Propulsion Elements, 2nd Edition, John Wiley & Sons, Inc., New York.

15. George C. Panelli, Lockheed Aircraft Corp., A Handbook of Performance Trade-offs for Solid Rockets, March 1965.

16. LTV Aerospace Corp., Propulsion System Study for Storable Liquid and Solid Propellant Rocket Motors, May 1964.

17. AIAA paper, A. L. Wahlqurst, Some Aspects of Hybrid Propulsion Systems, July 1964.

18. James G. Crum, Technical Paper No. 272, 20th National Conference, Society of Aeronautical Weight Engineers, Introduction to Solid Propellant Rocket Motors, May 1961.

19. Studies to Determine Dynamic Displacement of Seat/Man Center of Gravity Due to Rocket Thrust, Aerospace Crew Equipment Laboratory, NAEC-ACEL-531, 30 July 1965.

20. A-7D - I-C2 Seat C.G. Survey Structures and Systems Laboratories Test Information Release TR No. 67-59900-066, 1-30-69.

21. Nozzle Angle Verification Test Report Rocket Power P/N 2174-520 Rocket Catapult, Rocket Power, Inc., Document No. 8052, MPO 3394-01, 27 May 1965.

Unclassified
Security Classification

DOCUMENT CONTROL DATA - R & D

(Security classification of title, body of abstract and indexing annotation must be entered when the overall report is classified)

1. ORIGINATING ACTIVITY *(Corporate author)*

LTV Aerospace Corporation

2a. REPORT SECURITY CLASSIFICATION

Unclassified

2b. GROUP

3. REPORT TITLE

Study and Design of an Ejection System for VTOL Aircraft.
Part 1, Volume 2, Escape System Parameters Analysis

4. DESCRIPTIVE NOTES *(Type of report and inclusive dates)*

Final Report April 1969 - January 1970

5. AUTHOR(S) *(First name, middle initial, last name)*

I. L. Clinkenbeard
E. O. Cartwright, Jr.
C. R. Eldredge

6. REPORT DATE

March 1970

7a. TOTAL NO. OF PAGES

244

7b. NO. OF REFS

21

8a. CONTRACT OR GRANT NO.

F 33615-69-C-1692

b. PROJECT NO.

1362

c.

d.

9a. ORIGINATOR'S REPORT NUMBER(S)

9b. OTHER REPORT NO(S) *(Any other numbers that may be assigned this report)*

AFFDL-TR-70-1, Part I, Volume 2

10. DISTRIBUTION STATEMENT

This document is subject to special export controls and each transmittal to foreign governments or foreign nationals may be made only with prior approval of the AF Flight Dynamics Laboratory (FDFR). Wright-Patterson AFB, Ohio

11. SUPPLEMENTARY NOTES

12. SPONSORING MILITARY ACTIVITY

Air Force Flight Dynamics Laboratory
Wright-Patterson Air Force Base,
Ohio 45433

13. ABSTRACT

Ejection seat system differential equations are derived which describe the system trajectories from escape initiation to crew recovery. The equations are solved by digital computer through a numerical integration algorithm, and time history plots are presented for preliminary design information. Trajectory dynamics are computed for the seat as it is catapuled along a set of flexible rails constrained to translate with the aircraft. The impetus of seat-rail separation is simulated, and the airplane and seat trajectories are portrayed as the seat responds to a sequence of forces from rockets and parachutes. Acceleration loads on the man are computed throughout the time history, demonstrating the effects of parachute projection, snatch forces, and opening shocks as well as catapult and sustainer rocket forces. A comparative analysis of catapult and sustainer rocket techniques is included.

This document is subject to special export controls and each transmittal to foreign governments or foreign nationals may be made only with prior approval of the AF Flight Dynamics Laboratory (FDFR), Wright-Patterson AFB, Ohio

DD FORM 1 NOV 65 1473 (PAGE 1)

S/N 0101-807-6801

Unclassified
Security Classification

14 KEY WORDS	LINK A		LINK B		LINK C	
	ROLE	WT	ROLE	WT	ROLE	WT
DD1473						
Escape initiation						
Crew recovery						
Solid cloth parachutes						
Ribbon type parachute						
Drag parachute						
Seat Tip-off						
Seat-man Equations of Motion						
Parachute Equations of Motion						
Rail Equations						
Rocket and Catapult Equations						